



Enhancement of the fatigue performance of Ti-6Al-4V implant products.

WIMALASIRI, Dematapaksha H.R.J.

Available from the Sheffield Hallam University Research Archive (SHURA) at:

<http://shura.shu.ac.uk/20552/>

A Sheffield Hallam University thesis

This thesis is protected by copyright which belongs to the author.

The content must not be changed in any way or sold commercially in any format or medium without the formal permission of the author.

When referring to this work, full bibliographic details including the author, title, awarding institution and date of the thesis must be given.

Please visit <http://shura.shu.ac.uk/20552/> and <http://shura.shu.ac.uk/information.html> for further details about copyright and re-use permissions.

Adsetts Centre, City Campus
Sheffield S1 1WD

102 046 626 X



Sheffield Hallam University
Learning and Information Services
Adsetts Centre, City Campus
Sheffield S1 1WD

REFERENCE

ProQuest Number: 10701199

All rights reserved

INFORMATION TO ALL USERS

The quality of this reproduction is dependent upon the quality of the copy submitted.

In the unlikely event that the author did not send a complete manuscript and there are missing pages, these will be noted. Also, if material had to be removed, a note will indicate the deletion.



ProQuest 10701199

Published by ProQuest LLC (2017). Copyright of the Dissertation is held by the Author.

All rights reserved.

This work is protected against unauthorized copying under Title 17, United States Code
Microform Edition © ProQuest LLC.

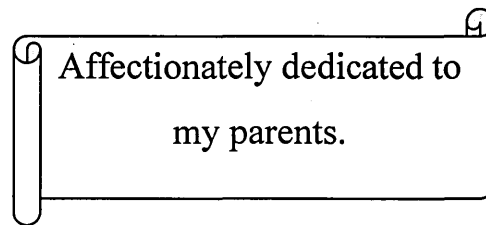
ProQuest LLC.
789 East Eisenhower Parkway
P.O. Box 1346
Ann Arbor, MI 48106 – 1346

Enhancement of the Fatigue Performance of Ti-6Al-4V Implant Products

**Dematapaksha Hewage
Ruminda Jeewantha Wimalasiri**

**A thesis submitted in partial fulfilment of the requirements of
Sheffield Hallam University
for the degree of Doctor of Philosophy**

January, 2009



Affectionately dedicated to
my parents.

PREFACE

This thesis is submitted in partial fulfilment of the requirements of Sheffield Hallam University for the degree of Doctor of Philosophy. This thesis is based on the findings of research carried out in the Faculty of Arts, Computing, Engineering and Sciences, Sheffield Hallam University.

The content of the thesis is original except where specific references and acknowledgments are made to other work. No part of this thesis has been submitted for any degree or diploma at this, or any other university.

D.H.R.J. Wimalasiri

January, 2009

ACKNOWLEDGMENTS

I am particularly indebted to my Director of Studies, Professor Robert Akid for his valuable guidance and constructive advice to keep me focused on the research work and to his kind friendship. The advice and support extended by Dr. Upul Fernando is sincerely acknowledged. I would also like to thank my other supervisors Professor Roger Eccleston and Dr. Syed Hassan for their assistance. I would like to thank Faculty of ACES, Sheffield Hallam University for the opportunity to undertake postgraduate study and providing necessary facilities and assistance to fulfil my research.

I sincerely acknowledge my external supervisors, Dr. Anita Clark and Mr. Keith Jackson, Joint Replacement Instrumentation (JRI) Ltd for their excellent support and encouragement. I would like to thank JRI Ltd and the members of the staff for providing material, test samples, machine and workshop assistance, expert advice and relevant information regarding the Ti-6Al-4V implant products and financial assistance towards the final year and providing me a friendly environment to work through my research.

I would like to thank the Department of Mechanical Engineering, The Open University of Sri Lanka for providing me study leave to complete my postgraduate studies and for financial assistance towards first two years of the research.

I would like to thank members of the technical staff, notably Dr. Keith Wheelhouse, Mr. Tim O'Hara, Mr. Bob Burton, Mr. Mac Jackson, Mr. John Bradshaw, Mr. Steve Magowen, Mr. Tony Earnshaw, Mr. Stuart Crease, Mr. Brian Didsbury, Mr. Roger Tingle, Mr. John Bickers and Mr. Bob Grant for their support throughout my research.

I would like to thank Dr. Rohan Tittagala, Mr. Anura Uthumange, Dr. Willie Brink, Mr. Shivaraj Alavandimath and all who helped and inspired me to complete this research.

Finally I would like to thank my wife Sharnileka and daughter Oneli for their support, devotion and understanding during the cause of this research.

ABSTRACT

Implants surgery, in particular hip implants, is fast becoming a routine, popular approach for curing diseases such as, osteoarthritis and rheumatic arthritis. However one potential problem with the insertion of a metal implant is that of the risk of fatigue failure. Numerous factors affect the propensity of a metal to fatigue, none more so than the physical and stress state of the surface. This research is focused on an assessment of the role of manufacturing processes on the fatigue performance of hip implants made from a Ti-6Al-4V alloy.

The role of surface defects, surface residual stresses and material microstructural properties which influence fatigue performance were examined. Characterization of the implant material and of the processes involved in actual hip implant manufacturing were conducted. Rotating bend fatigue testing using hour glass shaped specimens was conducted to evaluate the fatigue performance at selected manufacturing stages. The surface roughness/defects and residual stresses were measured prior to conducting fatigue tests. A variation of fatigue limit, attributed to variations of surface roughness and surface residual stress was observed. The influence of parameters such as, stress ratio and mean stress effect, variation of fracture mechanics parameters (*e.g.* ΔK_{th}) and the limiting threshold conditions for different stages of cracks were investigated in the context of Kitagawa-Takahashi (K-T) type diagrams. Experimental data was used to develop models which were used to calculate, (i). fatigue life at respective stress amplitude and, (ii). the fatigue limit of components with known surface roughness/defect size and residual stress. To evaluate material crack growth properties a surface replication method was used. The output from both models showed good correlation with experimental data. Comprehensive fractography was conducted using optical, secondary electron, and infinite focus microscopy to support the results obtained from fatigue testing.

Analysis was performed on in-vivo hip implant failure data covering the last 12 years. Fatigue failures occur in two locations on the implant stem, namely the cone area and the neck area. These two locations were investigated separately to identify the factors, such as; the category of implant most vulnerable to failure, service life, design features, fixation with the host bone, crack initiation features and propagation details. An attempt was made to compare in-vivo fatigue features with experimental fatigue results.

X-ray diffraction (XRD) was used to investigate the surface residual stresses resulting from different manufacturing processes. The results were confirmed and software and hardware settings were calibrated in accordance with the results obtained from XRD analysis conducted at National Physical Laboratories (NPL), UK. Surface roughness measurements were also conducted using stylus type surface profilometer.

The knowledge gained from this research can be used to understand the causes and modes of in-vivo fatigue failure of hip implants made of Ti-6Al-4V. Understanding the fatigue/mechanical properties of the implant material enables recommendations and optimization of good practice in manufacturing to eliminate in-vivo fatigue failures.

CONTENTS

PREFACE	I
ACKNOWLEDGMENTS	II
ABSTRACT	III
CONTENTS	IV
<u>CHAPTER 1: INTRODUCTION</u>	1
<u>CHAPTER 2: LITERATURE REVIEW</u>	6
2.1. Introduction	6
2.2. Hip Implants	7
2.3. Implant Grade Titanium Alloy (Ti-6Al-4V)	9
2.4. Use of Hydroxyapatite Ceramic (H-AC) in Implants	11
2.5. Metal Fatigue	12
2.5.1. Introduction	12
2.5.2. Fatigue Crack Initiation	13
2.5.3. Fatigue Crack Propagation	15
2.5.4. Stress Life (S-N) Approach of Fatigue Analysis	18
2.5.5. Microstructural Effects on Fatigue Behaviour	20
2.5.6. Mean Stress Effect on Fatigue Behaviour	22
2.5.7. Kitagawa-Takahashi (K-T) Type Diagram	25
2.5.8. Concluding Remarks of Metal Fatigue	28
2.6. Fatigue Failure in Very High Cycle Regime	29
2.7. Fatigue Behaviour of Ti-6Al-4V Alloy	32
2.8. Fatigue in Hip Implants	37
2.9. Stress Distribution in Hip Implants	38
2.9.1. Methodology of Analysis	38
2.9.2. Stress Distribution in Neck Area	40
2.9.3. Stress Distribution in Cone Area	41

2.10. Surface Roughness and Its Influence on Fatigue Behaviour	42
2.10.1. Effect of Surface Roughness on Fatigue Performance	42
2.10.2. Parameters of Surface Roughness Measurements	43
2.11. Residual Stresses and Its Effects on Fatigue Performance	45
2.12. X-ray Diffraction (XRD) Technology for Residual Stress Measurements	48
2.12.1. Introduction	48
2.12.2. Bragg's Law	49
2.12.3. Measurement of Residual Stress	50
2.12.4. Different Positions of Diffractometer Movements	53
2.12.5. Depth of Penetration	53
2.12.6. Selection of Crystallographic Plane $\{hkl\}$	54
2.12.7. Sample Preparation	55
2.12.8. Irradiated Area on the Sample by the X-ray Beam	55
2.13. Manufacturing Processes and Influence to Fatigue Performance	57
2.13.1. Introduction	57
2.13.2. Grit Blasting, Ultrasonic Cleaning and Plasma Spraying Processes	57
2.13.2.1. Effects of Grit Blasting	58
2.13.2.2. Effects of H-AC Coating on Titanium Substrate	58
2.13.3. Influence of Manufacturing Processes on Fatigue Performance	60
<u>CHAPTER 3: FAILURE ANALYSIS OF HIP IMPLANTS</u>	63
3.1. Introduction	63
3.2. Fatigue Failures of JRI Furlong® H-A.C. Supravit® Coated Hip Replacements Made out of Ti-6Al-4V	65
3.2.1. Introduction	65
3.2.2. Failures at the Cone Region	66
3.2.2.1. Design Modification at Cone Region	66
3.2.2.2. Failure Distribution	67

3.2.3. Failures at the Neck Region	68
3.2.3.1. Design Modification at Neck Region	69
3.2.3.2. Failure Distribution	70
<u>CHAPTER 4: REVIEW OF MANUFACTURING PROCESSES USED IN HIP IMPLANT PRODUCTION</u>	72
4.1. Introduction	72
4.2. JRI Processes Involved in Manufacturing in Hip Implants	72
4.2.1. Manufacturing of Cone Region	73
4.2.1.1. Cone Region Manufacture (Route.1)	73
4.2.1.2. Cone Region Manufacture (Route.2)	76
4.2.2. Neck Region Manufacture (Route 03)	77
<u>CHAPTER 5: EXPERIMENTAL PROCEDURE</u>	79
5.1. Introduction	79
5.2. Fatigue Tests	79
5.2.1. Rotary Bending Fatigue Tests Specimen	79
5.2.2. Rotary Bending Fatigue Testing Apparatus and Test Procedure	80
5.2.3. Stress Calibration of the Rotary Bending Machine in High Cycle Fatigue	82
5.2.3.1. Need for Calibration	82
5.2.3.2. Calibration Procedure	83
5.2.4. Fatigue Tests – Phase.1	84
5.2.4.1. Test Program – Phase.1	84
5.2.4.2. Sample Preparation	85

5.2.5. Fatigue Tests – Phase.2	85
5.2.5.1. Test Program – Phase.2	85
5.2.5.2. Sample Preparation	86
5.3. Determination of Surface Roughness	87
5.4. Residual Stress Measurement by X-Ray Diffraction Technique	89
5.4.1. Introduction	89
5.4.2. X-ray Diffraction Apparatus	89
5.4.3. Hardware Parameters Used for Stress Analysis	90
5.4.4. Stress Analysis Software	92
5.4.5. Optimising Scan Duration	94
5.4.6. Repeatability Tests	94
5.4.7. Assumptions Encountered in Determination of Stress Using $\text{Sin}^2\psi$ Approach	97
5.4.8. Verification of the Residual Stress Results	97
5.5. Fractography and Metallographic Analysis	99
5.5.1. Examination Using Optical Microscope	99
5.5.2. Examination Using Secondary Electron Microscope (SEM)	99
5.5.3. Examination Using Infinite Focus Microscope (IFM)	100
5.6. Fatigue Crack Monitoring by Surface Replication	100
5.7. Microstructure and Grain Size Determination of Ti-6Al-4V Alloy	101
<u>CHAPTER 6: EXPERIMENTAL RESULTS</u>	102
6.1. Introduction	102
6.2. Chemical Analysis of Ti-6Al-4V Alloy	102
6.3. Grain Size Determination	102
6.4. Fatigue Tests – Phase.1	104
6.4.1. Surface Roughness and Residual Stress Measurements	104
6.4.2. Fatigue Test Results (Phase.1)	107

6.5. Fatigue Tests – Phase.2	110
6.5.1. Route.1	110
6.5.2. Route.2	113
6.5.3. Route.3	115
6.6. Analysis of Surface Cracks by Surface Replication Technique	118
6.7. Fractography Analysis Using SEM and Optical Microscopes	121
<u>CHAPTER 7: FATIGUE CRACK GROWTH MODEL</u>	123
7.1. Introduction	123
7.2. Crack Growth Models	123
7.3. Determination of Parameters	125
7.4. Development of Computer Model	128
7.4.1. Basic Steps Followed to Develop Computer Model	129
7.5. Results	130
<u>CHAPTER 8: DISCUSSION</u>	131
8.1. Introduction	131
8.2. In-Vivo Failure Analysis of Hip Implants	132
8.2.1. In-Vivo Failures at the Cone Region	132
8.2.2. In-Vivo Failures at the Neck Region	135
8.3. Fatigue Tests (Phase.1) - The materials Characterization of Ti-6Al-4V Alloy	137
8.3.1. Variation of Fatigue Limit with Surface Roughness and Surface Residual Stress Values	137

8.3.2. Residual Stress or Mean Stress Effect on Fatigue Performance of Ti-6Al-4V	138
8.3.3. Effect of Stress Ratio to Fatigue Performance of Ti-6Al-4V	140
8.3.4. Representation of Results in the Form of K-T Plots	141
8.4. Fatigue Tests (Phase.2) - Characterization of Manufacturing Process	144
8.4.1. Discussion on Fracture Analysis and Variation of Fatigue Limit of Route.1	144
8.4.2. Discussion on Fracture Analysis and Variation of Fatigue Limit of Route.2	152
8.4.3. Discussion on Fracture Analysis and Variation of Fatigue Limit of Route.3	156
8.5. Development of K-T Plots for Different Stages in Manufacturing Routes	162
8.5.1. K-T Plots for Route.1	162
8.5.2. K-T Plots for Route.2	164
8.5.3. K-T Plots for Route.3	166
8.6. Variation of Fatigue performance with Surface Roughness (Surface Defect Size) and Residual Stress Values for Ti-6Al-4V	168
8.7. Fatigue Crack Growth Modelling and Life Time Predictions	175
8.8. Observations Obtained in Very High Cycle Fatigue Regime	178
<u>CHAPTER 9: CONCLUSIONS</u>	180
<u>CHAPTER 10: SUGGESTIONS AND FUTURE WORK</u>	185
LIST OF REFERENCES	187
APPENDICES	200

Fatigue failure occurs in components subjected to cyclic or fluctuating stress at nominal stresses that are often less than the static yield strength of the material. The mechanisms of fatigue crack initiation are complex and wide ranging, but it is considered to occur by permanent damage due to structural and microstructural changes which lead to the creation of microscopic cracks. These microstructural flaws or cracks grow and form a dominant crack which propagates further until it creates structural instability ending with complete failure. At certain stress amplitudes microstructural short cracks will not propagate, simply because of their inability to overcome microstructural barriers associated with the grain structure of the material. This initiation of micro-defects and the methodology and the rate of propagation of the dominant crack to final failure are strongly influenced by a wide range of factors related to material microstructural properties, loading conditions and operating environment. Generally fatigue of engineering components can cause devastating consequences, and obviously the fatigue has been a problem for over 150 years and continues to be so.

Under in-vivo service conditions, the components of implants are subjected to randomly varying fluctuating loads several times in magnitude that of a person's weight. Design and manufacture of such components to avoid fatigue failure is therefore an important requirement. This research programme examines hip implants made of Ti-6Al-4V alloy coated with Hydroxyapatite ceramic (H-AC). Manufacturing of surgical implants is one of the largest applications of wrought Ti-6Al-4V. The use of Ti-6Al-4V in the medical industry has grown rapidly because of its excellent biocompatibility and appropriate mechanical properties. H-AC coating has been used in implant manufacturing to improve bone absorption and establish stronger and firm fixation between the implant and the host bone. H-AC is a synthetic ceramic version of Hydroxyapatite (H-A) which 69% of the bone consist of. The total hip replacement (THR) is the standard treatment for patients with the diseases such as osteoarthritis and rheumatic arthritis, which prevents normal functionality of human hip joint. THR is very popular and the demand for this treatment keeps on increasing day by day, world-wide. Hip implants are designed and manufactured to be in service for at least 10 years. However for various reasons implants fail in less than 10 years and these failures are difficult to predict.

Fatigue failure is one of the primary hip implant failure mechanisms. When an implant fails revision surgery is required to remediate the problem.

Manufacturing of titanium based implants involves several key operations, from initial material processing such as rolling material to bar stock, forging to shape, machining, grinding, polishing, grit blasting and vacuum plasma spraying of selected locations. Each of these processes may introduce residual stresses and surface microscopic defects, which can exist in the final product. The presence of small crack-like defects, in particular at highly loaded regions in the implant would not only reduce the load bearing capacity but such defects may grow progressively to cause premature fatigue failure under dynamic loading. In the case of H-AC coated implants the coating process itself may introduce micro defects at the interface. Understanding the shape, size and distribution of the manufacturing defects and their growth behaviour under dynamic loading is essential for the prevention of fatigue failure. Residual stress can have a significant impact on the fatigue performance of engineering components, where near-surface tensile residual stresses tend to accelerate the initiation and propagation of defects while surface compressive residual stresses prolong the fatigue life by retarding the fatigue crack growth rate. The nature of the manufacturing route is paramount in controlling the final surface finish and surface residual stress state of the component.

The main objectives of this research programme were to investigate; (i). the characteristic microstructural/physical properties of material (Ti-6Al-4V), (ii). the physical surface finish/defects introduced in the sample by the manufacturing practices, (iii). the nature of the residual stress levels of the component introduced during manufacturing, and (iv). to evaluate their relationship to fatigue performance, as illustrated in Fig.1. The knowledge gained from this work will be used to provide recommendations on good practice for implant manufacturing and help alleviate/reduce in-vivo fatigue failures of implants manufactured from the Ti-6Al-4V alloy.

This research is performed in association with Joint Replacement Instrumentation (JRI) Ltd, UK.

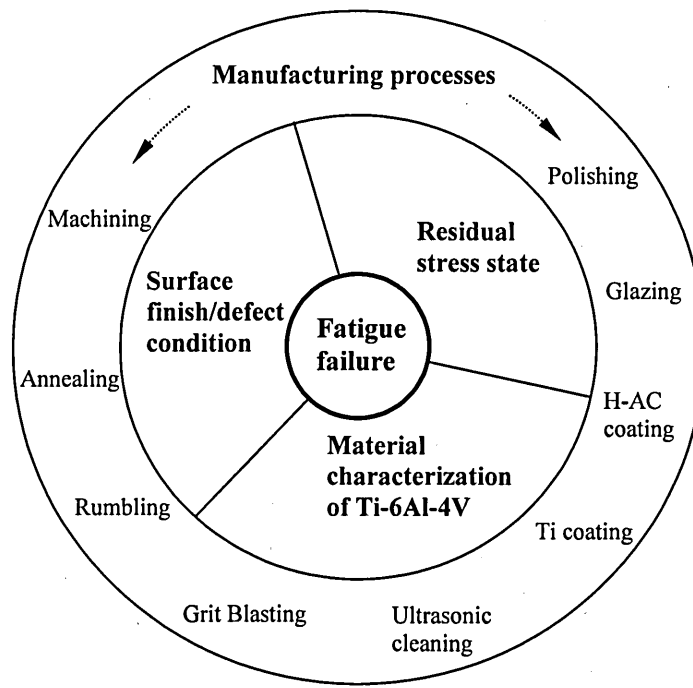


Fig.1: Main components considered in investigation of fatigue behaviour of hip implants made out of Ti-6Al-4V alloy.

This research project was divided into three main activities;

1. Analysis of in-vivo hip implant failures.

The main focus is to understand the causes and modes of in-vivo fatigue failure of hip implants made from Ti-6Al-4V. Analysis of data based on in-vivo failures, accumulated by JRI Ltd over last 12 years, was performed. The size of stem implant most vulnerable to failure, failure location, implant design features and fatigue crack initiation and propagation details were identified. Fatigue failure occurs in two locations of the stem part of implant, namely the cone area and the neck area.

2. Study on the fatigue behaviour of Ti-6Al-4V alloy.

The fatigue behaviour of the alloy has been investigated in order to understand the role of defect size and residual stress state on fatigue failure. Fatigue experiments have been performed using rotating bend apparatus for known surface and residual stress conditions. A total of 58 fatigue samples were tested to understand the variation of fatigue limit with different conditions of surface roughness and residual stresses.

Threshold conditions of different stages of crack growth are discussed with the help of Kitagawa-Takahashi (K-T) type plots and effect of stress ratio and mean stress on threshold conditions is also discussed. A surface replication method was used to investigate the material crack growth properties.

3. Evaluation of JRI hip implant manufacturing processes.

The manufacturing of implants involves several key operations where each operation may introduce residual stresses and microscopic defects into the final product. The manufacturing processes involved in producing the cone area and the neck area were identified and investigated. Three distinct manufacturing routes have been identified. The critical operations which are likely to introduce surface defects and residual stresses, for each route, were selected. Rotating bend test samples were prepared to simulate the surface/residual stress state in actual implant manufacturing. A total of 108 samples were fatigue tested to understand the variation of fatigue performance attributed by each manufacturing process.

Two mathematical models were developed; (i) a fracture mechanics model was developed to quantify the fatigue life at given stress amplitudes, based on fatigue results of smooth surface samples. Here short and long crack growth models were used and the respective values of material constants were calculated by using smooth specimen *S-N* data. Fatigue crack growth data were also used to finalize the material constants used in these equations. (ii) a second model was derived to quantify the fatigue limit for a given surface roughness/defect size and surface residual stress state. This equation allows the fatigue limit of a component with known surface roughness/defect size and residual stress state to be calculated. Kitagawa-Takahashi (K-T) type plots were developed to evaluate the safe fatigue envelop.

This thesis consists of ten chapters. **Chapter 2** is an extensive literature review which covers topics such as, hip implants, properties of Ti-6Al-4V and other materials in use, metal fatigue and fatigue of Ti-6Al-4V and fatigue failures of hip implants, K-T type plots, stress analysis in hip implants, surface roughness and its effects to fatigue performance, residual stress and its influence to the fatigue performance, measurement of surface roughness and residual stress and the influence of manufacturing processes to

fatigue performance. The in-vivo failure analysis of JRI implants is presented in **Chapter 3**. A description of the manufacturing processes is given in **Chapter 4**. The experimental procedure and experimental results are given in **Chapter 5** and **Chapter 6** respectively. The comprehensive description of crack growth modelling is given in **Chapter 7**. **Chapter 8** is devoted to discussion. Issues related to failure analysis, material characterization of material (Ti-6Al-4V) and manufacturing process, development of K-T plots, the derived mathematic models and their accuracy and observations of very high cyclic failures in Ti-6Al-4V, were discussed. The conclusions are given in **Chapter 9** and **Chapter 10** provides suggestions and future work.

2.1. Introduction

This research is mainly focused on fatigue failures of medical implants made out of Ti-6Al-4V alloy and investigates the causes of failures. Such awareness of these failures and the causes of failures will help develop methods to enhance the fatigue performance of medical implants, mainly by optimising the processes involved in manufacturing implant products.

It is important to understand the fatigue performance of hip implants since they are exposed to cyclic loading under in-vivo conditions. The aim of this chapter is to present a review in order to understand the main concepts and current know-how of important issues related to medical implants, fatigue failures, properties of Ti-6Al-4V alloy and manufacturing aspects of medical implants, within the context of the research. The main focus is given to hip implants made from Ti-6Al-4V alloy. The effects of residual stress and surface defects/roughness on the fatigue performance of the alloy are discussed. The material properties of Ti-6Al-4V, such as microstructure, fatigue failure initiation and propagation, along with quantitative models in fracture mechanics to assess fatigue properties are discussed. The experimental procedures to evaluate fatigue properties are also reviewed.

The literature related to the above-mentioned issues is extensive and well documented. Therefore this literature review is mainly focused on the aspects related to the aims and objectives of the present research. The methodologies and concepts are reviewed where appropriate, to give clear information and understanding of the perceptions addressed in subsequent chapters in this thesis.

2.2. Hip Implants

The human hip may suffer from diseases such as primary osteoarthritis and rheumatic arthritis which may lead to severe damage, pain and may also prevent normal functionality and reduce quality of life. In such cases one of the solutions is to replace the natural hip joint with an artificial hip implant that may restore normal functionality of the joint. A hip implant or prosthesis is a device that is placed surgically inside the human body and expected to remain there for a substantial period of time, for example approximately 10 years or more.

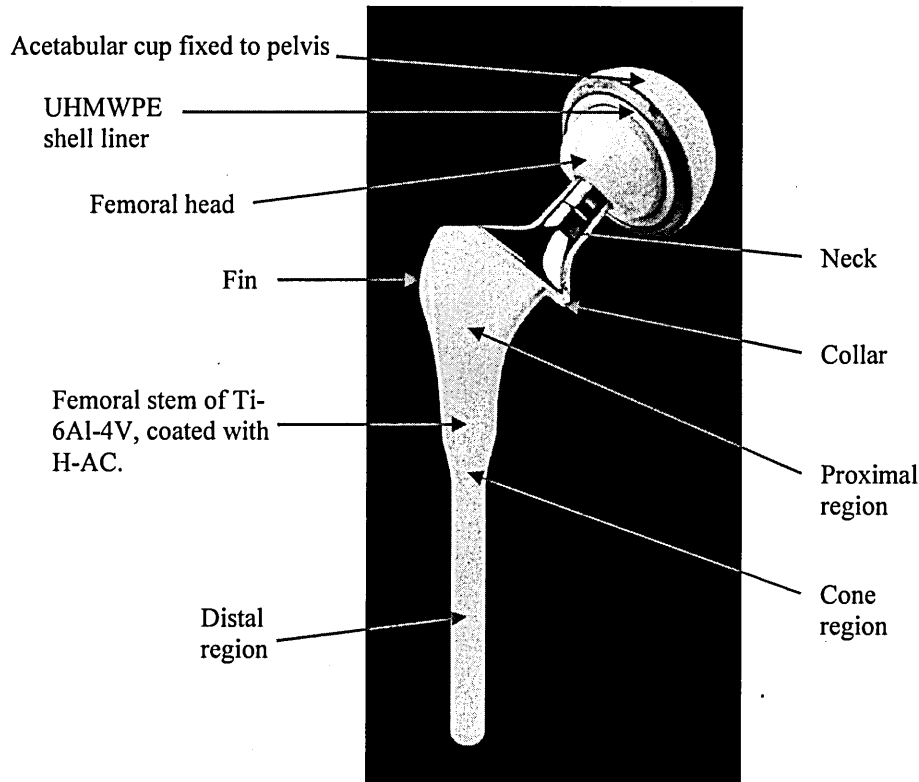


Fig.2: JRI Furlong[®] H-A.C. Supravit[®] coated hip replacements made out of Ti-6Al-4V.

A Furlong[®] H-AC (Hydroxyapatite Ceramic) total hip replacement made by JRI Ltd is shown in Fig.2. The stem has a triangular region (proximal region) just below the neck with a small fin to prevent rotation. Below there is a cone shaped region to create mechanical stability followed by a cylindrical distal region. In coated implants proximal, cone and distal regions are totally coated with H-AC. The collar to tip of the neck region is machined and polished. The distal cylindrical section comes in different sizes to accommodate different patient groups. Also larger diameters and longer length stems are needed in revision implant replacement surgeries.

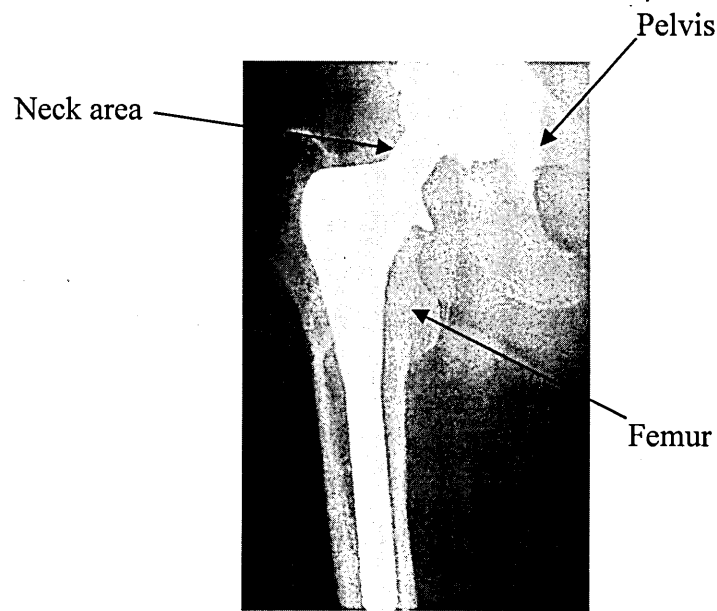


Fig.3: Hip implant fixation, under in-vivo conditions [1].

As shown in the Fig.3 the acetabular cup is firmly fixed to the pelvis and the H-AC coated proximal and distal regions are guided into the femur. The bone tissues are expected to grow into the H-AC coating and firmly fit to act as an integral part. The well polished neck area of the implant is exposed to the body fluids.

During service, hip bones are subjected to cyclic loading as high as 10^6 cycles per year [2]. The average static load on a hip joint is estimated to be up to three times body weight and the peak load during running/jumping can be up to as high as 10 times body weight [3]. Designing hip implant components to withstand such high fluctuating loads is a necessity. Under in-vivo conditions the femoral stem of the total hip prostheses is subjected to two kinds of loads; bending (caused by activities such as ordinary standing and walking) and twisting (which try to rotate the stem within the bone femur, e.g. when a patient rises from a chair or climbs the stairs). Usually the stem is attached to the bone using bone cement. In case of H-AC coated stems, bone tissue grows onto the coated surface with time and the total hip joint becomes an integrated part of the skeleton.

The factors in designing hip implants are well documented and Charnley [4] presented a paper in 1966-67 which addresses factors such as geometry, forces and directions of forces, design of the neck, ball and socket design, materials, etc.

Different parts of hip implants are manufactured using different materials such as metals, polymers, and ceramics. The stem is mainly manufactured from titanium alloys, stainless steel and cobalt-chrome alloys. This research is mainly focused on the implant grade Titanium alloy, Ti-6Al-4V.

2.3. Implant Grade Titanium Alloy (Ti-6Al-4V)

Currently, manufacture of surgical prostheses has become one of the largest applications of the wrought Ti-6Al-4V with aerospace, nuclear and automotive applications. Use of Ti-6Al-4V in the medical industry grew rapidly in Europe and North America in the 1970s [5] because of its excellent biocompatibility, low modulus of elasticity, low stiffness, good tensile properties and high fatigue strength. Titanium forms a bio-inert natural titanium oxide on the surface which resists corrosion. Ti-6Al-4V possesses low rates of metal ion release and therefore little tendency to cause adverse cell or tissue reactions [6].

Pure titanium undergoes microstructural transformation at 882.5°C [7] changing from hexagonal closed pack (*cph*), *i.e.* the α phase to body centred cubic (*bcc*), *i.e.* the β phase. This transformation is controlled by alloying elements. α stabilisers like *Al*, *O*, *N* and *C* increases the transition temperature and β stabilisers like *V* decreases the transformation temperature [7]. Ti-6Al-4V is categorized as α - β alloy due to the presence of both α and β phases at room temperature. It has been subjected to extensive research and shown to have good fatigue strength due to a fine equiaxed microstructure consisting of α and β grains [8].

The microstructure of Ti-6Al-4V is shown in Fig.4 [9]. The microstructure of implant grade wrought Ti-6Al-4V alloy should conform to plates A1 - A9 of the ETTC publication 2 in order to comply with BS 7252 – Part 3 (1997) [10]. The minimum requirements for mechanical properties of heat treated Ti-6Al-4V is listed in Table.1. The chemical composition requirements are given in Table.2.

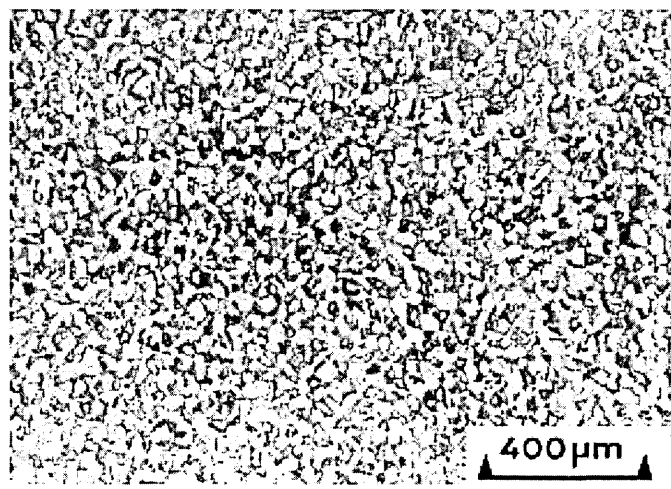


Fig.4: Microstructure of equiaxed Ti-6Al-4V, $\alpha + \beta$ phases [9].

Tensile Strength (MPa)	Proof stress of non proportional elongation (MPa)	% Elongation
860	780	10

Table.1: Minimum mechanical properties of Ti-6Al-4V alloy bar [10].

Element	Limit according to BS 7252 - Part 3 (mass %)
Aluminium	5.5 – 6.75
Vanadium	3.5 – 4.5
Iron	0.3 max
Oxygen	0.2 max
Carbon	0.08 max
Nitrogen	0.05 max
Hydrogen	0.015 max
Titanium	Balance

Table.2: Chemical composition of Ti-6Al-4V implant grade alloy [10].

The Young's modulus and Poisson's ratio of implant grade Ti-6Al-4V alloy are 113.7GPa and 0.3 respectively [11].

2.4. Use of Hydroxyapatite Ceramic (H-AC) in Implants

The successful fixation of a prosthetic implant to a bone is complex and time dependent process. Titanium implants covered by oxide film cannot be tightly bonded to living bone due to poor mechanical adhesion [3]. This often leads to the loosening of the implant causing movement between implant and bone resulting in implant failure. This can be overcome by coating the implant surface with a material that would promote the formation and bonding with the bone. Hydroxyapatite (H-A) is a form of calcium phosphate which has a chemical composition of $\text{Ca}_5(\text{PO}_4)_3(\text{OH})$ [12]. It is known that 69% of the weight of the bone consists of H-A which contributes to its stiffness and strength [2]. H-AC is a synthetic ceramic version of H-A. H-AC coated hip implants were first introduced in 1985 [1] and H-AC as a coating is one of the most generally accepted and commercialized bioactive material [13]. Since then clinical trials have shown H-AC coating promotes superior bone absorption [14, 15], stronger and firm fixation between the implant and the host bone [16, 17, 18] with reduced healing time [19, 20]. Bioactive coating H-AC also reduces the metal ion release of titanium by simply acting as a physical barrier [21]. Also the H-AC layer promotes accelerated bone healing around the implant along with accelerated osteoconductivity [22, 23, 24].

The Furlong® H-AC total hip replacement (shown in Fig.2) is coated with H-AC with an average thickness of $185\mu\text{m}$. To facilitate secure bonding of H-AC, the Ti-6Al-4V alloy surface is first coated with a $50\mu\text{m}$ thick porous titanium undercoat [25, 26]. Both coatings are applied using vacuum plasma spraying (VPS) to provide bond strength in excess of 40MPa [25, 27]. However the application of H-AC coating by plasma spray technique is known to have an adverse effect on the fatigue performance of Ti-6Al-4V [28]. Also it is known that the thickness of the H-AC coating affects the fatigue performance of coated implants [19].

2.5. Metal Fatigue - Fundamental Principles

2.5.1. Introduction

It is believed one of the earliest studies of metal fatigue was conducted by a German mining engineer WAJ Albert in 1829 [cited in 29]. He has conducted repeated load proof tests on mine hoist chains made out of iron. After a tragic railway accident in France which killed around 1500-1800 people in 1842, detailed research of metal fatigue began [29]. A systematic investigation concerning fatigue was first conducted on railway axles by August Wohler [30], in 1860. Most of Wohler's work has been confirmed by Bauschinger in 1886 [cited in 29] and he established the difference in the elastic limit of metals in reversed loading from that in monotonic deformation. Thereafter fatigue and fatigue related research has grown all over the world and has led to an understanding of the concepts and mechanisms related to fatigue.

Fatigue failure occurs in a material subjected to cyclic or fluctuating stress at nominal stresses that are often less than the static yield strength of the material. The mechanisms of fatigue crack initiation are complex and wide ranging, but it is considered to occur by permanent damage due to structural and microstructural changes which lead to the creation of microscopic cracks. These microstructural flaws or cracks grow and form a dominant crack which propagates further until it creates structural instability and ends up with complete failure. This initiation of micro-defects and the methodology as well as the rate of propagation of the dominant crack to final failure are strongly influenced by a wide range of factors related to mechanical, microstructural and operating environment.

During the last four decades the knowledge in fatigue has improved due to advances in high resolution optical and electron microscopy. Use of these microscopic techniques has enabled researchers to understand important microscopic issues related to initiation, deformation and fracture. Identification and understanding of persistent slip bands, different stages of fatigue crack propagation and fatigue striations, are some important aspects which have helped to develop conceptual and quantitative models in fatigue.

Three fatigue analysis methods have been identified. They are; (i). the stress life approach, (ii). the strain life approach and (iii). the fracture mechanics approach.

Researchers have used the most appropriate method or methods for their particular problem.

2.5.2. Fatigue Crack Initiation

Fatigue cracks can initiate from scratches, pits, inclusions, grain boundaries and other high stress concentrations like sharp corners, on or near to the surface of the component. In ductile polycrystalline metals fatigue crack initiation starts from a weaker grain due to reversed shear stress associated with bands of intense slip [31]. These bands known as persistent slip bands (PSBs) were described by Thompson *et. al.* [32]. PSBs emerge at the free surface and generally appear in the form of intrusions and extrusions. When loaded, localized strain density at PSB's become higher than the adjacent matrix [33] and it has been noted that the strain within the PSB may be of the order of ten times greater than the adjacent matrix [34], which makes PSBs more susceptible for crack initiation.

In general, fatigue cracks may propagate in two stages. In the early stage the microcrack grows on planes of maximum shear. This is known as Stage I crack propagation. After traversing several grain boundaries the crack propagates along the planes of maximum principal stress. The latter stage is known as Stage II. Fig.5 [35] and Fig.6 [36] schematically illustrate the PSB formation and Stage I and Stage II crack growth directions respectively.

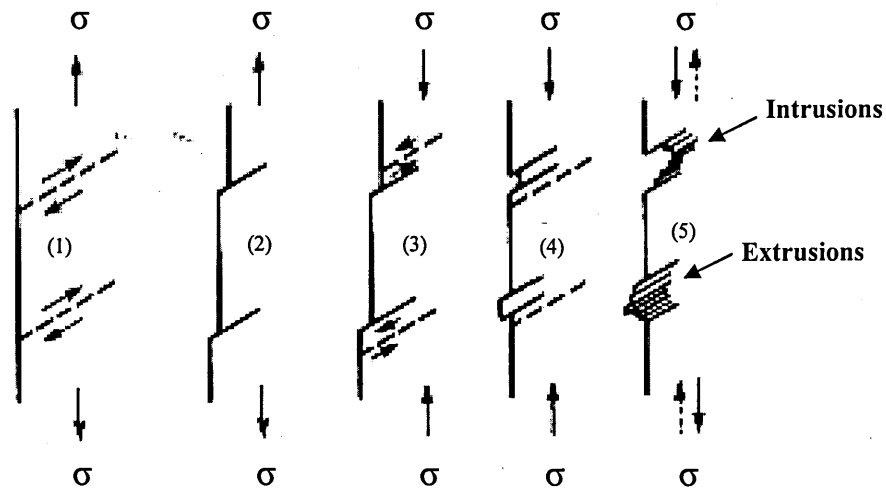


Fig.5: PSB formation [35].

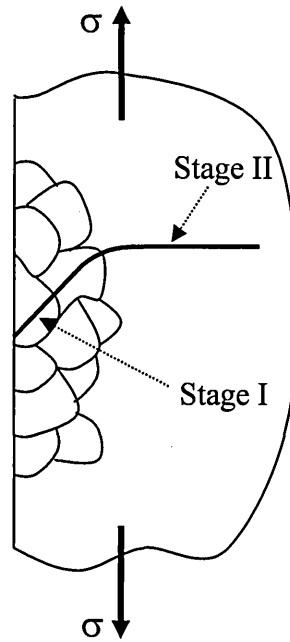


Fig.6: Stage I and Stage II fatigue crack growth [36].

Three basic modes of loading are identified in fracture mechanics, the schematic diagram of the crack surface displacements in these three modes is shown in Fig.7 [37]. Mode I is the opening or tensile mode which relates to Stage II fatigue crack propagation, where crack faces are pulled apart in the direction normal to the plane of the crack. Mode II is the in-plane shearing or sliding mode, which relates to Stage I fatigue crack propagation, where the crack surface slides over each other. Tearing or anti-plane shear mode is known as Mode III, where the crack surface move parallel to crack front relative to each other.

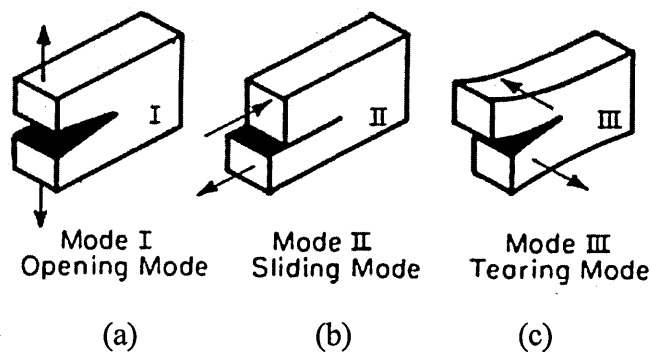


Fig.7: Three loading modes of fracture (a) tensile opening mode, (b) sliding mode and (c) tearing or anti-plane shear mode [37].

2.5.3. Fatigue Crack Propagation

Crack propagation curves, in terms of crack length (a) versus number of loading cycles (N), for two different stress amplitudes ($\Delta\sigma_1$ and $\Delta\sigma_2$), are schematically shown in Fig.8 [38]. It can be noted that for cracks developing from smooth surfaces, most of the fatigue life of a component is spent while the crack length is relatively small.

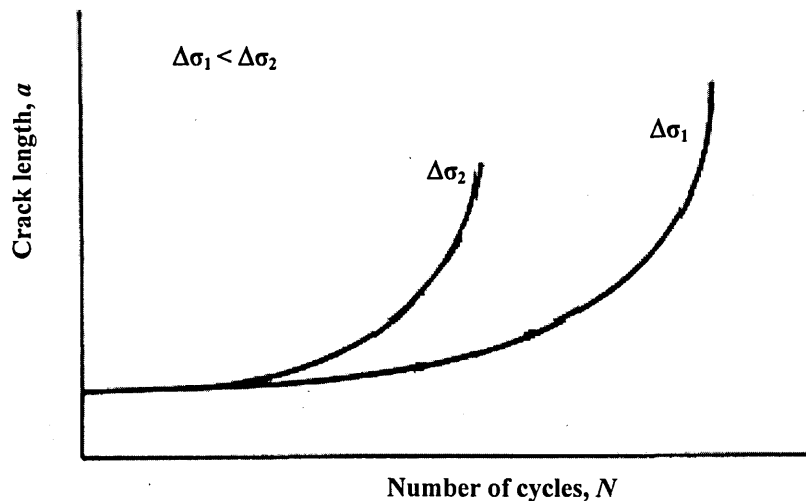


Fig.8: Typical crack growth behaviour in constant amplitude fatigue loading [38].

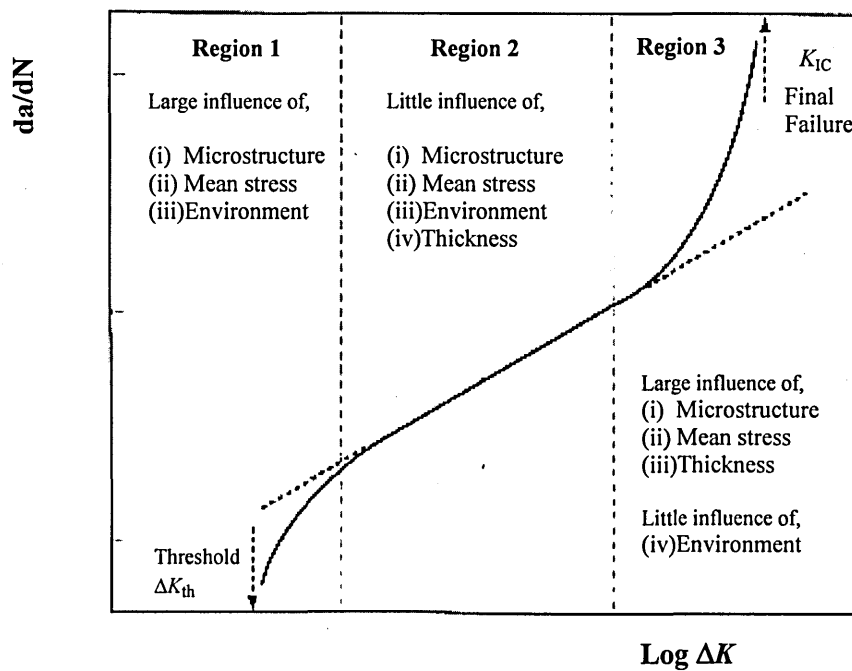


Fig.9: Schematic illustration of fatigue crack growth, da/dN versus ΔK [cited in 39].

The general crack growth behaviour of polycrystalline metals is shown in Fig.9 [39] as a curve da/dN versus stress intensity factor range ($\Delta K = K_{max} - K_{min}$). The curve can be divided into three regions;

Region I deals with low stress intensity values where crack behaviour is associated with the threshold stress intensity range (ΔK_{th}). This is the region where the crack propagation and life of the component is largely dependent on the microstructural properties of the material. Understanding the behaviour of microstructural short cracks, notably the cracks belonging to Region I is very important in estimation of fatigue life of engineering structures. The literature states that these cracks do not behave according to the predictions governed by the long crack theories. Typical growth rate curves for these microstructural cracks are shown in Fig.10 [40]. The figure illustrates the typical properties of the microstructural cracks; where each crack begins by growing more quickly than predicted by long crack growth models and some of them actually stop growing. Cracks which do not arrest come to a minimum growth rate and then speed up and eventually form long cracks. This ‘short crack’ behaviour is controlled by microstructural features, where grain boundaries act as barriers for crack propagation. The boundary is a barrier to plastic deformation and therefore crack extension which is a process of plastic deformation occurs easily within the first grain [40]. It is inevitable that the behaviour of crack growth in Region I is controlled by the microstructure and it is therefore imperative that any realistic theoretical model must take microstructural features into account.

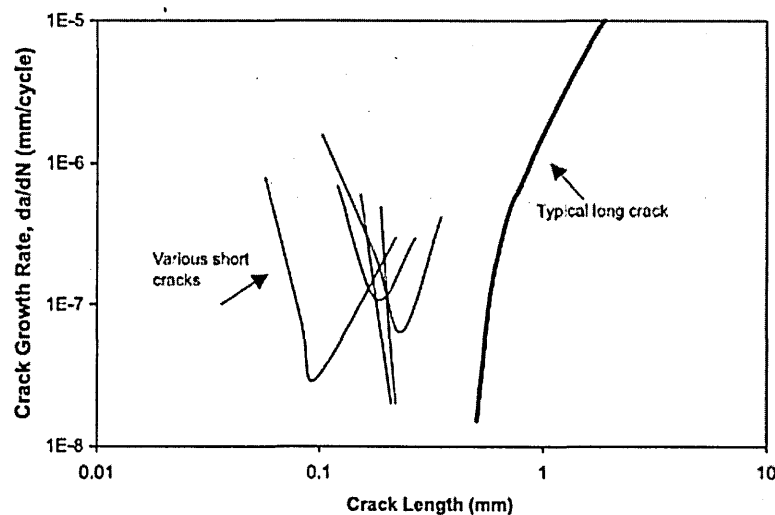


Fig.10: Typical crack growth rate data for short cracks [40].

For Stage I short crack growth Hobson [41] proposed an equation which describes the propagation of fatigue cracks within the first grain of a polycrystalline material. The equation considers the microstructural feature in terms of a barrier to propagation and its influence on fatigue crack growth. Thus,

$$da/dN = A (\Delta\sigma)^m (d - a) \quad (1)$$

where d is microstructural length parameter, A and m are material constants, a is the surface crack length and $\Delta\sigma$ is the stress range.

Opening mode or Mode I which relates to Stage II, crack growth equation has been expressed by Brown [42] as,

$$da/dN = B (\Delta\sigma)^n a - D \quad (2)$$

where B and n are material constants, D represents a crack growth threshold value.

Region II crack growth behaviour can be explained using Linear Elastic Fracture Mechanics (LEFM), well known Paris-Endogan [43] equation,

i.e., the
$$\frac{da}{dN} = C(\Delta K)^m \quad (3)$$

is applicable in Region II, where, C and m are material constants.

In **Region III** the crack is unstable and rapid crack growth occurs with failure at K_{IC} .

A schematic representation of crack propagation rate (da/dN) against crack length (a) shown in Fig.11 [44]. It is evident that significant difference exists between the behaviour of short and long fatigue cracks, as determined by LEFM. It can be seen a threshold value of stress intensity factor (ΔK_{th}) exists for long cracks, below which they do not propagate. However short cracks can grow at values of ΔK below the long crack threshold value, ΔK_{th} . It is observed that the crack propagation rates of short cracks are often significantly higher than the crack propagation rates of long cracks at the same

values of ΔK , as determined by LEFM. It is extremely difficult to calculate stress intensity factor (K) for short cracks [45] mainly due to the change in shape function, susceptibility of short cracks to local stress fields and difficulty in measurements.

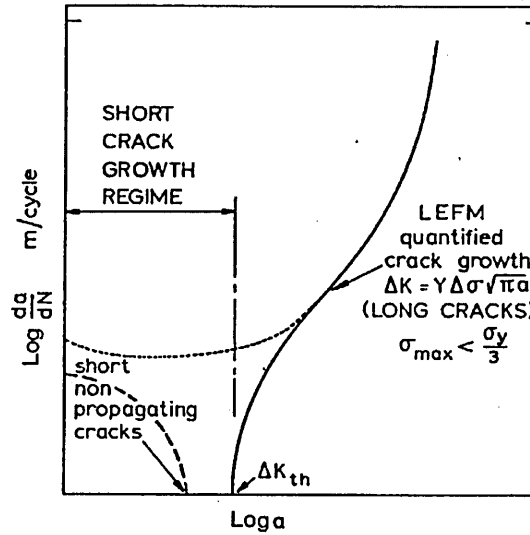


Fig.11: A schematic illustration of crack propagation rate (da/dN) against crack length (a) [44].

2.5.4. Stress Life ($S-N$) Approach of Fatigue Analysis

In 1860 Wöhler [30] pioneered a method for characterizing the fatigue properties using experimental data obtained from rotary bending tests on smooth hour glass shaped specimens. This approach can be also used in plane bending, uni-axial push pull, tension and tension cyclic loading situations. The curve of nominal stress amplitude (S) against the number of cycles (N) to failure is obtained from these experiments. The curve levels up typically beyond about 10^6 cycles, where corresponding stress amplitude is known as the fatigue limit or endurance limit which is the most important data from the $S-N$ curve. Below this stress amplitude it is assumed that the specimen may be cycled indefinitely without failure. This is considered as the 'safe region' in designs. A typical $S-N$ curve is shown in Fig.12 [29]. Wöhler's investigations led to the use of $S-N$ representation of data and the concept of fatigue endurance limit.

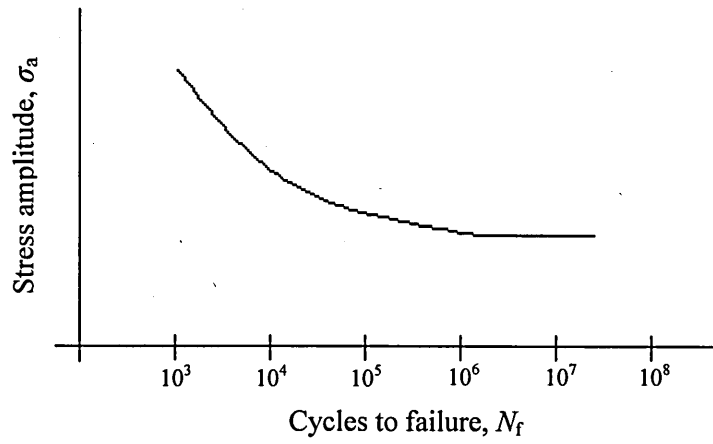


Fig.12: Schematic diagram of a stress-life ($S-N$) curve [29].

Studies on fatigue are usually divided into high cycle and low cycle fatigue in order to understand the crack nucleation and propagation concepts more clearly. For high cycle fatigue (HCF), Basquin (1910) [46] has proposed a power law which represents fatigue life,

$$\sigma_a = \sigma'_f (2N_f)^b \quad (4)$$

where σ_a - Stress amplitude, σ'_f - fatigue strength coefficient, N_f - number of load cycles and b - fatigue strength component or Basquin component.

For low cycle fatigue (LCF), Coffin [47] (1954) and Manson [48] (1954) independently developed an expression considering the plastic deformation which causes fatigue damage,

$$\frac{\Delta \varepsilon_p}{2} = \varepsilon'_f (2N_f)^c \quad (5)$$

where $\Delta \varepsilon_p$ - plastic strain amplitude, ε'_f - fatigue ductility coefficient, N_f - number of load cycles to failure and c - fatigue ductility exponent.

2.5.5. Microstructural Effects on Fatigue Behaviour

The grain size and orientation or morphology, are significant microstructural properties that most influence fatigue crack initiation and growth [49]. It is understood that small cracks will grow up to a barrier such as a grain boundary and then may arrest. Arrest depends on the microstructural characteristic dimension, d which is material dependent and the applied stress level [55]. It is understood that materials which have fine equiaxed microstructure show higher resistance to short crack propagation [56]. Other mechanical properties such as tensile strength and hardness also vary with changes in microstructure.

As explained in chapter 2.5, implant grade Ti-6Al-4V is a $\alpha + \beta$ alloy. The geometrical arrangement of these two phases can be changed to a great extent through different material processing conditions. Fig.13 [50] shows different microstructural morphologies for Ti-6Al-4V. Fig.14 [50] shows the influence of morphology of α and β on the fatigue limit of Ti-6Al-4V.

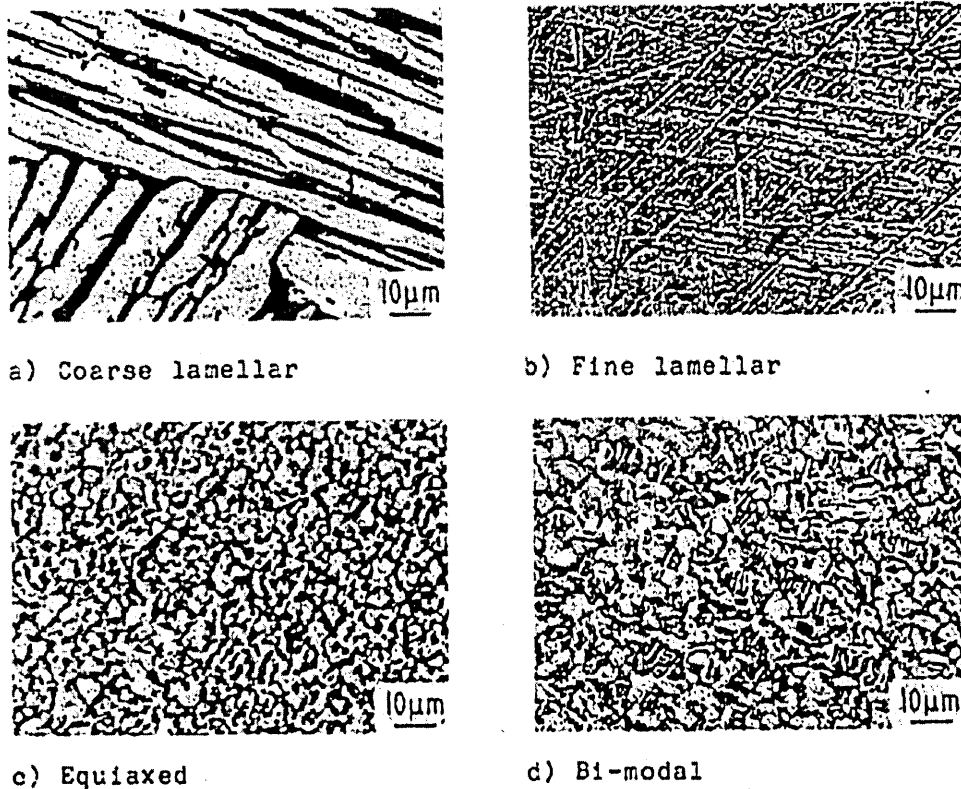


Fig.13: $\alpha + \beta$ structures for Ti-6Al-4V [50].

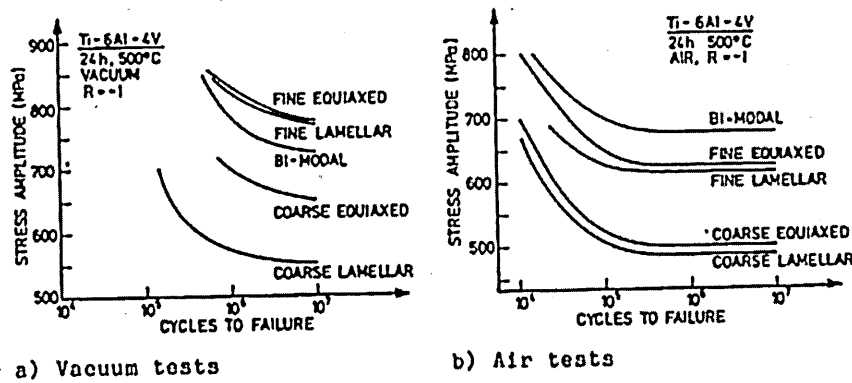


Fig.14: Influence of different $\alpha + \beta$ structures of *Ti-6Al-4V* (24h, 500°C), on fatigue strength; tests were conducted, (a) fully reversed loading under vacuum condition, (b) fully reversed loading under laboratory (air) condition [50].

It can be seen from Fig.14, that *Ti-6Al-4V* with fine equiaxed microstructure shows comparatively high fatigue resistance over other more coarse microstructures.

Behaviour of microstructural cracks, where the size is comparable to the grain size, is dependent on the grain size of the material. It is known that any microstructural parameter which increases the yield strength of the material and/or reduces the slip length should improve the fatigue strength [50]. A reduction in grain size decreases slip length and therefore should increase the fatigue strength. Fig.15 [50] shows that decrease in grain size from $100\mu\text{m}$ to $20\mu\text{m}$ has increased the fatigue limit from 610MPa to 675MPa . The grain size of the equiaxed structures can be varied by altering the annealing time in the two phase field.

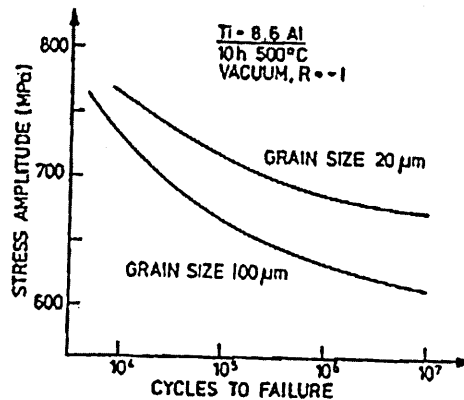


Fig.15: Influence of grain size on fatigue strength of *Ti-8.6 Al* (10h, 500°C), conducted under fully reversed loading condition under vacuum condition [50].

Lutjering *et. al.* [51] also showed, through comparison of average propagation rates of small surface cracks for two grain sizes that small surface cracks propagate at a lower rate in the fine grained material. This is illustrated in Fig.16 [51].

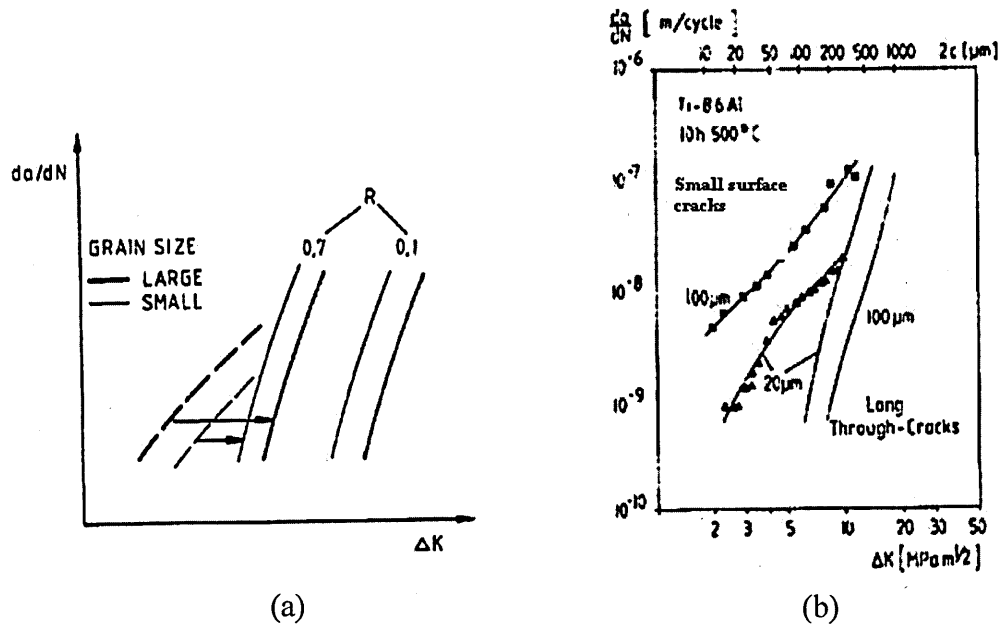


Fig.16: Influence of grain size on da/dN vs. ΔK behaviour for short surface cracks and long cracks , (a) Schématic diagram, (b) For *Ti-8.6Al* (10h, 500°C) [51].

2.5.6. Mean Stress Effect on Fatigue Performance

Referring to Fig.17 the stress amplitude (σ_a), mean stress (σ_m) and stress ratio (R) can be defined as,

$$\Delta\sigma = \sigma_{\max} - \sigma_{\min}$$

$$\sigma_a = (\sigma_{\max} - \sigma_{\min})/2$$

$$\sigma_m = (\sigma_{\max} + \sigma_{\min})/2$$

$$R = \frac{\sigma_{\min}}{\sigma_{\max}}$$

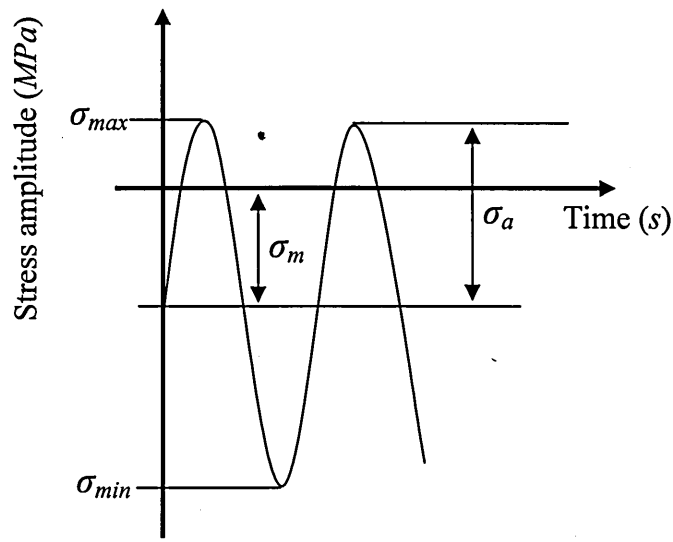


Fig.17: Schematic diagram of variation of stress amplitude against time describing the stress cycle parameters which affect fatigue performance

The S-N diagrams indicate the stress life relationship for a specified value of the mean stress (σ_m) or the stress ratio (R). Fatigue life is observed to be reduced with the increment of mean stress value. For rotary bending tests it is assumed as fully reversed loading ($R = -1$), with a zero mean stress. In some cases such as tension-tension cyclic loading, the imposed stress cycle is not fully reversed, and then the mean stress is not zero. This is possible in rotary bending tests also, if the test sample contains residual stresses. One obvious way of accounting for the influence of residual stress on fatigue behaviour is to consider the residual stress value as the local mean stress [52]. Hines *et al.* [53] concluded that the microcracks tested at $R = 0.5$ grow faster than those tested at $R = 0.1$ and different stress ratios alter the crack length threshold (a_{th}) and threshold stress intensity factor (ΔK_{th}), as shown in Fig.18 [53].

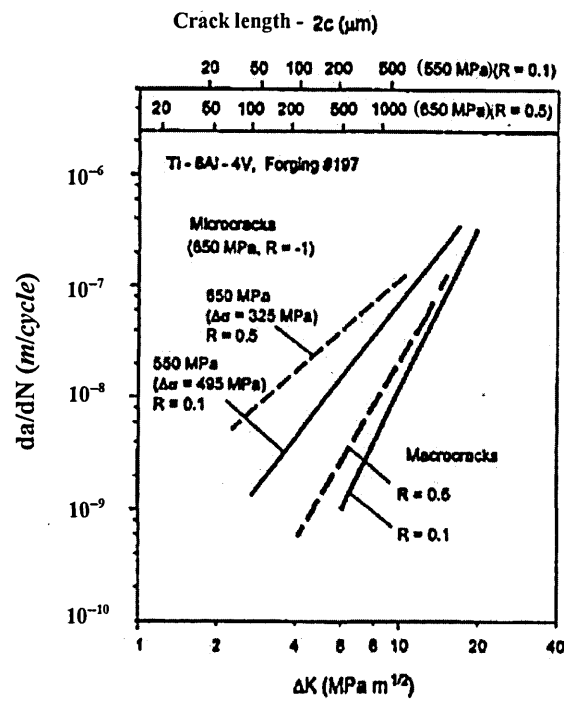


Fig.18: Short and long crack growth at $R = 0.1$ and 0.5 for Ti-6Al-4V forgings [53].

Mean stress (σ_m) effects on fatigue can be represented in terms of a constant life diagram. There are different models to which correlate the fatigue or endurance limit (S_e) in stress amplitude axis (y-axis) and ultimate tensile strength (S_u), yield strength (S_y) and fracture strength (σ_f) on mean stress axis (X-axis), to provide constant fatigue life. The most well known models [37] are Soderberg's criterion (1930), Goodman's criterion (1899), Gerber criterion (1874) and Morrow criterion (1960), illustrated in Fig.19 [37].

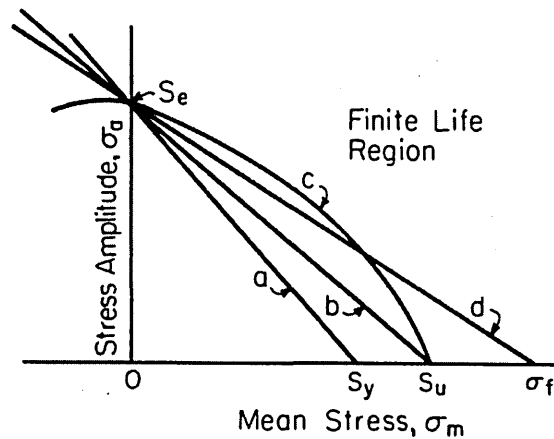


Fig.19: Comparison of mean stress equations- *a*. Soderberg, *b*. Goodman, *c*. Gerber and *d*. Morrow [37].

Goodman's criterion has been used for calculations of stress amplitude (σ_a) for the tests conducted in this project. The Goodman's criterion is given by,

$$\frac{\sigma_a}{S_e} + \frac{\sigma_m}{S_u} = 1 \quad (6)$$

where, σ_m - mean stress, S_e - fatigue or endurance limit and S_u - ultimate tensile strength, Using this equation the respective stress amplitudes can be calculated for different mean stress values.

2.5.7. Kitagawa-Takahashi (K-T) Type Diagrams

Observing and understanding the behaviour of short fatigue cracks whose size corresponds to that of the microstructural dimension of materials has enhanced the understanding of the fatigue limit phenomena. Before short fatigue crack growth studies, it was believed that below the fatigue/endurance limit cracks would not initiate. However current knowledge shows that very small cracks may exist but they may not propagate beyond microstructural barriers that are inherent with the material. Therefore microstructural characteristics like, grain size, phase distribution which resulted from chemical, mechanical forming and heat treatment would affect fatigue life and endurance limit [54].

The most common and traditional way of investigating fatigue behaviour of materials is the $S-N$ or total life approach, which has previously been explained in section 2.5.4. In the $S-N$ approach specimens are subjected to cyclic loading at various stress amplitudes (S) in order to determine the number of cycles to failure (N). On the other hand, fatigue crack propagation can be characterized by fracture mechanics based damage tolerant approach where crack growth rate per cycle (da/dN) studied against the linear elastic stress intensity range ($\Delta K = K_{max} - K_{min}$) during the loading cycle. Using this method the total number of cycles required to grow a pre-existing flaw to a size required to cause final fracture can be predicted.

The propagation of microscopic defects under dynamic loading can be analysed using Kitagawa-Takahashi type diagram (KT-Plot) [57], as illustrated in Fig.20 [58]. The upper margin of stress for the growth of microscopically short defects (crack size $< a_1$) is given by the smooth specimen fatigue limit ($\Delta\sigma_e$). The limit of stress for non-propagating long cracks is given by the threshold stress intensity factor range (ΔK_{th}). When the crack length $a > a_2$, LEFM conditions apply and when $a_1 < a < a_2$ the Elastic Plastic Fracture Mechanics (EPFM) conditions apply. Although it is considered that the KT-plot is a material property, it is believed that the plot will change due to manufacturing parameters such as residual stress.

Every engineering component has the possibility of containing surface cracks or defects [59]. Even the most carefully prepared engineering surfaces can have micro defects/notches to a depth of $2\text{-}3\mu\text{m}$ [55], as a result of manufacturing operations such as, machining, grinding or polishing. Microscopically small cracks behave differently from large cracks. As described in 2.5.3, it was also shown that microcracks grow faster than predicted by LEFM calculations in pure titanium and Ti-6Al-4V alloy [60, 61]. LEFM analysis can be used to calculate the stress-strain fields of engineering components containing defects, but as the size of the initial defect becomes smaller, the stress level needed to propagate the crack increases, and cracks can propagate below LEFM threshold crack lengths particularly at high stress levels [55]. According to the K-T method, the stress intensity at fatigue threshold (ΔK_{th}) can be expressed in terms of stress range and crack size.

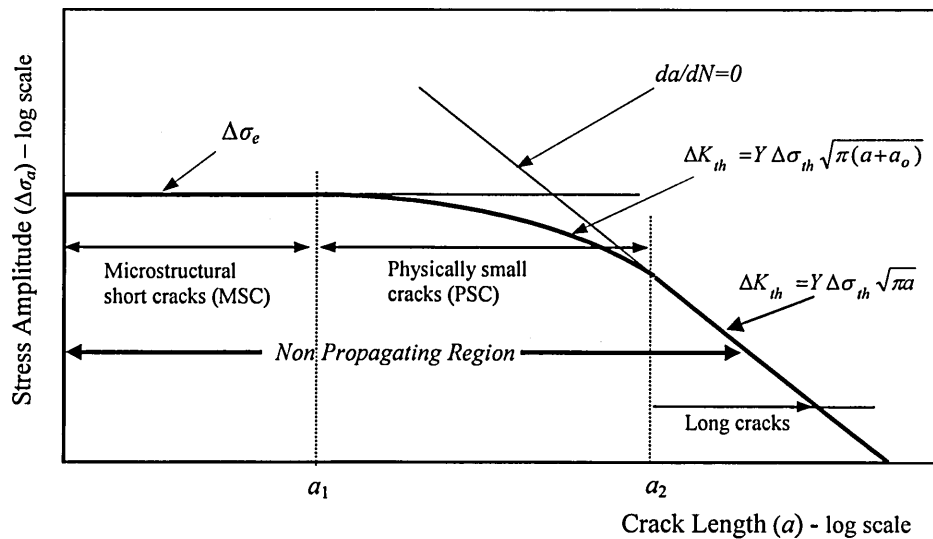


Fig.20: Schematic representation of K-T type diagram [58].

The LEFM threshold line distinguishes the propagation and non propagation regions of long cracks, and is given by the equation,

$$\Delta K_{th} = Y \Delta \sigma_{th} \sqrt{\pi a} \quad (7)$$

Where, ΔK_{th} - threshold stress intensity factor, $\Delta \sigma_{th}$ - stress amplitude, a - crack length and Y - the geometry factor. The equation can be represented as follows,

$$\log \Delta \sigma_{th} = -\frac{1}{2} \log a + \log \left(\frac{\Delta K_{th}}{Y \sqrt{\pi}} \right) \quad (8)$$

The fatigue limit of smooth specimen $\Delta \sigma_e$ ($= \Delta \sigma_{th}$, for microscopically short defects; crack size $< a_1$) can be found by conducting fatigue experiments.

In order to account for the breakdown of the LEFM concept for a small crack size, El Haddad *et. al.* [62, 63, 64] proposed an empirical relationship for the stress intensity factor range based on the notion of an effective crack length $(a + a_o)$. This covers both small and large crack limiting ranges.

$$\Delta K_{th} = Y \Delta \sigma_{th} \sqrt{\pi(a + a_o)} \quad (9)$$

The a_o value can be evaluated from the limiting condition where the physical crack size, a , approaches zero, i.e. $a_o \gg a$ and $\Delta \sigma_{th} = \Delta \sigma_e$ [65].

$$a_o = \left(\frac{1}{\pi} \right) \left(\frac{\Delta K}{Y \sigma_e} \right)^2 \quad (10)$$

2.5.8. Concluding Remarks on Metal Fatigue

Surface roughness is one of the main factors which affect the endurance or fatigue limit of a material. A rough surface introduces more stress raisers on the surface which influence fatigue crack initiation. As already discussed, **microstructure** of the material also affects the fatigue limit. Microstructural boundaries will act as barriers to crack propagation. Weak grains initiate cracks and these can propagate leading to failure if the stress amplitude is high enough to support. Another important factor is **surface residual stress** state. Compressive residual stresses increase the fatigue limit while tensile residual stresses reduce the fatigue limit. It is not possible to correlate any single parameter with the fatigue limit although it is evident that a combination of all the above factors effect the fatigue limit.

For example Eberhardt *et. al.* [66] could not find a correlation of fatigue performance only with surface roughness. Aderico *et. al.* [67] also tried to correlate surface roughness and fatigue limit. However they concluded that there is no correlation between surface roughness value and the fatigue limit, implying the fatigue limit could not be correlated to one single parameter.

2.6. Fatigue Failure in Ultra High Cycle Regime

The classical fatigue endurance limit which is explained in section 2.5.4 is a method of testing materials at a constant range of cyclic stress and investigating the stress range below which fatigue failures do not occur. But it is understood that Ultra-High Cycle Fatigue (UHCF) failures can occur at stress levels below the conventional high cycle fatigue limit [68, 69]. Fig.21 [70, 71] shows a schematic representation of multistage fatigue life diagram, which illustrates the variation of fatigue life with stress amplitude from low-cycle fatigue (LCF) to UHCF. Fig.21 shows a transition region (III) exists in UHCF range (where $N_f \geq 10^7$), which fatigue failure could occur at stress amplitudes less than conventional fatigue limit.

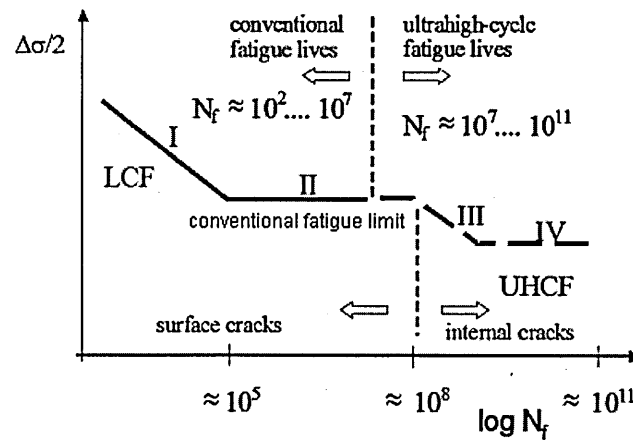


Fig.21: Schematic representation of S - N curve [70, 71].

Bathias [72] pointed out that several types of stress concentrations can be involved in gigacycle fatigue such as inclusions, pores and microstructural defects. Murakami *et. al.* [73] observed fracture initiations at subsurface non-metallic inclusions, such as Al_2O_3 , $Al_2O_3(CaO)_x$, TiN etc, and also in some cases they observed an optically dark area beside the inclusion at the fracture origin in high strength steels and suggested that this kind of formation is presumed to be influenced by hydrogen trapped by inclusions.

A distribution of fatigue failures in LCF and UHCF are shown in Fig.22 [73], which can clearly observe two distinct behavioural patterns of fatigue failures, one is failures originated at the surface of the components and the other is failures originated from sub-surface inclusions.

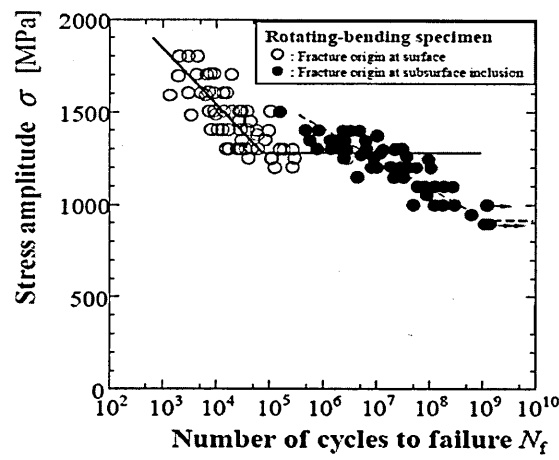


Fig.22: The distribution of S-N data of SAE52100 steel, obtained by rotary bending tests [73].

The fracture surface of UHCF failed sample generally exhibits a small bright spot at the crack initiation which is called a ‘fish-eye’ [74], which is a typical feature of UHCF fracture surfaces. Fig.23 [75] illustrates schematically the fish eye formation of a fracture surface of an internally initiated crack and Fig.24 [76, 69] show fish-eye growth in actual fracture surfaces.

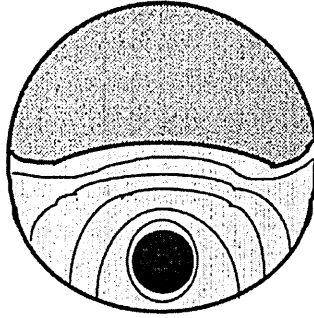


Fig.23: Schematic representation of a fracture surface initiated from sub-surface [75].

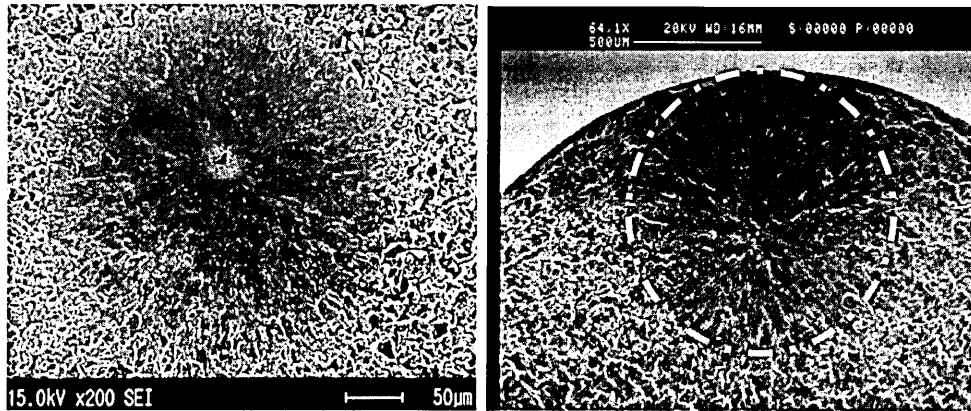


Fig.24: (a) Fish-eye fracture initiated from subsurface inclusion of about $10\mu\text{m}$ in SUJ2 steel [76], (b) Fish-eye fracture in high strength steel [69].

Wagner suggested that high cycle fatigue cracks often nucleate at subsurface at the position of maximum tensile residual stress as shown in Fig.25 [77].

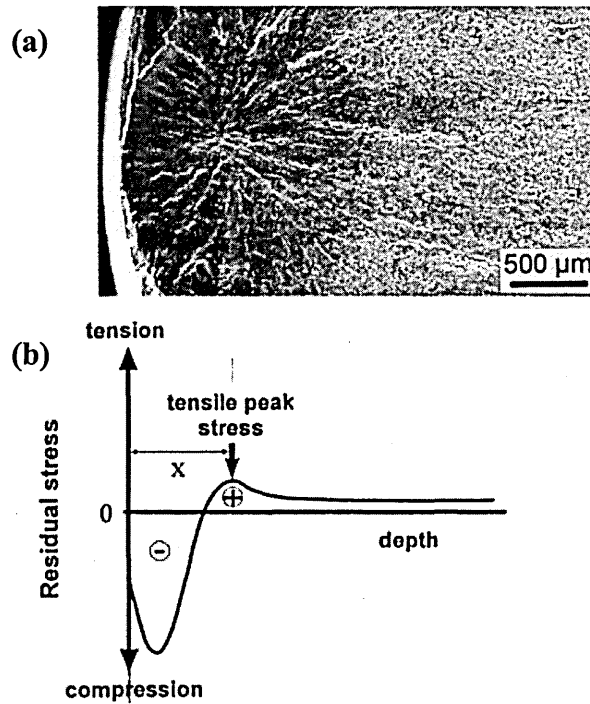


Fig.25: (a) Subsurface fatigue crack nucleation of $(\alpha+\beta)$ titanium alloy, Ti-6Al-7Nb, (b) schematic representation of stress profile [77].

2.7. Fatigue Behaviour of Ti-6Al-4V Alloy

Numerous studies conducted on the crack nucleation in $\alpha + \beta$ Ti alloys have revealed that the crack initiation is due to occurrence of heterogeneous deformation in the form of intense slip bands [78, 79, 80, 81]. Nakajima *et. al.* [78] investigated fatigue crack propagation in two kinds of $\alpha + \beta$ Ti alloys, Ti-6Al-4V and Ti-4.5Al-3V-2Fe-2Mo, and observed that multiple cracks initiated predominately in α grains. These incipient fatigue cracks initiated as stage I cracks. The early cracks which were almost the same size as the α grains appeared to grow on the planes of maximum shear stress [78]. Benson *et. al.* [79] demonstrated for notched mill annealed Ti-6Al-4V samples at room temperature, the nucleation sites were at slip bands in the α grain. He also revealed small cracks on the slip bands as early as 3% of the total life. At very low stresses α - β interfaces served as initiation sites with no detectable slip bands [79].

Eylon and Pierce [80] showed in Ti-6Al-4V alloy, the portion of life attributed to crack nucleation and growth to a detectable crack size is more than 85%. Le Biavant *et. al.* [82] also observed that in Ti-6Al-4V alloy, 80% of the fatigue life is consumed for crack initiation. So the crack growth rate in the LEFM region is higher and the propagation part of the fatigue life is smaller than the initiation part. Fig.26 [81] gives clear illustration on this point which emphasises the importance of the crack nucleation period in Ti alloys. Minimising the size of defects and microstructural features which grow under fluctuating loads would help to improve the fatigue life of components made out of Ti-6Al-4V.

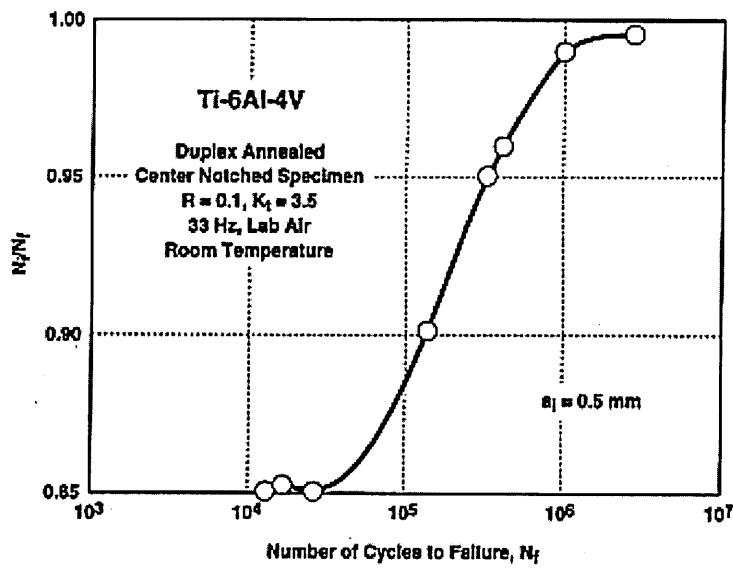


Fig.26: Fraction of total life consumed in initiation a 0.5 mm crack in flat centre notch, tested at $R = -1$, room temperature for Ti-6Al-4V [81].

Wagner and Lutjering [83] have investigated growth of short fatigue cracks in Ti-6Al-4V alloy with different microstructures. The results are shown in Fig.27. It can be seen that the crack nucleation is quickest in the coarse lamellar microstructure followed by the fine lamellar and equiaxed microstructures. It has been shown that the growth rate increased rapidly as the crack length is increased. This suggests that the initial size of defects is important as it may affect the fatigue life.

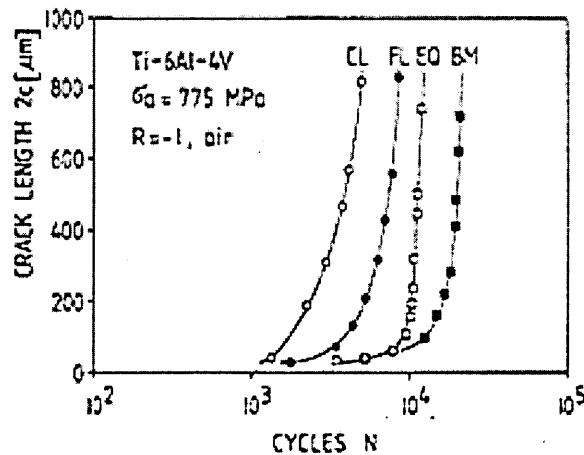


Fig.27: Growth of short fatigue cracks of different microstructures of Ti-6Al-4V at $R = -1$, in air at 775 MPa stress amplitude: CL; coarse lamellar, FL; fine lamellar, EQ; equiaxed, BM; bi-model [83].

Observations near the threshold region are very important in short fatigue crack studies. Fig.28 [84] and Fig.29 [11] shows experimental results of crack growth behaviour for Ti-6Al-4V alloy. Fig.28 illustrates the increment of threshold stress intensity factor, ΔK_{th} , can be observed with the reduction of stress ratio.

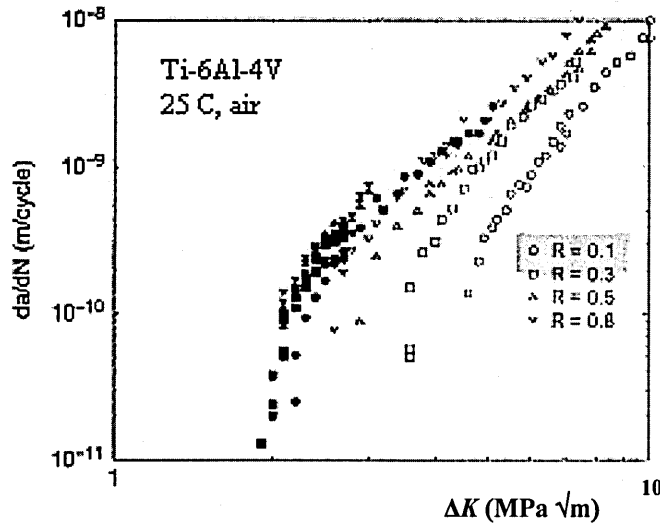


Fig.28: Crack growth rates as a function of ΔK in Ti-6Al-4V alloy at 25°C in air [84].

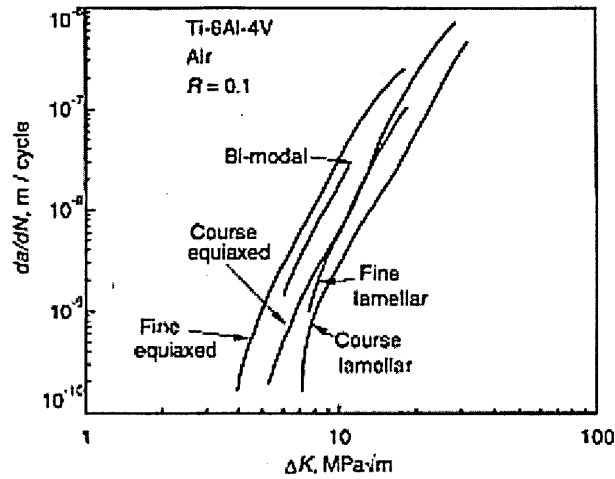


Fig.29: Crack growth rates vs. ΔK in Ti-6Al-4V at $R = 0.1$ in air, fine equiaxed structure and coarse equiaxed has average α grain size of $2\mu m$ and $12\mu m$ [11].

Research related to $(\alpha + \beta)$ titanium alloys has shown that the microstructure of the material can have an adverse effect on fatigue crack propagation and threshold behaviour for long cracks [83, 85, 86, 87]. Fig.29 shows the variation of ΔK_{th} for different microstructural arrangements and the material with fine equiaxed arrangement shows the lowest ΔK_{th} . It is clear that the material with fine equiaxed microstructure is

highly notch sensitive comparing to others. Fig.30 [86] shows the variation of ΔK_{th} with different grain sizes. It can be clearly seen that the threshold for fatigue crack growth increases with increasing grain size.

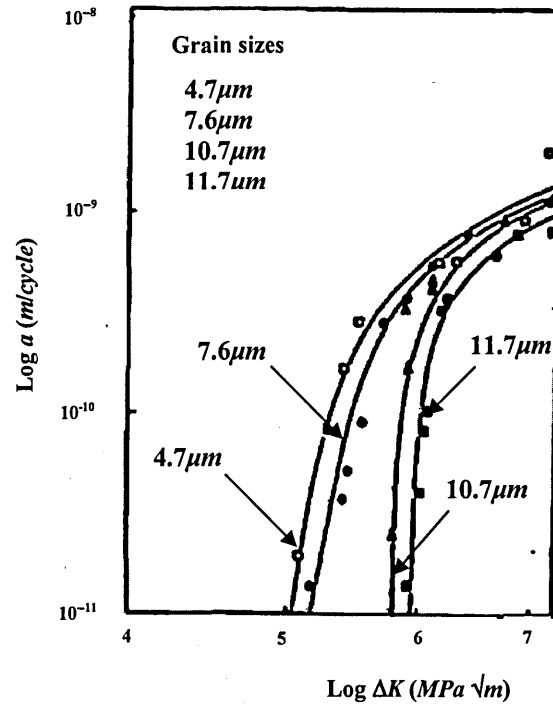


Fig.30: The effect of α grain size on the threshold for fatigue crack growth in equiaxed α with retained β microstructure for Ti-6Al-4V [86].

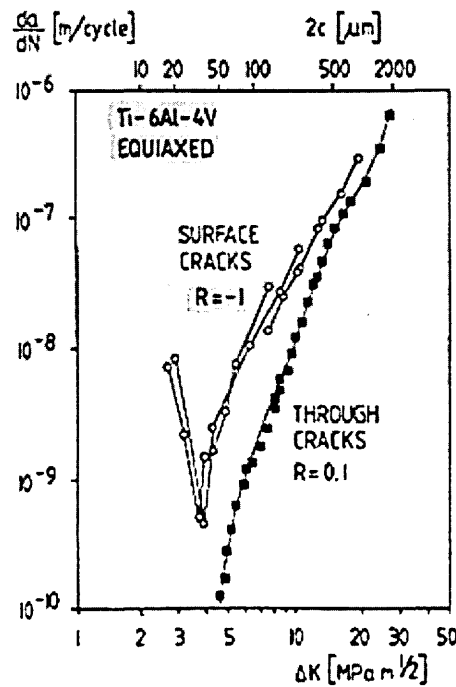


Fig.31: Fatigue crack propagation of short surface cracks as compared to long through cracks in Ti-6Al-4V with equiaxed microstructure [83].

Fig.31 shows the variation of fatigue crack propagation rate against the stress intensity factor range observed by Wagner and Lutjering [83] for Ti-6Al-4V alloy. They observed the crack nucleating at slip bands in α phase and propagation along slip bands in the equiaxed microstructure, where α grain boundaries and phase boundaries between α and β grains act as microstructural barriers for crack propagation.

The $S-N$ behaviour of Ti-6Al-4V with different microstructural grain size is shown in Fig.32 [31]. According to the results the fatigue strength increased from 550MPa to 720MPa, with α grain size decrease from 12 μ m to 2 μ m in the equiaxed structure.

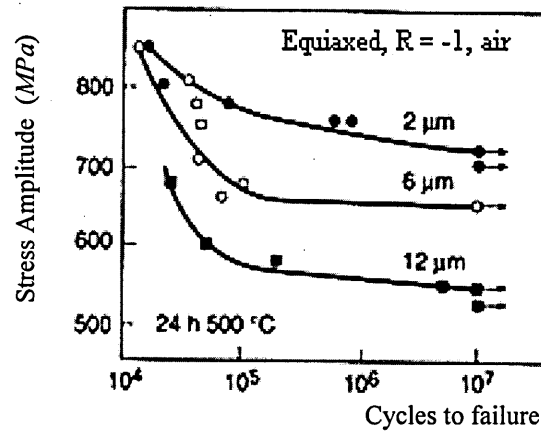


Fig.32: $S-N$ curves ($R = -1$ in air) in Ti-6Al-4V fully equiaxed microstructure, effect of α grain size [31].

The scatter of fatigue strength vs. tensile strength of Ti-6Al-4V is shown in Fig.33 [11]. Fatigue strength of smooth specimen made out of Ti-6Al-4V with a tensile strength of 1000MPa can be predicted at around 580MPa.

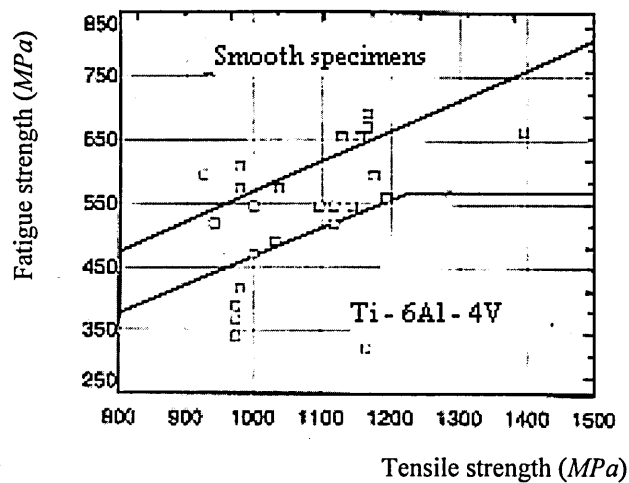


Fig.33: Fatigue strength vs. tensile strength for Ti-6Al-4V [11].

2.8. Fatigue in Hip Implants

Hip implants may contain defects which form during material processing, manufacturing, implanting, etc. Under in-vivo conditions, these defects can act as crack initiation points and these cracks then can then grow to cause ultimate failure of the component. Investigation of failed implants and failure locations would help to identify the possible manufacturing processes which may have influenced failure initiation.

There are two main locations in hip femoral components where fatigue failure is most likely to occur. They are, (i). the **neck region** of the implant as shown in Fig.34 [88], and (ii). the **cone region**, as shown in Fig.35 [26].

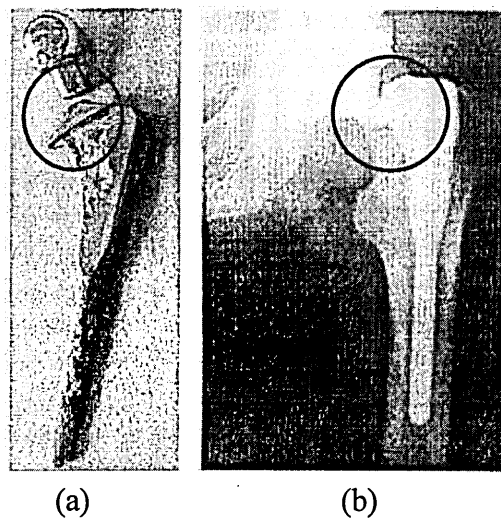


Fig.34: Hip implant failed in neck region [88].

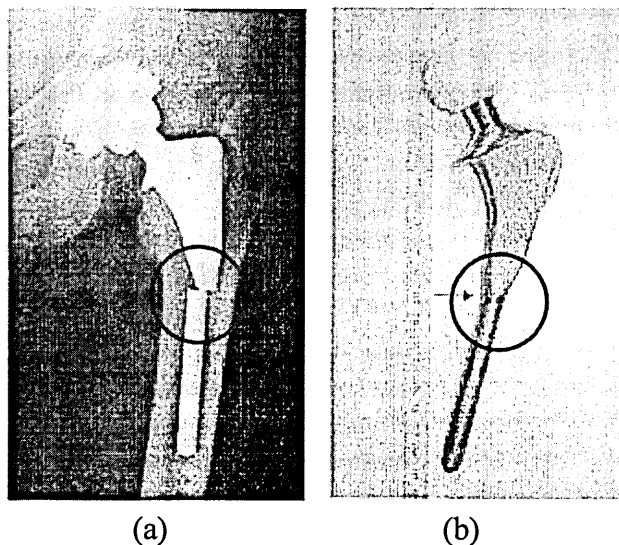


Fig.35: Hip implant failed at distal stem cone region [26].

The fixation of implant to the bone may not be uniform throughout the H-AC coated stem as expected. The stem could potentially be fixed to number of different depths proximally and distally. Two possibilities of fixation are shown in Fig.36. When an implant is fully fixed to the bone as shown in Fig.36(a), the most susceptible area for failure to occur is the neck region. The failure of a femoral stem at cone region is often associated with osteolysis and loss of proximal fixation as illustrated in Fig.36(b). Partial fixation of the stem with the bone which is known as flagpole fixation, makes the cone region the most critical area to fail [163].

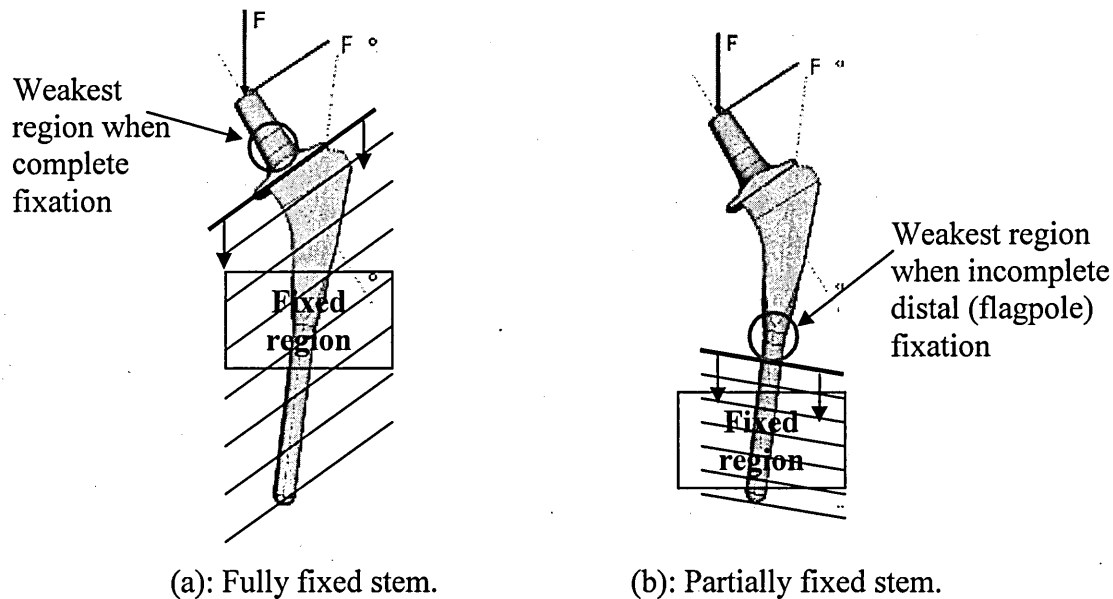


Fig.36: Two different possible fixations of implant with the bone.

2.9. Stress Distribution in Hip Implants

2.9.1. Methodology of Analysis

The finite element elastic stress analysis was conducted by Fernando [89, 90, 91] for JRI 9mm and 10mm H-AC coated hip implants made out of Ti-6Al-4V. This chapter is mainly based on an investigation carried out for 10mm JRI Furlong® H-AC total hip replacement made out of Ti-6Al-4V. The explanation will be more general which will fit to all sizes of hip implants.

The analysis was performed assuming a partially constrained condition of the femoral stem. The stem was constrained in accordance with BS 7251-Part5 (1990) [92]. In the constrained area all the mesh nodes were constrained in all 6 degrees of freedom. The femoral stem was analysed with two loading conditions, both are point loads, load step 1 and load step 2 as shown in Fig.37 [91]. Step 1 is compressive axial load of $3kN$ applied to the spigot end of the stem and step 2 is a load of $3kN$ applied normal to the axis of the spigot. Loading and load offsets have been conducted in accordance with ISO 7206-4 "Implants for Surgery-Partial and Total Hip Prosthesis - Part 4" [93]. The elastic analysis was performed using ABAQUS™ software. The results (Figs.38 - 40) [91] clearly show the high stress areas of the stem are neck and cone areas. Hence the neck and cone areas are the most susceptible regions to fail under in-vivo loading and fixation conditions. As explained in Chapter 2.7 if the stem is partially fixed the tendency is to fail at the cone area and in fully fixed conditions the most susceptible area to failure is the neck area.

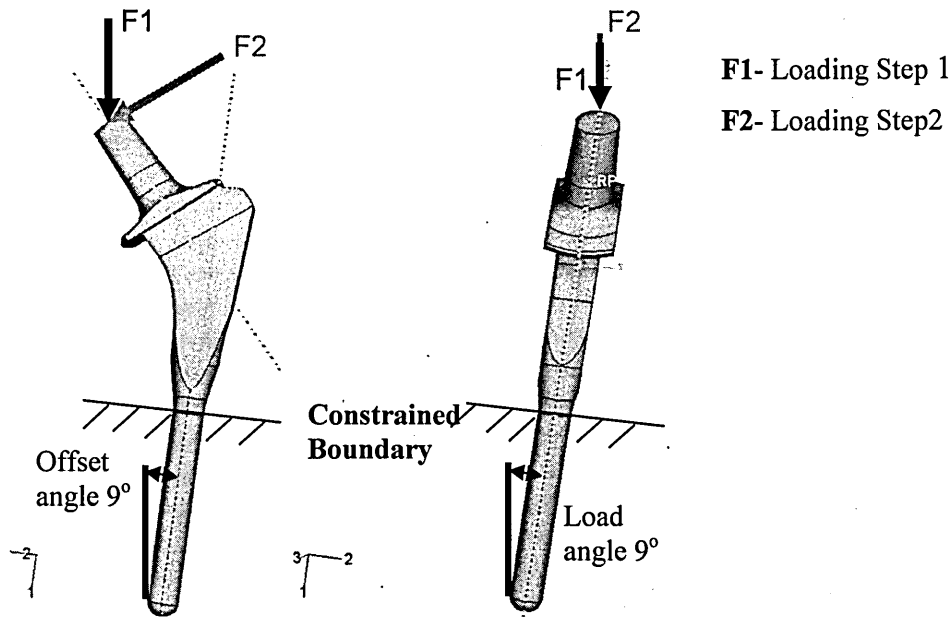


Fig.37: Implant model with constrained and the loading steps [91].

Figs.38 - 40 [91] shows clearly the high stressed areas of the stem. The analysis was carried out using 10mm stem model with Ti-6Al-4V mechanical properties.

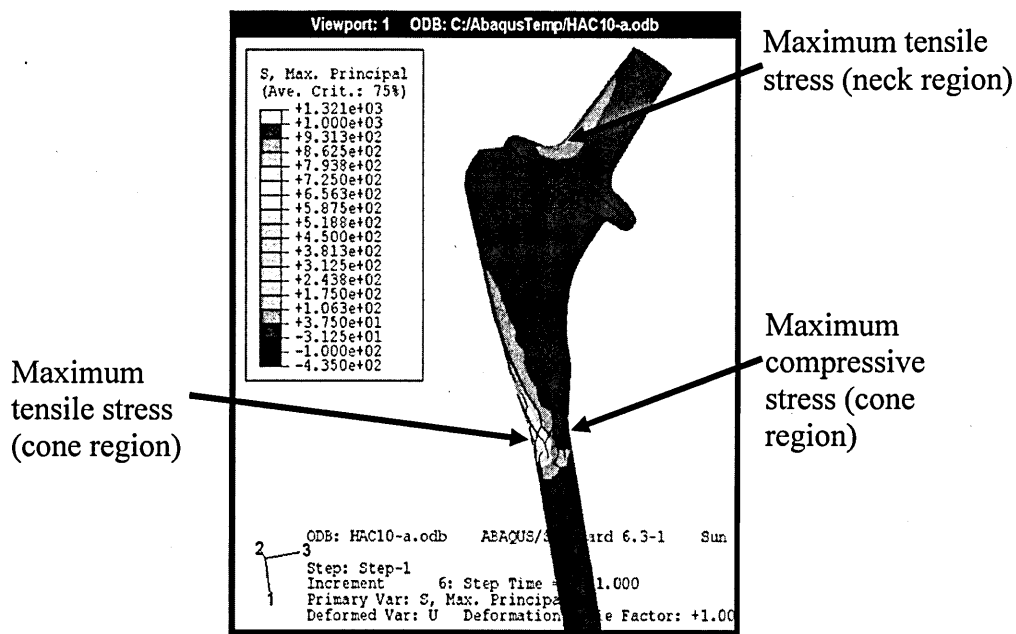


Fig.38: Overall stress distribution under load step 1 [91].

As shown in the Fig.38 the cone and neck areas are the most stressed areas under load step 1. The highest stress which is 1321MPa is at the cone region. The neck area is under maximum stress of 175MPa . It is reported that the maximum tensile and compressive stress are at the fixed boundary.

2.9.2. Stress Distribution in Neck Area

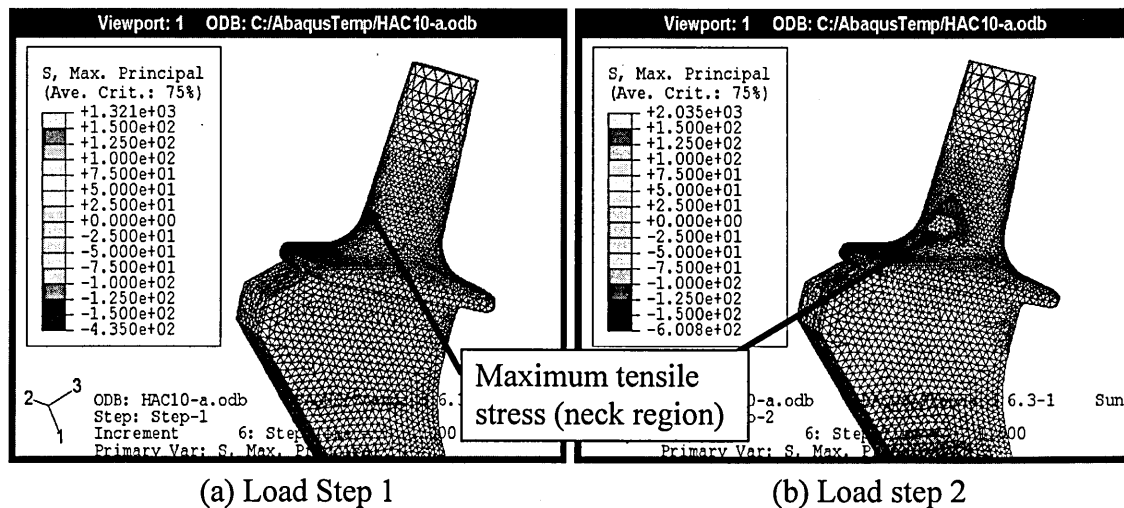


Fig.39: Stress distribution at the neck area under load step 1 and 2 [91].

The high stressed area at the neck region is slightly shifted to the front side (Fig.39(b)) with the application of load step 2. For both loading conditions the high stresses area remains on the posterior side of the hip implant.

2.9.3. Stress Distribution in Cone Area

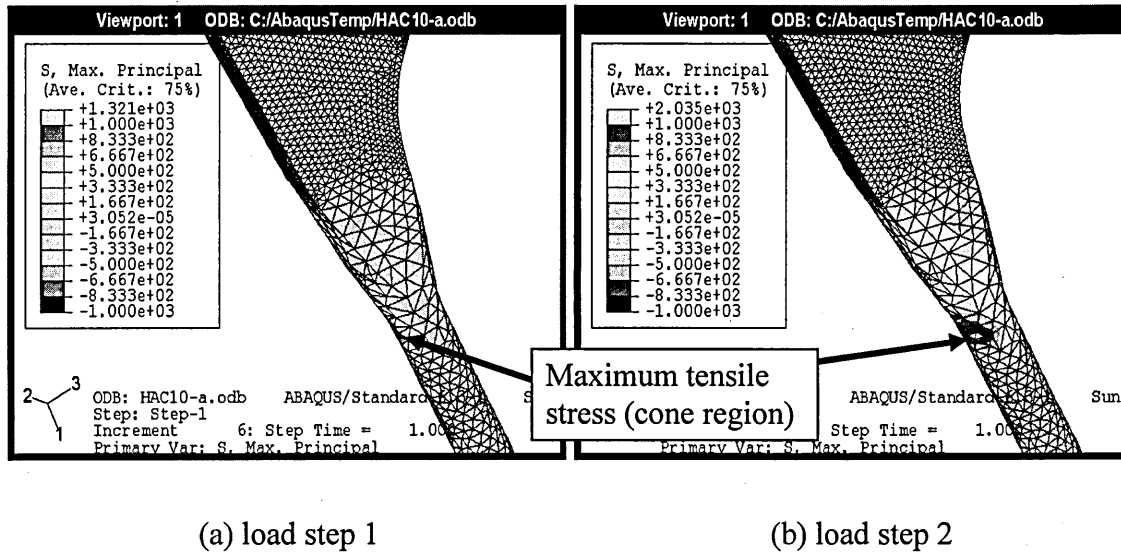


Fig.40: Stress distribution at the cone area under load step 1 and 2 [91].

The high stressed area at the cone region is slightly shifted to the front side (Fig.40-b) with the application of load step 2. For both loading conditions the high stresses area remains on the posterior side of the hip implant.

The value of the stress was found to be below the fatigue limit for H-AC coated Ti-6Al-4V alloy [94]. When the implant is fully strained over the whole of the H-AC coated region the majority of stress was concentrated in the neck region [94]. However the majority of load transfer from the stem to the bone occurs in the proximal (triangular) region of the stem [94]. Further details of the analysis, loading cases, boundary conditions and results in various forms are presented elsewhere [89, 90].

2.10. Surface Roughness and Its Influence on Fatigue Behaviour

2.10.1. Effect of Surface Roughness on Fatigue Performance

It is known that fatigue cracks mostly initiate at a free surface and this situation causes fatigue life sensitive to surface roughness. Surface roughness can often act as small notches and may influence the initiation of fatigue cracks. Surface finishing/roughness significantly influence S-N characteristics [95, 96]. Itoga *et. al.* [95] have investigated the variation of fatigue performance due to surface defects such as surface scratches, machine marks and dent-like features which roughen the surface. It has been shown that very high strength steel generally show a step wise S-N curve consisting of two parts, short life regime around 10^5 cycles and long life regime more than 10^7 cycles. Fig.41 shows a schematic illustration showing the effects of surface roughness on S-N characteristics of high strength steels.

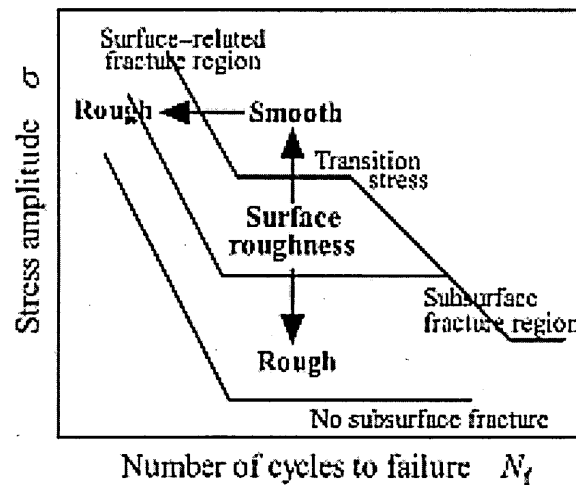


Fig.41: Schematic diagram of the effects of surface roughness on S-N characteristics [95].

It would seem obvious that the smoother the surface the higher the fatigue performance. Maiya [96] tried to characterize surface roughness and correlate it to fatigue crack initiation using hour glass shaped fatigue samples of stainless steel. Measuring the fatigue striation spacing he calculated the crack initiation life N_o , which is the number of cycles to initiate a crack length equal to 1mm . He formulated a relationship for N_o , which is $N_o = A(\text{surface roughness parameter})^{-\alpha}$, where A and α are constants. Fig.42 [96] shows the relationship of N_o against maximum depth of surface roughness $R_{z(max)}$.

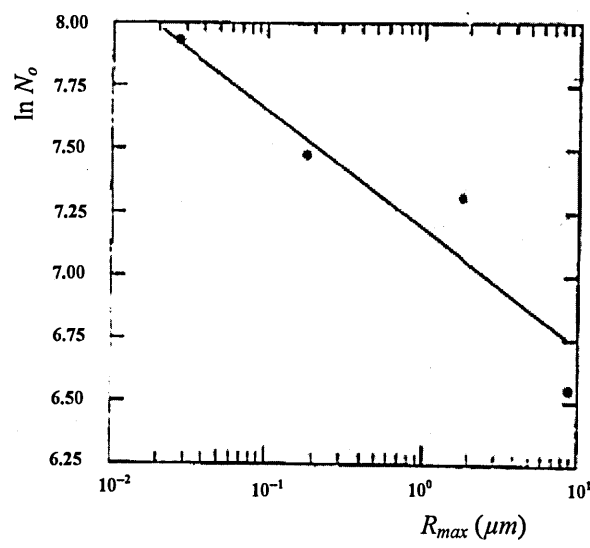


Fig.42: Fatigue crack initiation life N_o vs. maximum depth of surface roughness R_{max} [96].

Murakami *et. al.* [97, 98] proposed an equation for the prediction of the fatigue limit of specimens with small defects as,

$$\sigma_{w,p} = \frac{1.43(HV + 120)[(1 - R)/2]^\alpha}{(\sqrt{area})^{1/6}} \quad (11)$$

where $\sigma_{w,p}$ is the predicted fatigue life (MPa), HV the Vickers hardness (kgf/mm^2), \sqrt{area} the square root of defect area projected onto the principal stress plane (μm), R is the stress ratio and α is given by $0.226 + HV \times 10^{-4}$. The details of the parameters and evaluation were given in [98].

2.10.2. Parameters of Surface Roughness Measurement

There are different types of parameters which may be used to characterize the surface roughness. All these can be divided into three main categories; (i). Amplitude parameters, (ii). Spacing parameters and (iii). Hybrid parameters. The most commonly used roughness number is R_a , which is an amplitude parameter and represents the arithmetic mean of the absolute departure of the roughness profile from a mean line [100]. Since most fatigue failures initiate from the weakest point on the surface it is important to examine the maximum defect on the surface and the roughness number should represent the maximum defect size of the surface. The R_a is the arithmetic mean

over the sampling length; it does not represent the maximum defect size of the measured sample. Maximum roughness number, R_z , is another amplitude parameter which represents the maximum peak to valley height within the sampling length. Which is,

$$R_z = R_p + R_v \quad (12)$$

Where R_p and R_v , are the maximum depth profile below the mean line and maximum height profile above the mean line respectively. This parameter represents the maximum defect size of a sample and the fatigue failures are mostly vulnerable to initiate at the maximum defective point. The surface roughness number given throughout this thesis is the $R_{z(max)}$, which is the largest individual peak to valley from each sampling length as shown in the Fig.43 [100].

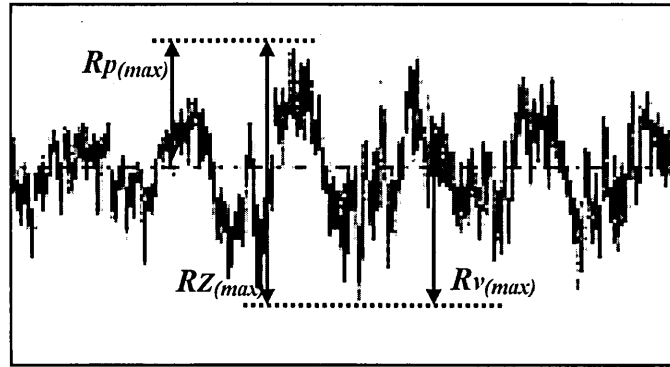


Fig.43: Surface roughness profile and the illustration of $R_{z(max)}$ roughness number [100] .

2.11. Residual Stresses and its Effects on Fatigue Performance

Residual stress is the internal stress existing in a body that is under no external loads. It is due to the localized plastic straining due to various loading conditions. Residual stress can have a significant influence on the fatigue life of an engineering component [38]. It is well known that near surface tensile residual stresses tend to accelerate the initiation and the growth phases of the fatigue process while compressive residual stress close to a surface prolong the fatigue life by retarding the fatigue crack growth rate [101,102,103].

Starting from the bar stock material through to the finished product, the medical implants have been subjected to various loads and stresses during manufacturing which can introduce plastic strain within the component which creates residual stresses. As an example, it is well known that residual stresses are induced as a result of coating deposited by the plasma spraying method [104,105]. It is therefore important to investigate the introduction of residual stresses by different manufacturing processes and study the effects.

Fig.44 [35] and Fig.45 [11] show the interaction between peak residual stresses against fatigue strength of Ti-6Al-4V alloy under different manufacturing practices.

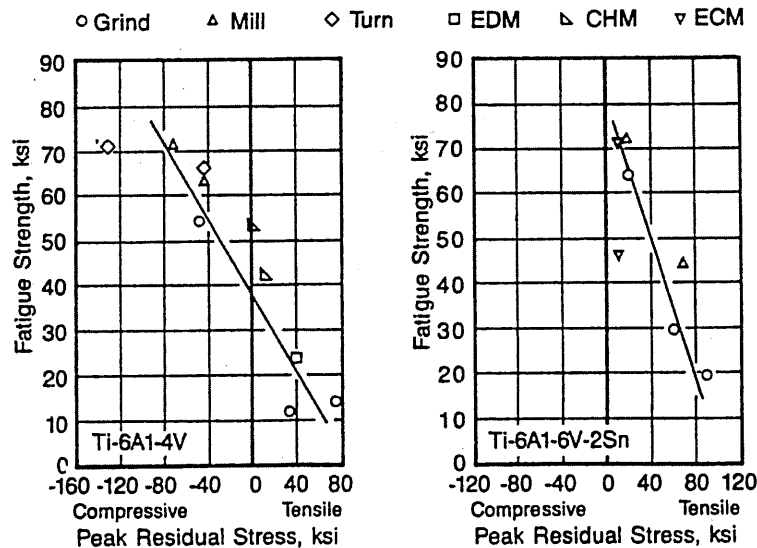


Fig.44: Correlation between fatigue strength and peak residual stress for Ti-6Al-4V and Ti-6Al-4V-2Sn materials [35]. (Note: EDM- electrical discharged machining, CHM- chemical machining, ECM- electrochemical machining)

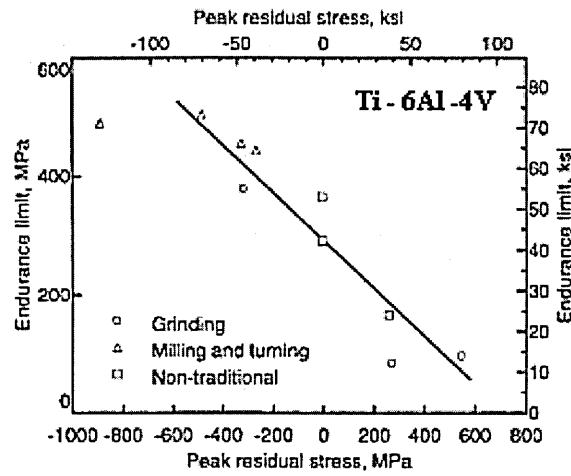


Fig.45: Correlation between fatigue strength and peak residual stress for Ti-6Al-4V material [11].

According to Fig.44 and Fig.45 it is clear that milling and turning operations induce compressive residual stresses and grinding operations induce both compressive and tensile residual stresses on the surface of the component.

Turning and grinding are chip removal processes which break small chips of material from the work piece. As a result these processes cause permanent elongation of the surface layer which ultimately introduces compressive residual stress to the surface and below surface the bulk of the material with tensile stresses [106]. Xiaoping Yang *et. al.* [107] also investigated the introduction of residual stresses due to manufacturing processes like turning (facing) and grinding on Ti-6Al-4V samples. They have used X-ray diffraction to measure residual stresses and one of the measured stress profiles is shown in Fig.46 [107]. It is notable that the turning operation introduces compressive surface residual stress on Ti-6Al-4V samples.

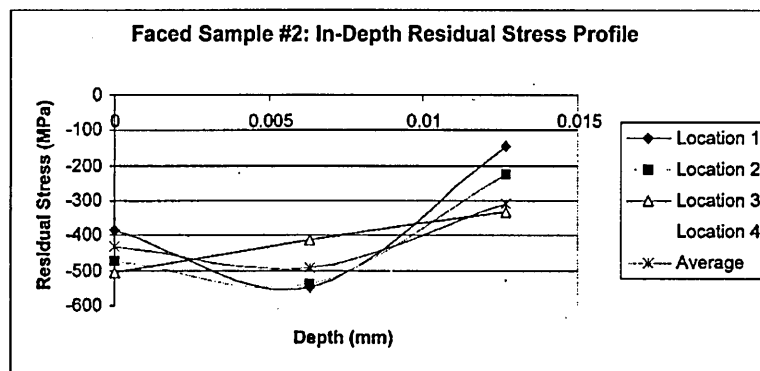


Fig.46: In-depth residual stress profile for faced sample [107].

The magnitude of residual stress changes with the depth of the sample. This stress status of a sample can be changed by conducting different heat treatments, with various treatment temperatures and durations. The residual stress distributions in Ti-6Al-4V alloy after different heat treatments are shown in Fig.47 [108]. According to this figure heat treatments of, 500°C for 1hr, 500°C for 30hrs and 600°C for 1hr significantly relieve the surface residual stress level. The specifications of the stress relief heat treatments are well documented in text books [109] and are shown in Table.3.

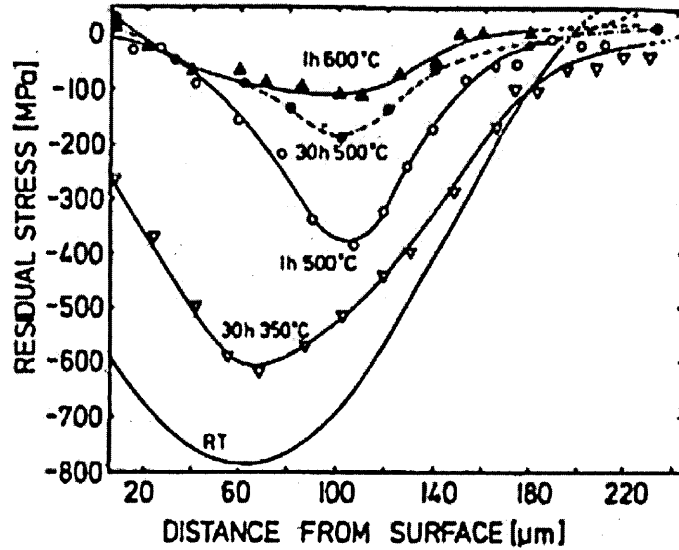


Fig.47: Residual stress profiles for different annealing treatments in Ti-6Al-4V alloy [108].

Alloy	Stress relief		
	Temp. (C°)	Time(h)	Cooling
Commercially pure Ti	480-600	0.25-1	air
Alpha	540-650	0.25-4	air
Near Alpha	480-700	0.25-4	air
Alpha-Beta	480-700	0.25-4	air
Beta	675-760	0.1-0.5	air

Table.3: Stress relief heat treatment specifications for titanium alloys [109].

2.12. X-ray Diffraction (XRD) Technique for Residual Stress Measurements

2.12.1. Introduction

There are different kinds of techniques used in measuring residual stress. Some are destructive techniques such as hole drilling and others are non-destructive techniques like X-ray diffraction (XRD) and neutron diffraction [110, 111], where each technique has its own advantages and disadvantages. Out of these, X-ray diffraction is one of the most commonly used non destructive techniques for residual stress measurement [101, 112, 113].

Although the term stress measurement is commonly used, stress is an extrinsic property that is not directly measurable. In XRD stress measurement, the strain in the crystal lattice is measured and associated residual stress which produces the strain is calculated.

When the X-ray beam is irradiated on a crystal structure, the beam is scattered or diffracted by the atomic planes. These diffracted wave fronts from various lattice planes travel different directions and distances, and they interfere constructively only where the difference in path length is an integral multiple of the X-ray wave length. This happens at specific angles, defined by Bragg's law of diffraction, see section 2.12.2. XRD technique measures the residual stress from the shift in X-ray diffraction peak position (2θ), caused by the change of lattice spacing due to the presence of residual strain. These superinforced diffracted wave fronts show peaks in the intensity plot. If the X-ray detector moves around the irradiated specimen it will find peaks in intensity at certain angles. Typical examples of peaks at different diffraction angle are shown in Fig.48 [114]. From these (2θ) angles the spacing between the planes of atoms can be calculated. If the crystal lattice structure is altered by an external force, it will create residual stress within the material; as a result the lattice spacing will be altered. The change in lattice spacing will also change the angular position of the X-ray peak. Using Bragg's Law, the new atomic spacing can be calculated by the new peak position and then the strain can be calculated by the difference between the old and new atomic spacing. Using calculated strain values the respective stress values can be calculated.

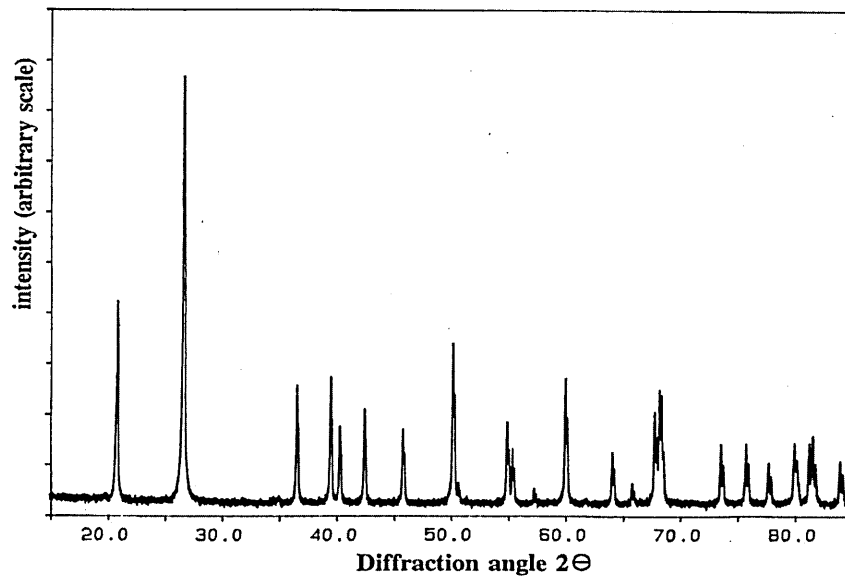


Fig.48: An example of X-ray diffractometer chart of intensity of the reflected beams vs. 2θ angle for quartz SiO_2 specimen [114].

The elastic constants of the material are used for the calculation, assuming linear elastic distortion of the crystal lattice. The technique of measuring residual stresses in a component using XRD is firmly established and explained in literature [101, 112, 115].

2.12.2. Bragg's Law

In order to measure the stress using X-rays, the X-ray beam should diffract in appropriate manner. X-ray diffraction relies on the fundamental interaction between the wavelength of the X-ray beam (λ) and the crystal lattice spacing (d). The diffraction of the X-ray beam on crystalline materials initially studied by the British scientist W.L Bragg in 1912 [cited in 115], and is called Bragg's law. This expression defines conditions necessary for diffraction of X-rays to occur and Bragg's law is commonly known as the fundamental basis for all X-ray diffraction measurements.

Fig.49 [116] illustrates the incident and reflected X-ray beam and the notations used. Any change in the lattice spacing, d , results a corresponding shift in the diffraction angle 2θ .

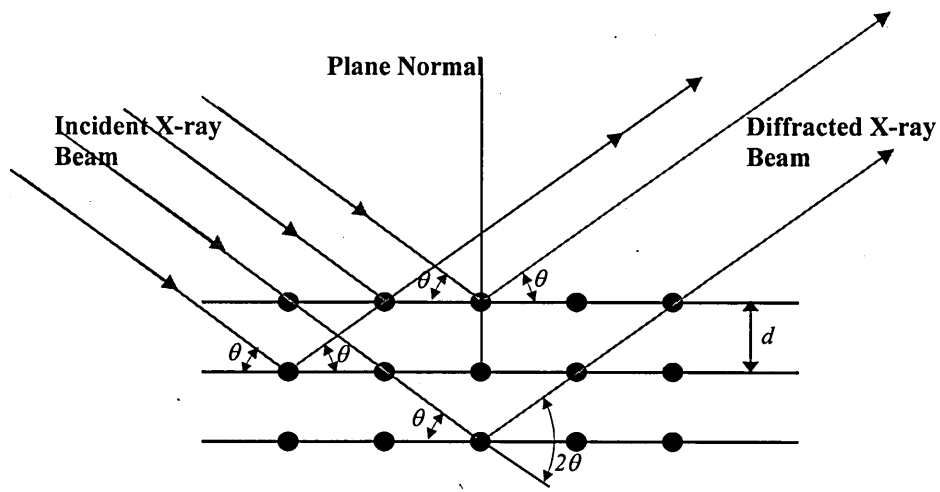


Fig.49: Illustration of X-ray diffraction by a crystal lattice [116].

Bragg's Law can be stated as,

$$n\lambda = 2d \sin \theta \quad (13)$$

where, λ - wave length
 d - lattice spacing
 θ - incident/diffraction angle
 n - integer denoting the order of diffraction

2.12.3. Measurement of Residual Stress

To perform strain measurements the component is placed in a X-ray diffractometer and exposed to an X-ray beam that interacts with the crystal lattice to cause diffraction patterns. When the material is stressed/strained the crystal lattice will elongate and contract accordingly. This changes the inter-planer spacing, d , which will cause a shift in diffraction pattern. By accurate measurement of the peak shift, the change in the interplanar spacing can be evaluated and thus the strain within the material can be obtained. If the unstrained inter-planar spacing is d_o , strain (ϵ) can be expressed as,

$$\epsilon = \frac{d - d_o}{d_o} .$$

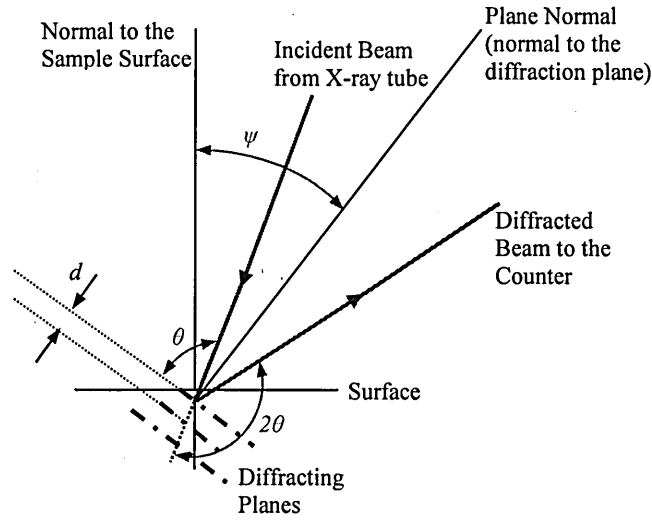


Fig.50: Incident and diffracted beams with angular notations; the plane normal which is the normal to the lattice plane is at an angle of ψ to the normal to the surface of the component.

As shown in the Fig.50 the angle between the normal to the sample surface to plane normal *i.e.* the normal to the measuring diffraction lattice plane is represented by ψ . By altering the tilt of the specimen or by tilting the X-ray tube and detector within the diffractometer, measurements of planes at an different ψ angles (d_ψ) can be made, and strains (ϵ) along respective directions can be calculated using, $\epsilon = \frac{d_\psi - d_o}{d_o}$.

The respective stress (σ) values can be calculated using Hooke's law which is in general terms, $\sigma = E\epsilon$, where E is the Young's modulus of the material. It is obvious that any tensile or compressive stress producing a strain in a particular direction will also create, not only linear strain in that direction of the stress, but also strains in the transverse directions. These components can be calculated using Poisson's ratio (ν) which is the ratio of the transverse to longitudinal strain.

Using the strain in terms of interplanar spacing the stress can be evaluated from the following equation,

$$\sigma = \frac{E}{(1 + \nu) \sin^2 \psi} \left(\frac{d_\psi - d_n}{d_n} \right) \quad (14)$$

where, E – Young’s modulus, ν – Poisson’s ratio, ψ – orientation of the plane normal to the normal to the sample surface, d_n – inter-planar spacing measured at plane normal (when $\psi = 0$) and d_ψ - inter-planar spacing measured at different ψ angles.

In XRD, several methods have been used in residual stress measurements. Some of them are, single angle technique, two angle technique, $\sin^2\psi$ technique and Marion-Cohen technique [108]. The common method used for stress determination is the $\sin^2\psi$ method, where several XRD measurements are made at different ψ angles and inter-planar spacing (d) is measured for respective ψ angles. The d against $\sin^2\psi$ is plotted which is a straight line as shown in Fig.51 [117].

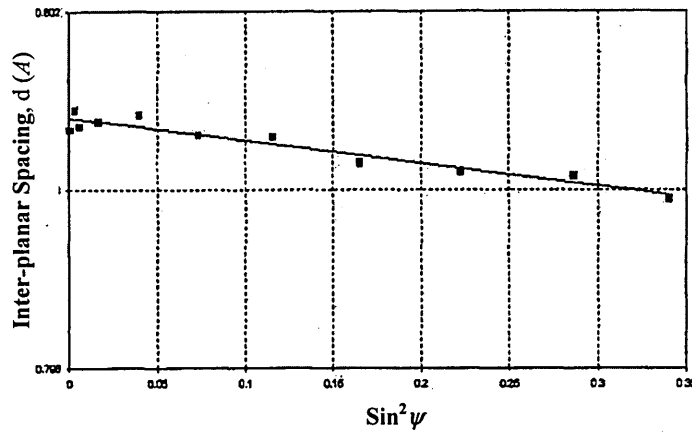


Fig.51: Example of an inter-planer spacing (d) vs. $\sin^2\psi$ plot measured for a shot peened Ti-6Al-4V sample [117].

Using the value of the gradient (m) of the straight line the stress can be evaluated. This method assumes a zero stress at $d = d_n$, where d is the intercept of the y axis when $\sin^2\psi = 0$. Thus the stress can be evaluated by,

$$\sigma = \left(\frac{E}{1+\nu} \right) m \quad (15)$$

A comprehensive explanation of the methodology with complete mathematical derivations is well documented and established [113, 118].

2.12.4. Different positions of diffractometer movements

According to the different positioning of X-ray tube and detector the ψ angle varies. Fig.52 shows three positions of the diffractometer with positive, negative and zero ψ angle values.

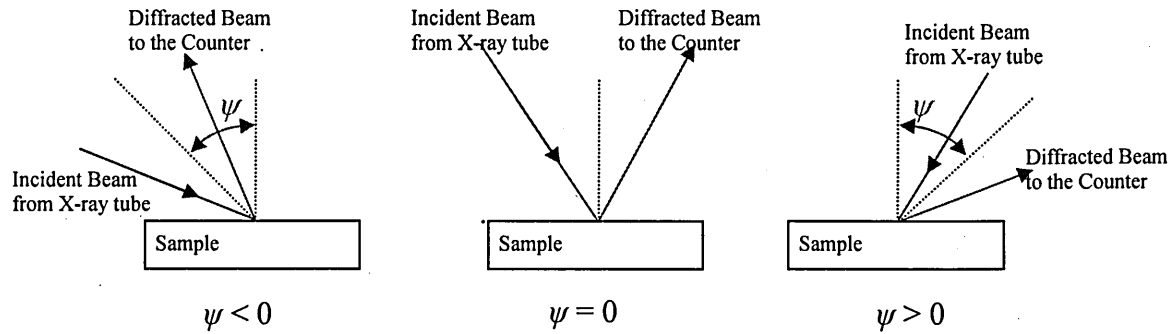


Fig.52: Different positions of the diffractometer with different stages of ψ offsets.

2.12.5. Depth of Penetration

The intensity of the incident X-ray beam is reduced in a very short distance below the surface. This occurs due to absorption of X-rays by most metallic surfaces. Generally the majority of the diffracted beam originates from a thin surface layer and hence the residual stress measurements represent only that layer of the material. It is observed that the intensity decreases exponentially with depth in the material [115]. The average depth information is defined as the depth from which 67% of the diffracted intensity has been absorbed. It is the depth at which the stress is evaluated if the stress gradient along the depth is linear. If the stress depth profile is required layers of the material are removed, using for example eletropolishing. It is assumed the removal method does not influence the stress state of the component. Expression for the thickness (x) of the effective layer of the material can be expressed as equation given below, where the complete derivation is given elsewhere [118].

$$x = \frac{\ln \left[\frac{1}{1 + G_x} \right]}{\mu \left[\frac{1}{\sin(\theta + \psi)} + \frac{1}{\sin(\theta - \psi)} \right]} \quad (16)$$

Factors such as measuring angle, intensity of voltage/energy and X-ray tube material affect the penetration of the X-ray beam into the material. The higher the θ angle the higher the depth of penetration of the X-ray beam. For maximum penetration in titanium alloys, it is recommended to use a copper tube. Fig.53 shows the depth of penetration obtained in titanium by using X-ray tubes made with different material [115, 119]. For titanium the maximum depth of penetration obtained using a copper tube is around $5\mu\text{m}$ to $6\mu\text{m}$.

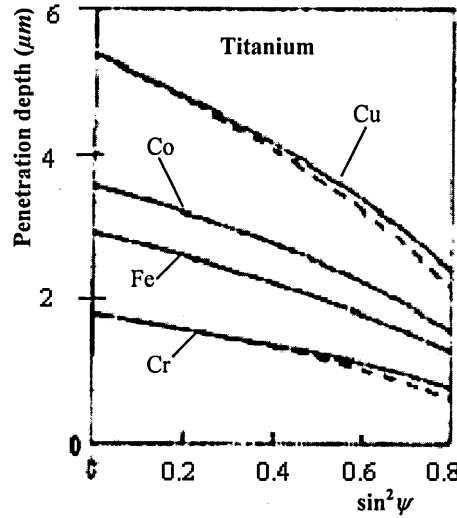


Fig.53: Penetration depth vs. $\sin^2\psi$ of Titanium for different radiations [115, 119].

2.12.6. Selection of Crystallographic Plane $\{hkl\}$

Different crystallographic planes respond differently under stress. As a result measurement made on different crystallographic planes is generally not comparable. Also measurements made with different radiations are not comparable because different radiations achieve different depth of penetrations of the X-ray beam into the sample. When conducting residual stress measurements using XRD, it is recommended to use a peak of a plane with high 2θ angle. So that a higher X-ray penetration, as well as accurate measurements, can be achieved. Table.4 [115] shows the recommended X-ray tube and $\{hkl\}$ plane for a variety of materials. For Ti-6Al-4V the recommended plane is $\{213\}$ where the approximate 2θ angle would be at 139.4° . The recommended X-ray tube anode is Copper $K\text{-}\alpha$.

Material	Bravais Lattice	X-ray Tube anode	K- β Filter	Wavelength Å (All K- α 1)	2-Theta Angle (Approx.)	{hkl}	Multiplicity ⁷
Ferrite, α -iron	BCC ⁵	Cr K- α	V	2.2897	156.1	{211}	24
Austenite, γ -iron	FCC ⁵	Mn K- α	Cr	2.1031	152.3	{311}	24
		Cr K- α	V	2.2897	128.8	{220}	12
Aluminium	FCC ⁵	Cr K- α	V	2.2897	139.3	{311}	24
		Cr K- α	V	2.2897	156.7	{222}	8
		Cu K- α	Ni	1.5406	162.6	{333}/{511}	32
		Cu K- α	Ni	1.5406	137.5	{422}	24
Nickel Alloy	FCC ⁶	Mn K- α	Cr	2.1031	152 - 162	{311}	24
		Fe K- α	Mn	1.9360	127 - 131	{311}	24
Titanium Alloy	Hexagonal ⁵	Cu K- α	Ni	1.5406	139.4	{213}	24
Copper	FCC ⁵	Cu K- α *	Ni	1.5406	144.8	{420}	24
		Cu K- α	Ni	1.5406	136.6	{331}	24
Tungsten Alloy	BCC ⁶	Co K- α	Fe	1.7889	156.5	{222}	8
Mo Alloy	BCC ⁶	Fe K- α	Mn	1.9360	153.2	{310}	24
α Al ₂ O ₃	Hexagonal ⁷	Cu K- α	Ni	1.5406	152.8	{330}	6
		Ti K- α	Sc	2.7484	156.5	{214}	24
γ Al ₂ O ₃	FCC ⁷	Cu K- α	Ni	1.5406	146.1	{844}	24
TiN (Osbornite)	FCC ⁷	Cu K- α	Ni	1.5406	125.7	{422}	24

Table.4: Recommended X-ray tube and {hkl} plane for some commonly used materials [115].

2.12.7. Sample Preparation

Generally the sample surface should be clean free from dirt, scale or grease. Any cleaning or removal of material must be done by a process that does not influence the residual state which thereby changes the stress to be measured.

2.12.8. Irradiated Area on the Sample by the X-ray Beam

The irradiated area can be varied by focussing the X-ray beam at the tube exit by means of rectangular slits and masks. When measuring residual stress of cylindrical samples it is important to optimize the irradiated area of the X-ray beam. Hence using slits and masks, the area must be controlled. When measuring stress in cylindrical samples, in the hoop direction for measurement of residual stress with an accuracy of 10% a spot size of 0.25 x radius of curvature is recommended. The intensity can be improved by elongating the beam in the axial direction. The main problem in reducing the irradiated area is the simultaneous reduction of the number of X-ray counts of which results in a weak peak and the stress measurements will have a considerable amount of error. In this

kind of situation the scan duration should be adjusted accordingly to obtain an accurate stress measurement.

The X-ray beam convergent slits and masks must be selected to optimize the irradiated area to keep the error margin as low as possible within the finalized scan duration.

The length of the area on the sample that is irradiated by the incident beam is dependent on the divergence of the X-ray beam. The divergence of the X-ray beam can be adjusted by using different type of divergence slits and masks. Slit size controls the irradiated length (L) and the mask size controls the irradiated width (w).

The irradiated length can be calculated using [120],

$$L = \frac{R \times (\sin \omega \times \sin \delta)}{(\sin^2 \omega - \sin^2 (\delta/2))} \quad (17)$$

where, L - irradiated length of the sample,
 R - radius of the goniometer,
 δ - divergence angle,
 ω - angle between incident beam and sample surface.

2.13. Manufacturing Processes and Influence on Fatigue Performance

2.13.1. Manufacturing of Hip Implants

Starting from bar stock to the finished forged stem stage, the material undergoes a sequence of manufacturing processes such as; extrusion, rumbling, shot blasting, flashing, heat treatments. During these processes the material has been subjected to different temperature levels and surface conditions.

This section concentrates mainly on grit blasting, ultrasonic cleaning and coating processes and the detailed explanation of all the processes used in manufacturing stem of the JRI Furlong[®] H-A.C. Supravit[®] coated hip replacements and specifications can be found in Chapter 4.

2.13.2. Grit Blasting, Ultrasonic Cleaning and Plasma Spaying Processes

Thermal plasma spayed H-AC coating fulfils several functions, of which improvement of the fixation of the implant to human bone is the main. A properly deposited plasma spayed coating with proper adhesion to substrate, is strongly dependent on prior surface preparation. It is obvious that the substrate roughness or topography plays an important role in the bonding mechanism. Grit blasting has been used to achieve optimum surface roughness [66] to promote physical attachment between porous coating and substrate. Generally there is no significant elemental inter-diffusion or any form of chemical bonding found at the Ti and H-AC interface; though bonding is mainly due to mechanical interlock at the interface [123]. However Huaxia *et. al.* [124] showed that some chemical bonding occurs at the interface in addition to mechanical interlocking, based on the presence of calcium titanate phase at the interface.

The grit blasting process leaves particles of grit blasting media on the blasted surface and it is important to remove them as they may act as sites for fatigue crack initiation. The main aim of ultrasonic cleaning is to remove inclusions from grit blasting with a secondary aim to remove surface contamination such as dust. As a result the adherence of H-AC coating is enhanced. Also ultrasonic cleaning is used to remove all kinds of

inclusions and foreign particulate matter resulting from other manufacturing processes such as polishing and grinding.

Plasma spraying is used to apply a Ti undercoat and H-AC outer coat on to the surface of the stem. H-AC coatings have been applied using different techniques [125]; for example, dip coating, electrophoretic deposition, hot isostatic pressing, ion-beam sputtering, ion-beam dynamic mixing, plasma spraying, conventional flame spraying and high velocity oxy-fuel combustion spraying. It is understood [126, 127, 128] that the plasma spraying technique is the most chemically controlled and efficient process, which minimize any reduction in substrate fatigue resistance.

2.13.2.1. Effects of Grit Blasting

Grit blasted surfaces contain highly complex topography. Grit blasted surfaces contain two types of surface damage [130], first is indentation type deformations produced by impact of sharp, angular grit particles and second is cutting type impacts due to sharp edged particles which cut into the metal. These two types of surface damage have been observed by Finnie *et. al.* [131] and also by Hutchins [132]. These types of surface features can act as stress concentration sites for fatigue crack initiation and thereby reduce the fatigue limit. Evans and Gregson [28], also identified small cracks, scratches and folded areas from SEM micrographs of grit blasted surfaces which again act as stress raisers and promote the fatigue initiation.

2.13.2.2. Effect of H-AC Coating on Ti-6Al-4V Substrate

There are number of ways in which a plasma sprayed coating could affect the fatigue behaviour of the substrate [28]; one can be the concentration of stresses at the cracks in the coating. Also since the process is associated with high temperature, there can be thermal or chemical effects on the substrate surface. Further there is a possibility of inducing of tensile residual stresses within the surface layer of the substrate due to the rapid cooling of the coating [28].

Fig.54 [28] shows a section of a grit blasted and plasma sprayed specimen where small fatigue cracks can be seen, these cracks which are initiated from sites of surface damage are likely to influence further propagation beyond coating substrate.

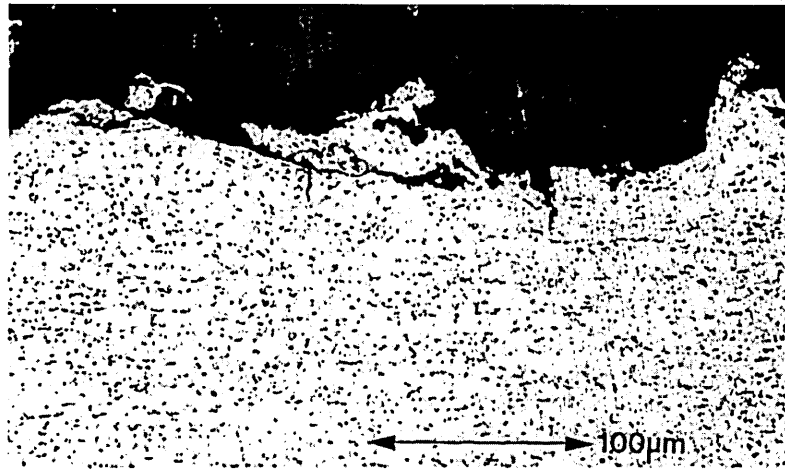


Fig.54: Longitudinal section through a fatigued grit blasted and plasma sprayed sample made with Ti-6Al-4V [28].

Nishida *et. al.* [133] experimentally evaluated the fatigue properties of plasma sprayed Ti-6Al-4V and found that the plasma sprayed samples have lower fatigue limit compared to conventional Ti-6Al-4V. The reduction is about 20% - 50% compared to conventional Ti-6Al-4V samples. They [133] also found that a large number of micro cracks initiate and propagate from specimen surface underneath the coating which is a reason of the reduction of fatigue performance.

Normally the thermal spraying process creates moderate temperatures around 400°C. Even though these temperatures are well below the stress relief level for Ti-6Al-4V they can cause changes to residual stress profile of the sample. The literature [67, 134, 135, 136, 137] suggests that while surface residual stress at the substrate is positive (which is tensile) they tend to be compressive in the coating or deposited material. These researchers have predicted the stress profile using validated numerical simulation methodology. Fig.55 [67] and Fig.56 [137] shows the predicted stress profiles in the substrate and deposit sections. Fig.56 shows the change of stress distribution by the spraying process. Since the spraying process creates tensile stresses at the substrate, it can promote fatigue crack initiation at the substrate on coated samples.

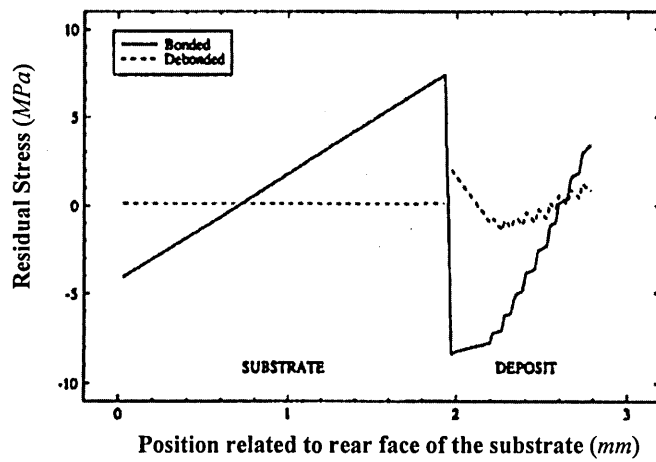


Fig.55: Predicted residual stress distribution in typical Vacuum Plasma Sprayed Commercially Pure-Titanium (deposit) / Ti-6Al-4V (substrate) system [67].

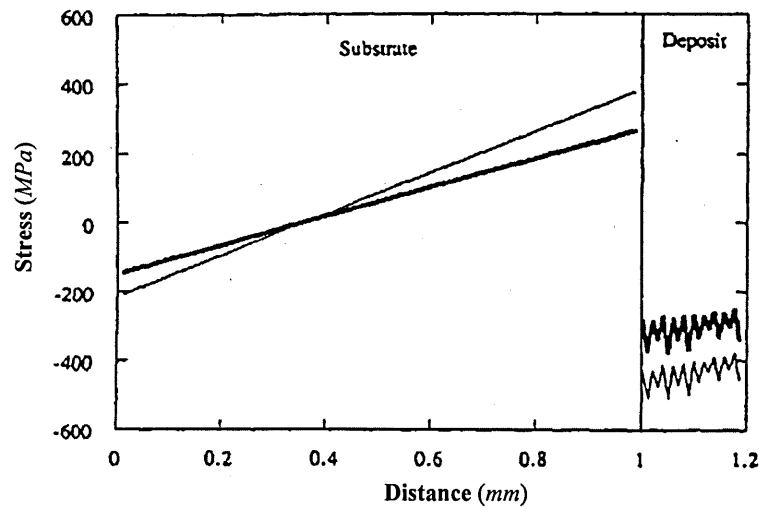


Fig.56: Predicted in-plane residual stress distributions, thick lines are for specimens sprayed at a minimum temperature of 400°C and the thin lines are for 600°C specimens [137].

2.13.3. Influence of Manufacturing Processes on Fatigue Performance

Manufacturing processes such as grinding, grit blasting, machining, polishing, VPS etc, create different surface topologies and surface residual stresses within the components and they are significantly influence the fatigue performance.

Plasma sprayed H-AC coatings are increasingly used to promote long term fixation of orthopaedic implants. Evans and Gregson [28] investigated the effects of such coatings

on the fatigue performance of Ti-6Al-4V using rotating bending fatigue experiments. The rotating bending fatigue experimental technique is explained in Chapter 5. The results are shown in Fig.57 [28], (a) and (b). The figures show the variation of fatigue limits due to different manufacturing processes. It can be seen that plasma sprayed samples have lower fatigue strength compared to samples prepared by other surface treatments.

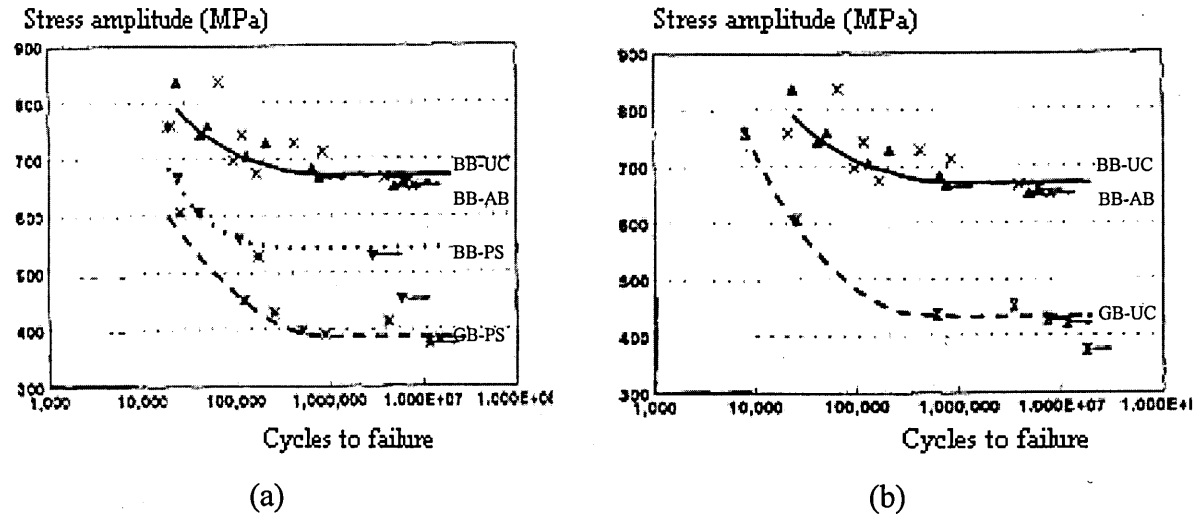


Fig.57: (a) The effects of plasma spraying, (b) the effect of grit blasting on Ti-6Al-4V: BB-UC; bead blasted, BB-AB; bead blasted-adhesive bonded H-AC, BB-PS; bead blasted-plasma sprayed H-AC, GB-UC grit blasted, GB-PS; grit blasted- plasma sprayed H-AC [28].

Wagner and Lutjering [83] investigated the influence of surface treatments; electro-polishing, shot peening, annealing and annealing followed by surface finishing, on fatigue behaviour of Ti-6Al-4V. The results are shown in Fig.58.

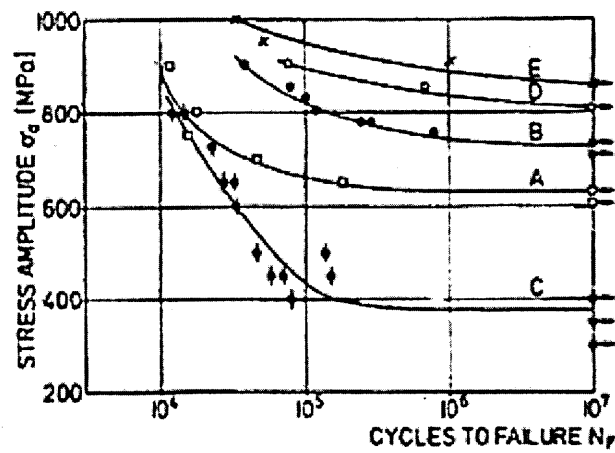


Fig.58: S-N curves from rotating bending experiments in air at $R = -1$ for fine equiaxed Ti-6Al-4V. A; electro-polished, B; shot peened, C; annealed for 500°C for 1hr. D,E: remove metal 20 μm by electropolishing from stage C [83].

Electropolishing is a process use to reduce surface roughness and it is understood that the electropolishing does not induce any residual stress on the component surface [129]. Therefore final electropolishing processes reduce surface roughness without changing the status of residual stresses, resulting an increment of the fatigue limit by about 485MPa (from about 390MPa at stage C to about 875MPa at stage E). This variation of fatigue limit is purely due to the change of surface finish. From stage B to C, annealing reduces the fatigue limit by about 310MPa. It is apparent that the annealing process has eliminated the compressive residual stress formed during shot peening and the reduction of fatigue limit is purely due to this. These results give a clear indication of the effects of surface roughness/defect size and the residual stresses on the fatigue limit.

3.1. Introduction

Since the introduction of hip implants in the 1960s, the total hip replacement has become the standard treatment for patients with osteoarthritis and other diseases which prevent normal functionality of hip joints [138]. The use of hip implants is growing all over the world and it is projected from 2005 to 2030 in United States, to increase by 174% to nearly 600 000 procedures annually [139].

Hip implants are designed and manufactured to be in service for at least 10 years. Delicate practices, special care and continuous quality checks are conducted in manufacturing hip implants using available modern technology [121]. But some implants fail in less than 10 years [151,163].

There are different types of failures which are related to different parts of the implant. Potential reasons for these failures can be categorized into three groups, namely; patient-related factors, implant-related factors and failures related to inadequate surgical practice [140, 141, 142]. Implant related problems such as, delamination of porous coating [142] and stem fracture [143, 144] can cause severe problems. Patient related factors like poor bone quality [145], infections [146] and various other factors [147] like smoking [148], body weight of the patient and activity level also will effect service duration. Surgical techniques also effect the implant lifetime such as wrong implant selection, malpositioning of the components or other technical problems [148, 149]. These will result in instability and may cause pain [150] to the patient.

Ulrich *et. al.* [151] conducted an investigation on failures of hip implants and they have classified the reasons for failures into six categories;

1. Aseptic loosening
2. Infection
3. Instability
4. Component failure
5. Peri-prosthetic fracture
6. Pain, due to medical reasons

Aseptic loosening is the most common reason for revision [152]. The risk of a component suffering a mechanical failure is not as great as aseptic loosening [153], but premature component failures like fatigue of the stem do occur [154, 155, 156, 157, 158, 159, 160, 161, 162]. The defective implant resulting from any kind of failure needs to be removed and a new revision implant must be inserted.

This research is focused on mechanical failures of the stem resulting from fatigue. Analysis is based on the JRI Ltd's quality complaint records [163]. Both primary and revision stem failures are taken into consideration.

3.2. Fatigue Failures of JRI Furlong® H-A.C. Supravit® Coated Hip Replacements Made Out of Ti-6Al-4V

3.2.1. Introduction

Hip implants are obviously subjected to cyclic loading under service conditions. In-vivo mechanical failures of hip implants mainly occur in the femoral stem section. Almost all stem failures were related to the mechanism of fatigue as shown in Fig.59. Stems of implants are manufactured by forging bar stock material and then undergoing various manufacturing processes which are explained in Chapter 4.

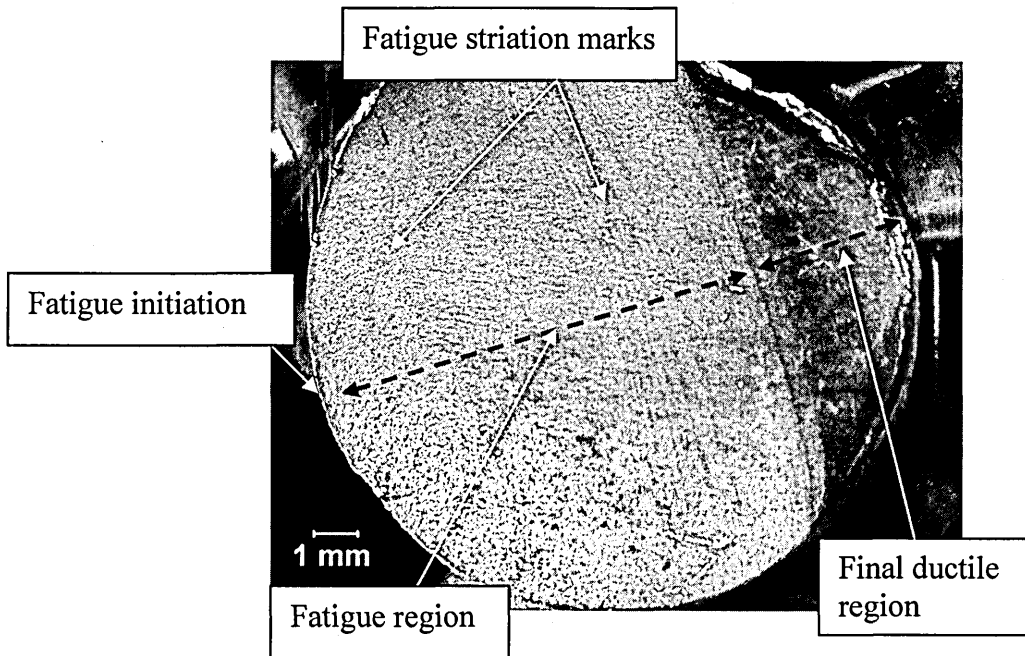


Fig.59: Typical fracture surface of a failed stem [163].

The stems of hip implants are made to different sizes to facilitate different patient conditions such as weight, medical aspects of femoral and pelvis bones, patient's activity level. There are mainly five different sizes of femoral stems namely, 9mm, 10mm, 11mm, 12mm and 14mm. These are the sizes of the diameter of cylindrical distal stem, *i.e.* if the femoral stem is 10mm; the diameter of the distal cylindrical area is 10mm. After investigating these factors the surgeon who conducts the operation decides which size of implant is most appropriate to the patient.

There are two locations where failures occur on a stem, namely the Cone area and Neck area. A comprehensive explanation regarding these failure locations and other related issues can be found in Chapter 2. This analysis considered three factors namely; (i). the

stem size, (ii). the time in service, (iii). any design modification incorporated and its effects on the failure distribution.

3.2.2. Failures at the Cone Region

According to the JRI quality complaints, the majority of stem failures occur in the cone region. An example of a stem failed at the cone region is shown in Fig.60. The figure shows no evidence of bone growth onto the implant. Likewise most of the cone failures show little or no fixation at the proximal area of the stem with the bone [163].

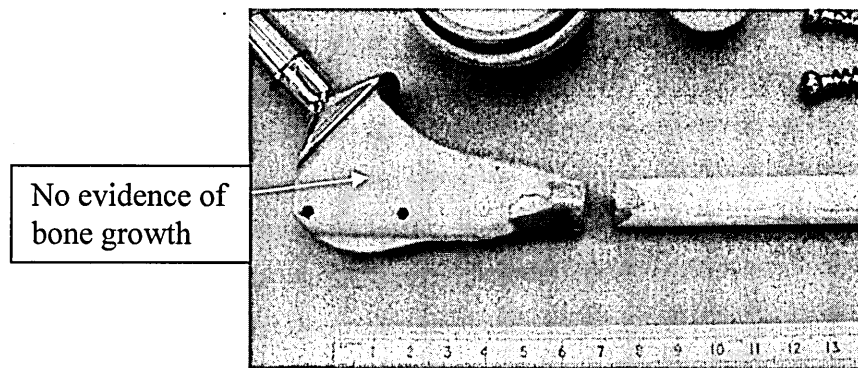


Fig.60: Failed stem at cone region [163].

3.2.2.1. Design Modification at Cone Region

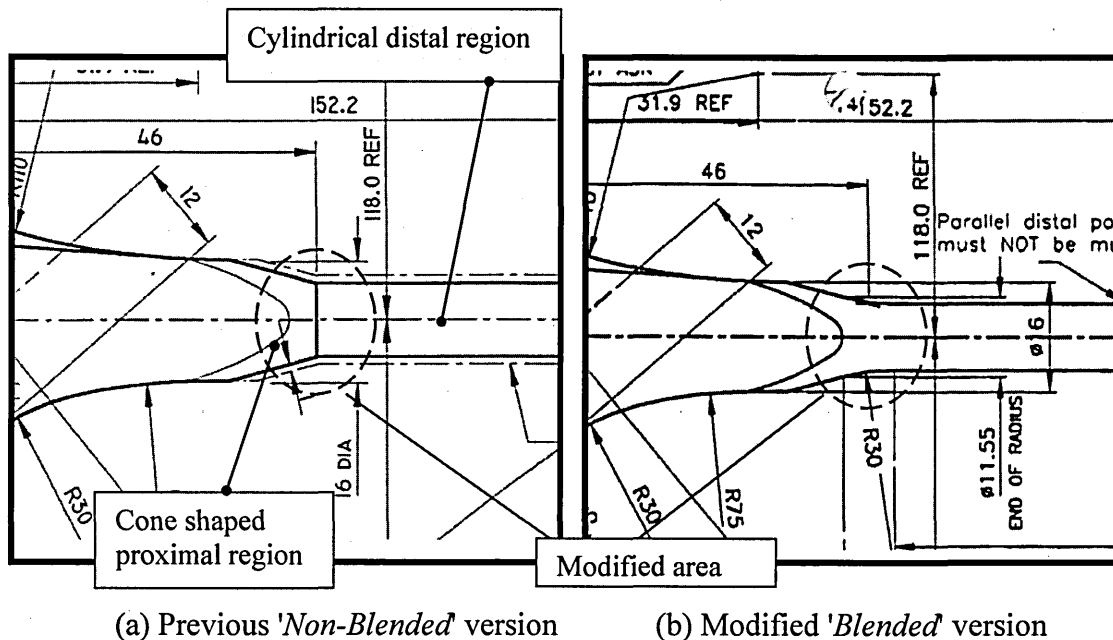


Fig.61: Design modification conducted at the cone region of the hip implants [164].

The previous and modified versions of the cone region of 10mm femoral stem are shown in Fig.61 (a) and (b) [164] respectively. This change was introduced to all types of JRI Furlong[®] H-AC coated stems in 1997.

As shown in Fig.61(a) the previous design has a demarcation feature at the cone area, where the distal region meets the proximal region of the stem. This is the feature which unions the cylindrical distal stem with the cone shape proximal stem. The new design has eliminated this feature by filleting the cone area, therefore redesigning of the cone region of the stem resulted in a relatively greater blending of this region. The transformation to cylindrical shape to cone shape occurs gradually and the feature which acts as a stress raiser has been eliminated. Both designs have similar dimensions except the blended feature. This blending of cone region is at the same location where in-vivo failures occurred.

3.2.2.2. Failure Distribution

Cone region failure records from 1996 to June 2008 were taken in to account and only the implants that failed in-situ within ten years were considered for this investigation. However these implants are intended to be in-service throughout the life time of the patient. During this period 26 cone failures were recorded. The JRI quality complaints records relating to these failures were investigated. Appendix.1 shows important information such as service time, defects at initiation, possible causes and related remarks, of several selected cone failures. The distribution of the service life of failed implants against the implanted year is shown in the Fig.62.

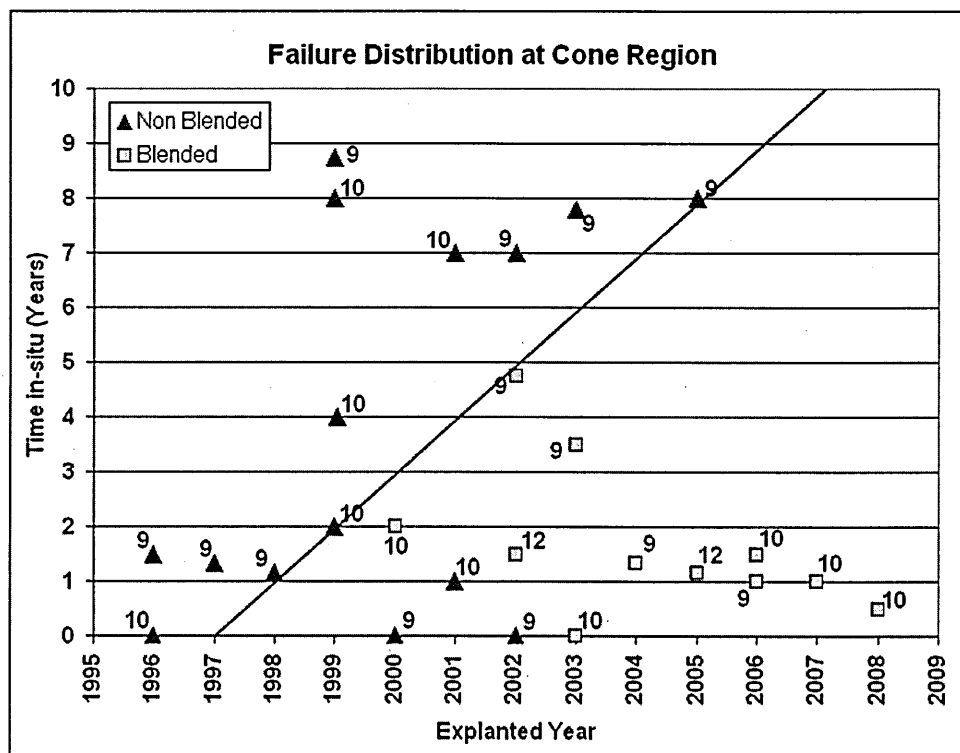


Fig.62: Distribution of failures at cone region

Triangular shaped points represent the failures of stems made to previous non-blended design and square shaped points represent the failures of blended design. Both type of points located along the zero time line represent the failures where the service lives are not available. The numbers noted along with each point represents the size of the failed stem. The line originated from 1997 demarcates the blended (below the line) and non-blended (above the line) stem failure regions. The sterility shelf life of implant products is 5 years. As a result one non blended failure can be found below the line.

3.2.3. Failures at the Neck Region

The neck region is well polished and exposed to body fluids. The processes involved in manufacturing the neck region are discussed in Chapter 4. As explained earlier there are different sizes of stems. But in all stem sizes the dimensions of the neck area remains unchanged. A picture of a failed stem at neck region is shown in Fig.63 [163]. Evidence of bone growth can be clearly seen which confirms a firm fixation between the stem and the bone. The majority of the implants that failed at the neck region show a firm fixation of the stem with the bone [163].

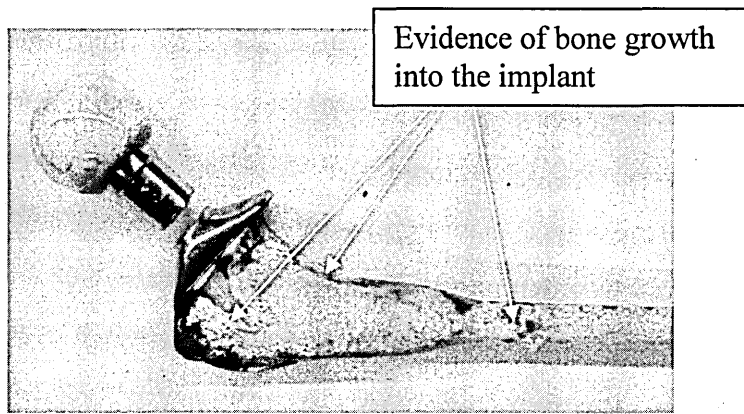
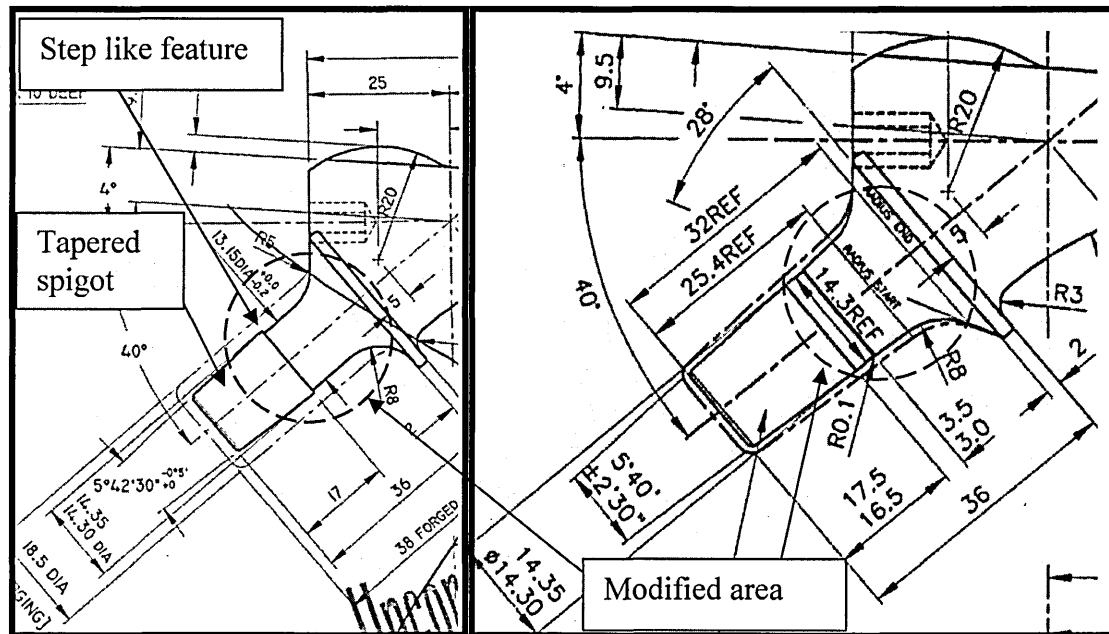


Fig.63: Failed stem at neck region [163].

3.2.3.1. Design Modification at Neck Region

The previous and modified versions of the neck region of a femoral stem are shown in Fig.64 (a) and (b) [164] respectively. This change was introduced to all types of JRI Furlong® H-AC coated stems in the year 2001.



(a) Previous 'Non-Blended' version

(b) Modified 'Blended' version

Fig.64: Drawings of the design modification conducted at the neck region of the hip implants [164].

As shown in Fig.64 (a), the tapered spigot is used for holding the femoral ball. A reduction of the diameter can be seen at the end of spigot and redesigning of the neck region of the stem resulted in a relatively greater blending of this region as shown in Fig.64 (b). The taper continues and is rounded off at the bottom. However the most critical area where failures occur is shown in Fig.65, which is just around the $R8$ radius start. This is also evident from Fig.63. It can be seen that the diameter of the critical area of the new design has increased from $13.15mm$ to just over $14.3mm$.

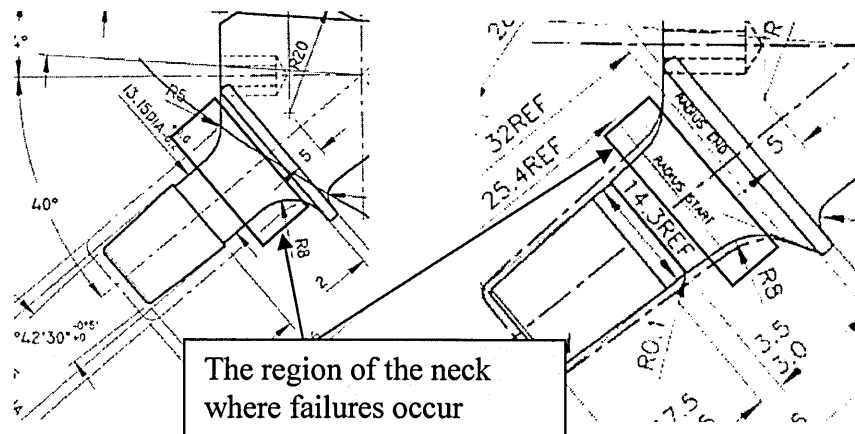


Fig.65: Critical area of the neck where failures occur.

3.2.3.2. Failure Distribution

Failure records from 1998 to June 2008 were taken in to account. As in the case of cone failures only the in-situ failed implants within ten years were considered for this investigation. During this period 15 neck failures were recorded. The JRI quality complaints reports under these failures were investigated. The Appendix.2 shows important information such as service time, defects at initiation, possible causes and related remarks, of several selected neck failures. The distribution of the service life of failed implants against the implanted year is shown in Fig.66.

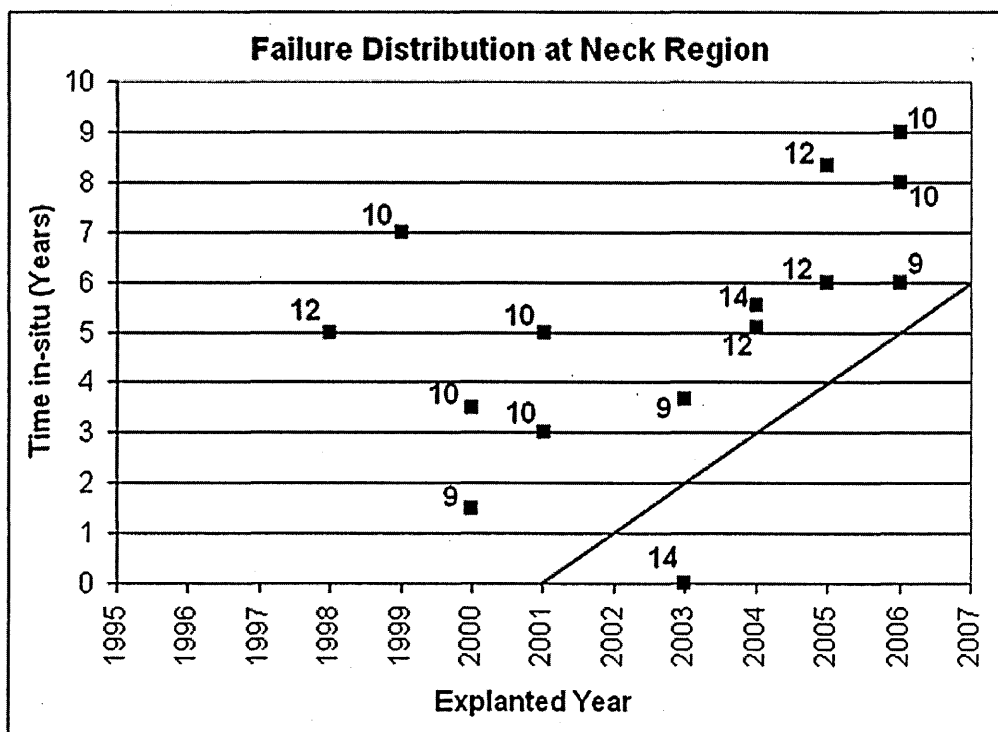


Fig.66: Distribution of failures at neck region.

Square shaped points represent the failures of stems made to the previous non-blended design. The points located along the zero time line represent a failure where the service life is not available. There were no failures in the neck area of the stems manufactured to the new design. The numbers along with each point represents the size of the stem, but the dimensions of the neck region are similar in all stems. The line originated from 2001 demarcates the blended (below the line) and non-blended (above the line) stem failure regions.

4.1. Introduction

Manufacturing implants at JRI involves different types of manufacturing operations. These operations can introduce residual stresses and surface microscopic defects which may remain through to the final product. Clearly the different residual stress states and surface defect/roughness would influence the fatigue limit. Experimental work under Phase.2 was targeted mainly to investigate this variation.

Three distinct process routes used to manufacture the cone and neck regions were identified. Under each route, the critical processes likely to induce surface anomalies and residual stress, which make an implant vulnerable to fatigue failure, were identified. Rotary bending test samples were prepared simulating similar manufacturing procedures and parameters as used in actual implant manufacture.

4.2. JRI Processes Involved in Manufacturing Hip Implants

The different components of an implant are manufactured by a combination of different manufacturing processes. Since the most susceptible locations of in-vivo fatigue failures are the cone and neck regions, the processes involved in manufacturing these regions were investigated. Fig.67 illustrates the main mechanical processes involved in manufacturing the cone and neck regions of a hip implant.

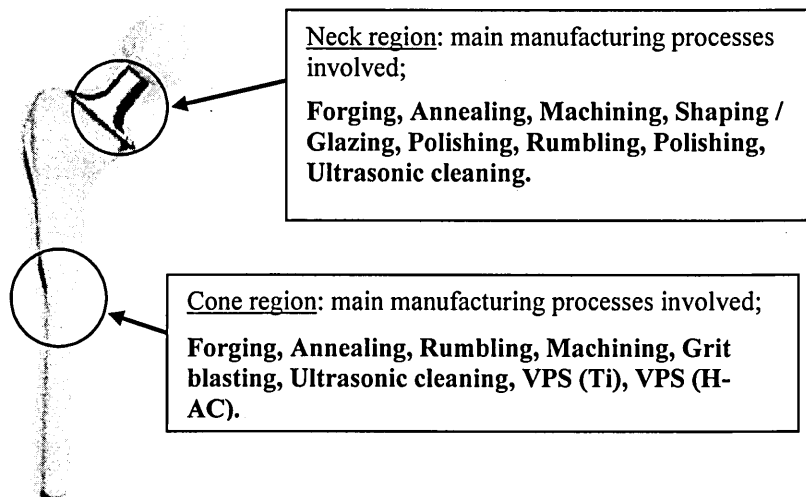


Fig.67: Processes involved in manufacturing cone and neck regions.

4.2.1. Manufacturing of Cone Region

The manufacturing of the cone area involves two slightly different manufacturing process sequences. Some of the implants, mainly primary implants, are made out of precision forged stems. Since they are forged to the final cone dimensions no additional machining needs to be done. This manufacturing process sequence involved in precision forged stems will be designated as Route.1. Another set of stems are forged oversize and need to be machined down to meet the required dimensions. Such stems are mostly used to produce revision implants. This manufacturing sequence of forged to oversize stems will be designated as Route.2.

4.2.1.1. Cone Region Manufacture (**Route.1**)

The flow chart in Fig.68 illustrates the manufacturing sequence of Route.1 and the number of samples tested under each stage. These samples were used to obtain the surface roughness/defect size, residual stress and fatigue performance data at each stage.

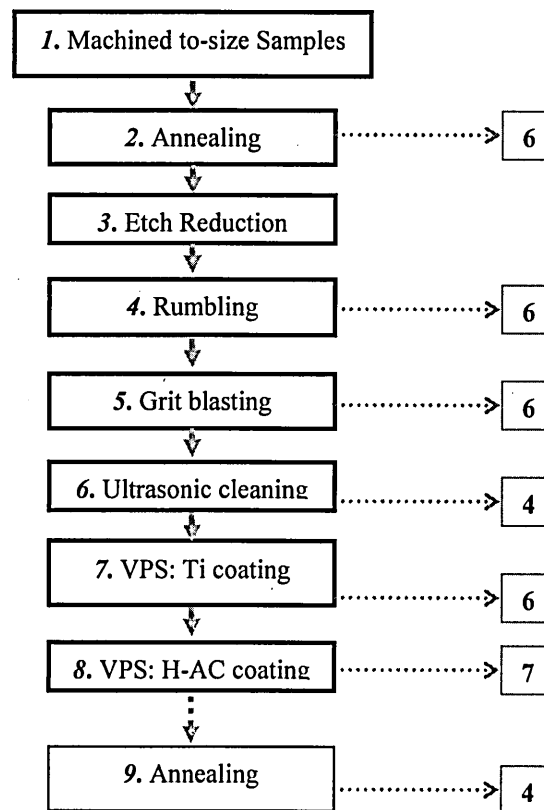


Fig.68: Manufacturing processes investigated under Route.1. Small boxes indicate the number of samples tested at each stage.

The annealing stage (stage 9) was incorporated to assess any changes in fatigue performance due to variation of residual stress status of coated samples. This step is not involved in actual implant manufacture.

The description of each of the processes under **Route 1**:

Machined Samples: Rotary bending samples (see Fig.71) were prepared by turning 12mm bar stock material to a nominal diameter of 8mm using CNC turning machines at JRI Ltd. The roundness of hour glass section of the samples was inspected against a shadowgraph. The machining was carried out using parameters similar to those used in turning the distal stem of actual hip implants. The JRI manual route card which explains operations, machining parameter and inspections is given in Appendix.4.

Annealing: This process is mainly conducted to relieve stresses in the component. Annealing was conducted at 700°C, which is the stress relieving temperature of Ti-6Al-4V alloy [109], for two hours and then air cooled.

Etch reduction: This process is conducted mainly to remove the surface anomalies introduced to the surface by previous operations and also to remove any oxide layers resulting from annealing. A thin layer of material thickness was removed by etching the sample.

Rumbling: Rumbling is a finishing operation conducted before grit blasting wherein the samples were loaded into a vibratory barrel filled with ceramic chips. When the barrel starts vibrating the surface of the samples and chips come into contact and the relative movement between chips and samples leads to scale removal.

All the manufacturing processes, parameters and inspection details were carried out as per actual stem production and any rectifications and rechecks were conducted accordingly as in the actual implant manufacturing process.

Grit Blasting: The necessity of conducting the grit blasting process prior to H-AC coating has been explained in Chapter 2.13. The blasting media, chemical composition and particle size distribution and the process settings, for example, jet -pressure, jet-angle and jet-to-work distance are listed in JRI work instruction [165].

Ultrasonic Cleaning: Ultrasonic cleaning is used to clean the surface of the sample, mainly to remove any embedded particular matter resulting from grit blasting and dust particles. Details of the necessity for ultrasonic cleaning are explained in Chapter 2.13. The samples were immersed in baths of de-ionized water in two stages where the samples were cleaned ultrasonically and then the samples were dried. The process details such as bath temperatures etc are given in JRI Work Instructions [166].

Titanium and H-AC coating by Vacuum Plasma Spraying (VPS): The VPS is used to coat the titanium bond coat and the H-AC upper coat to the Ti-6Al-4V parent metal. In VPS titanium or H-AC powder is injected into hot gas plasma that melts and projects the molten droplets at high velocity onto Ti-6Al-4V substrate to form a coating. To produce the coatings without oxidation after evacuation the VPS spray chamber is filled with inert gas and maintained at low pressure. The chamber consists of 5-axis robot to manipulate the plasma spraying gun. The specimens were mounted on two rotary turntables located inside the chamber. During VPS the temperature of the surface is maintained and monitored accordingly to obtain uniform coating and required material properties of coatings. More about the process and the necessity of VPS are explained in Chapter 2.13. Manufacturing settings and parameters were detailed in JRI Work Instructions [167,168].

Annealing: Annealing was conducted at 700°C for two hours and then cooled in the chamber under vacuum conditions. The annealing specifications are given in Appendix.5.

All related manufacturing settings and inspections were carried out as per producing actual implant production and the manual route card which identifies stage by stage description of the manufacturing of samples under Route.1 is given in Appendix.6.

4.2.1.2. Cone Region Manufacture (Route.2)

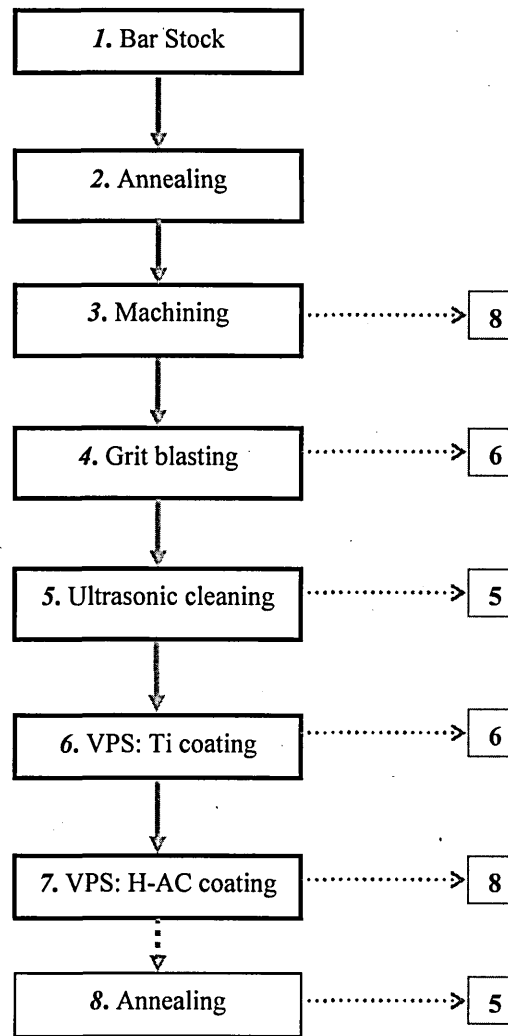


Fig.69: Manufacturing processes investigated under Route.2. Small boxes indicate the number of samples tested at each stage.

The process sequence conducted under Route.2 is shown in Fig.69.

Machining: Machining at stage 3 was conducted using similar specifications used in turning the distal stem of actual hip implant. In oversized stems the diameter of the cone area is reduced from $\approx 16.32\text{mm}$ to 9.6mm (in 10mm stems), using 0.5mm cuts and a 0.2mm final cut. Machining of fatigue samples also adhered to the similar order, *i.e.* the reduction of 12mm to 8mm was conducted using 0.5mm cuts with a final cut of 0.2mm .

Apart from machining, all the other processes were conducted as explained in Route.1. The manual route card which states complete stage by stage description of the manufacturing of samples under Route.2 is given in Appendix.7.

4.2.2. Neck Region Manufacture (**Route.3**)

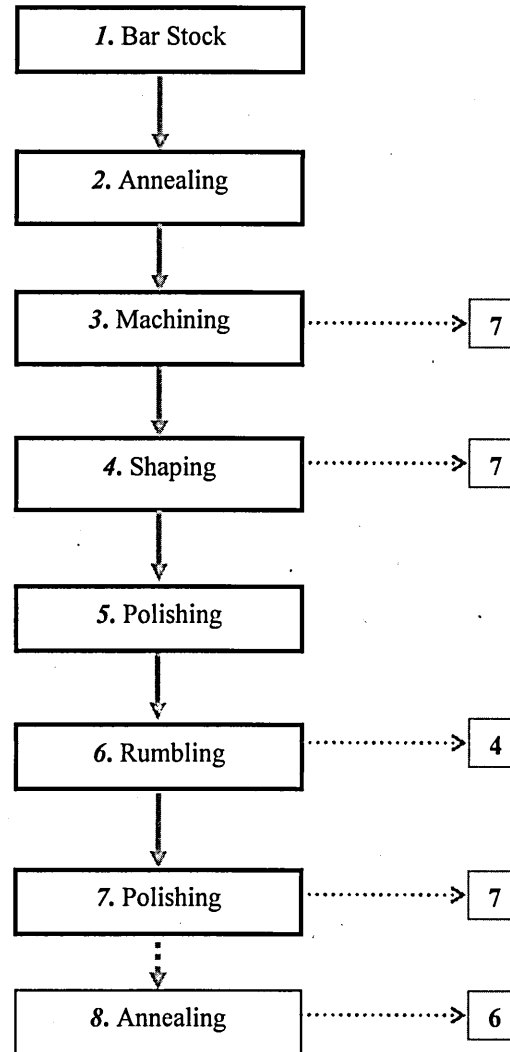


Fig.70: Manufacturing processes investigated under Route.3. Small boxes indicate the number of samples tested at each stage.

The neck area is not coated with Ti and H-AC and the alloy surface is subjected to a polished finish. The process sequence conducted under Route.3 is shown in Fig.70.

The description of each of the processes under **Route 03**:

Annealing: Annealing is done at 700°C for two hours and then air cooled.

Machining: In actual implant manufacturing the neck region is machined from oversized neck size to the actual dimension using 0.5mm depth of cuts and a final cut of 0.1mm . Machining of fatigue samples also adhered to the similar order, i.e. the reduction of 12mm to 8mm was conducted using 0.5mm cuts with a final cut of 0.1mm . After machining the samples were shaped, tumbled and polished.

Shaping: After machining the cone area needed to be shaped to the required dimensions. The shaping of the neck area was carried out by glazing using rotating belts.

Rumbling: Ceramic chips were used as the main rumbling media and the specimens were tumbled in the vibratory barrel.

Polishing: Final polishing operation is conducted manually by highly skilled operators.

The technical details and manufacturing parameters of shaping, rumbling and polishing and other operations conducted in JRI machining shop are given in JRI Work Instructions [169,170]. The manual route card which defines stage by stage process description of the manufacturing of samples under Route.3 is given in Appendix.8.

The main processes involved in manufacturing the cone and neck regions and the sequence of operations for the three routes are also given in Appendix.3 and the complete sequence of manufacturing operations and specifications are given elsewhere [121, 122].

5.1. Introduction

A variety of testing methods were used and this chapter provides a detailed account of the equipment and experimental techniques employed during this research programme. The test results are presented in Chapter 6.

5.2. Fatigue Tests

Bending fatigue tests were performed using a rotary bending fatigue testing machine. Tests were conducted in accordance with ASTM- F 1160-91 [171] and ASTM-F 1659-95 [172] standards.

The rotating bending fatigue tests were mainly conducted in two phases. Phase.1 tests were to understand the general fatigue behaviour of Ti-6Al-4V implant grade material. Samples prepared to specific values of surface roughness and residual stress were used to assess the fatigue performance. Phase.2 fatigue testing was carried out to assess the influence of JRI manufacturing practices on fatigue performance.

5.2.1. Rotating Bending Fatigue Test Specimen

The test specimen used was an hour glass shape design, with a minimum diameter (d) of $8mm$ and a continuous fillet radius of $110mm$ as shown in Fig.71. The specimens were machined from $12mm$ Ti-6Al-4V alloy bar stock to tight tolerance using CNC turning machines at JRI Ltd. The samples were designed and manufactured to initiate failure at the test region whilst avoiding excessive stress concentrations. The elastic stress concentration factor for the critical region of the specimen was estimated to be 1.02 [192].

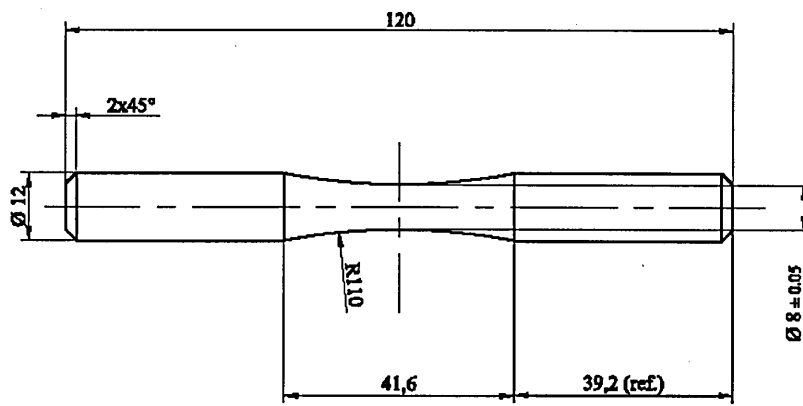


Fig.71: Hour glass shape fatigue specimen (Note: all dimensions are in *mm*).

5.2.2. Rotary Bending Fatigue Testing Apparatus and Test Procedure

Rotating bending fatigue test apparatus is one of the most commonly used fatigue testing machines [38, 173]. The sample is clamped between two coaxial shafts and subjected to a dead weight while bearings permit rotation. The assembly rotates while the specimen is subjected to bending. A given point on the circular cross section surface of the sample is subjected to sinusoidal stress amplitude cycling from compression to tension during each rotation. Thus rotary bending fatigue testing results pertain to fully reversed loading ($R = -1$), where the mean stress (σ_m) is zero. A four point bending arrangement was used with bending stress adjusted by addition of static weights to the hanger.

The rotating bending tests were conducted using two in-house developed rotary bending fatigue machines run at 22Hz which can accommodate a maximum static load of 1200N. A general view of the rotary bending fatigue testing machine and a close up view of the loading arrangement are shown in Fig.72 and Fig.73 respectively. The two machines were pre-calibrated to ensure accuracy of the stress amplitude during a high cycle fatigue test.

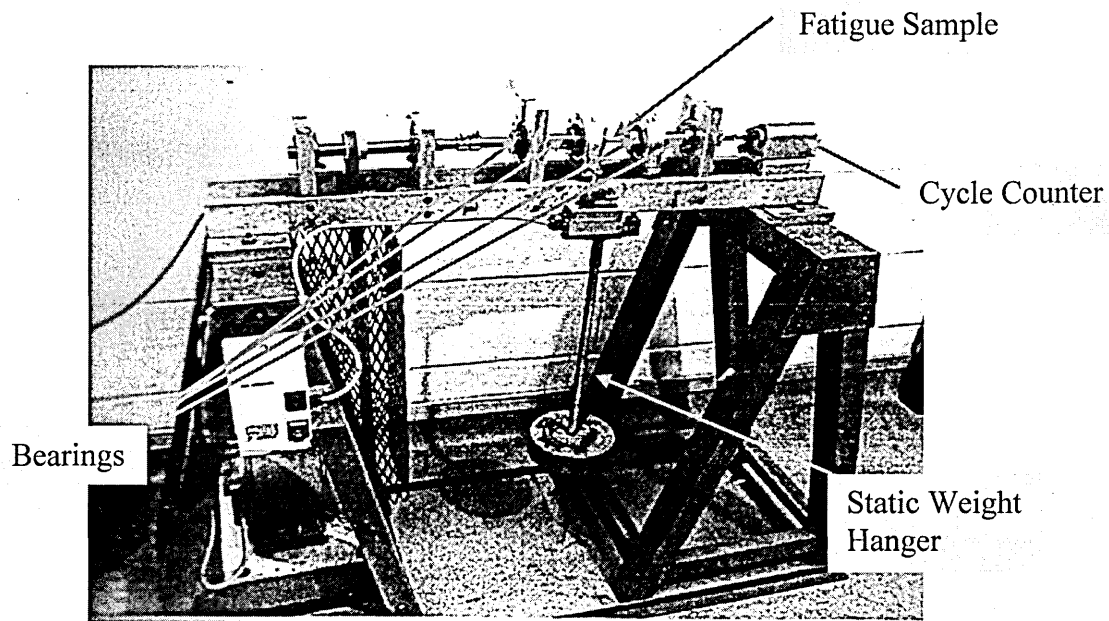


Fig.72: Rotating bending fatigue test apparatus.

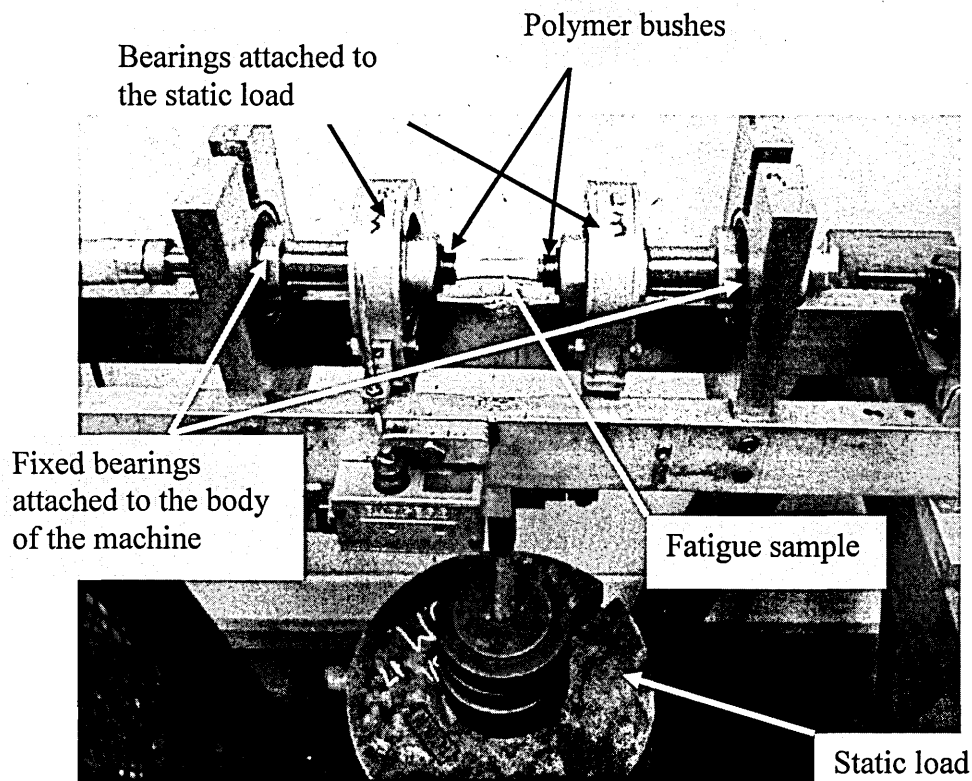


Fig.73: Rotating bending fatigue test configuration.

The schematic loading configuration is shown in Fig.74. The four point bending arrangement ensures a uniformly distributed bending moment over the entire test area of the specimen.

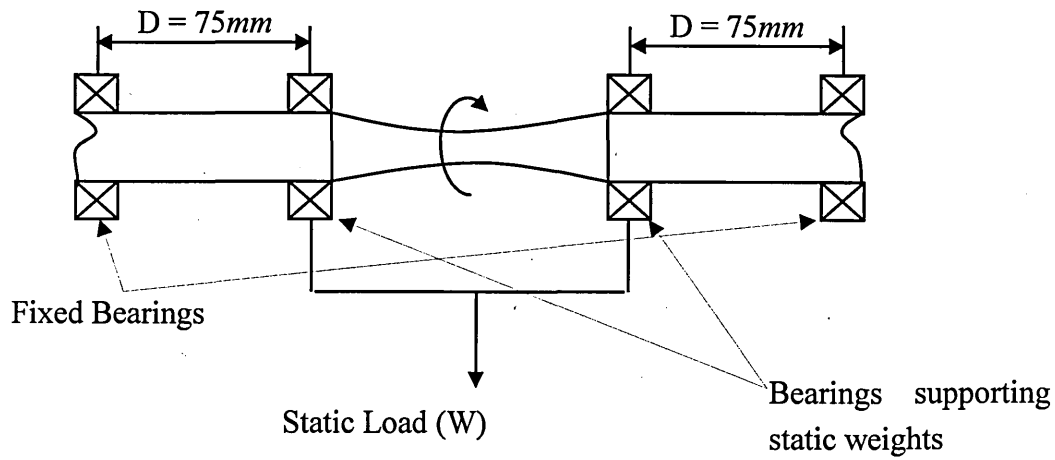


Fig.74: Schematic diagram of four point bending arrangement.

The distance between the bearings is 75mm (Fig.74). The relevant stress amplitude at the minimum diameter of the specimen for a given static load can be calculated using simple bending theory, *i.e.* $M/I = \sigma/y$, where σ – stress, M – bending moment $\left(= D(\text{mm}) \times \frac{W(\text{N})}{2}\right)$, I – moment of inertia $\left(= \frac{\pi d^4(\text{mm}^4)}{64}\right)$ and y – distance to the outer most layer of the component from the neutral axis $\left(= \frac{d(\text{mm})}{2}\right)$, in this case the minimum radius of the specimen. Thus bending stress amplitude can be defined as a function of static load (W) and the minimum diameter (d) of the sample;

$$\sigma (\text{MPa}) = \frac{M}{I} \times y$$

$$\text{Stress Amplitude (MPa)} = \frac{381.9}{d^3 (\text{mm})} \times W (\text{N}) \quad (18)$$

5.2.3. Stress Calibration of the Rotary Bending Machine in High Cycle Fatigue

5.2.3.1. Need for Calibration

To ensure accurate fatigue data, the imposed stress amplitude on the critical test region (*i.e.* the minimum cross section) of the fatigue sample due to static load should be a

constant value throughout the test duration. However, the polymer bushes used to grip the sample to the holder (see Fig.73) may loosen over a period of time and this may have an influence on the stress amplitude. Calibration of stress over a high cycle fatigue test was performed to check the stability of the stress amplitude over an extended number of loading cycles. A strain gauged fatigue sample was used and the strain values were recorded initially and after operating the machine for a specific number of cycles. The stress amplitude calculated from the strain values obtained from a strain indicator and that calculated theoretically from static load using simple bending theory, were compared.

5.2.3.2. Calibration Procedure

The specimen was assembled on the machine with a strain gauge attached to the test area. The strain gauge was connected to the strain indicator unit which directly displays the relevant strain readings. The sample was loaded with a static load of 450N and the strain readings recorded in three instances as given in Table.5. In each instance 36 strain readings were noted for ever 10° intervals from 0° to 360°. The strain readings were taken at 0, ≈ 2000000 and ≈ 7100000 cyclic intervals. The tabulation and the variation of strain values are presented in Appendix.9 and Appendix.10 for Machine *A* and *B* respectively.

Number of cycles	Stress Amplitude-MPa (Experimental)	Stress Amplitude-MPa (Theoretical)
Machine A		
0	347	336
2006745	345	336
7095687	349	336
Machine B		
0	357	345
2102046	349	345
7128139	349	345

Table.5: Comparison of experimentally calculated and theoretically calculated stress amplitudes.

A new strain gauge was used in every instant of strain measurements because they tend to loosen from the sample surface when running over a large number of cycles. The new strain gauge was placed at the same location as the previous one to ensure the accuracy

of calibration results. The FLA-5-11 type strain gauges were used with a gauge factor of 2.14.

Based on strain measurements recorded, respective stress values were calculated using Hooke's law, *i.e.* $\sigma = E\varepsilon$. By considering the static load, relevant maximum bending stress value was calculated using simple bending formulae, *i.e.* $M/I = \sigma/y$. According to the results Machine *A* has a maximum deviation of 3.7% and Machine *B* has a maximum deviation of 3.3%.

5.2.4. Fatigue Tests - Phase.1

Phase.1 fatigue tests were to investigate the general fatigue behaviour of Ti-6Al-4V implant grade alloy. Primary consideration was to study of fatigue limit as a function of manufacturing processes and hence surface characteristics.

5.2.4.1. Test Program – Phase.1

52 rotary bending fatigue test samples were used. Samples of four different surface roughnesses were prepared and in each roughness category two sub sets, one annealed (A) and another without annealing (WA) were prepared. Fig.75 illustrates the test schedule.

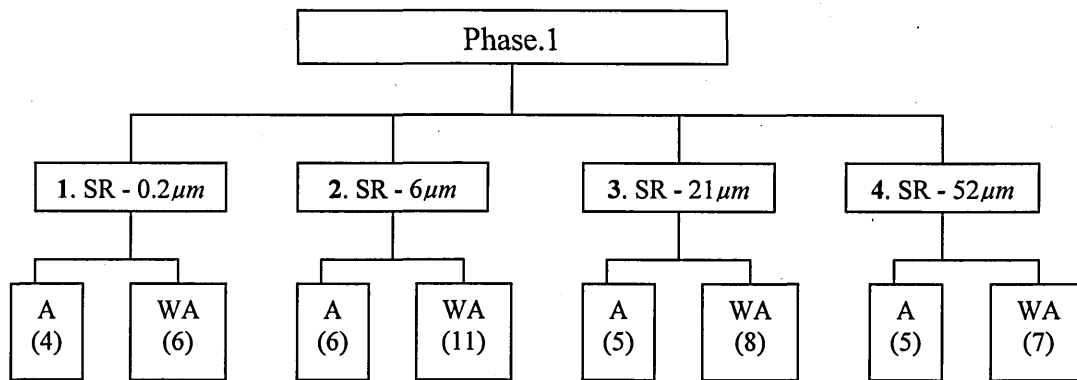


Fig.75: Phase.1 test program and number of samples tested under each batch; **SR**- surface roughness, **A**- annealed, **WA**- without annealed. Number of samples tested under each set is given within brackets.

5.2.4.2. Sample Preparation

All samples were initially machined and randomly separated to four batches. These four batches were prepared to $0.2\mu m$, $6\mu m$, $21\mu m$ and $52\mu m$ surface roughness as explained below. These roughness values represent $R_z (max)$, i.e. maximum peak to valley height. Each batch was then randomly separated to two sub batches, one annealed to relieve stresses and the other without annealing.

The surface roughness of as machined samples is $6\mu m$, which were directly used as Batch.2 samples. Batch.1 samples were prepared to $0.2\mu m$ surface finish, through polishing. Starting with grade $25\mu m$ diamond compound and then $14\mu m$, $6\mu m$, $1\mu m$ and finally $1/4\mu m$ diamond compound were used to obtain the required surface roughness, which is more like a mirror finish. The polishing was performed in longitudinal direction. Surface preparation for $21\mu m$ (Batch.3) and $52\mu m$ (Batch.4) were obtained by roughening the surfaces using No. P60 and P80 silicon carbide grinding papers respectively. All samples were cleaned thoroughly using industrial methylated spirit (IMS).

Annealing of sub-batches was carried out under vacuum conditions with a maximum temperature of $700^{\circ}C$ for 2hrs followed by furnace cooling. The annealing specifications are given in Appendix.5. Surface roughness and residual stress measurements were made prior to fatigue tests.

5.2.5. Fatigue Tests - Phase.2

Phase.2 fatigue testing was conducting to assess the influence of JRI manufacturing practices on fatigue performance.

5.2.5.1. Test Program – Phase.2

The test programme scheduled for Phase.2 is given in Fig.76. Under this phase 108 samples were tested. Samples were prepared according to identified three routes of manufacturing. Route.1 and 2 cover the main processes used to manufacturing the cone

region and Route.3 covers the neck region. The selected processes and the number of samples tested under each process are as shown in Fig.76. Additional information on manufacturing processes is given in Chapter 4.

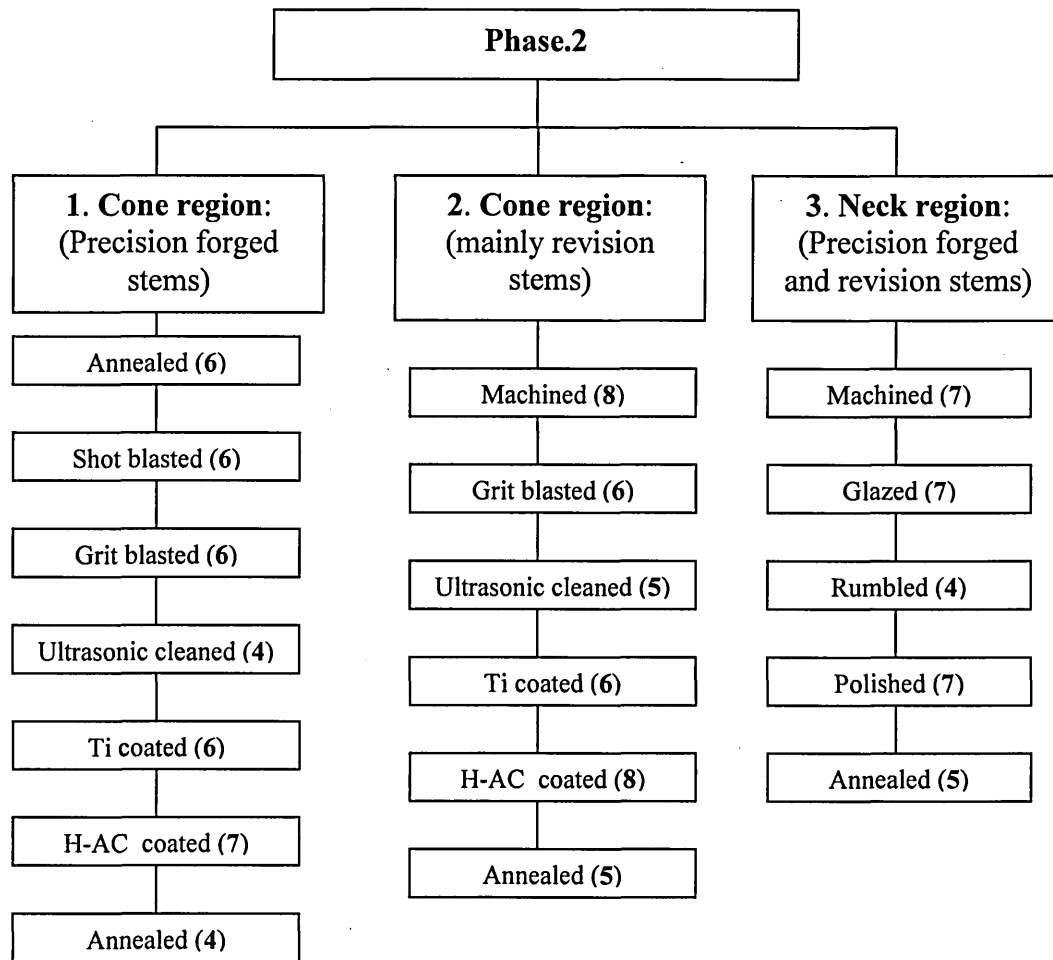


Fig.76: Phase.2 test program and number of samples tested at each stage under each process.

5.2.5.2. Sample Preparation

For Phase 2 the samples were prepared adhering exactly to the manufacturing parameters assessed in JRI practices involved in manufacturing the Furlong® H-AC stem. These samples were prepared by JRI Ltd. The manufacturing processes and parameters used are explained in Chapter 4.

5.3. Determination of Surface Roughness

The surface roughness was measured using a Taylor-Hobson Talysurf-120L, Stylus type apparatus with a $2\mu\text{m}$ stylus tip radius. Measurements were taken over a nominal 5mm length using 0.8mm cut off filter. Four readings were taken along the longitudinal direction around the sample at 90° angular intervals as shown in Fig.77(a) and these positions are numbered as 1, 2, 3 and 4. Ten readings were taken in transverse direction, five at each of the diametrically opposite positions 1 and 3, which are numbered as positions I, II, III, IV and V in Fig.77(b).

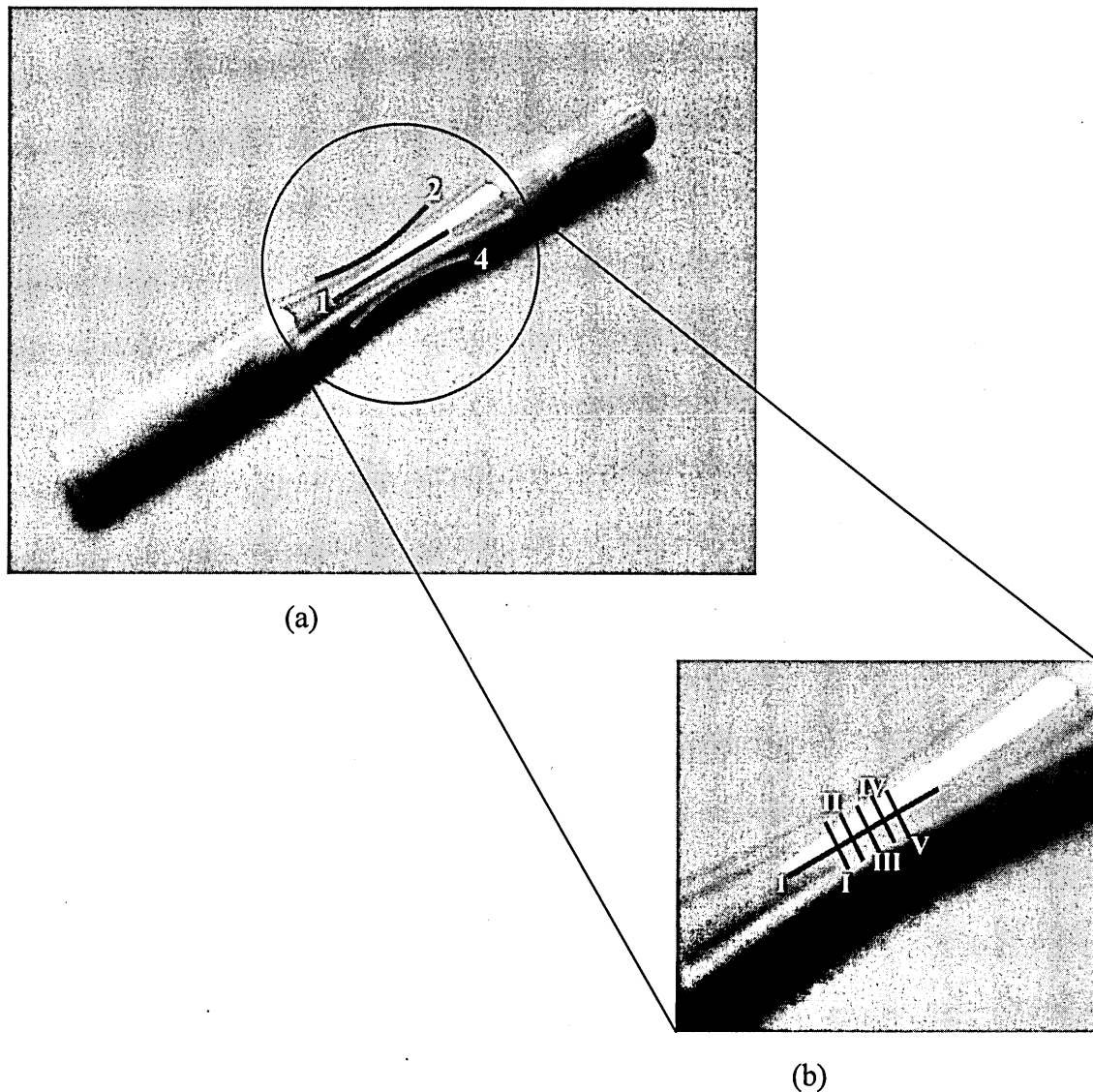


Fig.77: Locations at which surface roughness measurements were taken from fatigue samples.

A typical surface profile of a machined sample obtained from the Talysurf is shown in Fig.78.

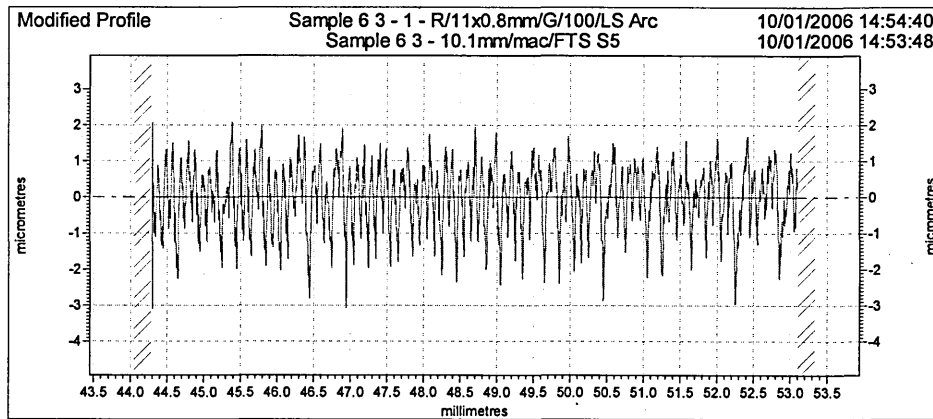


Fig.78: Typical surface profile of a machined sample obtained from *Talysurf*.

Only readings taken along longitudinal directions were considered because of fatigue crack initiation and propagation occur in transverse direction. The surface roughness was noted as three measuring parameters, namely R_a - average roughness, $R_{p(max)}$ - maximum peak height and $R_{v(max)}$ - maximum valley depth. The tabulation of longitudinal surface roughness measurements (R_a , R_v , R_p and $R_{z(max)}$) for both Phase 1 and 2 are given in Appendix.12.

5.4. Residual Stress Measurements using X-ray Diffraction Technique

5.4.1. Introduction

The XRD technique is used prior to testing to measure the residual stress status on the surface of rotary bending fatigue test samples. The critical area where the failure is expected to initiate is shown in Fig.79. Samples were used as manufactured without any sectioning or mechanical preparation. Before every scan samples were cleaned thoroughly with *IMS* or acetone.

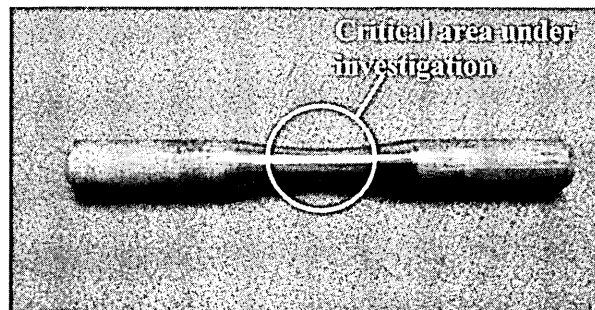


Fig.79: Critical area of the specimen where stress measurements were conducted.

5.4.2. X-ray Diffraction Apparatus

The Philips *PW3040 X'Pert Pro* XRD apparatus shown in Fig.80 with *X'Pert Stress* software housed at Materials Engineering Research Institute, Sheffield Hallam University, was used for stress measurement. The apparatus is subjected to periodic calibration to test the movement of the goniometer, measuring position with rotation, coincidence of the beam at the centre of rotation, and other important hardware settings. Copper X-ray tube was used, since copper tube gives more depth of penetration for titanium compared to *Cr*, *Fe* and *Co* tubes, which is about $6\mu\text{m}$ (refer Fig.53). Philips *X-Celerator* type detector was used, which is most suitable for shorter wave lengths, texture measurements and rapid data collection.

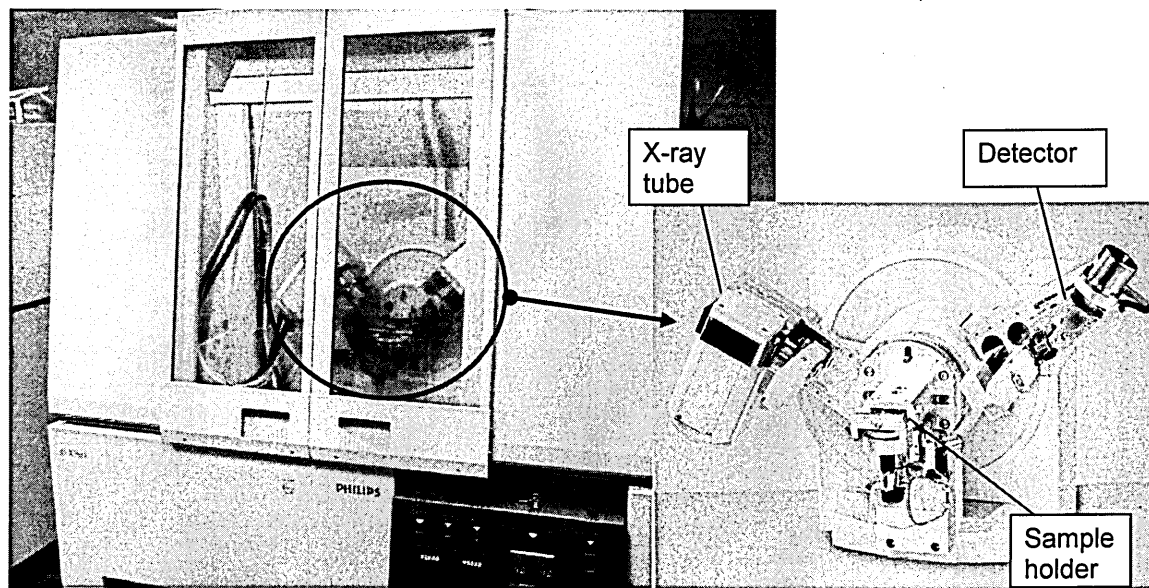


Fig.80: Philips PW3040 X'Pert Pro XRD apparatus.

The XRD apparatus with a fatigue sample is shown in Fig.81.

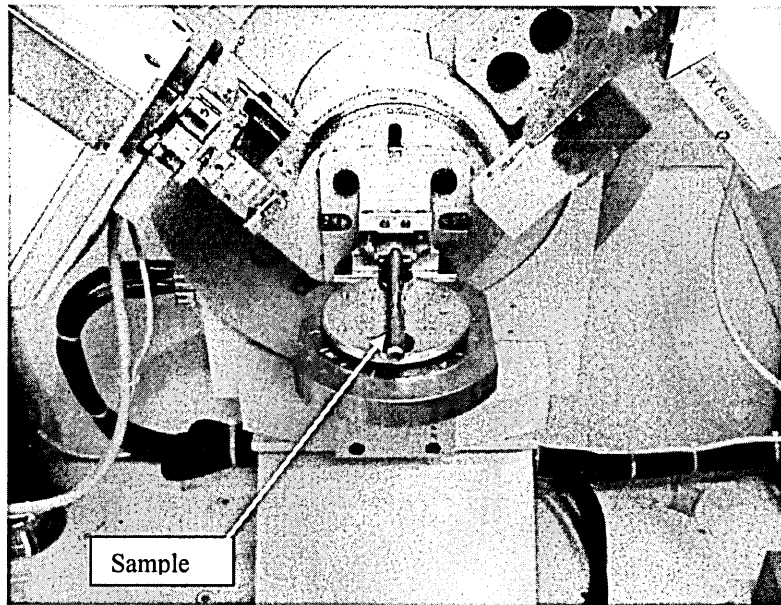


Fig.81: X-ray diffraction apparatus with hourglass sample fixed to sample stage.

5.4.3. Hardware Parameters Used for Stress Analysis

Uniaxial $\sin^2\psi$ method was used for stress analysis. To find the most appropriate 2θ , a full scan was conducted over 180° . As explained in Chapter 2, the recommended 2θ

angle for *Ti* alloys is around 139.4° and the lattice plane is {213}. For pure titanium the recommended peak is at 138.46°. But after the complete scan it was identified that for Ti-6Al-4V implant grade alloy, the corresponding peak is slightly shifted to around 142°. Therefore the 2 θ scan was adjusted to start from 138° to 146° to cover the peak at 142°.

To reduce the uncertainty within residual stress measurements and to improve the accuracy of the fit, 9 ψ measurements were utilized for measurements where the ψ tilts were chosen to give equal $\sin^2\psi$ steps. A $\sin^2\psi$ range of 0.5 was used; the recommended range is 0 – 0.6. The main hardware parameters used for XRD measurements can be listed as in Table.6.

Parameter	Setting
Diffractometer type	X'PERT PRO
Detector type	X'Celerator
Anode material	Copper K-alpha
Scan axis	2 theta-Omega
Tilt axis	Omega
Tilt range	Positive and negative
Divergence slit	5
Masks	1/2
Monochromator usage	yes
Generator voltage	40kV
Tube current	40mA
Pre set counts	10000
Scan axis	gonio
Data angle range (2 θ)	138° to 146°
Maximum ψ	45°
Maximum $\sin^2\psi$	0.5
No. of ψ steps	9
No. of scans	9
Step size	0.040
No. of points	200
Scan type/mode	continuous
Time per step	28sec
Scan speed	0.02°/sec.
Total time	≈ 15hrs

Table.6: Hardware settings used with *X'pert* XRD apparatus for stress measurements.

The main operating window of the *X'pert stress* software is shown in Fig.82. Selecting and defining the parameters and appropriate corrections are important to obtain a stress reading with minimum error. The data obtained from measurements were treated accordingly to obtain accurate stress measurement. As shown in the Fig.82 the data was corrected for absorption/transparency, background, Lorentz polarization, peak positioning and K-alpha2 stripping. The Young's modulus (E) and Poisson's ratio (ν) were defined to calculate the stress free lattice parameter (d). The stress measurement is calculated based on d .

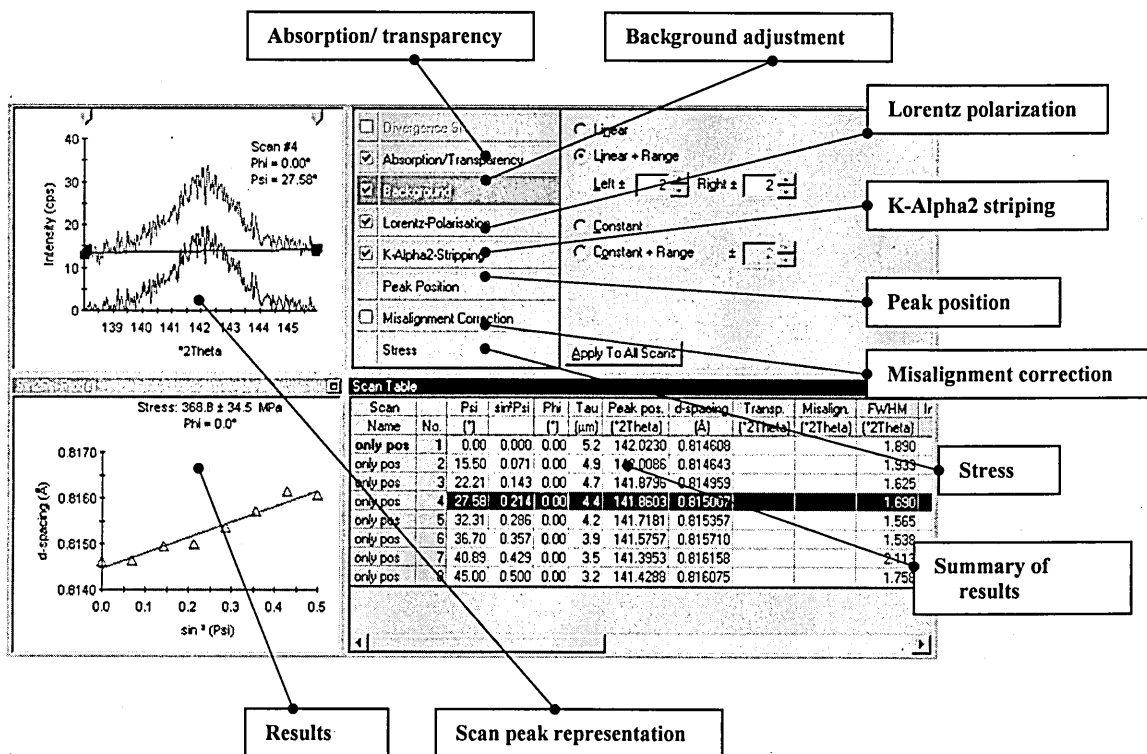


Fig.82: The operating window of *X'pert stress* analysis software with parameters.

Brief descriptions of the settings involved under each software parameter are given below.

Absorption/ Transparency

Diffracted intensities are influenced by absorption, which is directly related to path length of the incident and diffracted beams traverse in the specimen for a given

geometry [106]. The results were corrected according to the information depth and position correction. Linear absorption coefficient for Ti-6Al-4V was calculated as 913 cm^{-1} [113].

Background adjustment

This function is used to subtract unnecessary background intensity from a measurement. The background was adjusted by default, but fine adjustments needed to be carried out in order to get more accurate stress values. The graphical representation of peaks is shown in scan peak representation area shown in Fig.82 and the scan peak is displayed by the top graph and corrected peak by bottom graph. The background was adjusted accordingly to optimise the results.

Lorentz polarization (L-P) factor

There are three features, (i). number of grains which are oriented in order to give 2θ diffraction, (ii). diffraction intensity per unit length, (iii). relationship of diffraction intensity to one crystallite on 2θ , which define the L-P factor. For the adjustment of L-P factor a weak texture and large structural broadening were selected and the default value of monochromator factor was used.

K-Alpha2 stripping

This parameter eliminates that part of the data originating from the K-Alpha2 wavelength induced from the X-ray tube. As a result the overlap problems are eliminated before calculating the peak position and this simplify the stress analysis. This filter is specific to the tube anode. When selected, the K-alpha 2 stripping parameter the software consists of default setting to perform the filterisation related to radiation from copper tube.

Peak position correction

This function allows selecting the most appropriate fitting method to determine the position of the peak. Correct identification of the peak position from the curve is

important. The software offers the option of selecting the most suitable method out of nine methods. Considering the accuracy and consistency, the most appropriate method for stress analysis is *Pearson VII* and it was selected for stress measurements.

5.4.5. Optimising Scan Duration

To reduce the uncertainty within residual stress measurements and to improve the goodness of fit rather than the statistical quality of the diffraction peaks, the most suitable method is to increase the number of ψ measurement tilts (refer section 2.12.4) rather than the scan time within each peak. But scan time of the peak also need to be optimized to obtain an accurate stress measurement. A total number of nine ψ angles were used. These angles were selected to cover both positive and negative quadrants. Tests were carried out to investigate the optimum time duration in order to obtain a more stable and accurate stress reading. The results obtained from scans conducted for 5hrs, 10hrs, 15hrs and 20 hrs are given in Table.7 and Fig.83.

Scan duration (hrs)	Stress measurement (MPa)
5	- 442.3 \pm 211
10	- 345.6 \pm 79
15	- 301.8 \pm 45
20	- 301.3 \pm 23

Table.7: Stress results of the investigation of scan duration.

Considering the Fig.83 it can be seen that after 15hrs and 20hrs scans give almost similar value, where the graph flatted out after 15hrs. It has finalized that the most appropriate duration for stress measurement as 15hrs.

5.4.6. Repeatability Tests

After optimising the scan duration for 15hrs, repeatability of XRD measurements was investigated. The measurements were taken at the same location of the sample using identical software and hardware settings as used in all other stress measurements. The results are given in Table.8 and Fig.83.

Scan duration (<i>hrs</i>)	Stress measurement (<i>MPa</i>)
15	- 301.8 ± 45
15	- 302.1 ± 50

Table.8: Results of repeatability scans conducted for 15hrs.

The error of repeatability of residual stress measurements is very good since it is less than 1%.

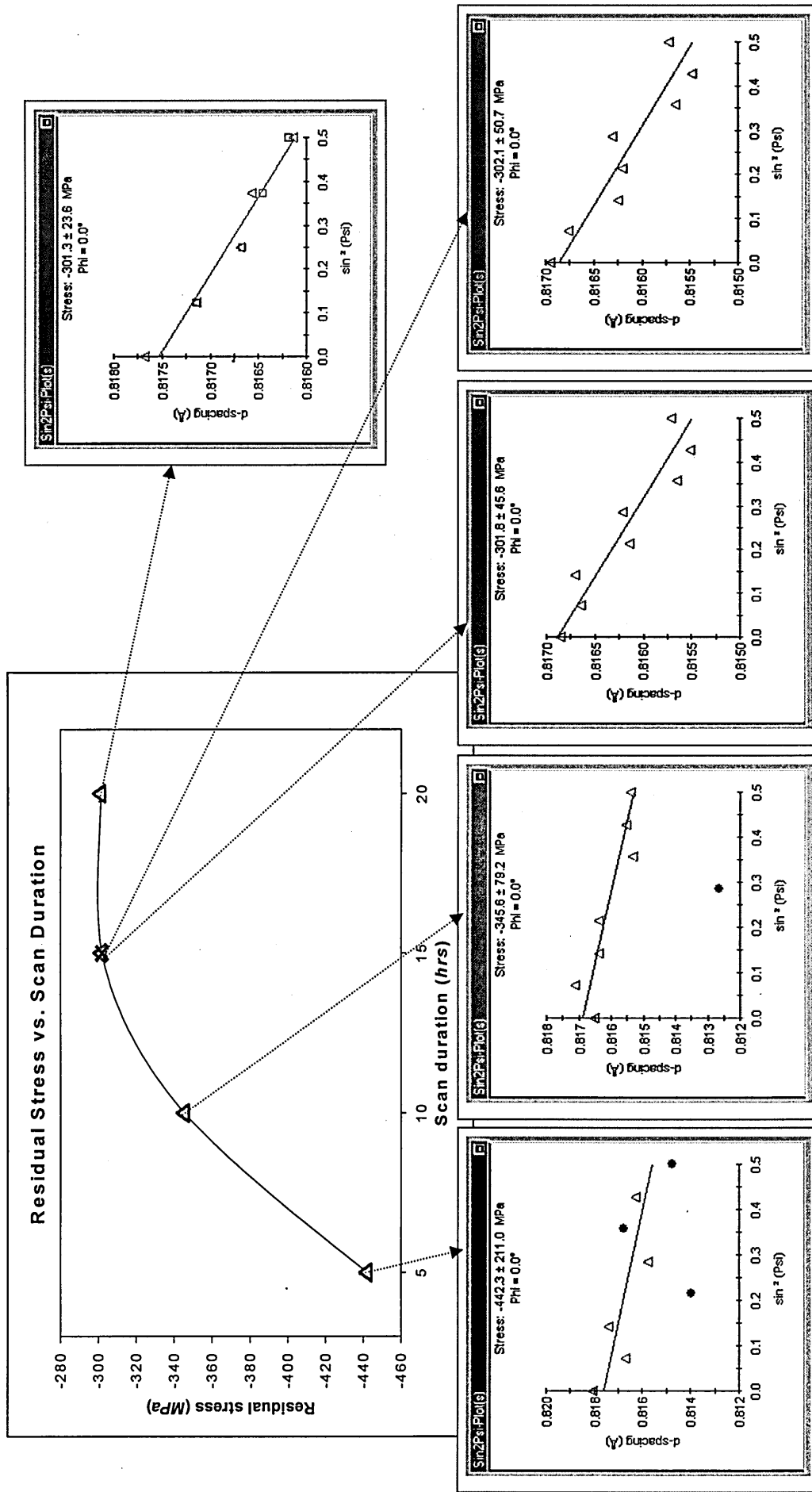


Fig.83: Stress results conducted to optimize the scan duration and the repeatability of the measurements.

5.4.7. Assumptions Encountered in Determination of Stress Using $\text{Sin}^2\psi$ Approach

The assumptions made in stress analysis using XRD technique are;

- A biaxial stress state exists within the sample surface.
- Plane stress conditions are valid (longitudinal strains are related to transverse strains by the Poisson's ratio effect, where $\varepsilon_x = \varepsilon_y = -(\nu \cdot \sigma_y)/E$).
- Material properties are assumed to be isotropic.
- A homogeneous state of stress exists.
- Measured lattice planes have the same modulus as the bulk material.
- The specimen conforms to the generic assumptions applied to $\text{Sin}^2\psi$ X-ray measurements.

5.4.8. Verification of Residual Stress Results

In order to verify the accuracy and repeatability of the measured residual stresses *Five* samples; 3 flat samples (FS) and 2 rotary bending samples (RBS), were sent to National Physical Laboratory (NPL), Middlesex, UK, which is an independent laboratory, specializing in X-ray diffraction method of residual stress measurement. NPL has used *Siemens D500* X-ray diffractometer. The *pseudo voigt* method of peak fitting was used by the NPL compared to *Pearson VII* method used at SHU. NPL has used *Cu* X-ray tube and 3° and 1° slits to control the irradiated area on the flat and hour glass shaped samples respectively with 0.15° slit placed before the detector in both cases. The tube settings in NPL were $40kV$ and $30mA$. Both at NPL and at SHU, data was corrected for absorption, background, Lorentz polarization and alpha 2 stripping. A comparison of settings used by NPL and SHU are shown in the Table.9.

Parameter	SHU	NPL
Scan axis	<i>2Theta-Omega</i>	<i>Theta-2Theta</i>
Scan mode	<i>Continuous</i>	<i>Step</i>
Start angle	<i>138</i>	<i>138</i>
End angle	<i>146</i>	<i>146</i>
Step size	<i>0.04</i>	<i>0.02</i>
Time per step	<i>28sec</i>	<i>5sec</i>
No. of steps	<i>200</i>	<i>400</i>
Tilt axis	<i>Omega</i>	<i>Omega</i>
Tilt range	<i>Positive and negative</i>	<i>Positive and negative</i>
Max. ψ	± 45	± 40
Max. $\sin^2 \psi$	<i>0.5</i>	<i>0.41</i>
No. of ψ steps	<i>9</i>	<i>9</i>
No. of scans	<i>9</i>	<i>9</i>
Total time	<i>$\approx 15hrs$</i>	<i>5hrs</i>

Table.9: Comparison of XRD measurement settings between NPL [174] and SHU.

The agreement between the stress measurements in both facilities is given in Table.10.

Sample	Normal Stress (MPa) - SHU	Normal Stress (MPa) - NPL	Agreement
FS (Machined)	-350 \pm 35	-311 \pm 23	Good
FS (Machined / Annealed)	-158 \pm 23	-136 \pm 17	Good
FS (Machined / Polished / Annealed)	+90 \pm 10	+76 \pm 4	Good
RBS (Machined)	-327 \pm 40	-340 \pm 21	Good
RBS (Machined/ Polished/ Annealed)	+63 \pm 14	+63 \pm 4	Good

Table.10: Comparison of results of NPL [174] and SHU.

5.5. Fractography and Metallographic Analysis

5.5.1. Examination using Optical Microscope

A *Carl Zeiss* optical microscope with *Spot Advance Version 4.0.6* software was used extensively in this research. Fracture surfaces were prepared and investigated initially under the optical microscope to locate macro features such as initiation sites, fatigue striations, final ductile fracture region and surface defects. It was also used to investigate the microstructural features of Ti-6Al-4V alloy. Furthermore, the optical microscope was also used to examine surface replicas to locate fatigue cracks and to understand crack propagation.

Once macro examination under optical microscope was carried out, it is easy and less time consuming to investigate minute and specific features using SEM.

5.5.2. Examination using Scanning Electron Microscope (SEM)

The SEM is one of the most versatile instruments for investigating the microstructure and details of fractured surfaces of materials. It provide high resolution images with a magnification which extends beyond $\times 10000$ up to $\times 150000$ with a depth of focus ranging from $1\mu m$ at $\times 10000$ to $2mm$ at $\times 10$ [175].

For fractography investigations three modes of SEM, (i). Secondary electron (SE) mode, (ii). backscattered electron (BS) mode, and (iii). x-ray spectroscopy mode, were routinely used. To investigate surface topography, material contrast and microstructure, SE and BS modes were used; x-ray mode was used for elemental distribution.

The *Philip's XL40* Analytical Scanning Electron Microscope equipped with an *Oxford Instruments ISIS 300* energy dispersive analyser was used. Samples required to investigate were placed on aluminium (Al) stubs using a conductive adhesive media and mounted on the sample stage situated inside the chamber, which then were ready for SEM examination. SE and BSE modes were used for imaging and EDX analysis was

carried out on identified specific features such as foreign particles, inclusions and coating materials.

5.5.3. Examination Using Infinite Focus Microscope (IFM)

The Infinite Focus Microscope is a digital light microscope which has 3D measurement and image analysis capabilities. IFM allows capturing and calculation of sharp images with virtually infinite depth of focus. It can capture images with almost 1000-times enlarged depth-of-focus and able to visualize and analyse. IFM can capture surfaces topographic specimens with large height and profile differences quickly and produces high-resolution digital colour images [176].

The *alicon*® *Infinitefocus* IFM equipped with an *alicon*® software was used to investigate the surface topography of the samples and to detect fatigue cracks on plastic replicas.

5.6. Fatigue Crack Monitoring by Surface Replication

Surface replication is a method of duplicating surface features of a component on to an acetate film for microscopic examination [177]. The main advantages of this technique are the replication can be done and surface examination can be conducted using replicas whilst the sample is undergoing fatigue testing and this technique is non-destructive.

The material used for surface replication was cellulose acetate of a thickness 35 micron. First a piece of material was cut to a suitable size to cover the area to be replicated. A drop or two of acetone were placed on to the specimen surface as well as acetate paper and the film of paper was immediately applied on top of the specimen surface. The film was then left to dry for about 10 minutes, removed and taped on to a glass slide. These replicas can be examined under an optical microscope. For SEM examination the replicas have to be coated with a sputtered conductive carbon film.

5.7. Microstructure and Grain Size Determination of Ti-6Al-4V Alloy

Two samples were prepared from the bar stock material used to machine fatigue samples, to examine the microstructure in longitudinal and transverse directions. The samples were embedded in bakelite and mirror polished as shown in Fig.84. For microstructural examination the prepared samples were etched using Kroll's reagent (4ml HNO_3 , 2ml HF and 94ml H_2O) [178].

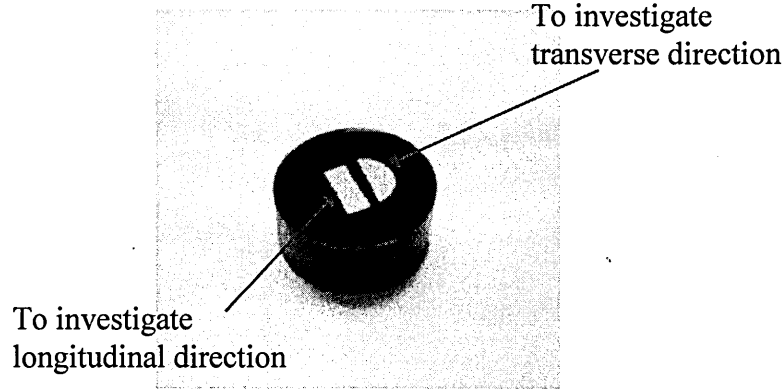


Fig.84: Sample prepared for microstructural investigation.

These samples were then investigated under the optical microscope at a magnification of 200 times.

The average grain size was determined using mean linear intercept (MLI) method in accordance with BS 4490:1989 Section 3 [179]. According to the MLI method the number of grain boundaries intercepting linearly (N) for a total length of (L) were counted. The mean number of intercepts (\bar{N}) was determined evaluate the mean number of intercepts over the total distance, i.e. (\bar{N}_L).

$$\bar{N}_L = \frac{\bar{N}}{L} \quad (19)$$

The grain size (\bar{d}) was expressed as the mean value of the intersected segment since the material microstructure is equiaxed.

$$\bar{d} = \frac{1}{\bar{N}_L} \quad (20)$$

6.1. Introduction

The results obtained from laboratory work are presented in this chapter.

A single batch (cast analysis No. A26875 and heat/batch No. L777 [191]) of Ti-6Al-4V bar stock material has used throughout the experimental work to minimize the variability in the results due to material composition and treatment variants.

6.2. Chemical Analysis of Ti-6Al-4V Alloy

The chemical composition of the material is presented in Table.11. The analysis was performed on a sample taken from the bar stock used to manufacture fatigue sample.

Element	Results from chemical analysis (mass %)	Limit according to BS 7252 - Part 3 (mass %)
Aluminium	6.4	5.5 – 6.75
Vanadium	4.46	3.5 – 4.5
Iron	0.27	0.3 max
Oxygen	0.121	0.2 max
Carbon	0.032	0.08 max
Nitrogen	0.01	0.05 max
Hydrogen	38ppm	0.015 max
Titanium	Balance	Balance

Table.11: Results of chemical analysis and standard requirements of Ti-6Al-4V implant grade alloy.

These results show that the chemical composition met the material specification requirements [10] for implant grade wrought Ti-6Al-4V alloy, used to this research. The material chemical composition was analysed at Sheffield Testing Laboratories and the test certificate is given in Appendix.11.

6.3. Grain Size Determination

The microstructure of the Ti-6Al-4V alloy is shown in Fig.85. The average grain size was determined using the mean linear intercept (MLI) method in accordance with BS

4490:1989 Section 3 [179] as explained in section 5.7. The grain size is calculated as $7\mu\text{m}$. The microstructure is in accordance with plate A1 of the ETTC Publication 2, and complies with BS 7252-Part3 (1997) [10].

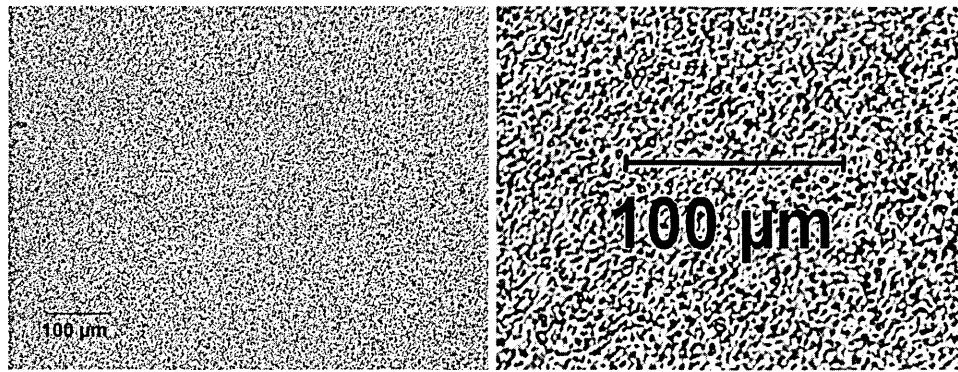


Fig.85: Microstructure of implant grade wrought Ti-6Al-4V alloy in transverse direction.

Annealed samples were also used in fatigue tests (both Phase 1 and 2) and the samples were annealed at 700°C for 2hrs and cooled in the furnace. The microstructure of the annealed sample is shown in Fig.86. No apparent differences were observed in the microstructures (Figs.85 and 86), both possessing equal average micro-grain sizes and both in accordance with plate A1 of the ETTC Publication 2. It can be concluded that no change has occurred to the microstructure of the material during the annealing process.

The microstructural features of the Ti-6Al-4V alloy used in actual implants [163] are also shows similar microstructural characteristics like grain size and orientation and also in accordance with ETTC Publication 2.

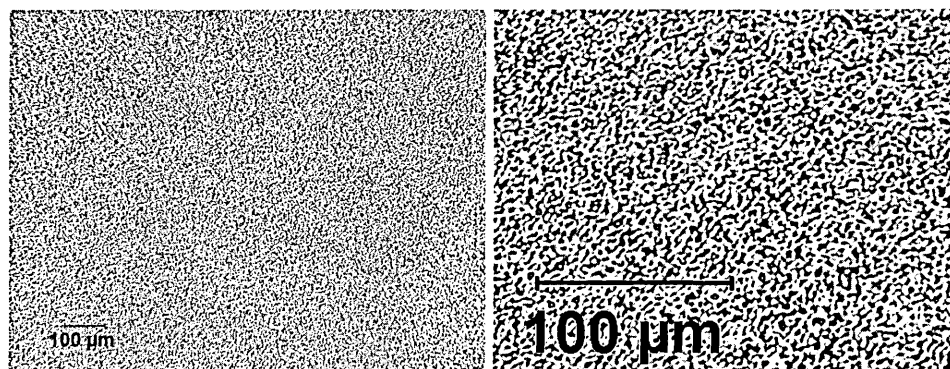


Fig.86: Microstructure of implant grade wrought Ti-6Al-4V alloy in transverse direction annealed at 700°C for 2hrs and cooled in the furnace.

6.4. Fatigue Tests - Phase.1

6.4.1. Surface Roughness and Residual Stress Measurement (Phase.1)

As explained previously Phase.1 consists of samples prepared in four different surface conditions, *i.e.* $0.2\mu\text{m}$, $6\mu\text{m}$, $21\mu\text{m}$ and $52\mu\text{m}$, having each two sub sets; annealed (*A*) and other without-annealing (*WA*). The samples of each group are shown in the Fig.87.

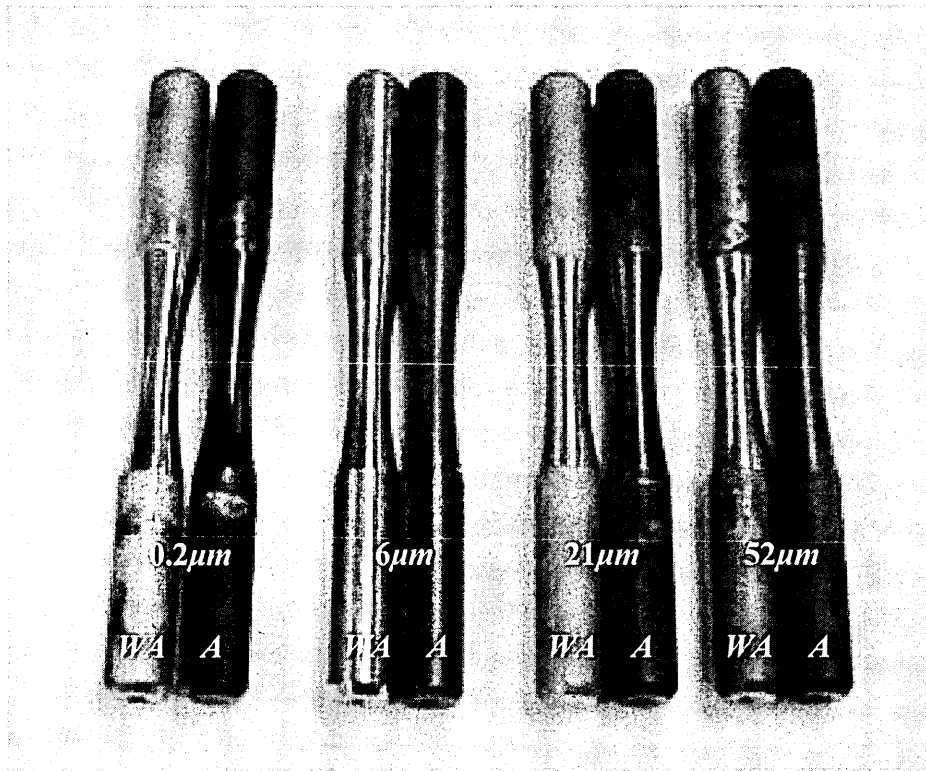


Fig.87: Four samples types prepared for Phase.1 fatigue tests.

Fig.88 and Fig.89 shows the surface roughness profiles and residual stress results for $0.2\mu\text{m}$ samples for *WA* and *A* conditions respectively. Surface roughness measurement results of Phase.1 and Phase.2 are given in Appendix.12.

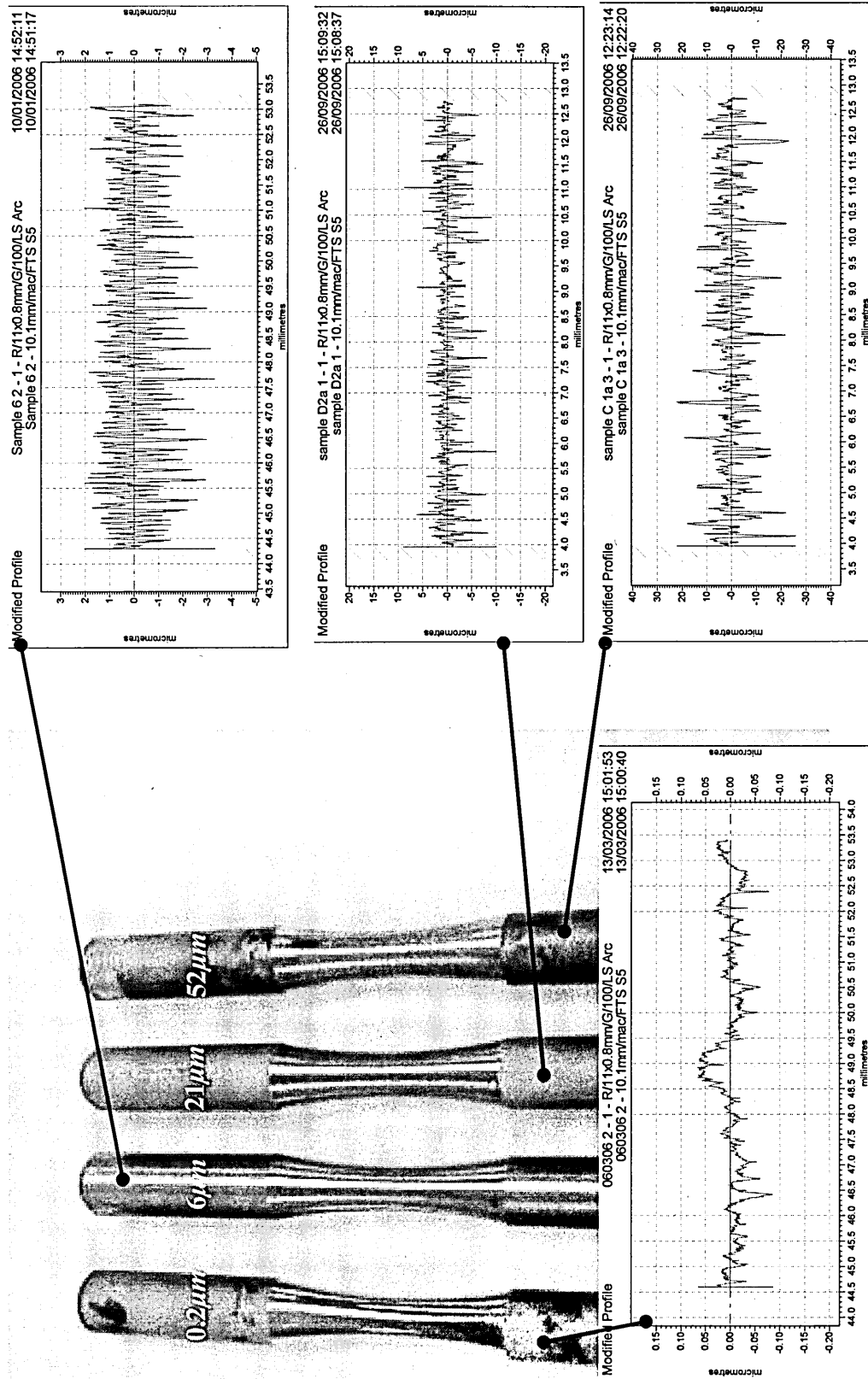
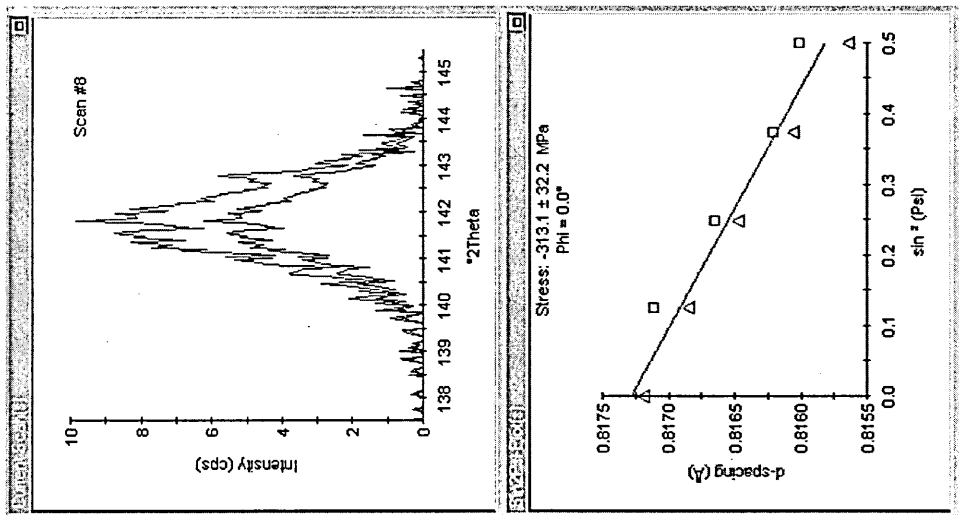
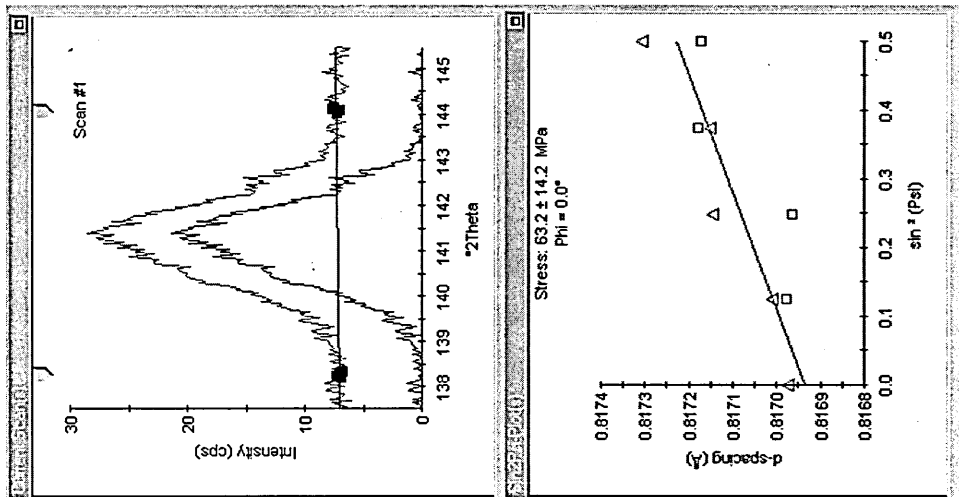


Fig.88: Surface profiles of four different surface conditions (Phase.1 fatigue tests).



(a) 0.2 μm sample (WA)



(b) 0.2 μm sample (A)

Fig. 89: Residual stress measurements of samples surface finished to 0.2 μm (a) without-annealing (b) annealed.

Tabulation of surface roughness and residual stress values for Phase.1 tests are given in Table 12. Residual stress is measured for at least two samples from each batch and the most accurate measurements have been considered for investigation.

Surface roughness (μm)	Residual Stress (MPa)	
	Samples without annealing	Annealed samples
0.2	-313	+64
6	-255	+136
21	-211	+164
52	-204	+175

Table 12: Residual stress values under each stage of Phase.1 tests.

6.4.2. Fatigue Test Results (Phase.1)

Fatigue tests were conducted and $S-N$ diagrams obtained at each stage. Fig.90 shows the variation of fatigue endurance limit of non-annealed (WA) samples.

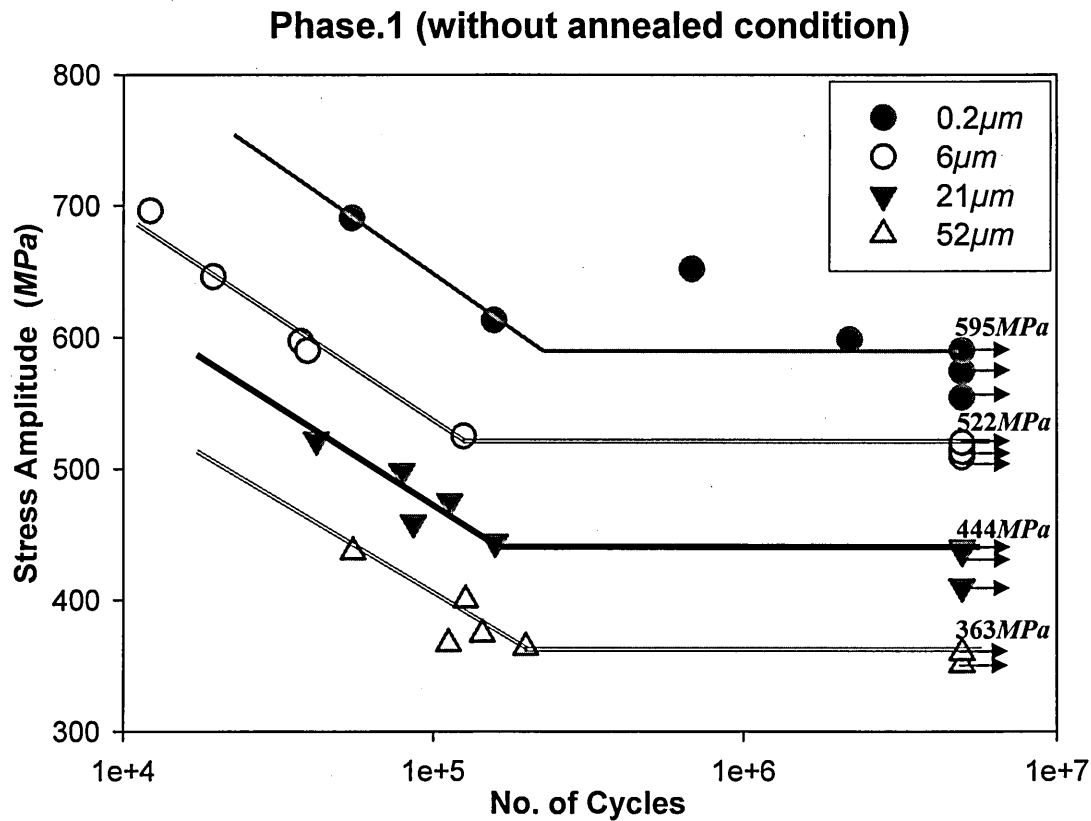


Fig.90: Variation of fatigue endurance limits of samples WA condition. Respective fatigue limits are noted.

The variation of fatigue limit due to annealing for different surface roughness of $0.2\mu m$, $6\mu m$, $21\mu m$ and $52\mu m$ are shown in Fig.91, Fig.92, Fig.93 and Fig.94 respectively.

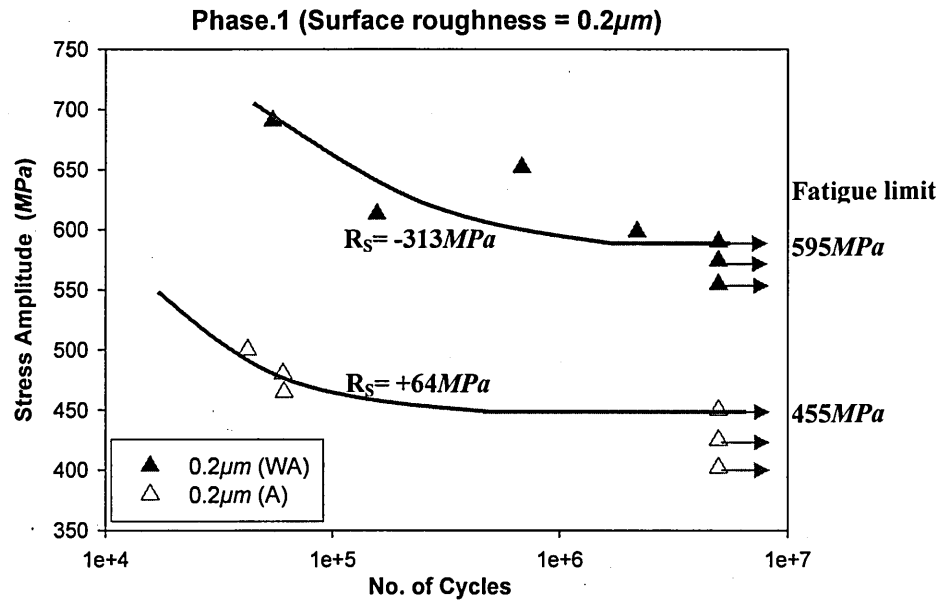


Fig.91: Fatigue curves of samples finished to a surface roughness of $0.2\mu m$; *A* and *WA* conditions. Respective values of residual stress and fatigue limit are noted.

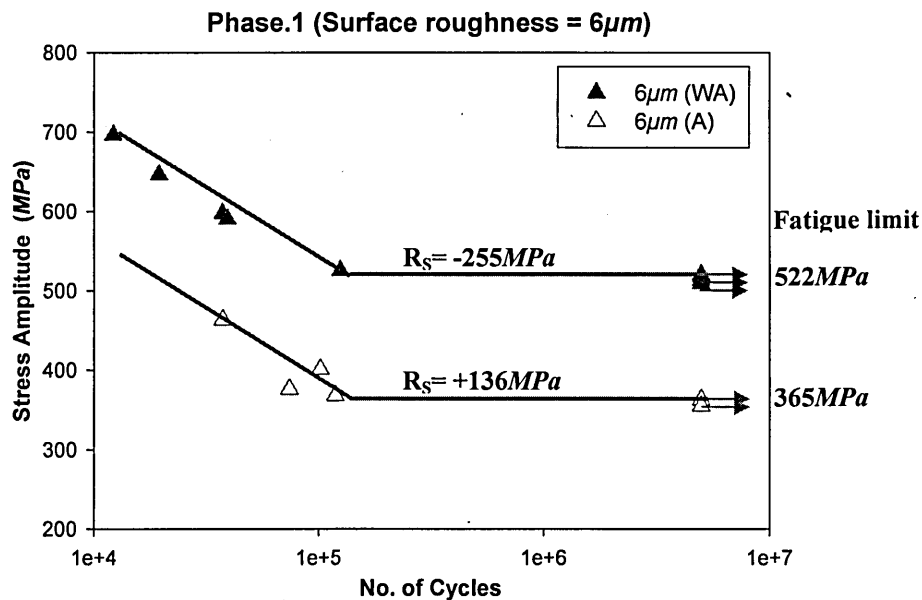


Fig.92: Fatigue curves of samples finished to a surface roughness of $6\mu m$; *A* and *WA* conditions. Respective values of residual stress and fatigue limit are noted.

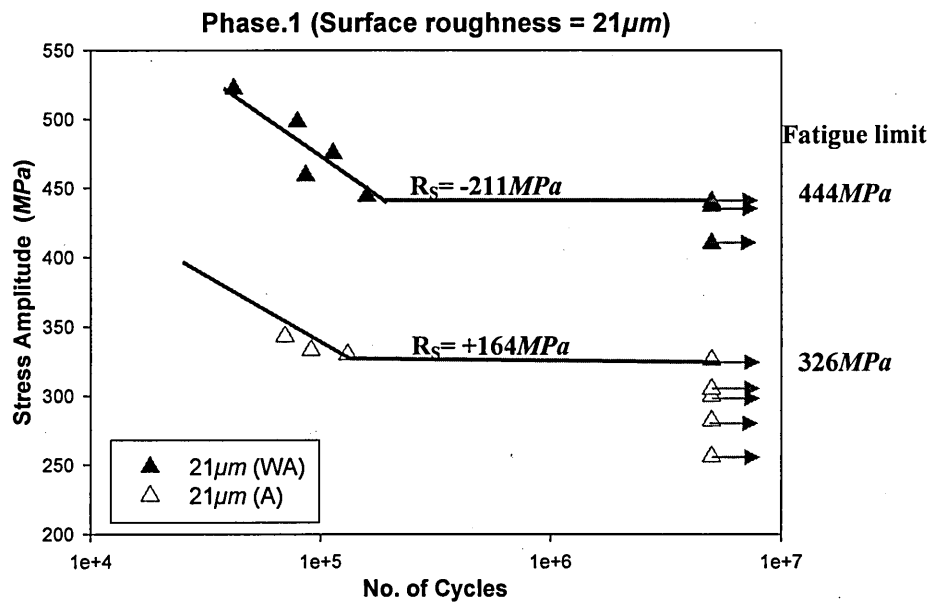


Fig.93: Fatigue curves of samples finished to a surface roughness of $21\mu\text{m}$; *A* and *WA* conditions. Respective values of residual stress and fatigue limit are noted.

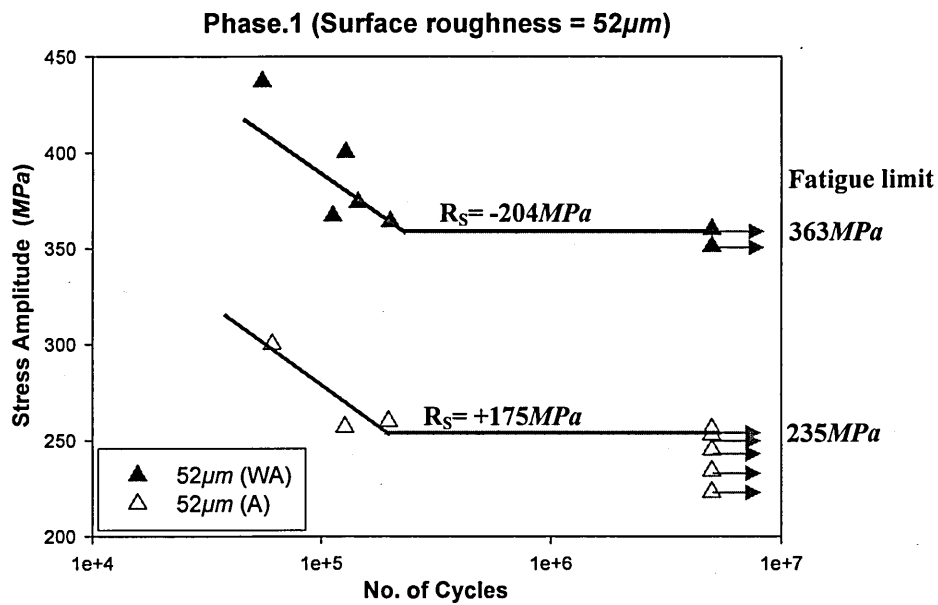


Fig.94: Fatigue curves of samples finished to a surface roughness of $52\mu\text{m}$; *A* and *WA* conditions. Respective values of residual stress and fatigue limit are noted.

A summary of the variation of fatigue limit as a function of surface roughness, for both *A* and *WA* conditions is shown in Table.13.

Surface roughness (μm)	Fatigue limit (MPa)	
	Samples without-annealed	Annealed samples
0.2	595	455
6	522	365
21	444	326
52	363	235

Table.13: Fatigue endurance limit based on different conditions under Phase I tests.

6.5. Fatigue Tests - Phase.2

6.5.1. Route.1 - Manufacturing cone region of precision forged stems

Variation of the residual stress (RS) surface roughness (SR) and fatigue limit (FL) values are shown in Fig.95.

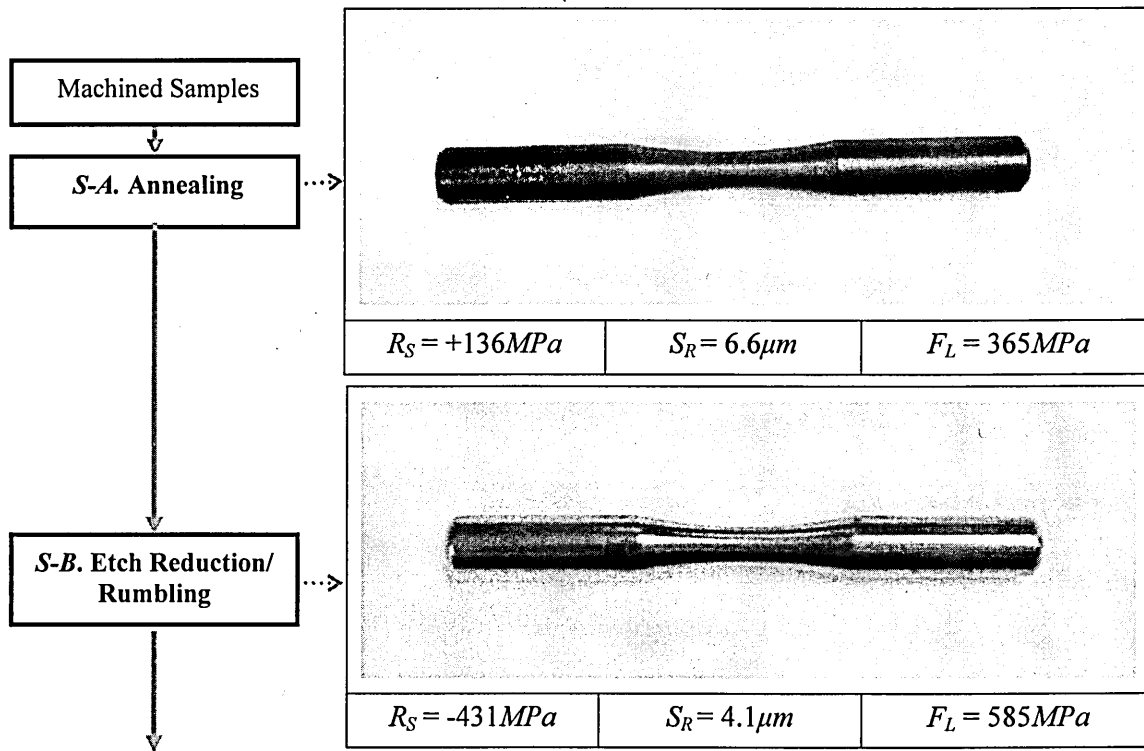
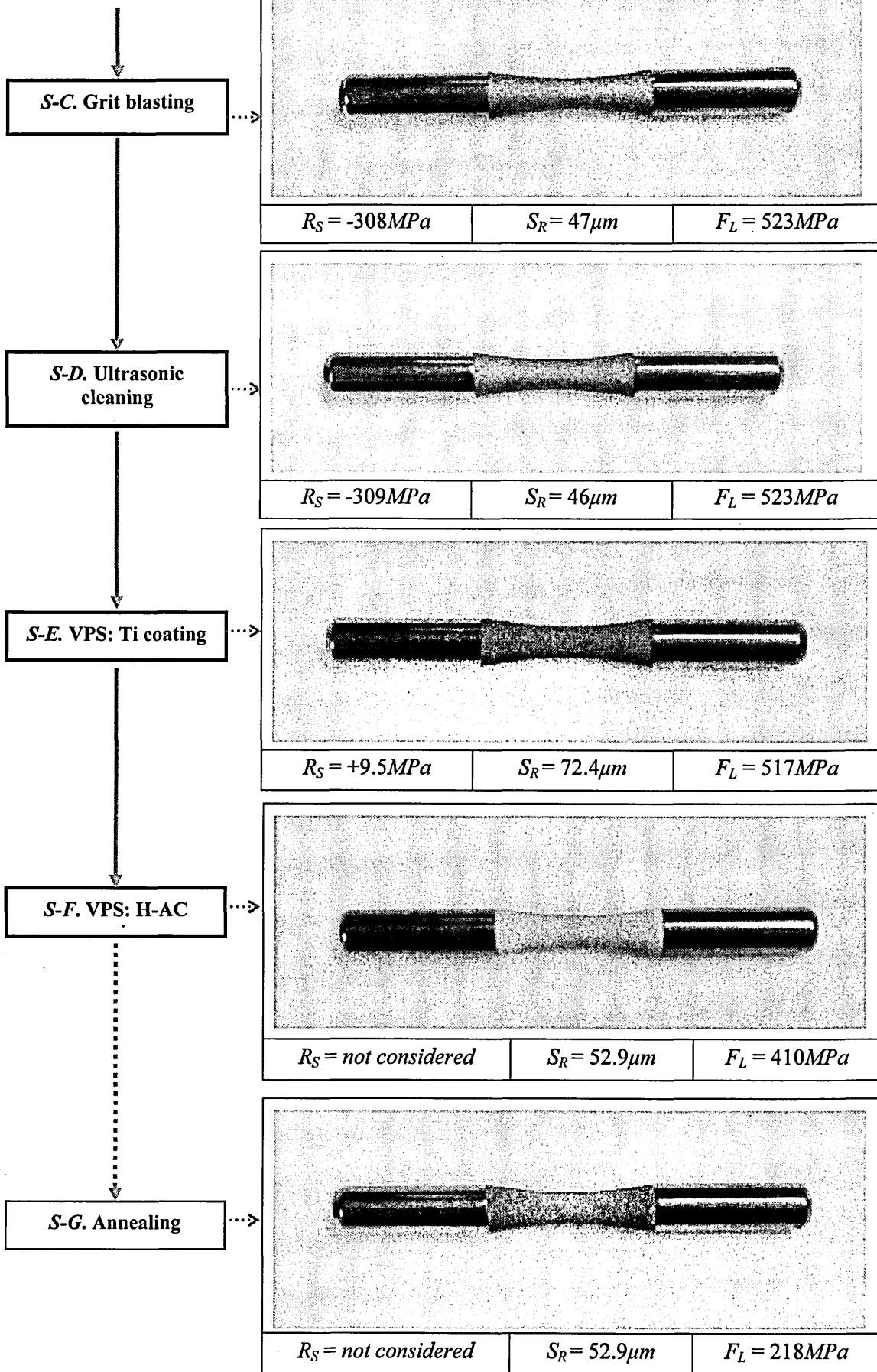


Fig.95: The fatigue limit with residual stress and surface roughness values of the samples taken at each stage and with a picture of a sample (Route.1).

Fig.95 (contd);



The variation of fatigue limit at each manufacturing stage for Route.1 is shown in Fig.96.

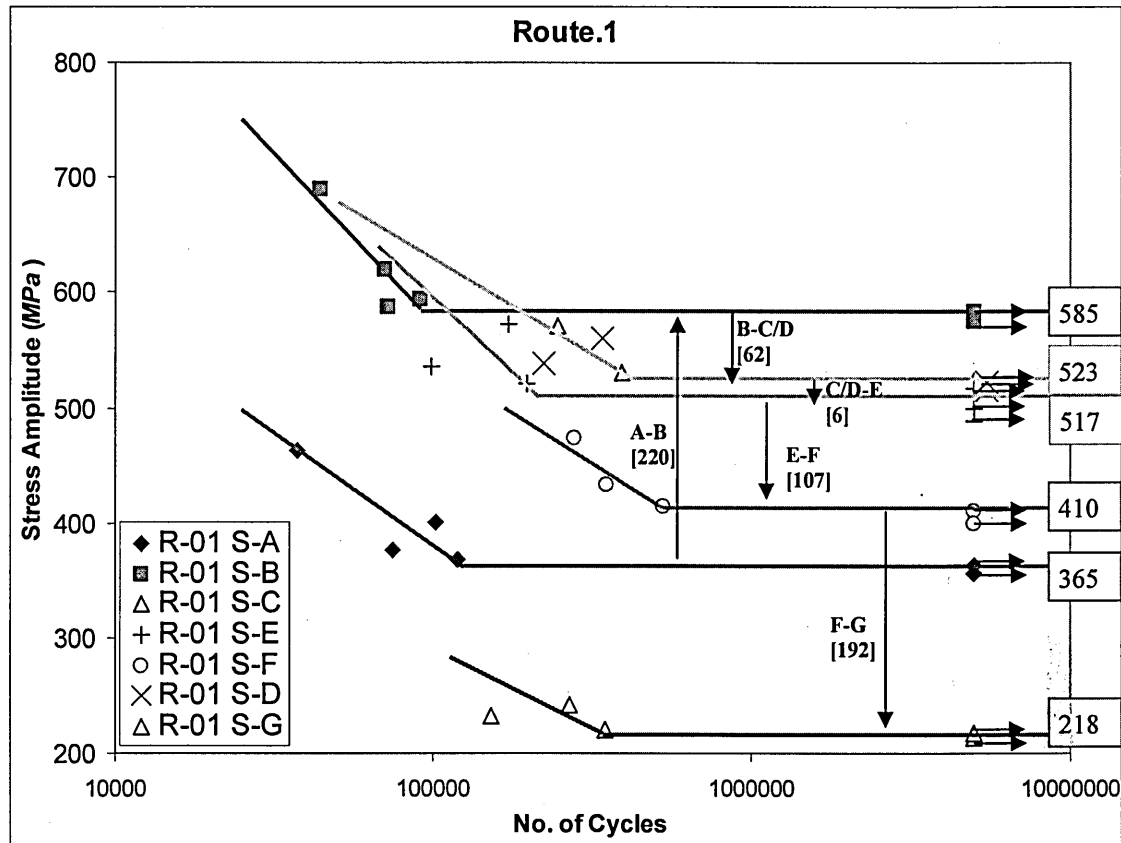


Fig.96: Fatigue endurance limit at each stage for Route.1.

Note; Vertical arrows represent the variation of fatigue limit from Stage-A to Stage-G.

The difference in fatigue endurance limit (in *MPa*) is indicated in square brackets.

Fatigue limit (in *MPa*) at each stage is noted in the box.

The fatigue limit of annealed (Stage-A) sample is 365*MPa*. Rumbling (Stage-B) increases the fatigue limit by 220*MPa* to 585*MPa*. Grit blasting (Stage-C) decreases the fatigue limit to 523*MPa*, which is a reduction of 62*MPa*. The fatigue limit remains unchanged after ultrasonic cleaning (Stage-D). Titanium coating (Stage-E) has only a minor effect on fatigue performance where it reduces the fatigue limit by only 6*MPa*. However H-AC coating process (Stage-F) decreases the fatigue limit by a considerable margin, notably 107*MPa*. After H-AC coating the fatigue limit is 410*MPa* and this is further reduced to 218*MPa* after final annealing (Stage-G).

6.5.2. Route.2 - Manufacturing cone region of stems forged to oversize (mainly revision stems)

Variation of the residual stress (RS) surface roughness (SR) and fatigue limit (FL) values are shown in Fig.97.

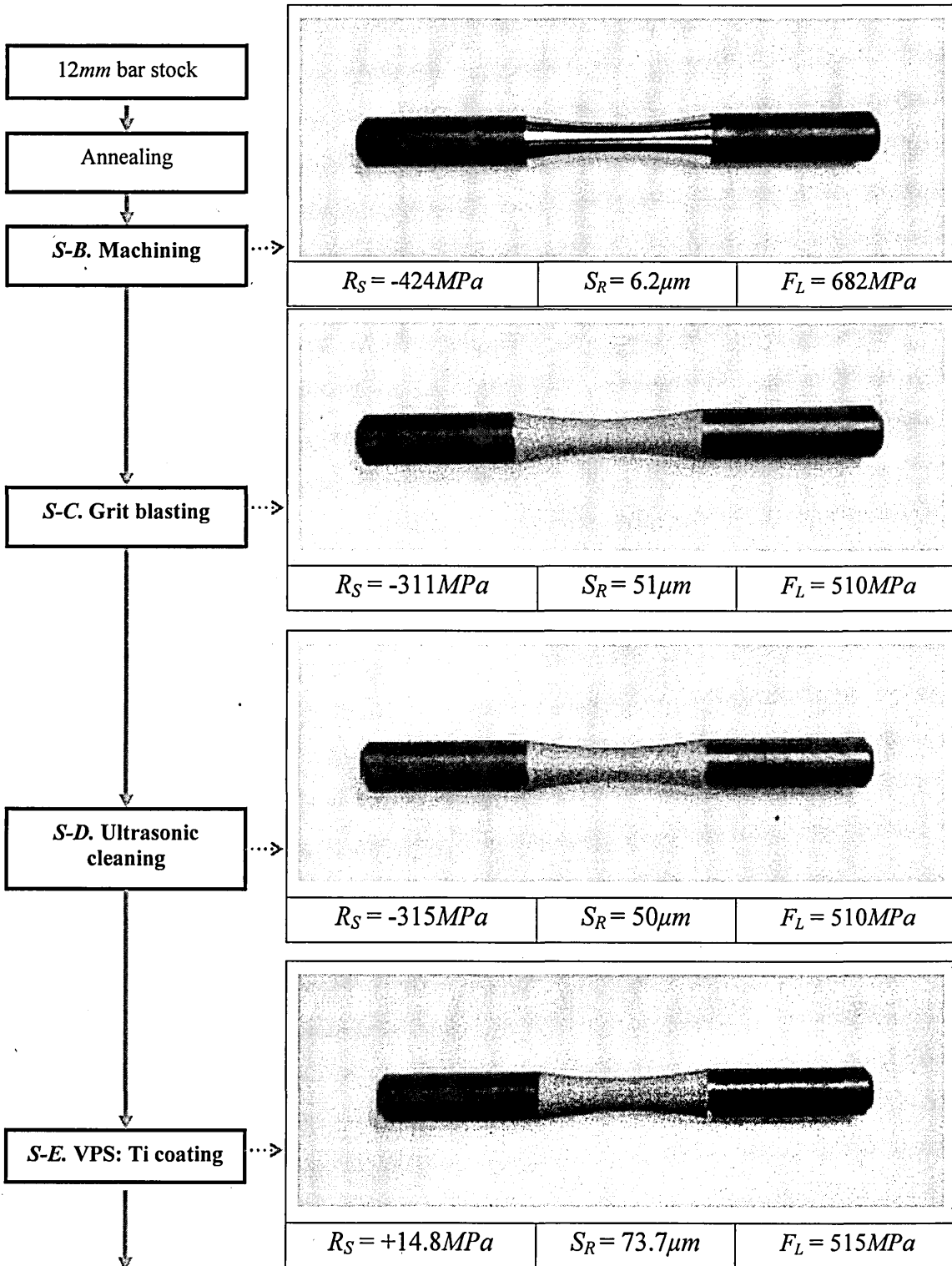
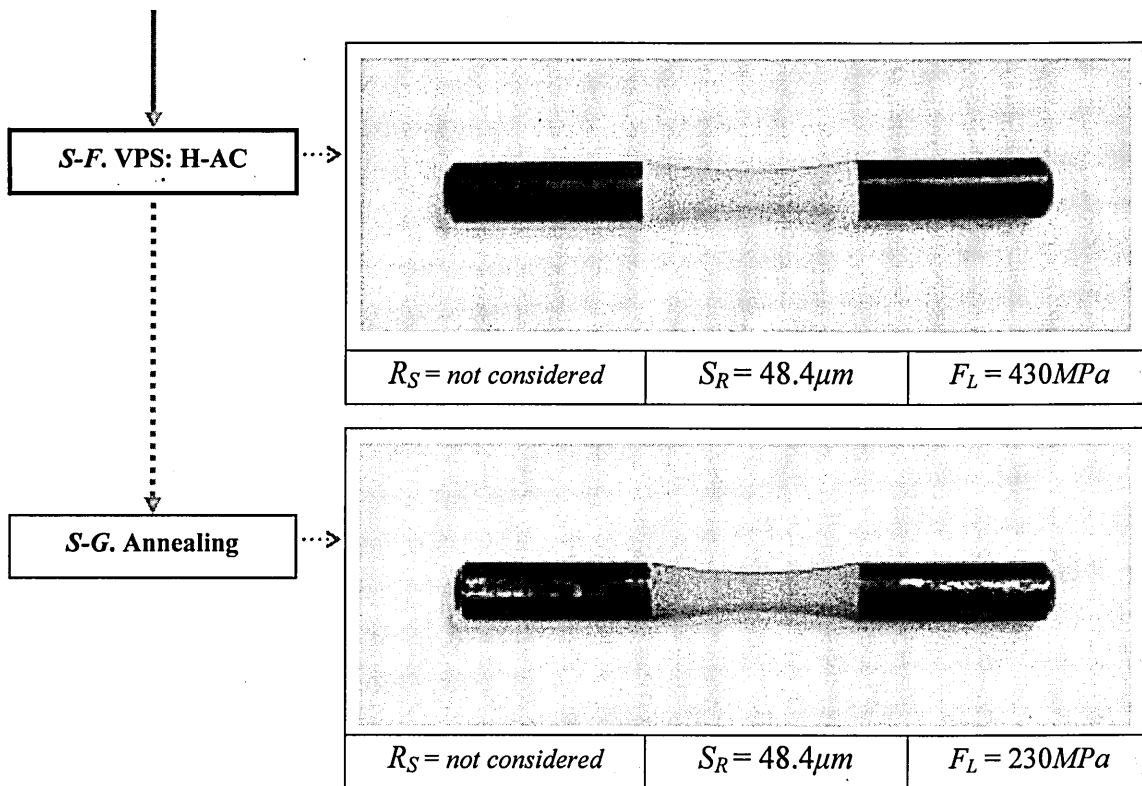


Fig.97: The fatigue limit with residual stress and surface roughness values of the samples taken at each stage and with a picture of a sample (Route.2).

Fig.97 (contd);



The variation of fatigue limit at each manufacturing stage for Route.2 is shown in Fig.98.

The fatigue limit of the machined samples is $682MPa$, which the highest values for Route.2. Grit blasting decreases the fatigue limit to $510MPa$, a reduction of $172MPa$. The fatigue limit remains unchanged after ultrasonic cleaning. Applying a titanium coating has a minor effect on fatigue performance where the fatigue limit increases by only $5MPa$. However application of H-AC coating decreases the fatigue limit to $430MPa$, a decrease of $85MPa$. Final annealing causes a considerable reduction in the fatigue limit. The final value of fatigue limit is $230MPa$, being the same order as Route.1.

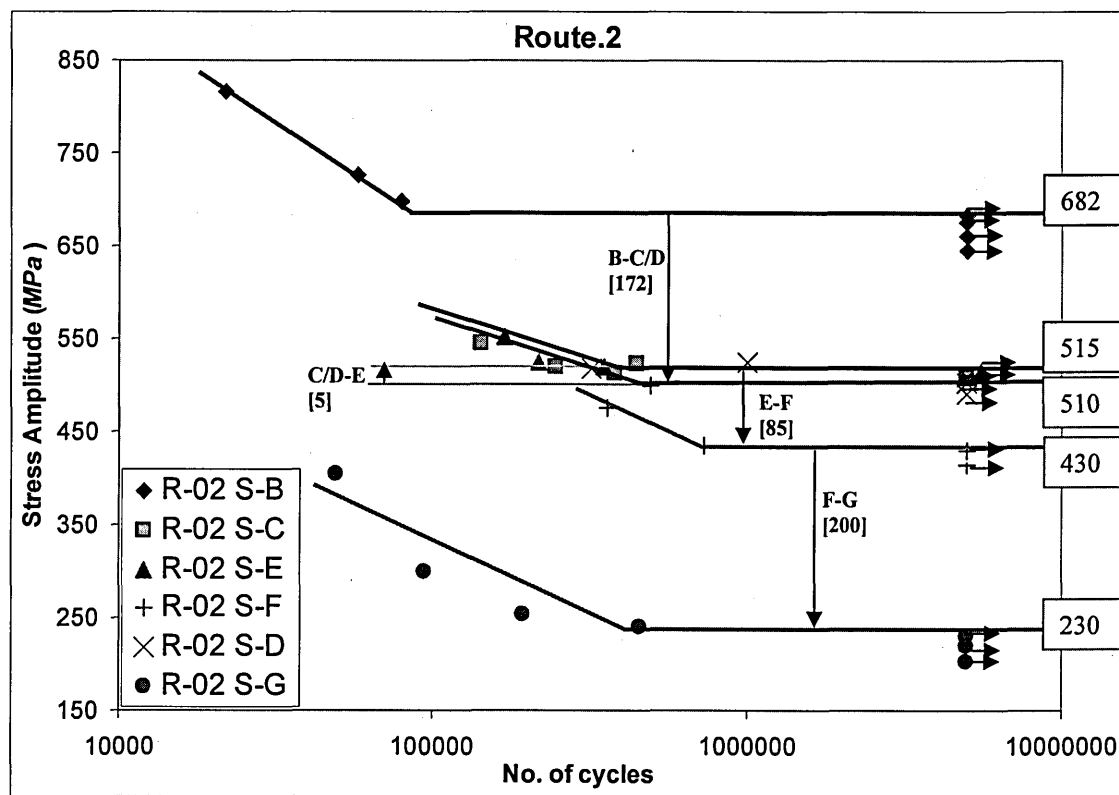


Fig.98: Fatigue endurance limit at each stage for Route.2.

Note; Vertical arrows represent the variation of fatigue limit from Stage-B to Stage-G.

The difference in fatigue endurance limit (in MPa) is indicated in square brackets.

Fatigue limit (in MPa) at each stage is noted in the box.

6.5.3. Route.3 - Manufacturing of neck region

Variation of the residual stress (RS) surface roughness (SR) and fatigue limit (FL) values are shown in Fig.99.

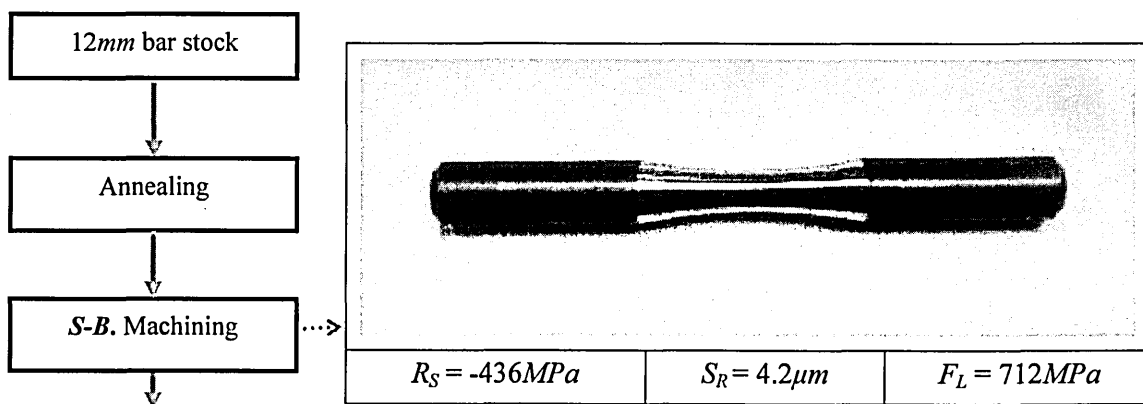
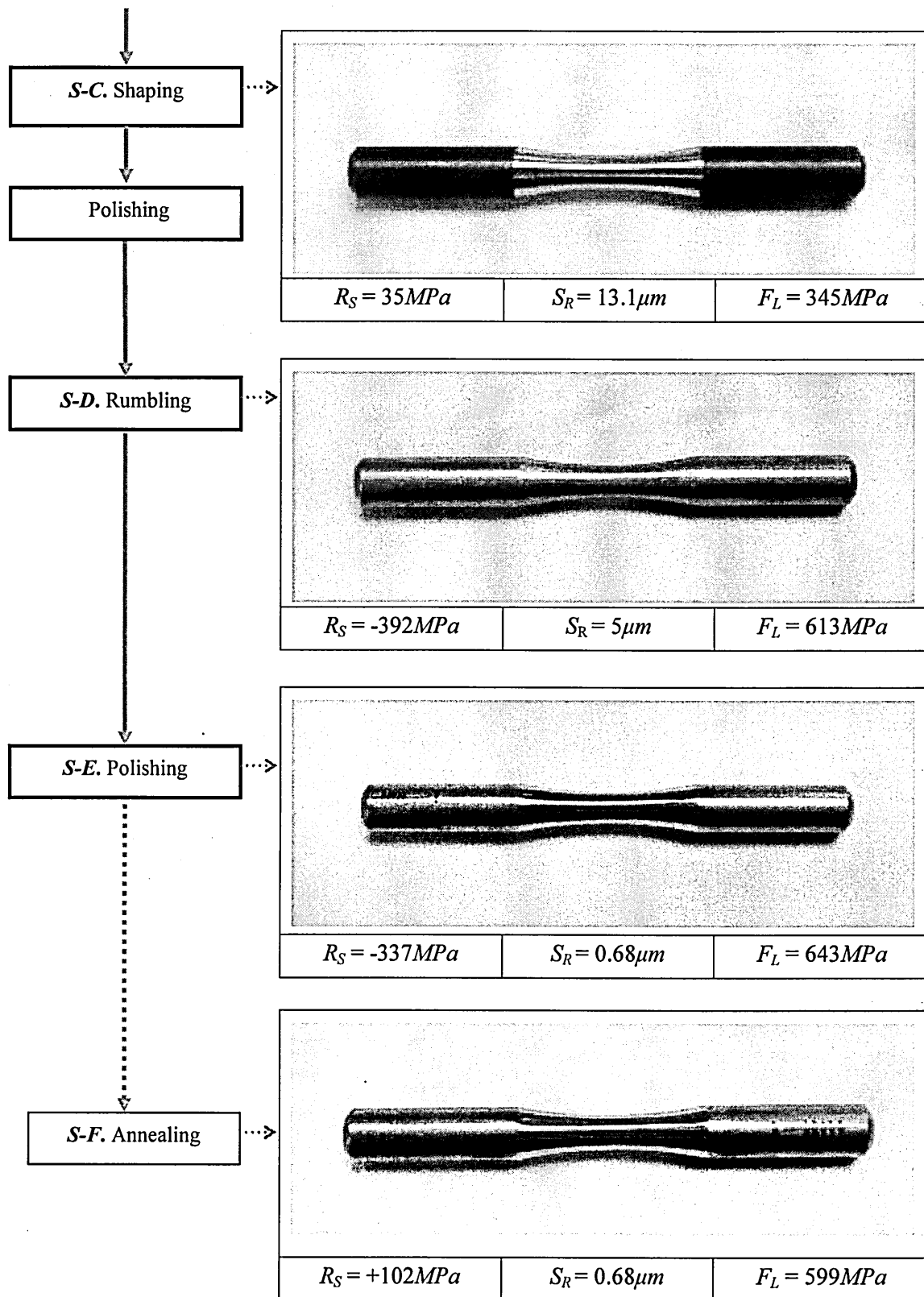


Fig.99: The fatigue limit with residual stress and surface roughness values of the samples taken at each stage and with a picture of a sample (Route.3).

Fig.99 (contd);



The variation of fatigue limit at each manufacturing stage for Route.3 is shown in Fig.100.

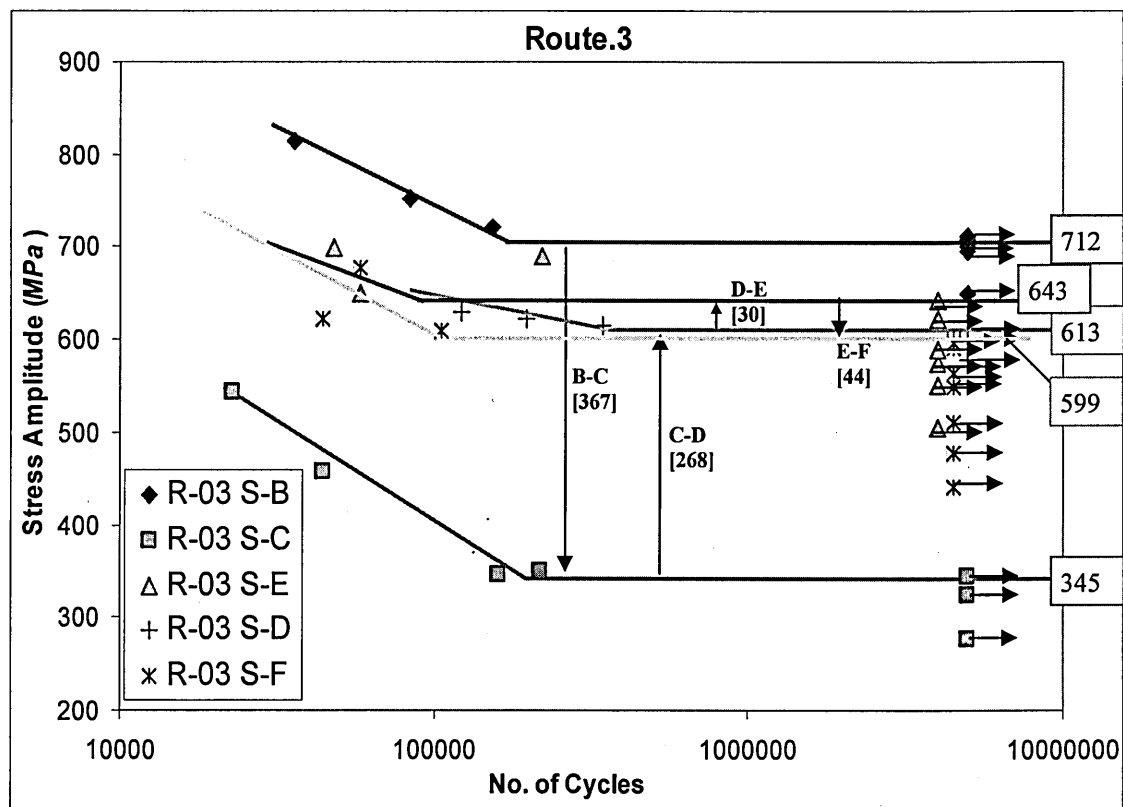


Fig.100: Fatigue endurance limit at each stage for Route.3.

Note; Vertical arrows represent the variation of fatigue limit from Stage-B to Stage-F.

The difference in fatigue endurance limit (in *MPa*) is indicated in square brackets.

Fatigue limit (in *MPa*) at each stage is noted in the box.

The fatigue limit of machined samples is 712*MPa*, which the highest values for Route.3. The shaping process decreases the fatigue limit to 345*MPa*, a reduction of 367*MPa*. The rumbling processes increase the fatigue limit to 613*MPa*, an increase of 268*MPa*. Polishing increases the fatigue limit by 30*MPa*; after polishing, the fatigue limit is 643*MPa*. The final annealing process causes a reduction of 44*MPa*, with a final fatigue limit of 599*MPa*.

6.6. Analysis of Surface Cracks using a Surface Replication Technique

The surface replication method (see section 5.6), has been used to evaluate the crack propagation behaviour in Ti-6Al-4V. Mirror-like polished samples with a surface roughness of $0.2\mu\text{m}$ were used in this investigation. Samples were tested at stress amplitude of 630MPa , where the fatigue endurance limit of a batch of similar samples is 595MPa . Where cracks were found, pictures were taken at increasing number of cyclic intervals; some of them are shown in Fig.101. The fraction of the life (N/N_f) at each interval is noted with the figure.

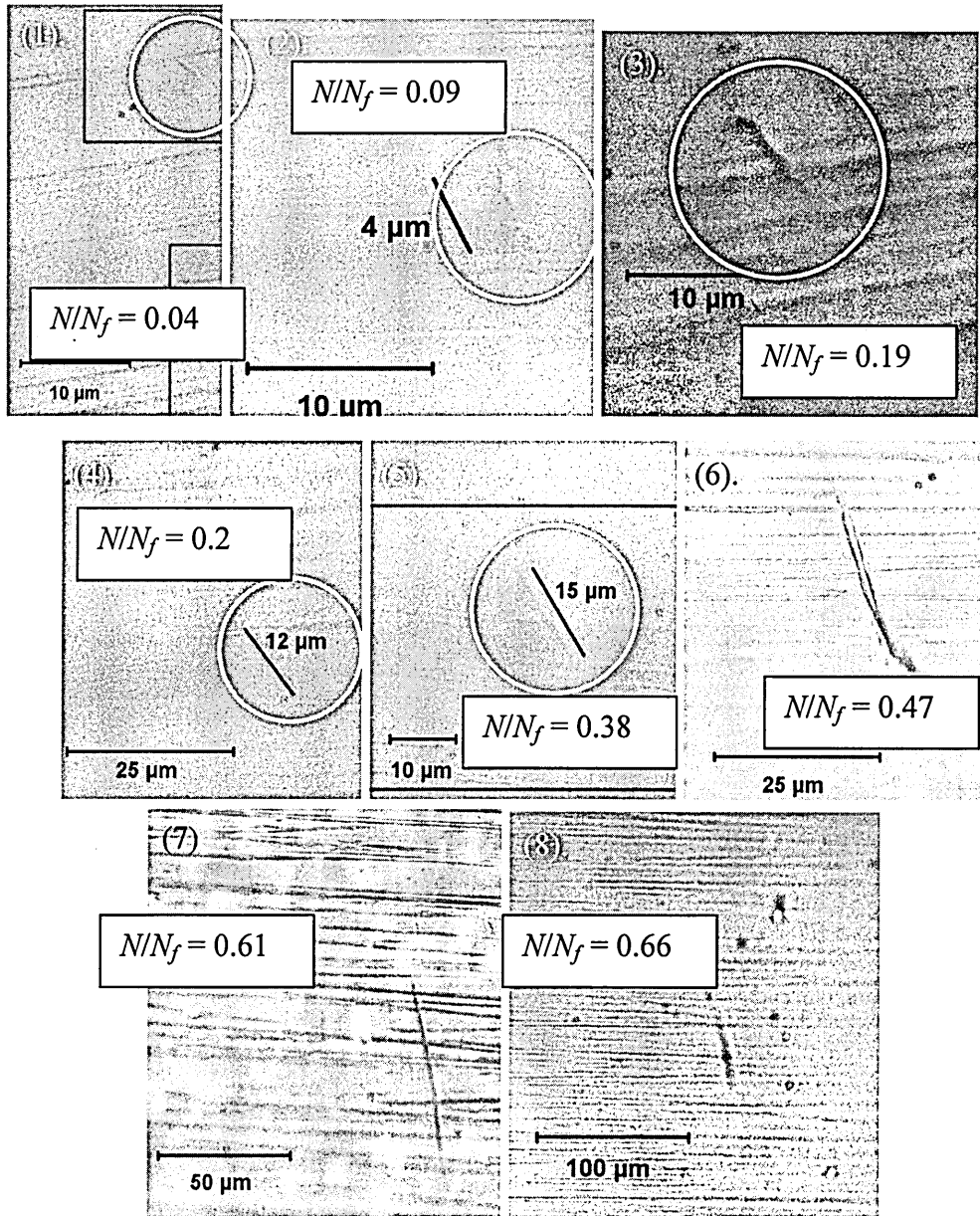
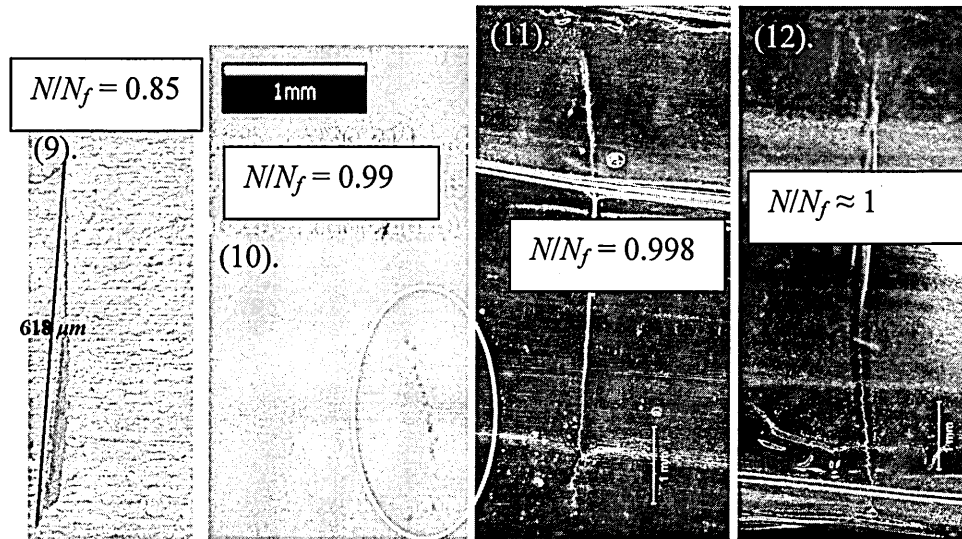


Fig.101: Pictures of fatigue cracks obtained by surface replication. (Note: figures 1-9 are investigated by optical microscope, figures 10-12 are investigated by IFM)

Fig.101 (contd);



The variation of crack length with the number of cycles is illustrated in Table.14 and Fig.102.

No. of cycles	Crack length (μm)
10000	2
20000	4
40000	5
50000	7
80000	12
90000	15
100000	21
110000	40
130000	57
140000	90
150000	150
160000	240
170000	334
180000	619
200000	1200
209267	6360
209487	6700
209873	10450

Table.14

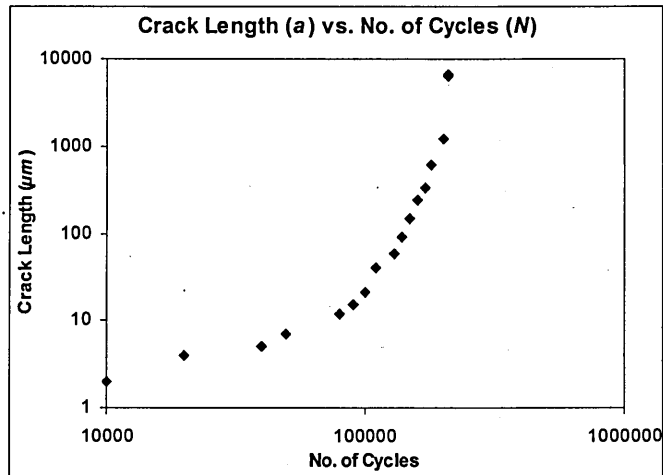


Fig.102

Table.14, Fig.102: Crack length against the number of cycles.

Based on the crack measurements fatigue crack growth rate (da/dN) against the crack length (a) can be determined, as shown in Fig.103. According to this figure it can be assumed that there is a reduction of crack growth when the crack length approaches a crack length of around 7-8 μm.

Based on the a versus N data and applied stress the fatigue crack growth rate (da/dN) against stress intensity factor (ΔK) curve can be determined, as shown in Fig.104. According to the figure it can be assumed that there is a threshold value of the stress intensity factor around $3\text{-}5\text{MPa}\sqrt{m}$. This compares favourably with literature values of around $5\text{MPa}\sqrt{m}$ [86,83]. The respective values ΔK corresponding to cracks lengths were calculated using equation (7). The value of the geometrical factor, Y , is approximated as unity [186,187,188].

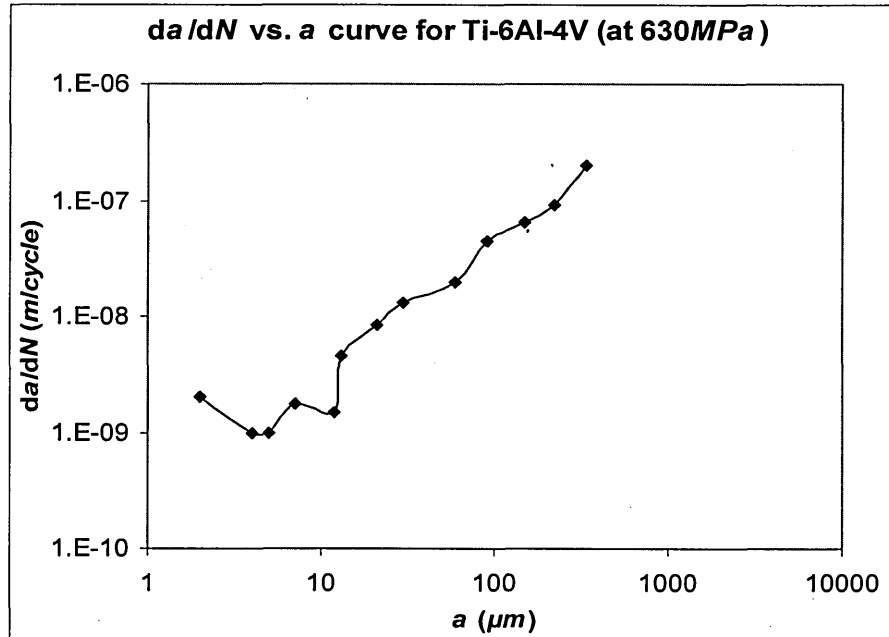


Fig.103: Variation of fatigue crack growth rate (da/dN) against the crack length (a)

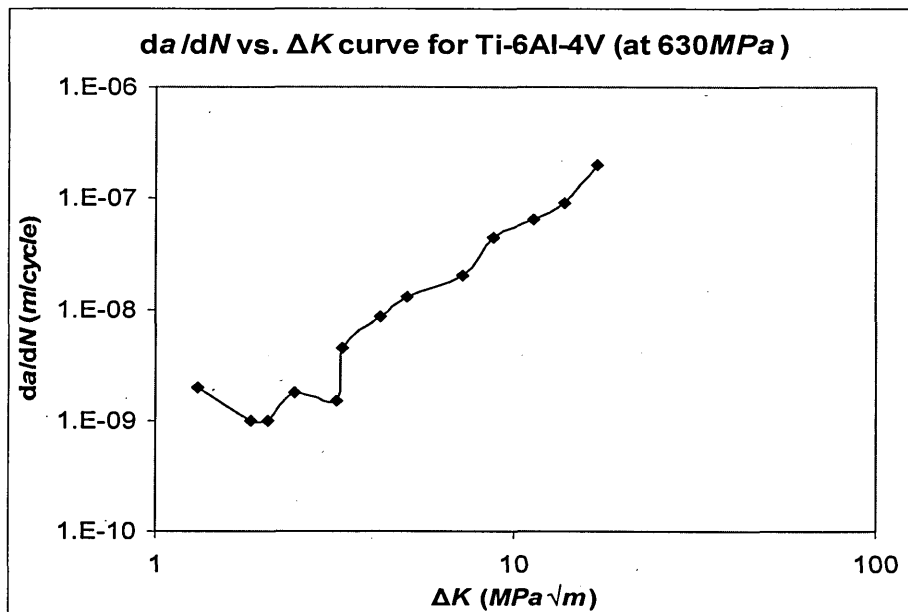


Fig.104: Variation of da/dN against stress intensity factor (ΔK).

6.7. Fractographic Analysis Using SEM and Optical Microscopes.

The fracture surfaces of failed samples were analysed to understand the failure mode, notably, failure initiation, propagation and possible causes of failure. Fig.105 shows the *S-N* curve and fractographic representation of the failed samples for Route.1 / Stage-B. Full detailed illustrations of each stage for all the three routes are given in Appendix.13 – Appendix.28.

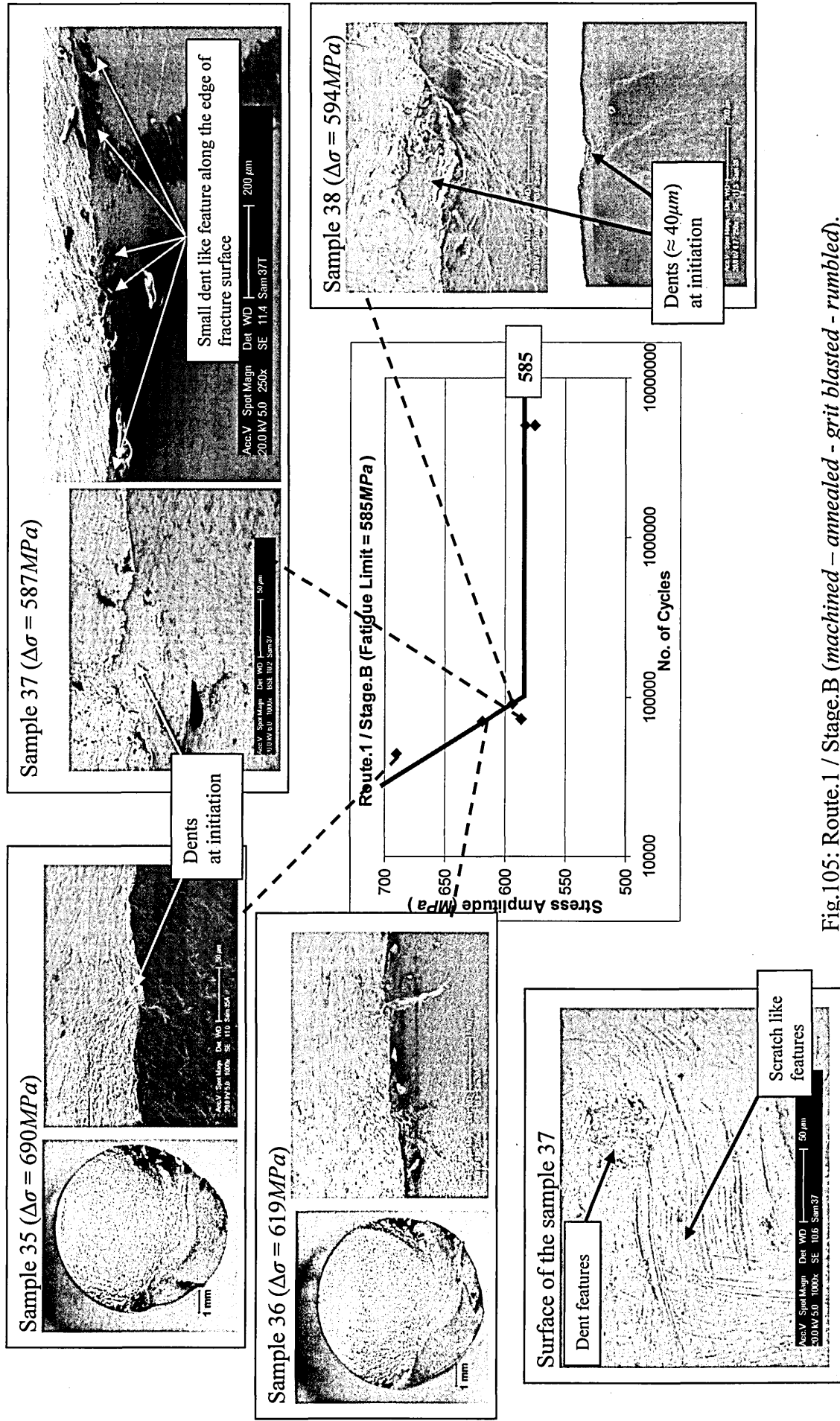


Fig.105: Route.1 / Stage.B (machined – annealed – grit blasted – rumbled).

7.1. Introduction

Components invariably have defects which are formed by manufacturing, fabrication, and assembly. On loading these defects may initiate cracks that grow with time, finally leading to failure of the component [59].

Fatigue crack growth can be classified into three regimes, namely microstructural short crack (MSC), physically small cracks (PSC) and long cracks (see Fig.20). For stress levels around the fatigue limit short fatigue crack growth in the MSC and PSC regimes are the most dominant regions where most of the total fatigue life is spent. In the MSC regime, the size of the grains and the obstruction to crack propagation, notably grain boundaries can play an important roll in fatigue performance. The short crack growth region represents a significant proportion of the fatigue life time and any effective changes in stress state can change the crack growth rate. This short fatigue crack growth behaviour is dependent on the operating stress amplitude, loading mode, environment and the material properties.

Here short and long crack growth equations (see section 7.2) were used to develop a crack growth model, which allows the fatigue life at a given stress amplitude to be calculated. The material constants used in these equations were calculated by using smooth specimen fatigue data. Similar methodology has been used by Angelova and Akid [183], Wheelhouse [184], Al-Alkawi [185] and Zhang [180]. However all the above models were developed for different materials and it was not possible to find a similar model which had been developed for Ti-6Al-4V implant grade alloy.

7.2. Crack Growth Models

The crack growth model developed is based on equation (1) by Hobson and equation (2) expressed by Brown (see section 2.5). Hobson's equation considered mainly the crack growth rate in MSC regime which considered the microstructural features of the material, and Brown's equation considered both PSC (EPFM) and LEFM fatigue crack growth regimes.

Analysis of fatigue cracks in MSC regime in this research is based on Hobson's equation expressed in the form,

$$da_{msc}/dN = A (\Delta\sigma)^m (d - a_{msc}), \quad (1)$$

where d is microstructural length parameter, A and m are material constants, a_{msc} is the surface crack length in MSC regime and $\Delta\sigma$ is the stress range. The fatigue crack will continue to grow if the applied stress is sufficient to overcome the microstructural barriers and then the crack grows into the PSC region finally propagating as a long crack to failure. Analysis of fatigue cracks in the PSC regime is based on Brown's equation expressed in the form,

$$da_{psc}/dN = B (\Delta\sigma)^n a_{psc} - D, \quad (2)$$

where B and n are material constants, D represents a crack growth threshold value, a_{psc} is the surface crack length in the PSC regime and $\Delta\sigma$ is the stress range.

The fatigue life spent in the MSC (N_{msc}) and PSC (N_{psc}) regions can be obtained by integrating equation (1) and (2) respectively as,

$$N_{msc} = \frac{1}{A(\Delta\sigma)^m} \cdot \ln \left[\frac{d - a_i}{d - a_{th}} \right] \quad (21)$$

and,

$$N_{psc} = \frac{1}{B(\Delta\sigma)^n} \cdot \ln \left[\frac{a_{th} - (D/B(\Delta\sigma)^n)}{a_f - (D/B(\Delta\sigma)^n)} \right], \quad (22)$$

where a_i is the initial crack length which is the surface finish, a_{th} represents the transition length of cracks from MSC to PSC and a_f corresponds to the failure crack length.

The total lifetime (N) is equal to the sum of the short and long crack fatigue lifetimes, *i.e.*,

$$N = N_{msc} + N_{psc} \quad (23)$$

7.3. Determination of Parameters

Determination of parameter d : The parameter d represents the crack length where crack growth rate decreases to a minimum and cracks tend to slow down and may arrest. This corresponds to a position where the crack front meets the main microstructural barrier such as a grain boundary (refer Fig.106). For this model the value of d was taken as the α -grain size of the material, since the α -grains are the sites for micro-crack nucleation and stage I crack growth [78,79] in Ti-6Al-4V alloy. The mean grain size is taken as $7\mu\text{m}$, and the determination of grain size is explained in section 5.7 and 6.3. Also the da/dN vs. a curve obtained from the data obtained from surface replication (see Fig.103) also supports the existence a barrier at $\approx 7\mu\text{m}$.

Determination of parameter a_i : The parameter a_i is the initial defect size where fatigue failure nucleates. It is considered as the surface finish (initial defect size) of the smooth specimens (highly polished samples to mirror surface finish). The surface finished to $0.2\mu\text{m}$ (see section 5.3 and 6.4) which considered as a_i value.

Determination of parameter a_f : The parameter a_f represents the final crack length and this is taken to be half of the minimum diameter of the test specimens which is $4000\mu\text{m}$ ($= 8\text{mm}/2$).

Determination of parameter a_t : The transition crack length can be calculated using equations (1) and (2), which the crack growth rates of both MSC and PSC should be equal, i.e.,

$$\text{At } a_t; \quad \frac{da_{msc}}{dN} = \frac{da_{psc}}{dN},$$

$$\text{which can be expanded as; } a_t = \frac{A(\Delta\sigma)^m [d_1 + (t.\text{grain} - 1)d_2] + D}{A(\Delta\sigma)^m + B(\Delta\sigma)^n}, \quad (26)$$

where $t.\text{grain}$ is the grain number which the crack transfer from MSC to PSC, and it is considered as $d_1 = d_2 = d_3 \dots = 7\mu\text{m}$ for the model.

Determination of parameter D : The parameter D is a material constant. Considering equation (2) the value of D can be expressed as $D = B(\Delta\sigma)^n a_{th}$. In other words the

value of D is the intercept of da/dN vs. a curve (PSC region which is governed by the equation 2), as shown in Fig.106.

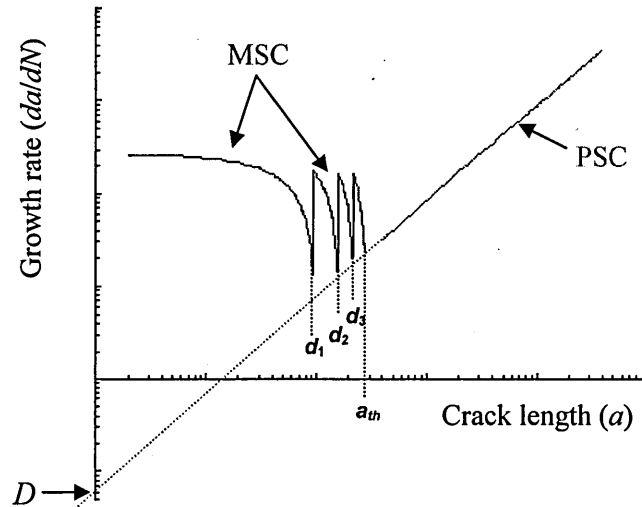


Fig.106: Typical da/dN vs. a representation of fatigue cracks in MSC and PSC regions

The value of D can be calculated using the fatigue crack growth data in PSC regime ($a > 40\mu m$) obtained by surface replication, which are given in Fig.102. The da/dN vs. a curve can be obtained as shown in Fig.107 and the value of D (interception of Y-axis) can be calculated as 3.99×10^{-3} .

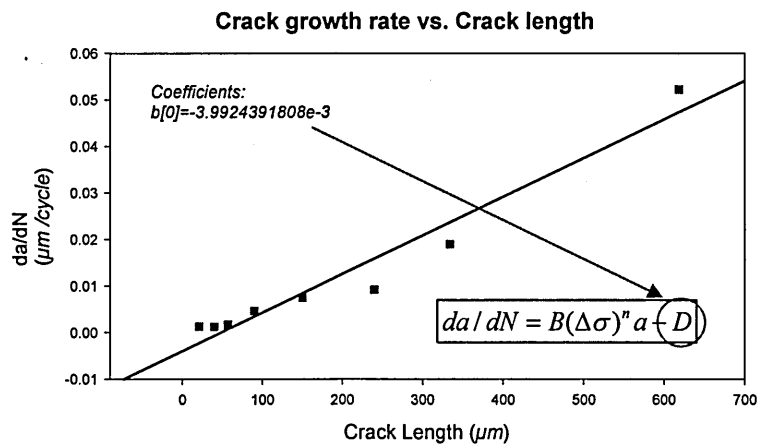


Fig.107: da/dN vs. a curve for PSC regime obtained using surface replication data, to determine the value of parameter D

Consideration of plastic zone at grain boundaries: The model assumes a crack retardation threshold condition at the crack arrest ($da/dN \rightarrow 0$) due to existence of a

plastic slip zone ahead of the crack front in MSC growth. If r_p is the extent of crack front plastic zone size, a_{msc} and d can be represented as shown in Fig.108. The plastic zone size is constrained by the grain boundaries which the cracks propagate into the next grains.

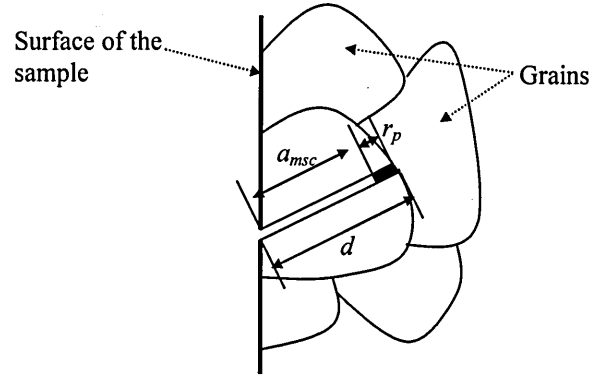


Fig.108: Schematic illustration of the crack tip plastic zone in MSC.

The a_{msc} can be represented as [193],

$$a_{msc} = \alpha \cdot d \quad (24)$$

The value α is dependant on the microstructure of the material, which can be represented as,

$$\alpha = 1 - \left(\frac{r_p}{d} \right) \quad (25)$$

The value of α is considered as 0.95 [193].

7.4. Development of Computer Model

Fig.109 represents the simple chart which illustrates the model.

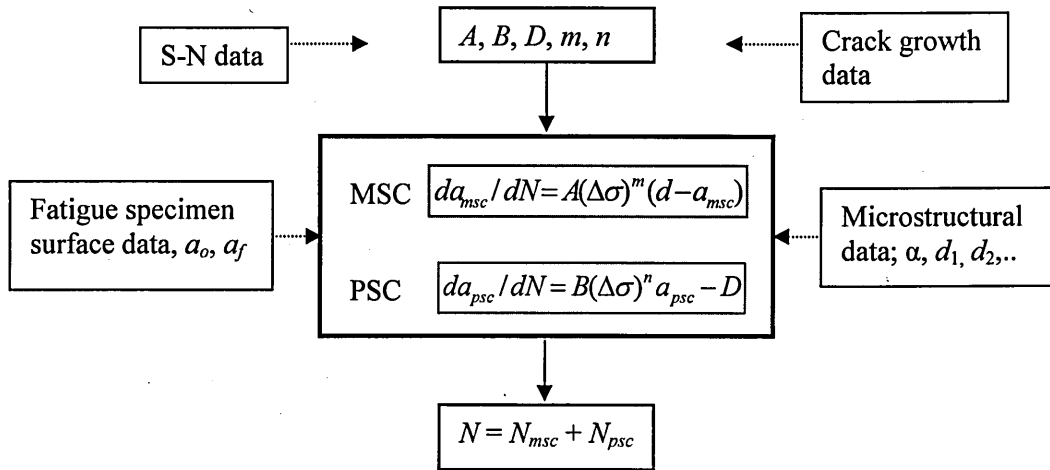


Fig.109: Simple illustration of mathematical model

MATLAB and Microsoft Excel computer software were used to develop the mathematical models to determine the fatigue life of samples. Equations (1) and (2) were used to generate S-N curves and correlate the calculated data with fatigue data obtained experimentally.

The constants A, B, D, m and n are material dependent and are generally determined empirically. In this work these constants were determined using S-N fatigue data obtained experimentally and fatigue crack growth data obtained by surface replication. These constants for MSC and PSC regimes are difficult to determine and needed extensive mathematical iteration procedures. The results obtained from the fatigue model are equated to the experimental data.

7.4.1. Basic Explanation of Steps Followed to Develop Computer Model

Fig.110 is a schematic representation of crack growth pattern considered to develop the crack growth model. The figure shows arbitrary growth transition point from MSC to PSC (a_t) at grain 3. However this transition point varies according to the working stress amplitude, *i.e.* under higher stress amplitudes PSC growth can occur at a lesser grain number as shown in Fig.110.

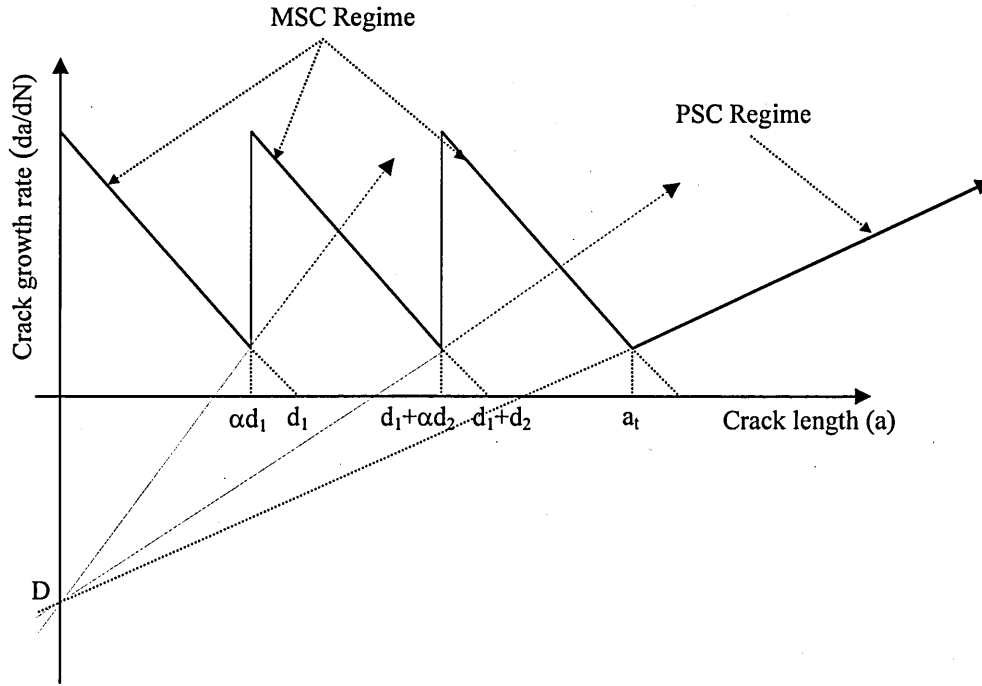


Fig.110: Schematic diagram which represent the MSC and PSC propagation

The main steps of the model are,

Step.1. Considering equation (1) and (2), crack rates of MSC $\left(\frac{da_{msc}}{dN}\right)$ and PSC

$\left(\frac{da_{psc}}{dN}\right)$ growths were calculated.

Step.2. The transition number of grains (*t.grain*) was calculated according to crack growth values.

Step.3. The value of a_t was calculated.

Step.4. The number of cycles sustained in MSC (N_{msc}) and PSC (N_{psc}) regimes are calculated for different stress amplitudes according to the transition point (a_t) determined under step.3.

Step.5. Calculate the total number of cycles ($N = N_{msc} + N_{psc}$) sustained before failure.

7.5. Results

The material constants were determined by theoretical analysis using the computer models developed by Matlab and Microsoft Excel. The values give best fit values for the experimental S-N data obtained from smooth specimen rotary bending fatigue tests.

$$A = 8.9 \times 10^{-7}$$

$$B = 6.585 \times 10^{-27}$$

$$D = 3.99 \times 10^{-3}$$

$$m = 1.01$$

$$n = 7.854$$

The MSC and PSC fatigue crack growth equations for Ti-6Al-4V alloy were derived as,

$$\text{MSC growth: } \frac{da}{dN} = 8.9 \times 10^{-7} (\Delta\sigma)^{1.01} (d - a)$$

$$\text{PSC growth: } \frac{da}{dN} = 6.585 \times 10^{-27} (\Delta\sigma)^{7.854} a - 3.99 \times 10^{-3}$$

Units of the parameters are, da/dN in $\mu\text{m}/\text{cycle}$, $\Delta\sigma$ in MPa , a and d in μm .

8.1. Introduction

The main issues discussed in this chapter are;

1. The fatigue failures in hip implants, locations of failures, possible reasons and other important features under in-vivo failure.
2. Fatigue performance of Ti-6Al-4V based on the results obtained in Phase.1 including; variation of fatigue limit due to the change of surface roughness and residual stress levels; mean stress and stress ratio effect on fatigue limit; development of K-T plots to identify the operational 'safe' region.
3. Fatigue performance based on the results obtained in Phase.2 including; variation of fatigue limit at each manufacturing stage; fractographic analysis conducted on fracture surfaces at initiation and propagation sites; influence of manufacturing practices and details of in-vivo failures.
4. Development of K-T plots using Phase.2 results to gain an awareness of the maximum safe working stress amplitudes for given defect sizes at corresponding stages of Routes 1, 2 and 3.
5. The relationship between fatigue limit (F_L), surface roughness (S_R) and residual stress (R_S) and the development of a mathematical model between these three parameters based on the fatigue results for both Phases.1 and 2.
6. Accuracy of the crack growth model equation developed to calculate the fatigue life (presented in Chapter 7).
7. Fatigue failures observed in the very high cycle region.

8.2. In-Vivo Failure Analysis of Hip Implants

Cone and neck areas were identified as the only locations where fatigue failures occur in hip implants. Further information regarding this is given in Chapter 2 and more specifically in Chapter 3, where the failure distributions related to each failure location are discussed. For simplicity in discussion the service life of implants for both cone and neck failures are divided into three regions as, (i). low life failures (LL) where, service life $< 2\text{yrs}$, (ii). medium life failures (ML) where, $3\text{yrs} < \text{service life} < 6\text{yrs}$, and (iii). high life failures (HL) where, service life $> 7\text{yrs}$.

8.2.1. In-Vivo Failures at the Cone Region

The failure distribution (service life vs. implanted year) is shown in Fig.62 in section 3.2.2.2. Fig.111 shows the number of cone failures recorded within each year after implantation.

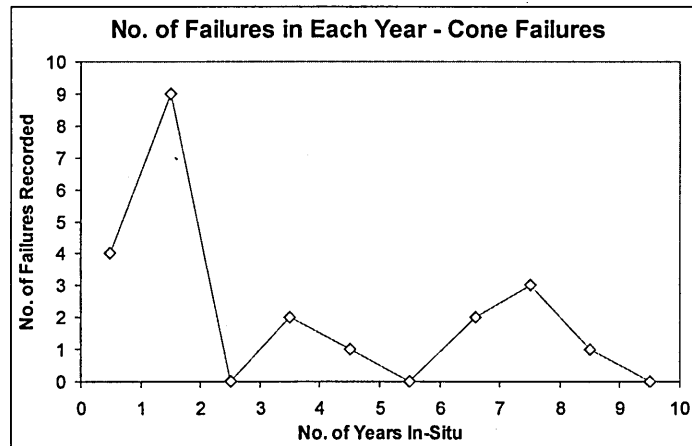


Fig.111: Number of failures occurred in each year within 10 years service life.

Low life failures: LL failures with a service life below 2 years can be found at least one per year continuously over the period analysed and these are irrespective of blended or non blended designs. Fig.111 indicates most failures have occurred in the LL region, amounting to about 65% of total failures. Out of these failures 41% occur in 9mm stems, 47% in 10mm stems and the rests in 12mm stems. This mixture of commonly used hip implants implies that failures are not dependent on the size of the implant. It is further

suggested that the design modification has no effect for LL fatigue failures, as failures kept on occurring even after the modification and irrespective of the implant size. The failure reports (refer Appendix.1) indicate that some of the failures (<2years in-vivo) initiate at surface features such as notches and inclusions, as shown in the Fig.112, a, b and c. However fatigue initiation occurs not only because of surface features. In the blended design flagpole loading creates loads that are sufficiently high to initiate failure. Finite element stress analysis see Fig.40 (section 2.9.3), also confirms the maximum stress is at the cone area when the stem is fixed at distal region. Failure at the cone will not occur unless this condition is met.

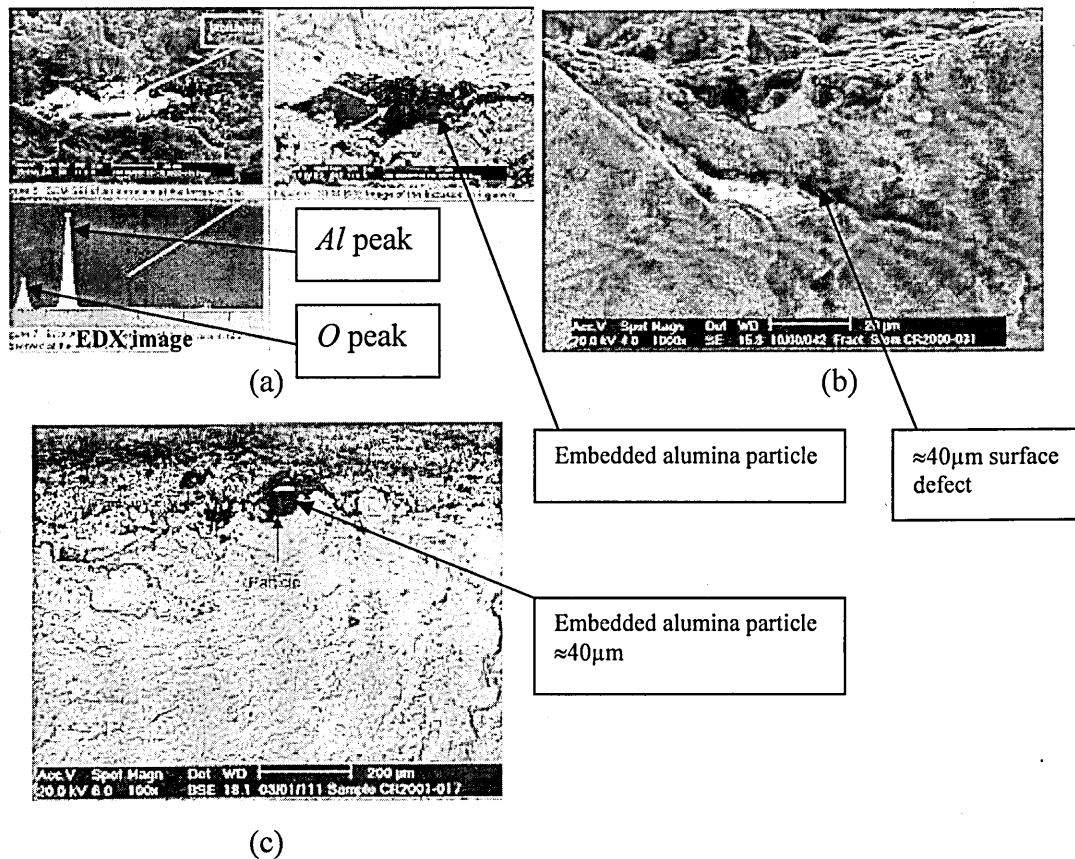


Fig.112 : Initiation features of selected cone failures (a) service life - 1y 6m, (b) service life - 2y, (c) service life - 1y [163].

Medium and high life failures: Only 3 failures occurred in the ML region. Out of these 1 is a non-blended design and 2 are blended design stems. 23% of failures occurred in the HL region and all of these failures are non-blended type designs. There are no failures recorded for blended stems in HL region. It is not clear and too early to conclude that the design change has eliminated these failures. Since the modification

has eliminated the possible stress-raiser on the surface, there is a possibility of enhancing the service life of HL failures to extend beyond 10 years.

Explants failed at the cone region show little evidence of proximal fixation, as shown in Fig.113 a, b, c and d, resulting in flagpole fixation within the distal region. In such a case the highest bending moment acts on the cone region and this can be an influential factor for cone failures.

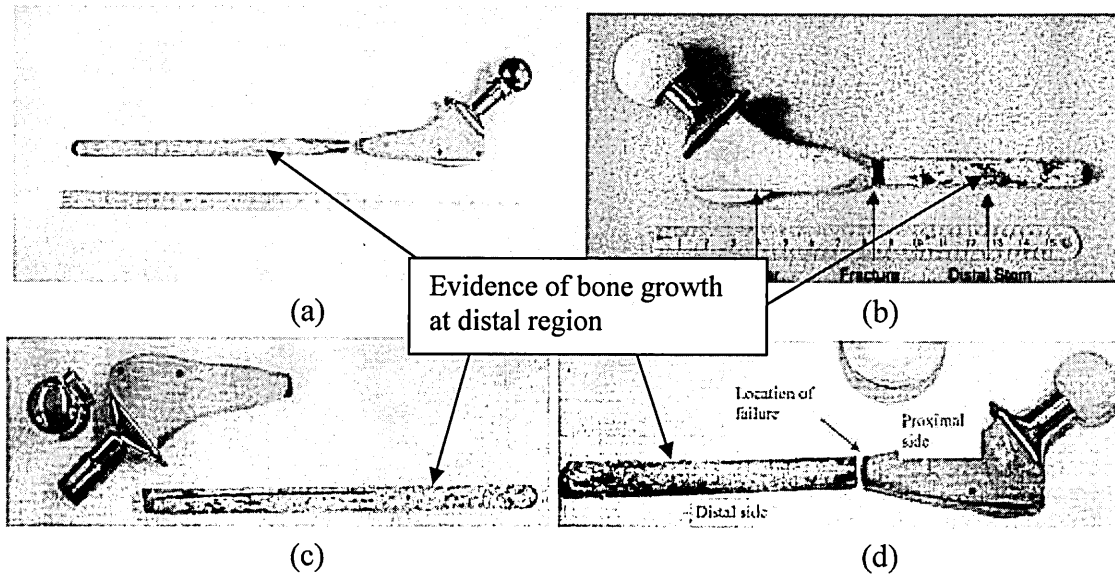


Fig.113 : Integration of the implants with the bone of selected cone failures, evident of little or no bone growth in the proximal region, (a) service life - 2y, (b) service life - 1y, (c) service life - 1y 6m, (d) service life - 1y 2m [163].

It is understood that the stem part is designed to have secure proximal fixation with the bone. There are various reasons such as, surgical mistakes, poor bone quality and bone infection, which influence fixation of the implant to the bone. The activity level of the patient may also affect fixation and potentially fatigue initiation. Therefore it is difficult to assign one clear reason to these cone failures.

A summary of important factors related to in-vivo stem failures at the cone area are given in Appendix.1.

8.2.2. In-Vivo Failures at the Neck Region

The failure distribution (service life vs. implanted year) is shown in Fig.66 (section 3.2.3.2). Fig.114 shows the number of neck failures recorded each year after implantation.

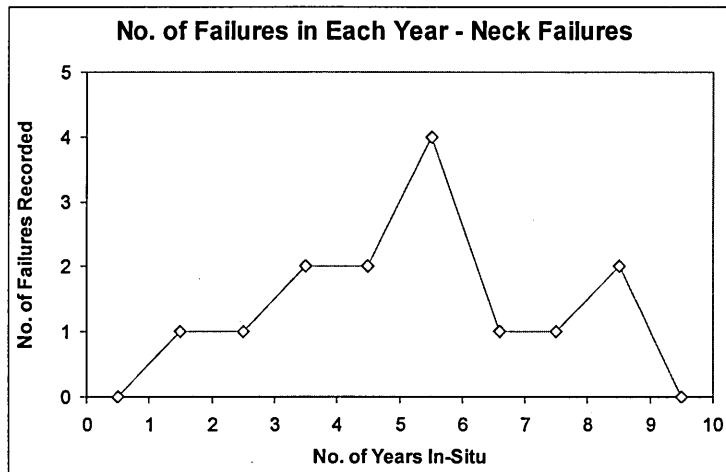


Fig.114: Number of neck failures occurred in each year within 10 years service life.

The distribution of neck failures (see Fig.66) consists of all sizes of stems *i.e.* 9mm, 10mm, 12mm and 14mm and the dimension of the neck area in each of these stem are the same. Therefore it is suggested that the neck failures are also not dependent upon the size of the implant.

As shown in Fig.114, 67% of the failures have occurred in ML region where service life is between 3 to 7 years. The remaining failures are; 13% in LL region and 20% in HL region. Generally neck region failures have an average service life of around 5 years.

As explained in Chapter 3 the design modification has increased the diameter of the critical area where failures occur, from 13.15mm to 14.3mm. This represents an 8.7% increase of the diameter and results in a 22.2% reduction in applied stress at the surface. The reduction of applied stress definitely prolongs the fatigue life and has a significant positive impact on fatigue performance in the neck area of the stem highlighting the possibility of eliminating neck failures.

Explants failed at the neck region show a firm proximal and distal fixation with the femoral bone as shown in Fig.115. In such a case the highest bending moment acts on the neck region and this can be an influential factor for neck failures. Under proximal fixation condition the neck area is the only possible area of the stem in which a fatigue failure may take place.

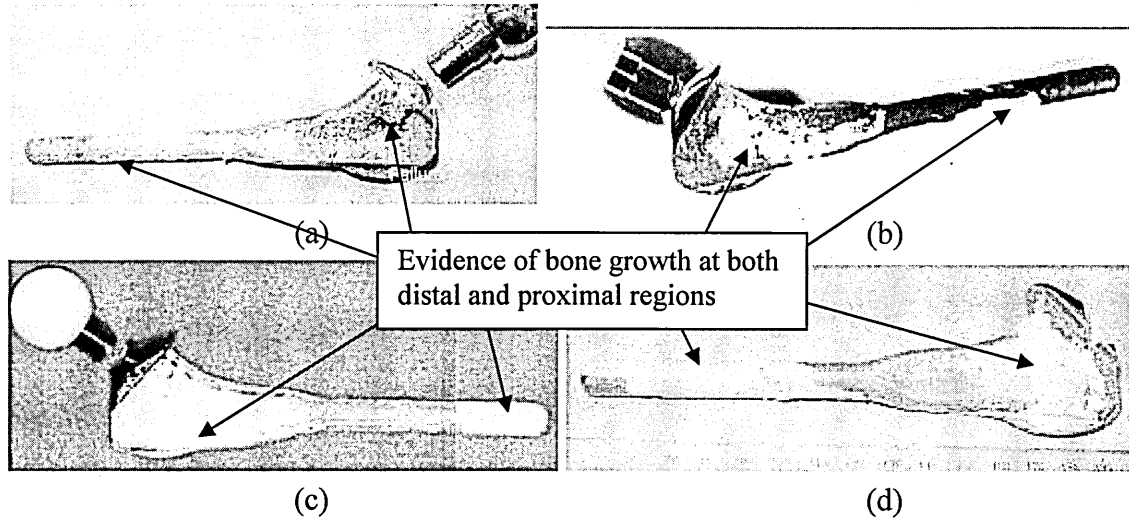


Fig.115: Integration of the implants with the bone of selected neck failures, evidence of firm fixation at the proximal region, (a) service life - 2y, (b) service life - 1y, (c) service life - 1y 6m, (d) service life - 1y 2m [163].

A summary of important factors related to in-vivo stem failures at neck area is given in Appendix.2.

8.3. Fatigue Tests Under Phase.1 - The Materials Characterization of Ti-6Al-4V

Fractographic investigations conducted using SEM and optical microscopy verified that, for all test conditions, fatigue cracks initiated at the sample surface. Therefore any changes in the fatigue performance could be directly related to the surface and near surface properties, such as surface roughness/defect size and surface residual stress.

8.3.1. Variation of Fatigue Limit with Surface Roughness and Surface Residual Stress Values

The fatigue test results and relevant residual stress and surface roughness values under Phase.1 tests are given in Chapter 6. The variation of fatigue limit vs. residual stress and the surface roughness is shown in Fig.116. Before annealing (*WA* samples) the residual stresses in the samples are compressive and after annealing these stresses become tensile, which will significantly influence the possibility of fatigue initiation and subsequent propagation. Fig.116 clearly shows the reduction of fatigue performance after annealing at each surface roughness condition (noted within square brackets), which results purely due to the variation of residual stress within the samples. Note: annealing causes the residual stresses to change without any change to the surface roughness.

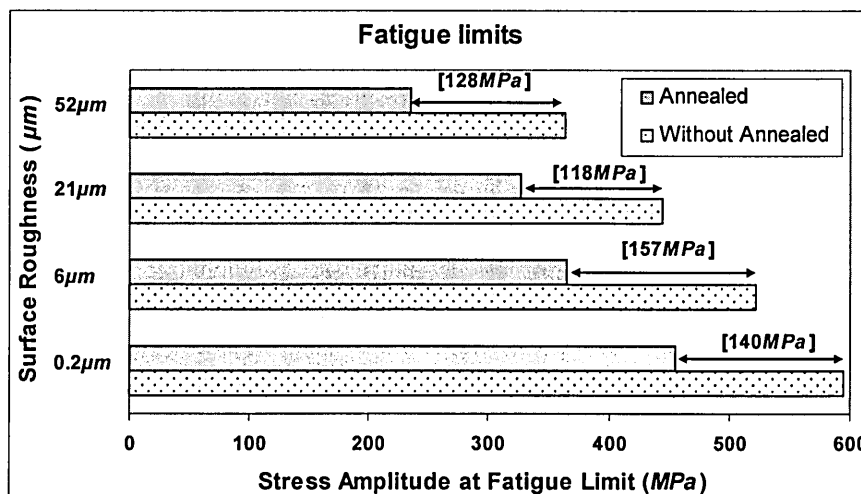


Fig.116: Variation of fatigue limit due to the change of surface residual stress.

Note: variations of fatigue limits are noted in square brackets.

8.3.2. Residual Stress or Mean Stress Effect to Fatigue Performance of Ti-6Al-4V

In rotary bending fatigue tests it is assumed that the sample undergoes a load cycle of zero mean stress ($\sigma_m = 0$) with -1 stress ratio ($R = -1$). However due to the existence of residual stresses the $\sigma_m \neq 0$, and equals to the magnitude of residual stress. The stress ratio (R) is also not -1.

Consider a rotating bending fatigue test running at stress amplitude of σ_a , and the surface residual stress of the test sample is R_s . The schematic diagram of actual load cycle is as shown in Fig.117.

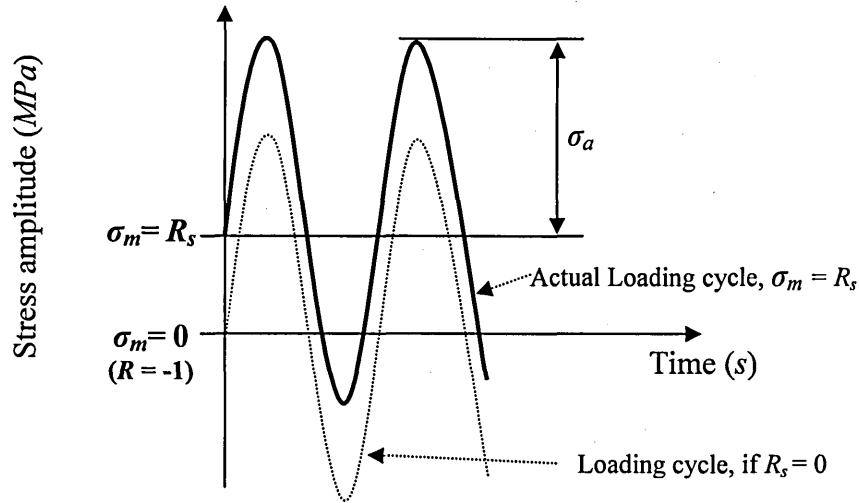


Fig.117: Variation of mean stress with residual stress

Goodman's criteria given in equation (6) (see section 2.5.6.) can be used to determine the stress amplitude at the fatigue limit (σ_a) for $R = -1$ ($\sigma_m = 0$).

Stress ratio R can be defined as.

$$R = \frac{\sigma_m + \sigma_a}{\sigma_m - \sigma_a} \quad (31)$$

From equation (6) and (31), σ_a at R stress ratio, can be derived as,

$$\sigma_a = \frac{S_u S_e (1 - R)}{S_e (1 + R) + S_u (1 - R)} \quad (32)$$

where S_e is the fatigue limit and S_u is the tensile strength. Using equation (32), the stress amplitude at fatigue limit (σ_a) can be found for any given stress ratio (R).

If the stress amplitude (σ'_a) at the fatigue limit is known for samples having a certain residual stress R_s , the stress amplitude at fatigue limit for any stress ratio (R) can be derived using equations (6) and (32) as,

$$\sigma_a = \frac{\sigma'_a S_u (1 - R)}{\sigma'_a (1 + R) + (S_u - R_s)(1 - R)} \quad (33)$$

At any instance if the residual stress value (R_s) is known and the stress amplitude at the fatigue limit at that instance (σ'_a) is known, the stress amplitude (fatigue limit) for any given R value can be calculated using equation (33).

The fatigue limit at $R = -1$ (eliminating the effect of residual stress) is calculated using equation (6), and the results are tabulated in Table.15. The main reason for this analysis is to understand the effect of surface roughness on the fatigue performance of Ti-6Al-4V.

Surface roughness (μm)	Anneal status	Rotating bending fatigue test results (MPa)	Calculated fatigue limit at $R = -1$ (MPa)
0.2	Without Annealed	595	455
	Annealed	455	485
6	Without Annealed	522	418
	Annealed	365	421
21	Without Annealed	444	368
	Annealed	326	388
52	Without Annealed	363	302
	Annealed	235	284

Table.15: Calculated fatigue limits for $R = -1$.

Fig.118 shows the variation of fatigue limits for different surface roughness conditions. Since the fatigue values are calculated at $R = -1$ and for zero mean stress, the variation of the fatigue limits represent the effect of surface defect size.

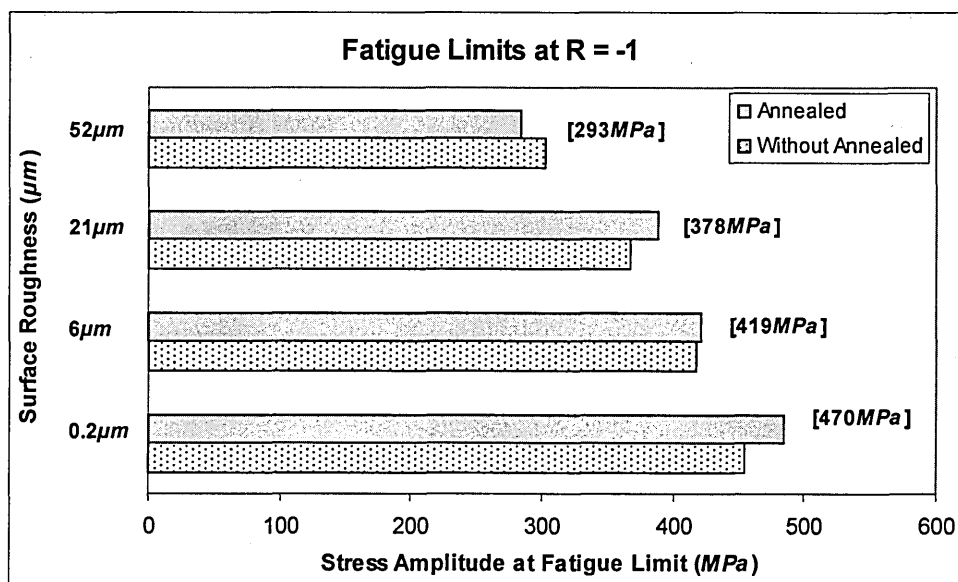


Fig.118: Calculated fatigue limits for $R = -1$. Average fatigue limits of both WA and A condition at each roughness level are noted within square brackets.

8.3.3. Effect of Stress Ratio to Fatigue Performance of Ti-6Al-4V

The fatigue limits for positive stress ratio (at $R = 0.1$) has also been calculated for comparison purposes using equation (33) and are shown in Table.16 for both annealed and non-annealed conditions, at $R = 0.1$. The calculated fatigue limits for $R = 0.1$ are illustrated in Fig.119.

Surface Roughness	Fatigue limit at $R = 0.1$ (MPa)	
	Without Annealed	Annealed
0.2 μm	295	307
6 μm	278	280
21 μm	255	265
52 μm	222	212

Table.16: Calculated fatigue limits at $R = 0.1$.

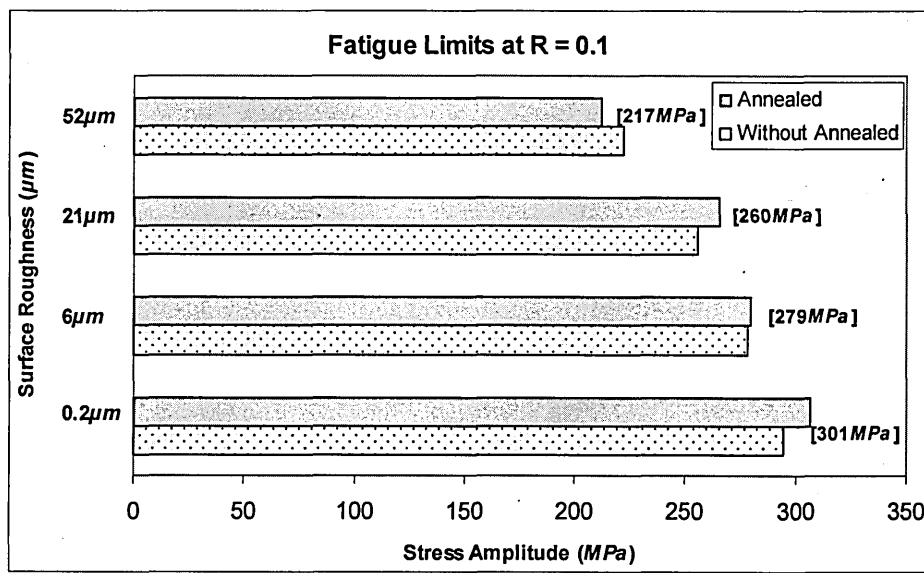


Fig.119: Calculated fatigue limits for $R = 0.1$. Average fatigue limits of both WA and A condition at each roughness level are noted within square brackets.

8.3.4. Representation of Results in the Form of K-T Plots

On the basis of S-N data obtained from experiments, the K-T type plots for Ti-6Al-4V are developed using equations (7) and (9). These diagrams define the variation in the stress amplitude to cause fatigue failure in Ti-6Al-4V alloy as a function of crack size. The safe region is sensitive to working stress ratio, and K-T plots have been plotted to assess variations in the safe region. K-T plots representing different stress ratios can be developed using Goodman's criteria, *i.e.* equation (6) and equation (33). The value of the threshold stress intensity factor (ΔK_{th}) can be calculated by applying a linear regression analysis to a plot of a versus $\Delta\sigma_{th}^{-2}$, using equation (9). The value of the geometrical factor, Y , is approximated as unity [186, 187, 188]. Values of Y for specific crack configurations and loading conditions can be found in [189, 190].

The K-T diagrams for without annealed (WA) and annealed (A) conditions are shown in Fig.120. The threshold stress intensity factor for the WA and A conditions are $5.9 \text{ MPa}\sqrt{m}$ and $3.55 \text{ MPa}\sqrt{m}$ respectively. This compares favourably with literature values of $5 - 6 \text{ MPa}\sqrt{m}$ [86]. When the crack length reaches around $100\mu\text{m}$ the propagation behaviour approaches that of long cracks. The reduction of the safe working envelope of annealed samples is due to the change of surface residual stress,

which changes from compressive to tensile following annealing. The threshold stress amplitude for microstructural fatigue cracks reduces from 595MPa to 455MPa due to annealing. The importance of residual stress level in fatigue performance, in particular the positive impact from compressive residual stresses can be observed in Fig.120.

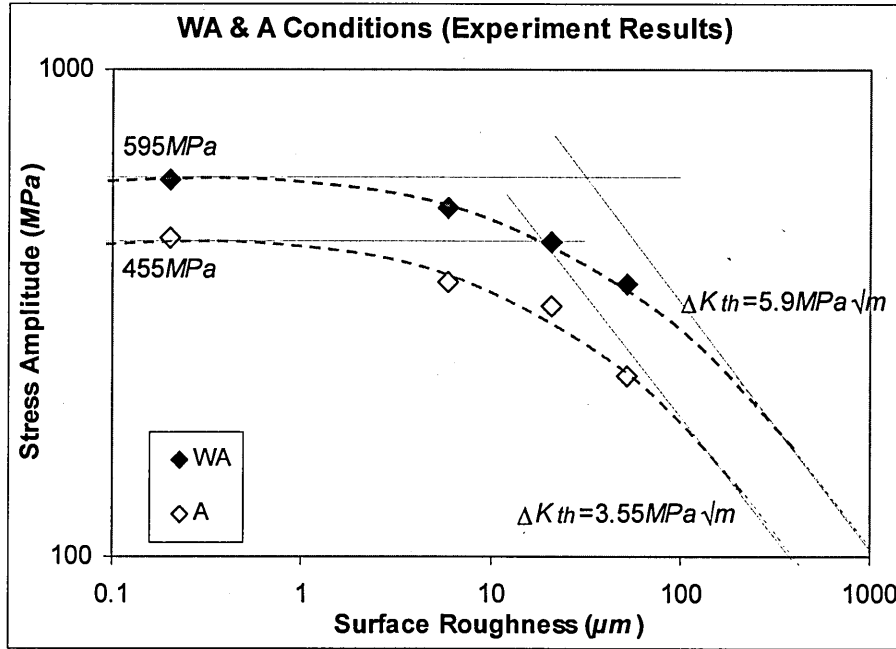


Fig.120: K-T type diagram showing the estimated threshold stresses for *WA* and *A* conditions.

Fig.121 shows the variation in 'safe' regions for *WA*, *A* and $R=-1$ conditions. The calculated fatigue limits for $R=-1$ are given in Table.15 and illustrated in Fig.118. The variations of the K-T plots for components with compressive residual stress (*WA* condition), zero residual stress ($R=-1$ condition) and tensile residual stress (*A* condition) are clearly illustrated in Fig.121. The value of a_o can be calculated at $R=-1$ using equation (10), as $33.1\mu\text{m}$.

The comparison of K-T type plots for $R = -1$ and $R = 0.1$ is shown in Fig.122. The calculated fatigue limits for $R=0.1$ are given in Table.16 and illustrated in Fig.119. A clear reduction of smooth specimen threshold stress amplitude (MSC) and the safe working stress amplitudes for different crack lengths can be observed. The threshold stress intensity factor (ΔK_{th}) can be calculated as $4.8\text{MPa}\sqrt{\text{m}}$ for $R=-1$ condition and $4\text{MPa}\sqrt{\text{m}}$ for $R=0.1$ conditions. Other researchers [11, 64, 84] investigating the fatigue

crack growth in Ti-6Al-4V show the ΔK_{th} value at $R=0.1$ is around $4 \text{ MPa}\sqrt{m}$, which shows good agreement between the experiments and the cited values within the literature.

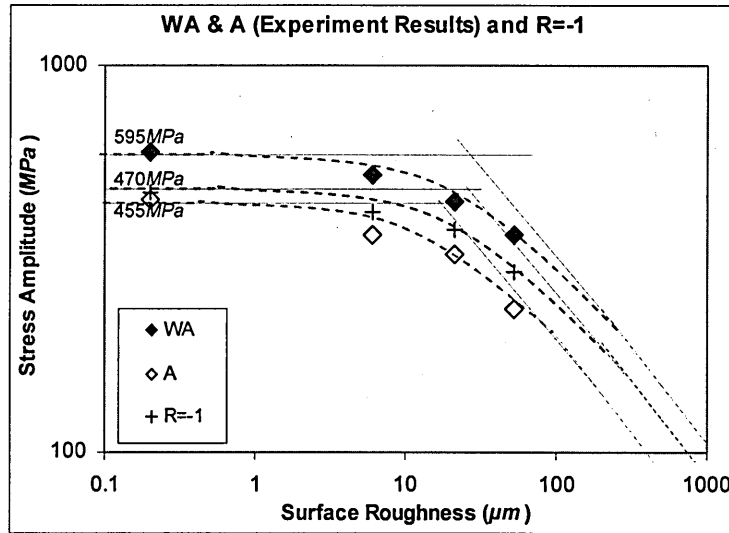


Fig.121: K-T type diagrams at WA , A and at $R = -1$ conditions.

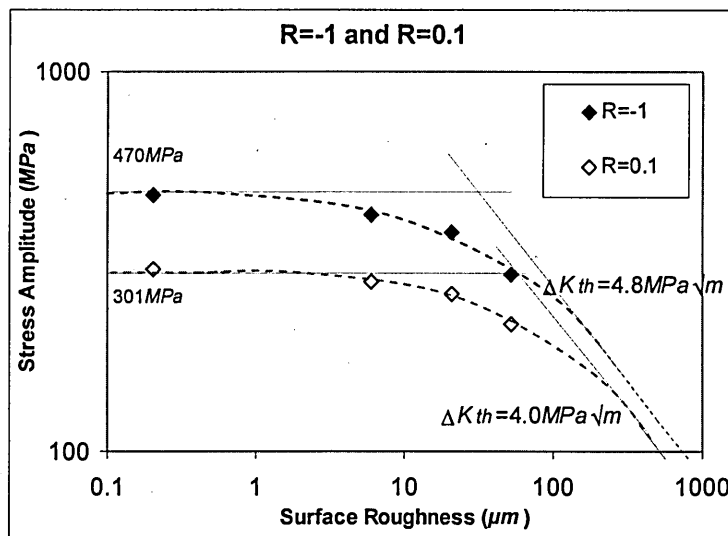


Fig.122: K-T type diagrams at $R = -1$ and at $R = 0.1$ conditions.

For known flaw sizes, these diagrams allow quantitative evaluations of the risk of premature fatigue failures of the components to be made.

8.4. Fatigue Tests Under Phase.2 – Characterization of Manufacturing Processes

8.4.1. Discussion on Fracture Analysis and Variation of Fatigue Limit of Stages in Route.1 (Manufacturing cone region of precision forged stems)

Any mechanical surface treatment such as polishing, blasting, turning, rumbling, generally leads to an increase in the dislocation density in the surface layers. Due to the localized plastic deformation residual micro-stresses are developed and the surface topography is changed, which may have an influence on the fatigue strength. The results obtained from fatigue tests representing each manufacturing stage have been used to evaluate the variation of fatigue strength due to individual operations. Fractography examination was also carried out at each stage to evaluate the effect of surface features on fatigue initiation. The variation of the fatigue limit at each manufacturing process is discussed in section 6.5.1. Each stage of the three routes is discussed in this chapter giving consideration to fatigue performance and fractographic investigation.

Route.1 / Stage.A (*machined – annealed*): The fatigue limit at this stage is 365MPa.

Surfaces of samples from this stage contain uniformly distributed machining marks along cutting tool paths as shown in Fig.123(a). These marks appear as transverse grooves, which have influenced the initiation of failures and these features influence the propagation direction along the outer surface and fatigue cracks are found running along the base of the groove. In each case initiation is not found at a single point but rather from a 50 μ m to 100 μ m length along the machining path. These cracks later propagate and coalesce to form a single dominant crack. Small surface cracks like tear marks are distributed between adjacent tool paths appearing on most of the fracture samples, as shown in Fig.123(b). Small cracks can influence the crack to jump from one tool path to another to keep the crack front within the high stressed area. All samples manufactured with the as-machined condition failed due to fatigue crack initiation from a machining mark as per the data in the Appendix.13; which provides more fractography results and a summarized description about this stage.

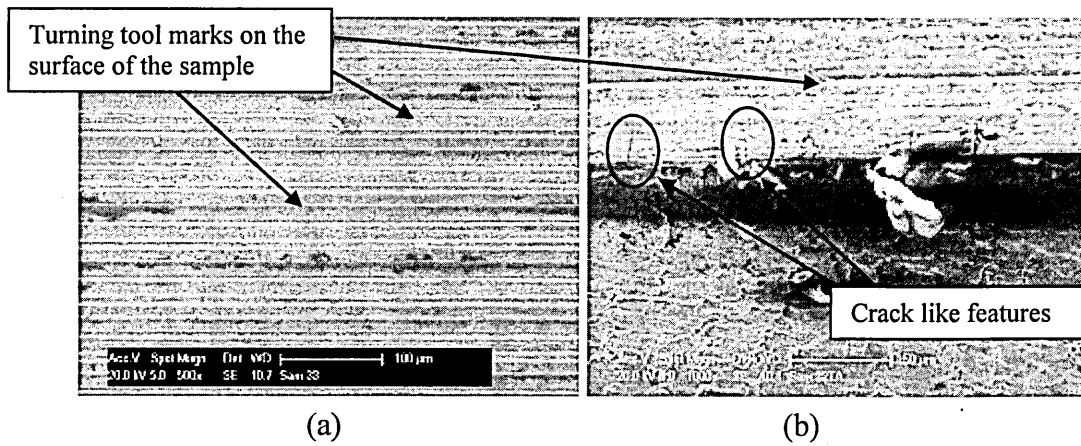


Fig.123: (a) Surface of a sample at Route.1/ Stage.A (Sample No.33), (b) Fatigue initiation region of Sample No.32.

Route.1 / Stage.B (*machined – annealed - rumbled*): The fatigue limit at this stage is 585MPa ; an increment of 220MPa from Stage.A.

Surface scratch marks and circular dent like features can be commonly found on the surface as shown in Fig.124(a). These features are the result of the blasting/rumbling process. The average (R_p+R_v) of the surface is $4.1\mu\text{m}$ with the depths of some of these dents ranging from about $30\mu\text{m}$ - $50\mu\text{m}$, as shown in Fig.124(b). These features can remain on the surface of finished implants and initiate failure. In actual stems these feature have minimum influence with respect to neck failures because the neck region always undergoes a machining operation after blasting/rumbling. However they can significantly influence cone failures in implants. Actual in-vivo ex-plants initiation regions can be found with dents, which remain underneath the coatings (see Fig.112(b). It is possible that these features (dent, scratch mark, notch) are the cause of initiation for cone failures where there is no observed foreign particle.

The increment of the fatigue limit by 220MPa is mainly due to the introduction of compressive residual stresses to the component by the rumbling process. Here the change in residual stress status is from $+136\text{MPa}$ (tensile) to -431MPa (compressive). More fractography results and a summarized description about this stage is given in Appendix.14.

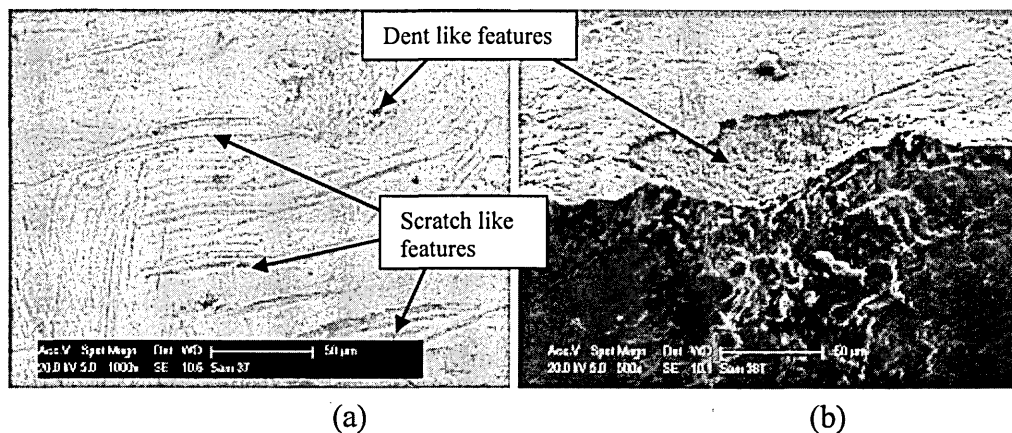


Fig.124: (a) Surface of a sample (Sample No.37) at Route.1, Stage.B, (b) Fatigue initiation region of Sample No.38.

Route.1 / Stage.C and Stage.D (*machined – annealed - rumbled - grit blasted - ultrasonic cleaned*): Fatigue limit at this stage is 523MPa ; a reduction of 62MPa from Stage.B.

After grit blasting the stems undergo an ultrasonic cleaning stage. According to the fatigue results there is no difference in fatigue limit of grit blasted samples to ultrasonic cleaned samples. Therefore both processes are investigated together. The surface of grit blasted samples contains embedded particles rich in aluminium and oxygen. These particulates can be found even in ultrasonically cleaned samples (Stage.D), as shown in Fig.125(a). One failed sample shows failure initiation is influenced by particles rich with *Al* and *O* as shown in Fig.125(b). EDX analysis shows that the *Al* quantities are larger than expected for this type of alloy and these particulate inclusions can be clearly identified in backscatter images, since they appear as dark areas (lower atomic mass). These alumina particles can remain embedded in the Ti / Ti-6Al-4V interface. Also dent like defects as shown in Fig.125(c) were found at the initiation areas of two failed samples. Note: the aspect ratio to the defects found in previous rumbling stage (Stage.B) were similar. These are thought to be defects remaining from the previous rumbling operation. At this stage the surface is highly irregular.

The grit blasting process is very important and controls the adhesion behaviour of any subsequent coating, as described in Chapter 2. Since the primary adhesion mechanism is mechanical 'keying' of the coating to the substrate surface it is important to have correct surface roughness with a lot of peaks, valleys and hook shaped profiles, to enhance

adhesion. However the main problem is that the process leaves embedded blasting media particles which diminish the fatigue life of the component. It is necessary to understand the process parameters such as media size, angle and distance of the blast, which will minimize the quantity of embedded particles but at the same time, optimize coating adhesion. Evans *et. al.* [28] observed that Ti-6Al-4V samples prepared by bead blasting and vacuum plasma (VP) coated have about $156MPa$ increment in fatigue limit above the grit blasted and VP coated samples, as shown in Fig.57. Further investigation is however needed to understand the effect on the adherence of the coating, which is of paramount importance to the performance of the implant.

Creation of a rougher surface with stress-raisers and also reduction of compressive residual stresses can cause a reduction of the fatigue limit. In this case a reduction in fatigue limit of $62MPa$ moving from Stage.B. More fractography results and a summarized description about this stage is given in Appendix.15.

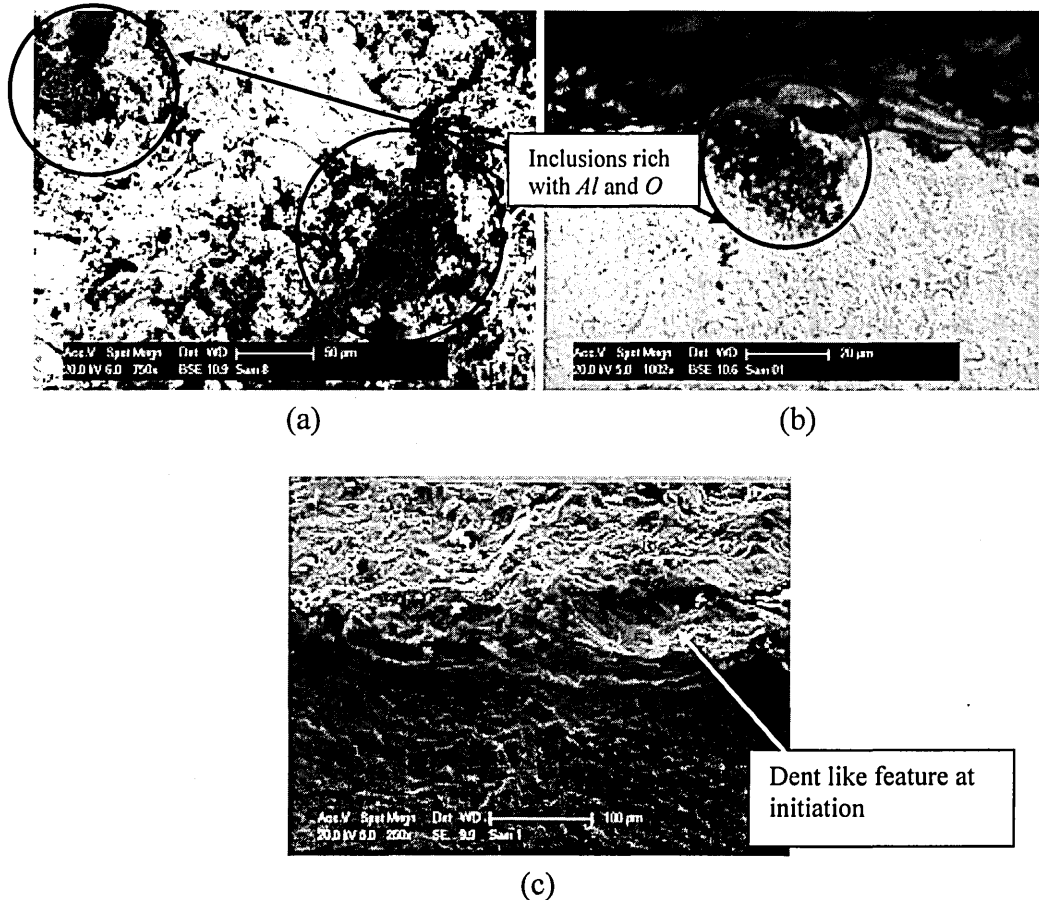


Fig.125: (a) Surface of a sample (Sample No.8) at Route.1, Stage.D/C, (b) Fatigue initiation region of Sample No.1, (c) Defect found at the initiation area of Sample No.7.

Route.1 / Stage.E (*machined – annealed – rumbled – grit blasted – ultrasonic cleaned – Ti coated*): The fatigue limit at this stage is 517MPa; a reduction of 6MPa from Stage.D.

Fracture surfaces indicate fatigue failures initiated at the Ti and Ti-6Al-4V interface. The failures nucleated at the interface and propagated by a dominant single crack. Step like features near initiation can be seen in Fig.126(b). This is a common feature in most of the Ti coated and H-AC coated test specimens and actual in-vivo stem failures where failure occurs at the cone region.

The surface of the sample shown in Fig.126(a) is rough and globules of Ti can be seen. The roughness of the sample surface appears to have no direct effect on fatigue initiation since fatigue crack nucleation always occurs at the Ti / Ti-6Al-4V interface. The surface of the Ti layer consists of tiny cracks as shown in Fig.126(a). Sub-surface separation between Ti-6Al-4V and Ti layer can be seen in Fig.126(b) and also dent like feature can be seen in Fig.126(c). These dent like features are probably introduced at the rumbling or grit blasting stages. XRD measurements reveal the residual stress at the surface of Ti coating is almost zero. Since the fatigue initiation is taking place at the Ti / Ti-6Al-4V interface the residual stress value at the surface of the coating is immaterial, and does not represent the actual residual stress status at the Ti and Ti-6Al-4V interface.

According to the fatigue tests results the Ti coating process does not have much affect on the fatigue performance. The fatigue limit is almost equal (only 6MPa difference) to the grit blasted samples. Additional fractography results and a summarized description about this stage is given in Appendix.16.

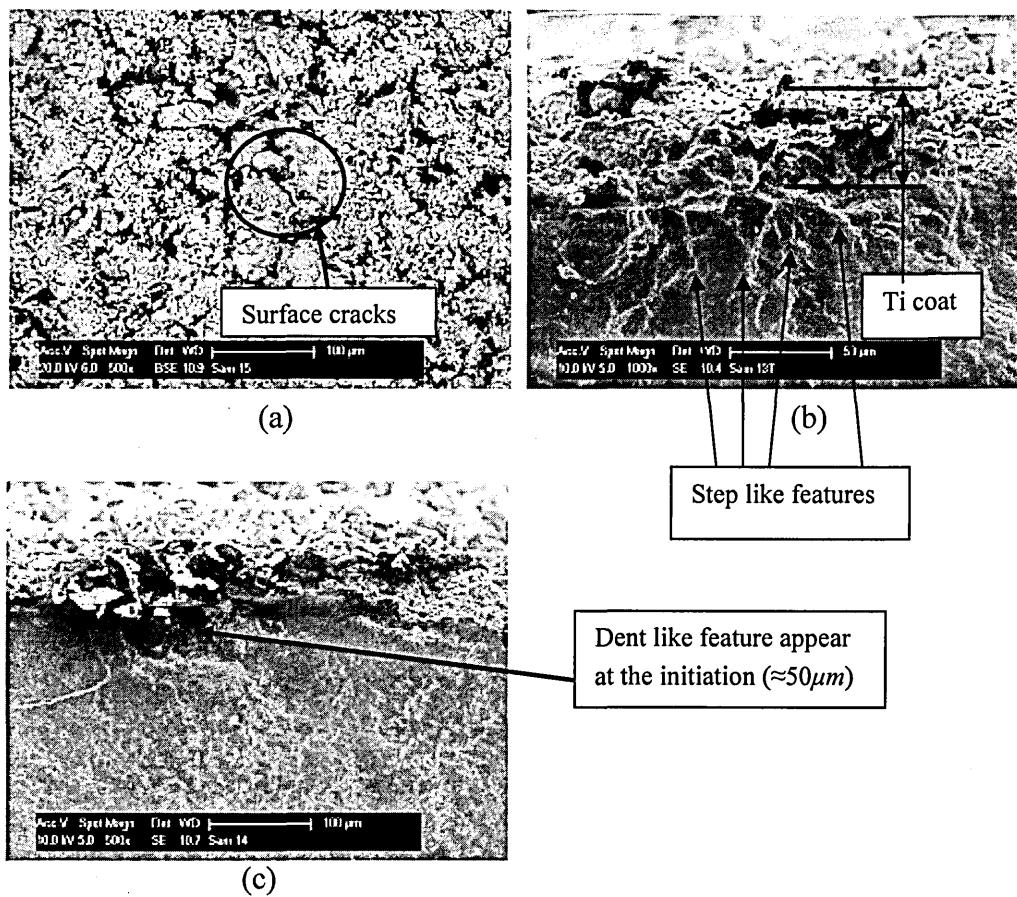


Fig.126: (a) Surface of a sample (Sample No.15) at Route.1, Stage.E, and fatigue initiation regions of samples; (b) Sample No.13, (c) Sample No.14.

Route.1 / Stage.F (machined – annealed - rumbled - grit blasted - ultrasonic cleaned - Ti coated - H-AC coated): The fatigue limit at this stage is 410MPa; a reduction of 107MPa from Stage.E.

As in the case of Stage.E, the fatigue nucleation sites indicate dominant single initiation area, which is quite a common feature in actual stem failures at the cone region. EDX spot analysis shows two failed samples having embedded alumina (Al_2O_3) particles at the Ti / Ti-6Al-4V interface near fatigue crack nucleation region, possibly as a result of the grit blasting process, as shown in Fig.127(b).

Surface cracks are visible in the H-AC coatings as shown in Fig.127(c). These cracks which originate from the surface of the coating seem to propagate towards the substrate and then along the substrate coating interface allowing delamination of the coating from the substrate, which is evident in Ti and H-AC coated samples as shown in Fig.127(a).

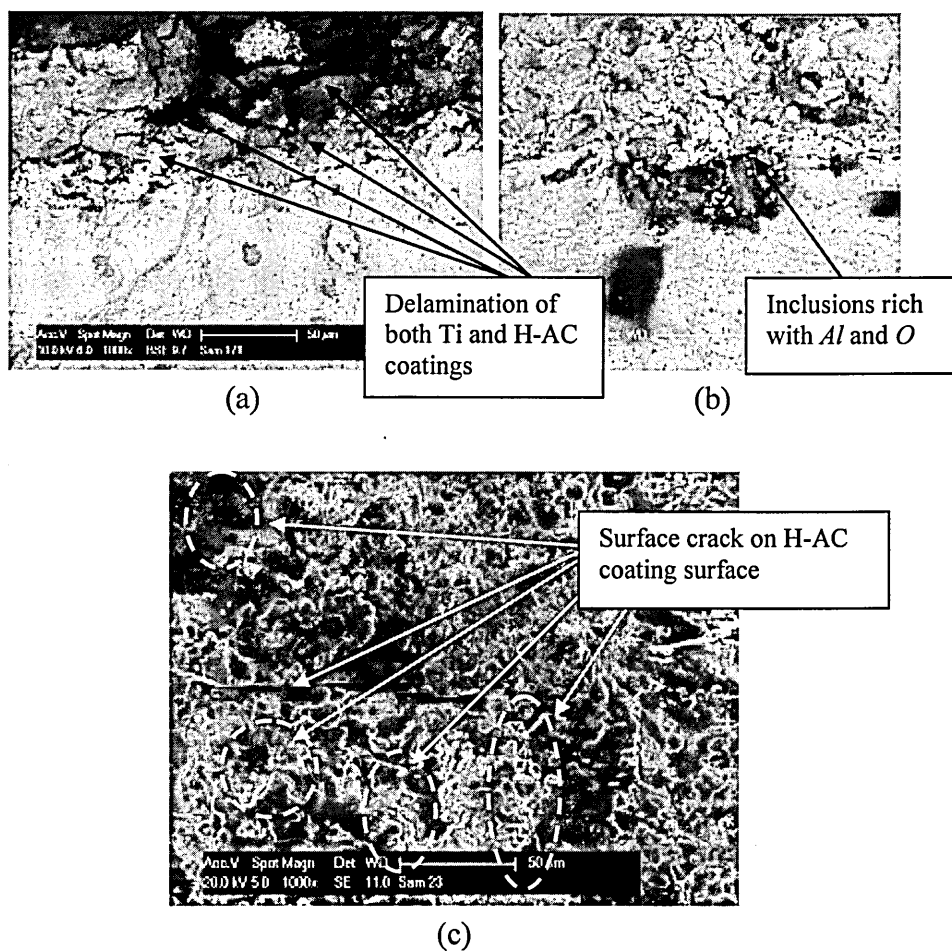


Fig.127: Fatigue initiation region of samples; (a) Sample No.17, (b) Sample No.18 and (c) surface of H-AC coating (Sample No.23)

The introduction of the H-AC coating process significantly reduces the fatigue limit; a reduction of 107MPa compared to the Ti coated samples. Reasons for this reduction following the plasma sprayed H-AC process may be, (i) a reduction in hardness at the substrate and, (ii) introduction of tensile residual stresses [181]. The residual stress level of the surface layer may change for two reasons [181], (i). cooling of spray particles from their solidification temperature and, (ii). differences between the thermal expansion coefficients values of coating and sub-surface material. It has been reported in the literature that the plasma spray process induces tensile residual stresses in the coating substrates [182]. Also the variation of residual stress can affect the adhesion of the coating to the substrate. It is noted that the higher the coating adhesion the higher the fatigue strength [130]. If the H-AC coating process introduces tensile residual stress within the substrate, as shown in Fig.55 [67] and Fig.56 [137], it will clearly reduce fatigue crack initiation resistance thereby reducing the fatigue strength. Evans and Gregson [28] identified small cracks in the base metal in grit blasted and plasma sprayed samples (see Fig.54). If this is the case such features also contribute to the

reduction of the fatigue limit. Further fractography results and a summarized description about this stage is given in Appendix.17.

Route.1 / Stage.G (*machined – annealed - rumbled - grit blasted - ultrasonic cleaned - Ti coated - H-AC coated - annealed*): The fatigue limit at this stage is 218MPa; a reduction of 192MPa from Stage.F.

Fatigue crack nucleation and propagation is mostly similar to Ti coated (Stage.E) and H-AC coated (Stage.F) specimens.

The annealing process significantly reduces the fatigue limit of the H-AC coated samples. Since the samples have only been annealed there is no change in the physical surface condition of the samples therefore only the residual stress condition will lead to a change in fatigue limit. This is the result of the introduction of tensile residual stresses at the Ti / Ti-6Al-4V interface.

Separation of layers can be seen in all the samples and traces of inclusions rich in *Al* and *O* can be seen at the initiation site of one sample, as shown in Fig.128(a) and (b) respectively. Further fractography results and a summarized description about this stage is given in Appendix.18.

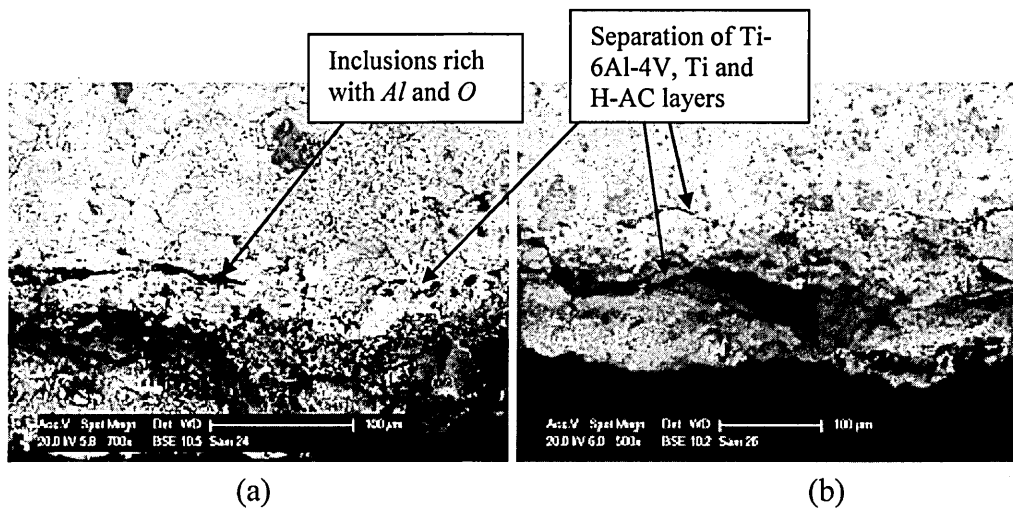


Fig.128: Fatigue initiation region of samples; (a) Sample No.24, (b) Sample No.26.

8.4.2. Discussion on Fracture Analysis and Variation of Fatigue Limit of Route.2
(Manufacturing cone region of stems forged to oversize, mainly revision stems)

The variation of the fatigue limit along Route.2 is illustrated in section 6.5.2.

Route.2 / Stage.B (annealed – machined): The fatigue limit of the machined samples is 682MPa (The highest value in Route.2).

As discussed for Route.1 Stage.B, surfaces at this stage contain uniformly distributed machining marks along cutting tool paths as shown in Fig.129(a). Fracture surfaces for samples 40 and 41 are shown in Fig.129(b) and (c) respectively. These images show that crack initiation occurs from minute surface defects. Fracture surfaces indicate plastic deformation possibly due to contact (relative movement) of two fracture surfaces. Further fractography results and a summarized description about this stage is given in Appendix.19.

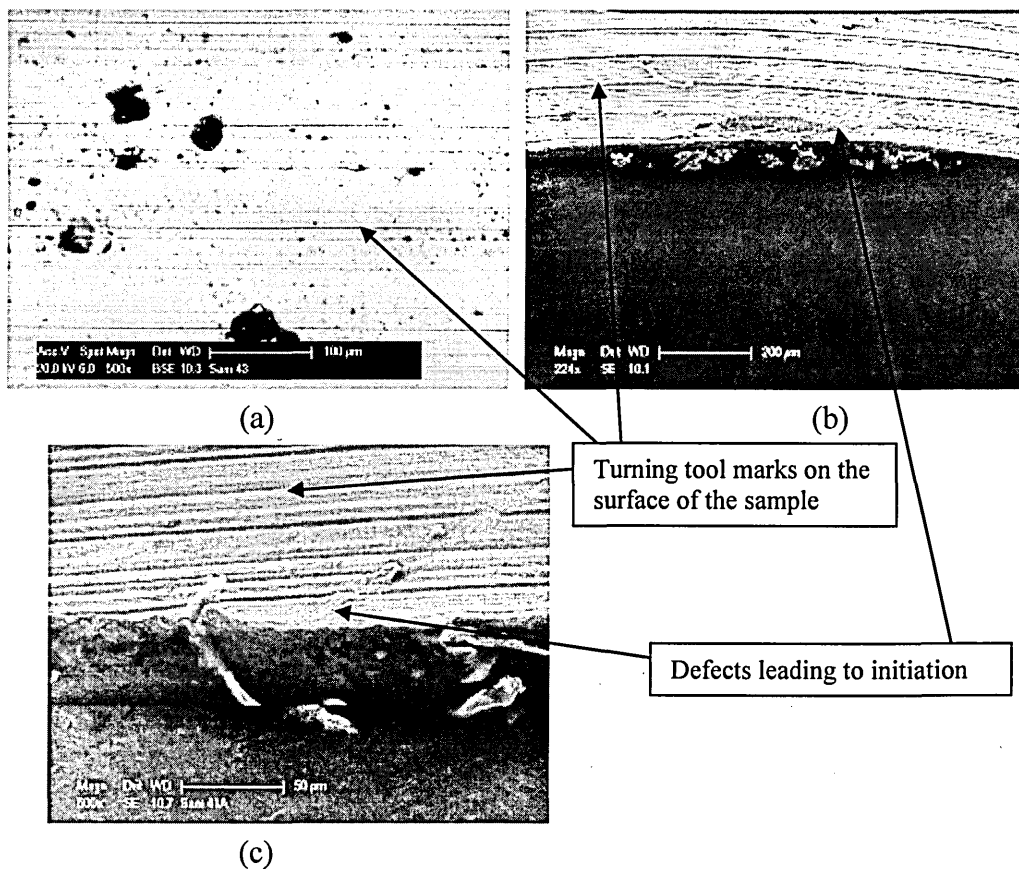


Fig.129: (a) Surface of a sample (Sample No.43) at Route.1, Stage.E, and Fatigue initiation region of samples; (b) Sample No.41, (c) Sample No.40.

Route.2 / Stage.C and Stage.D (annealed – machined - grit blasted - ultrasonic cleaned): The fatigue limit at this stage is 510MPa; a reduction of 172MPa from Stage.B.

At this stage the surface is uneven due to grit blasting as shown in Fig.130(a). According to the fatigue tests results there is no difference in fatigue limit of grit blasted samples to ultrasonic cleaned samples. Therefore both stages are considered together for investigation. The initiation features appear similar to Route.1 / Stages C and D with surfaces containing embedded particles rich in *Al* and *O*, see Fig.130(b), which act as failure initiation sites. The most dangerous aspect of the presence of such particles is that they may be trapped between the Ti / Ti-6Al-4V interface in the finished components and can act as crack initiation sites.

The reduction in fatigue limit at this stage is a clear result in increased surface roughness as well as a slight reduction in surface compressive residual stresses compared with the previous stage. The fatigue limit remains unchanged after ultrasonic cleaning. Further fractography results and a summarized description about this stage is given in Appendix.20.

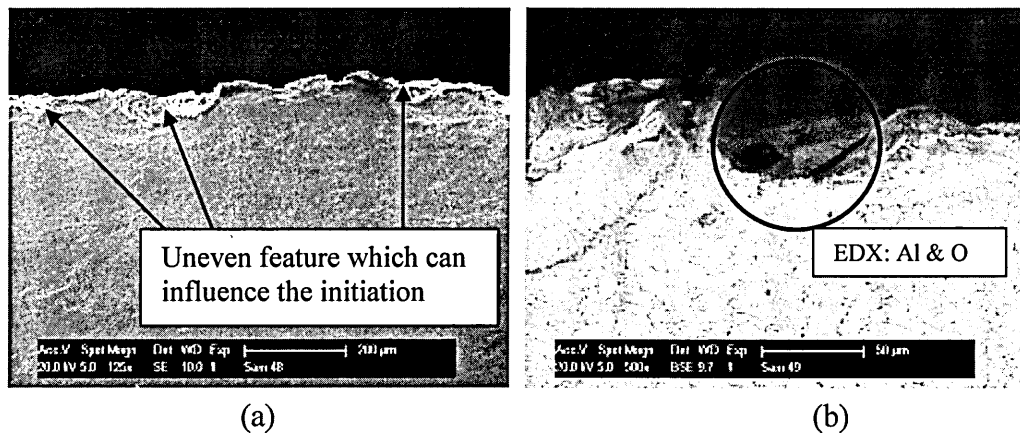


Fig.130: Fatigue initiation region of samples; (a) Sample No.48, (b) Sample No.49.

The cleaning of grit blasting media (inclusions rich with *Al* and *O*) from the blasted surfaces of the components is critical in the context of improving the fatigue life of components. As Griffiths *et. al.* [130] pointed out, any embedded particles may not only

act as fatigue initiation sites but will also significantly reduced the adhesion of the coatings lowering fatigue properties. Therefore it signifies the importance of having an effective cleaning process.

Route.2 / Stage.E (annealed – machined - grit blasted - ultrasonic cleaned - Ti coated): The fatigue limit at this stage is 515MPa ; an increase of 5MPa from Stage.D.

According to the fatigue test results the Ti coating process slightly changes the fatigue limit of grit blasted and ultrasonic cleaned samples. The initiation features are similar to Stage.E of Route.1. Surface dents can be seen at the initiation site of one sample as shown in Fig.131(a), which is possibly created by grit blasting. No Ti coating can be found at these dents; this suggests delamination has occurred during the fatigue process. Embedded particles rich in *Al* and *O* can also be found at the nucleation sites in two samples, as shown in Fig.131(b).

Considering there are only marginal changes in fatigue strength after Ti coating, it can be concluded that the Ti coating process does not change the status of the grit blasted sample surface with respect to surface roughness or residual stress state. Further fractography results and a summarized description about this stage is given in Appendix.21.

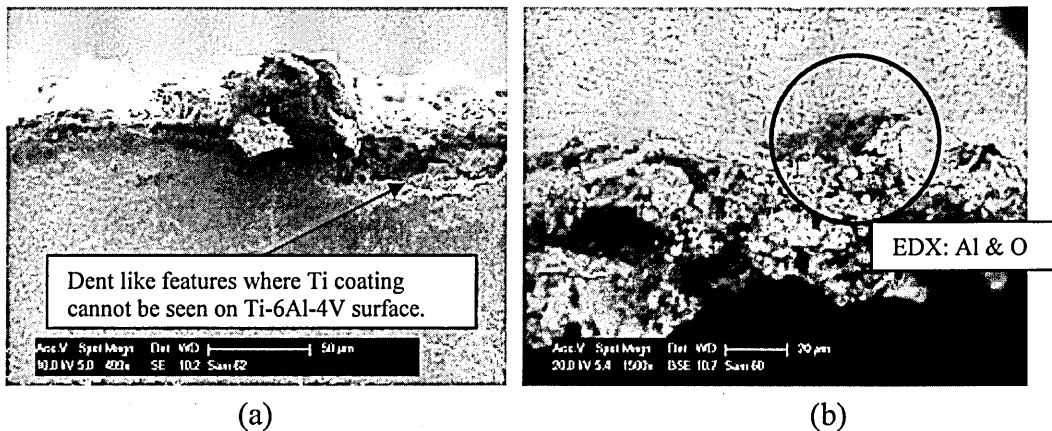


Fig.131: Fatigue initiation region of samples; (a) Sample No.62, (b) Sample No.60.

Route.2 / Stage.F (annealed – machined - grit blasted - ultrasonic cleaned - Ti coated - H-AC coated): The fatigue limit at this stage is 430MPa; a reduction of 85MPa from Stage.E.

Crack initiation occurs at the Ti / Ti-6Al-4V interface and the initiation features are very similar to Stage.F of Route.1. Particles can be found at initiation sites in two samples, as shown in Fig.132(b), and EDX spot analysis shows these are rich in *Al* and *O*. Also separation of Ti coating from Ti-6Al-4V parent metal and also H-AC coating from Ti can be found near the nucleation sites. The initiation process tends to reduce the adhesion between these layers. Fig.132(a) shows the inclusions of H-AC into the base metal through Ti layer. Both the layers appear to be irregular and not uniform throughout. These kinds of inclusions act as stress concentration features (notches) leading to fatigue crack initiation and propagation.

The significant reduction of the fatigue limit is attributed mainly to the introduction of tensile residual stress. Further fractography results and a summarized description about this stage is given in Appendix.22.

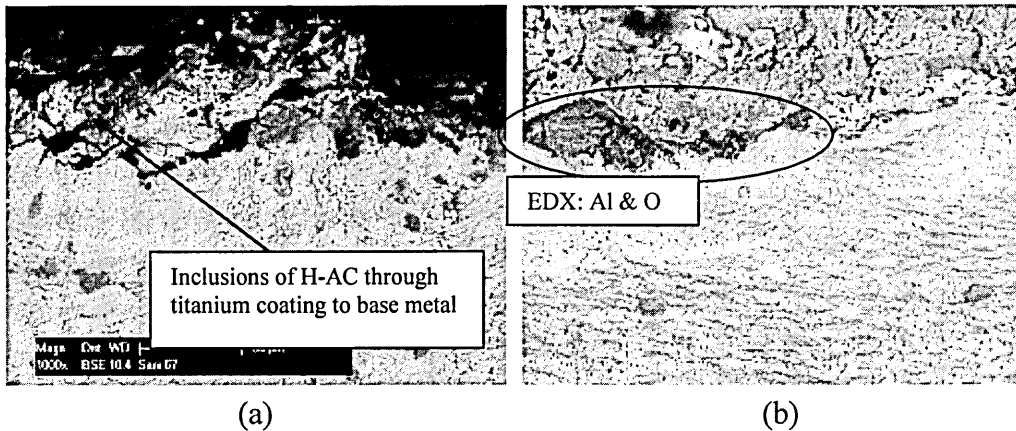


Fig.132: Fatigue initiation region of samples; (a) Sample No.62, (b) Sample No.60.

Route.2 / Stage.G (annealed – machined – grit blasted – ultrasonic cleaned – Ti coated – H-AC coated – annealed): The fatigue limit at this stage is 230MPa; a reduction of 200MPa from Stage.E.

As in Stage.G of Route.1, the final annealing process significantly decreases the fatigue limit. Foreign particles can be found at initiation site of one sample rich in *Al* and *O* as shown in Fig.133.

The reduction of the fatigue limit is due to the induction of tensile residual stress within the sample. As observed previously the annealing process introduces positive (tensile) residual stresses within the sample negating the beneficial effects of compressive residual stresses. Further fractography results and a summarized description about this stage is given in Appendix.23.

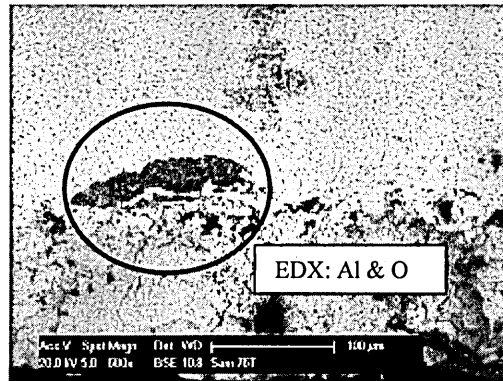


Fig.133: Fatigue initiation region of a failed sample (Sample No.76)

8.4.3. Discussion on Fracture Analysis and Variation of Fatigue Limit of Route.3 (Manufacturing of neck region)

The variation of fatigue limit along Route.3 is illustrated in section 6.5.3.

Route.3 / Stage.B (annealed – machined): The fatigue limit of machined samples is 712MPa (the highest value in Route.3).

Examination of sample surfaces show uniformly distributed machining marks, see Fig.134(a). Initiation sites were severely damaged and plastically deformed with step like features at these sites as shown in Fig.134(d). The fracture surface of sample 79 shows an initiation surface feature typical of a scratch mark near the nucleation site and also lip like feature as shown in Fig.134(b) and (c) respectively. The implication of cracking from scratch marks is that special care is required when implanting the hip stem. The surface finish at Route.3/Stage.B is better than machined surface finish of Route.2/Stage.B. The main reason for this is the depth of final finishing cut which is 0.1mm whereas the depth of cut in Route.2/Stage.B is 0.2mm. This stage has the highest fatigue limit in all three routes. Further fractography results and a summarized description about this stage is given in Appendix.24.

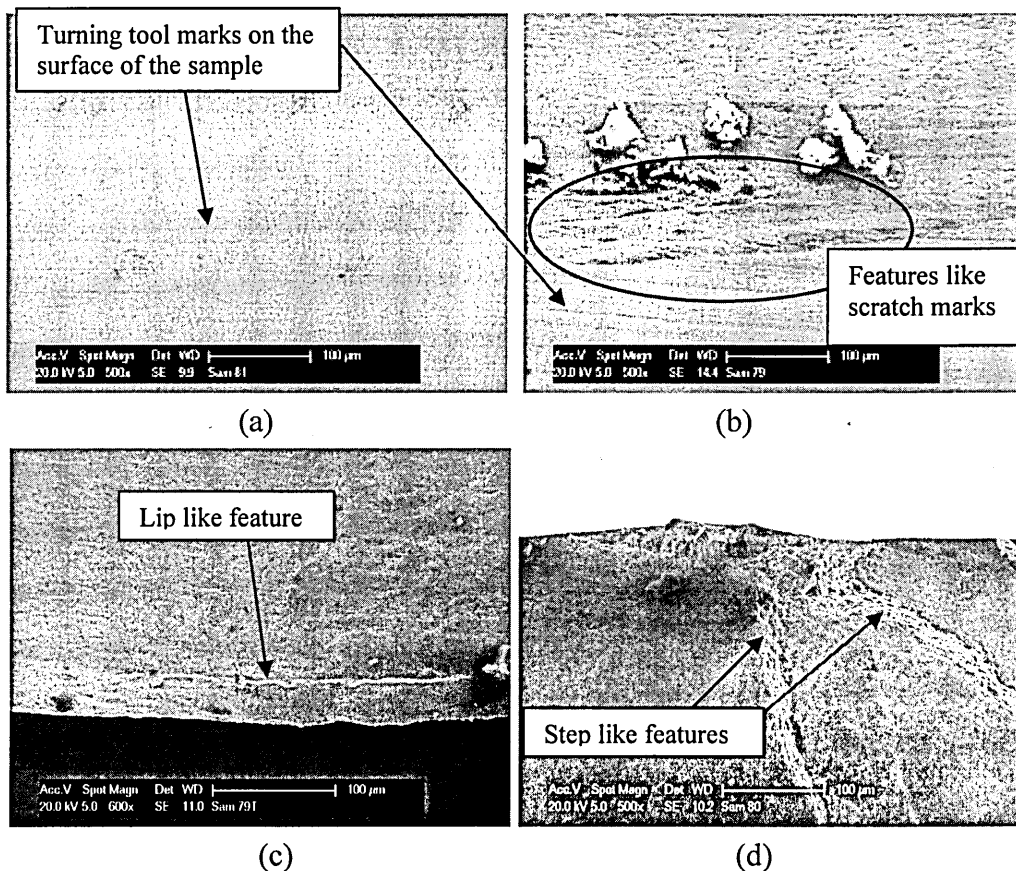


Fig.134: (a) Surface of Sample No.81, and fatigue initiation region of samples; (b) Sample No.79, (c) Sample No.79, (d) Sample No.80.

Route.3 / Stage.C (annealed – machined - shaped/glazed): The fatigue limit at this stage is 345MPa ; a reduction of 367MPa .

The glazing process increases the surface roughness from $4.2\mu\text{m}$ to $13.1\mu\text{m}$. Uneven deep groove marks can be found on the surfaces of glazed samples as shown in Fig.135(a) and (b). Multiple initiation points are observed, as shown in Fig.135(c) and (d) which initiated at deep uneven glazing marks which act as stress raisers on the sample surface. The cracks propagate from one glazing mark to another on the surface.

The fatigue limit is significantly reduced by 367MPa . The surface residual stress value has changed from -436MPa to slightly tensile stress ($+35\text{MPa}$), which promoted fatigue initiation and propagation and supports the reduction of fatigue limit. The increment of surface roughness with deep marks may act as stress risers and also result early crack initiation which help to reduce fatigue life. The reduction of residual stress can be as a result of localized heating induced by glazing operation. More fractography results and summarized description about this stage is given in Appendix.25.

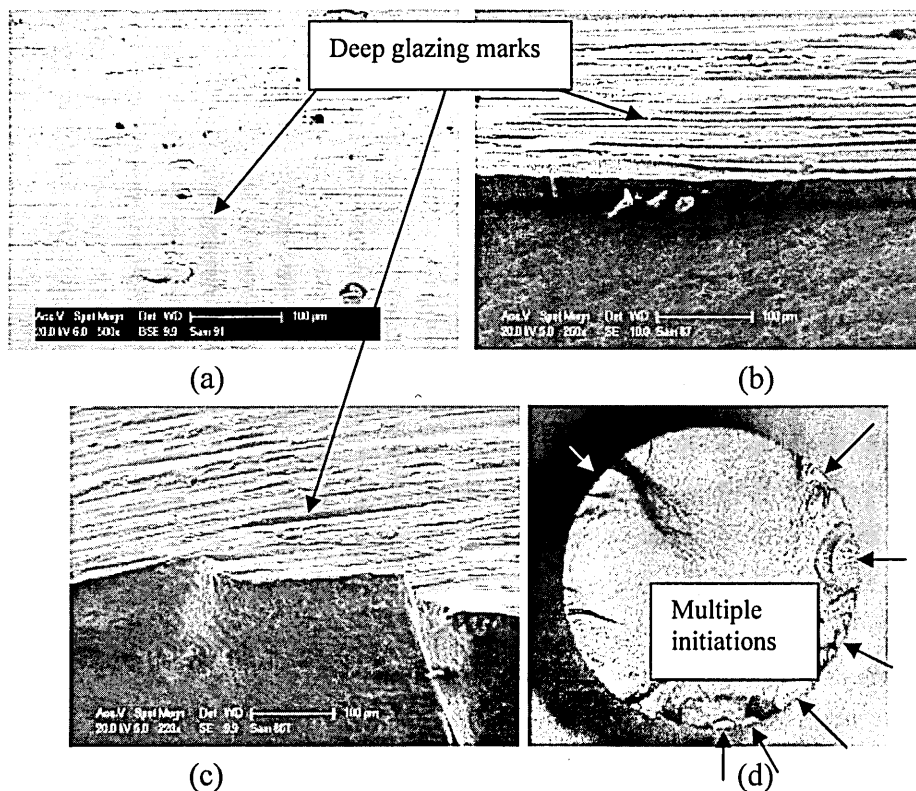


Fig.135: Route.1/Stage.E samples. (a) Surface of Sample No.91, and fatigue initiation region of (b) Sample No.87, (c) Sample No.86, and (d) multiple initiation sites of Sample No.85.

Route.3 / Stage.D (*annealed – machined – shaped/glazed – polished – rumbled*): The fatigue limit at this stage is 613MPa ; an increase of 268MPa .

Rumble marks can be seen on the sample surfaces as shown in Fig.136(a), these marks influenced fatigue initiation. Surface inclusions can be found at the nucleation site shown in Fig.136(b), which EDX analysis reveals inclusions rich in *Si* and *C*. These elements probably originate during the glazing or polishing process conducted before Stage.D. These embedded particles may also be present in the surface of actual implants with potential for initiating fatigue failures.

The polishing and rumbling processes increase the fatigue performance by 268MPa . Smooth surface finish and introduction of more compressive residual stresses to the surface of the sample can be affected to this increment. More fractography results and summarized description about this stage is given in Appendix.26.

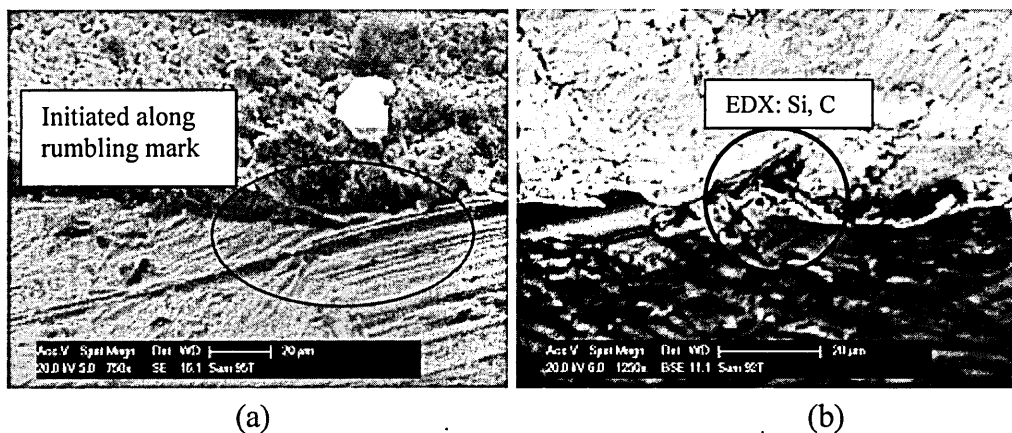


Fig.136: (a) Fatigue initiation region of a failed sample (Sample No.95), (b) Fatigue initiation region of a failed sample (Sample No.92).

Route.3 / Stage.E (*annealed – machined – glazed – polished – rumbled – polished*): The fatigue limit at this stage is 643MPa ; an increment of 40MPa .

A very smooth surface is created following these stages. However surface features can still be found near initiation sites, as shown in Fig.137(a) and (b). These features coincide with the polishing direction of the surface suggesting initiation is related to the polishing process. Since the surface is well polished the likelihood that multiple crack

initiation will develop is reduced. This leads to an increase in fatigue strength but increases the risk that one large notch/scratch controls the fatigue behaviour. This again emphasises the importance of creating the surface without any surface defects like notches and scratch marks which can induce local surface stresses to initiate fatigue failures.

The increase of fatigue strength (of 40MPa), may be due to the finer surface finish, even though a reduction of the compressive surface residual stress can be found. Further fractography results and a summarized description about this stage is given in Appendix.27.

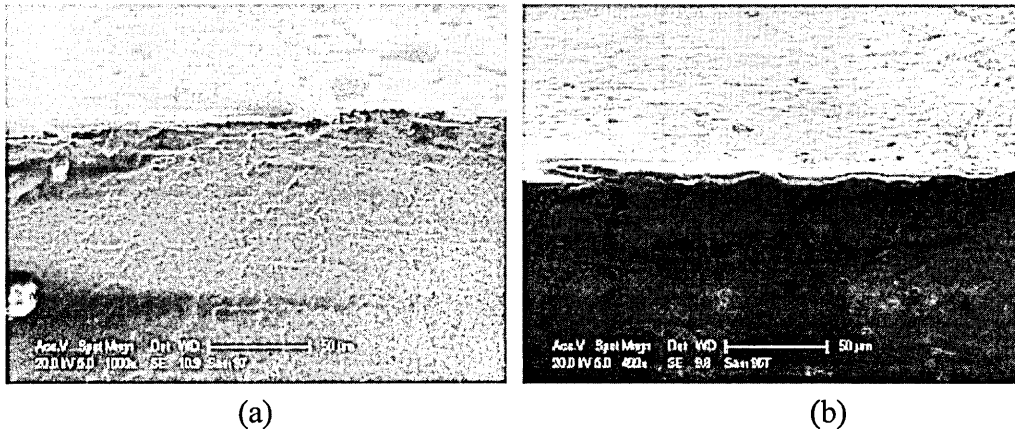


Fig.137: Fatigue initiation region of sample; (a) Sample No.97, (b) Sample No.96.

Route.3 / Stage.F (annealed – machined – shaped/glazed – polished – rumbled – polished – annealed): The fatigue limit at this stage is 599MPa ; a reduction of 44MPa .

Surface features like scratch marks and small dent like features can be found at the initiation sites, as shown in Fig.138(a) and (b). These defects can act as stress raisers to nucleate failure. The introduction of tensile residual stresses by annealing is responsible for the reduction in fatigue limit by 44MPa . However this reduction is not significant when compared to the change in residual stress. This may be due to the decrease in surface roughness of the highly smooth surface where limited surface features can support the initiation of fatigue cracks. Because of the finer surface finish the initiation and propagation of microstructural short cracks may consume a considerable amount of

the total life time. Further fractography results and a summarized description about this stage is given in Appendix.28.

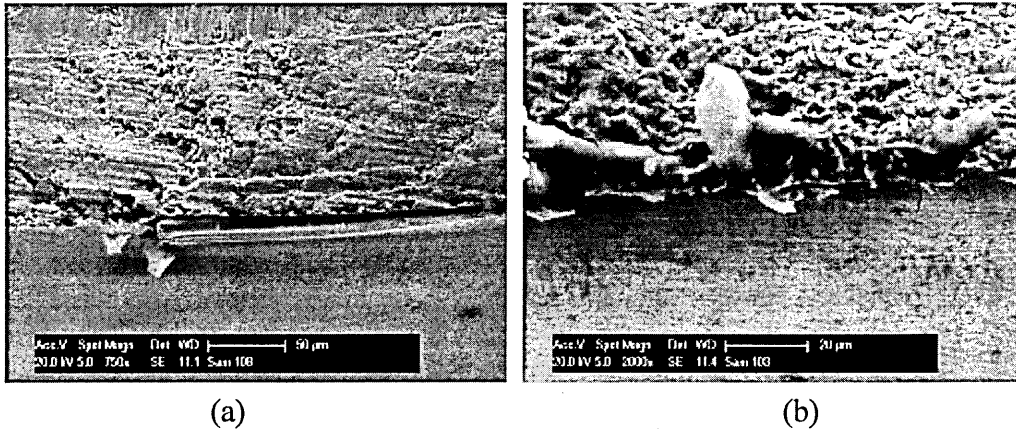


Fig.138: Fatigue initiation region of samples; (a) Sample No.108, (b) Sample No.103.

8.5. Development of K-T Plots for Different Stages in Manufacturing Routes

Each manufacturing stage creates its own surface characteristics, notably defects, surface roughness and residual stress state. The safe and unsafe regions of operation, *i.e.* safe stress amplitude to operate a component for a given surface defect size, can be represent by K-T plots. A comprehensive discussion regarding K-T plots was given previously in Chapter 2, section 2.5.7.

K-T plots have been developed for each manufacturing stage. The fatigue limit of the smoothest surface for all three routes (Route.3 / Stage.E) is considered as the smooth specimen fatigue limit (*i.e.* 643MPa), which is the threshold limit for microstructural short fatigue crack propagation. The K-T plots have not been developed for the final annealing process since this is not part of the actual implant manufacturing process. The LEFM conditions are calculated using equation (07).

8.5.1. K-T Plots for Route.1

As discussed previously the surface roughness of the Ti and H-AC coated samples are not representative of the actual effective defect sizes which influence the fatigue crack initiation, therefore the K-T plots have not been developed for these stages. The developed K-T plots are shown in Fig.139.

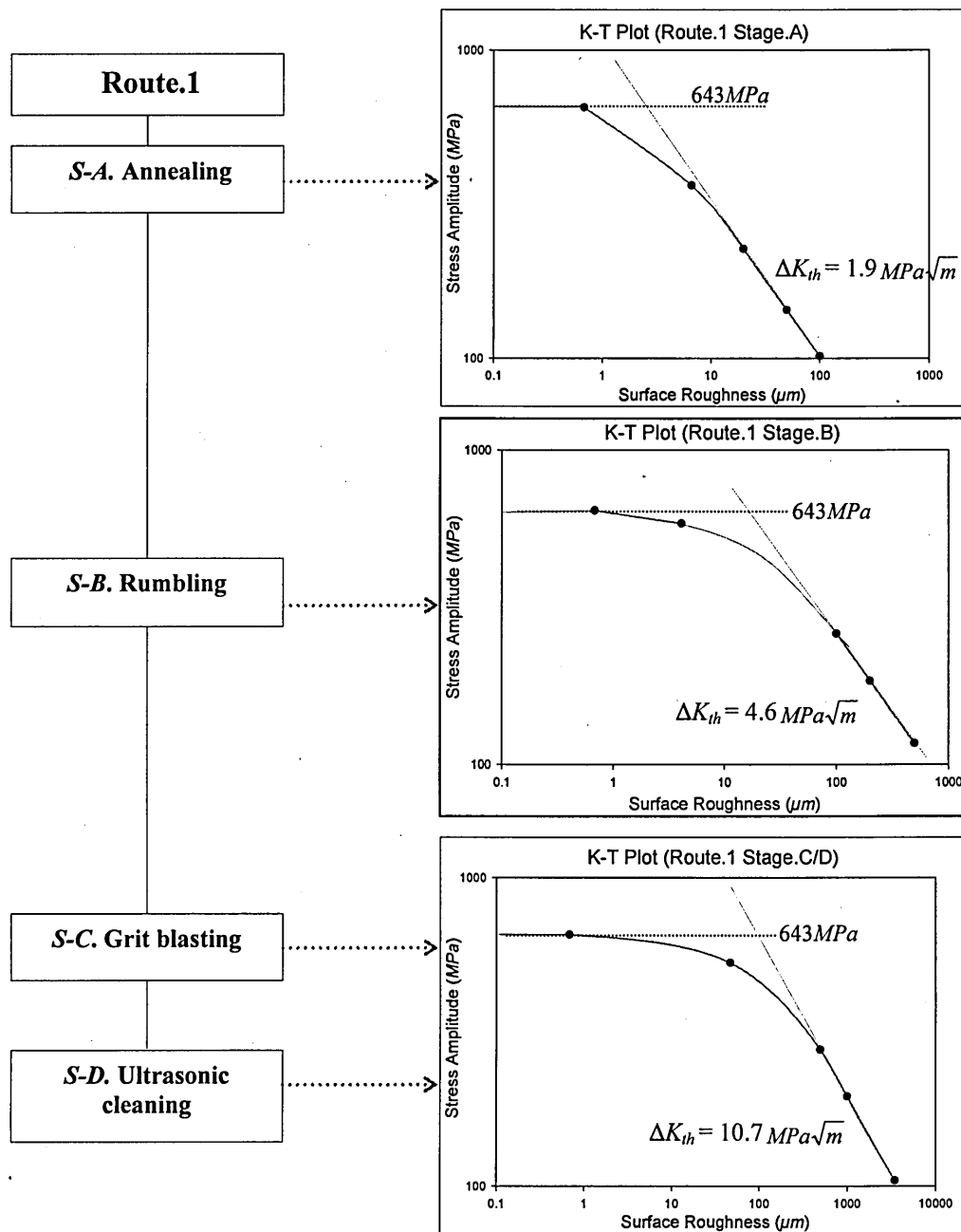


Fig.139: K-T Plots of Route.1 Stage A, B, C and D.

The fatigue limits are calculated for $R=-1$, fully reversed condition using equation (32). This eliminates the effects of residual stress and provides a clear understanding of fatigue performance related to surface roughness/defect size. The K-T plot at $R=-1$ condition for Route.1 is shown in Fig.140, which defines the safe region in Route.1 manufacturing stages.

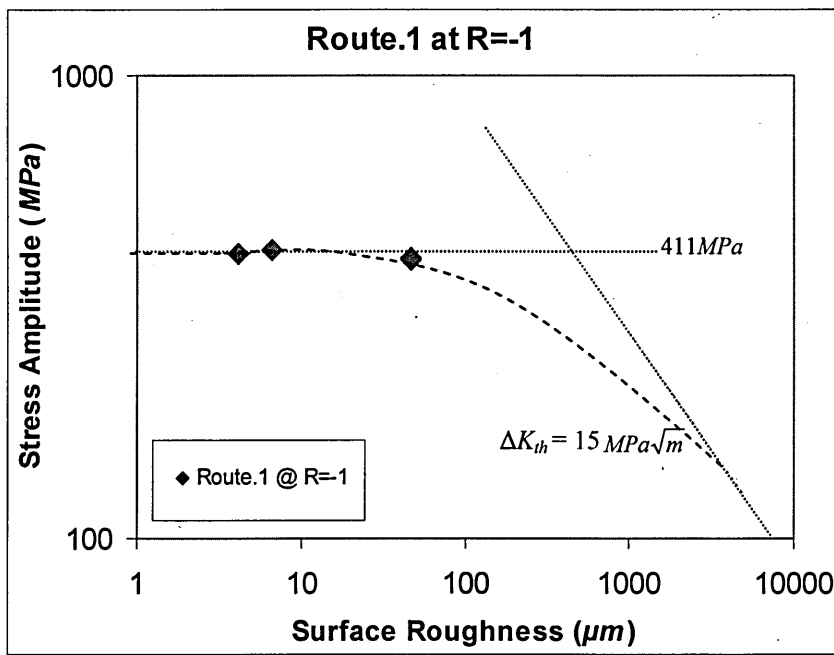


Fig.140: K-T Plot for Route.1 at $R = -1$.

8.5.2. K-T Plots for Route.2

As discussed previously K-T plots are not developed for Ti and H-AC coating stages. The fatigue limit of samples in Route.2 / Stage.B (machined condition) is considerably higher, even compared with the smooth finished sample. Therefore a K-T plot for Stage.B is not developed. The developed K-T plots for Route.2 are shown in Fig.141.

The K-T plot at $R = -1$ condition for Route.2 is shown in Fig.142, this figure defines the safe region related to Route.2 manufacturing stages.

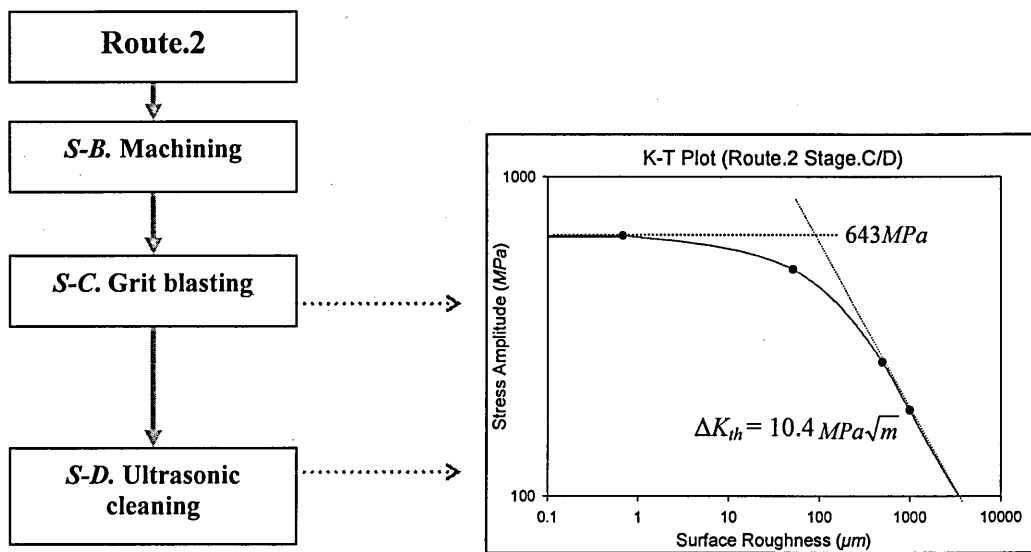


Fig.141: K-T Plots of Route.2 Stage C and D.

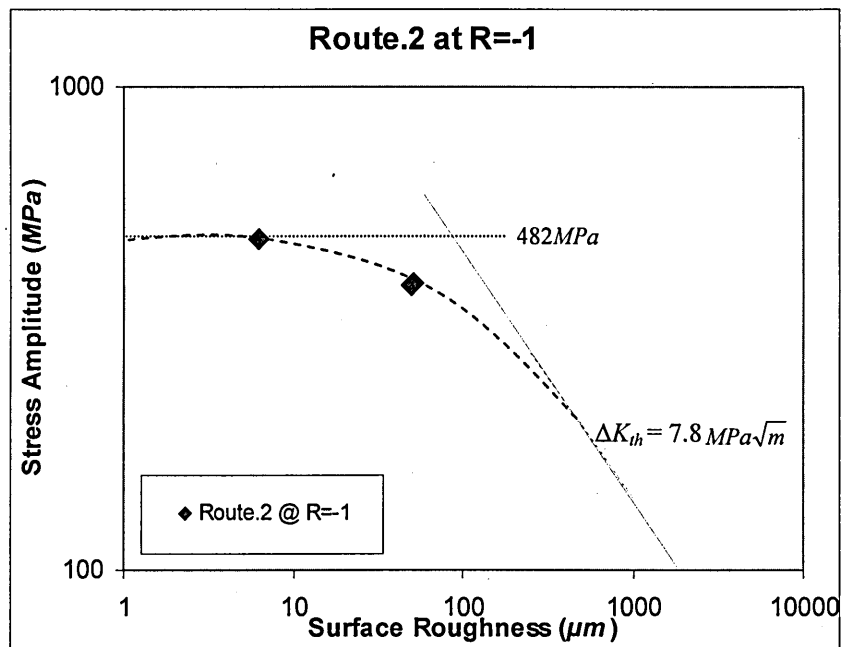


Fig.142: K-T Plot for Route.2 at $R = -1$.

8.5.3. K-T Plots for Route.3

Similar to Route.2 / Stage.B the fatigue limit of samples in Route.3 / Stage.B (machined condition) is considerably higher, than that of the smooth finished sample and a K-T plot for Stage.B is not developed. The developed K-T plots for Route.3 are shown in Fig.143.

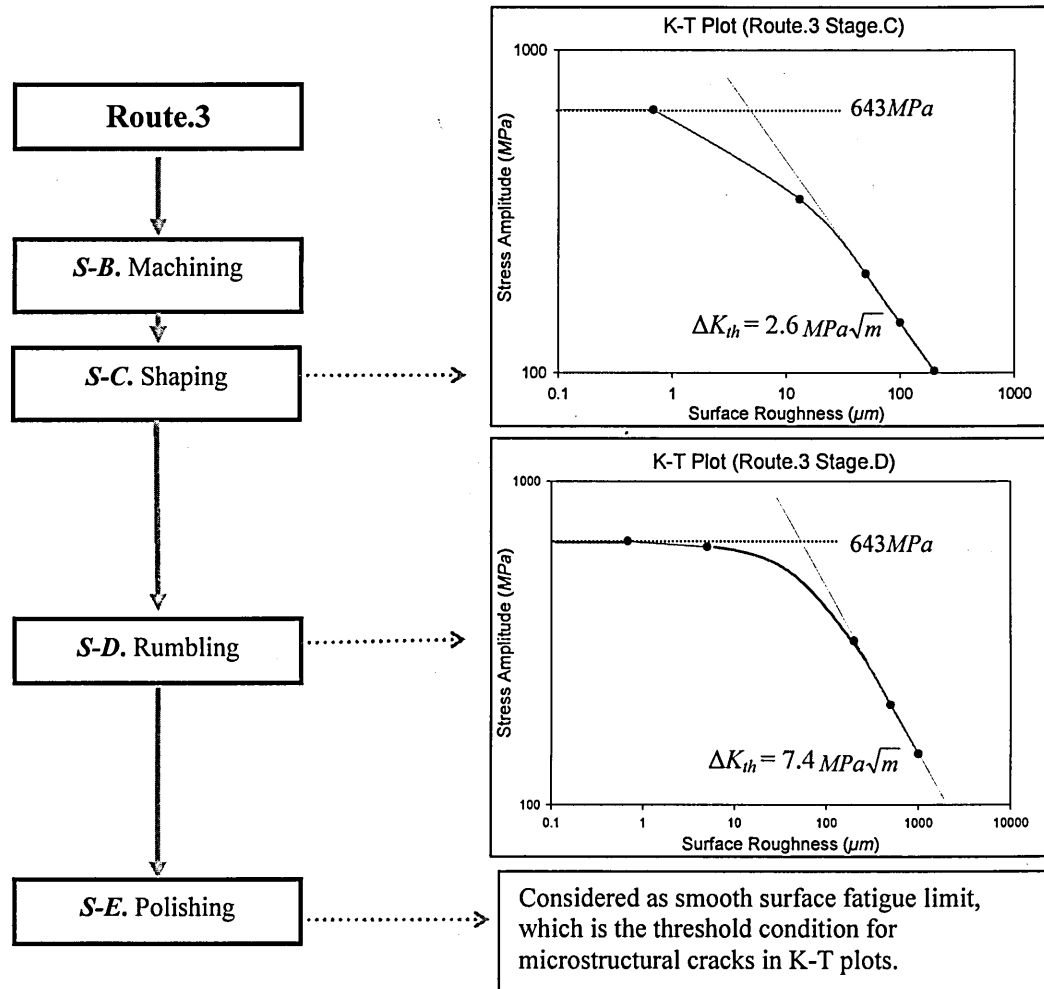


Fig.143: K-T Plots of Route.3 Stage C and D.

The K-T plot at $R=-1$ condition for Route.3 is shown in Fig.144, this figure defines the safe region related to Route.3 manufacturing stages. These K-T plots represents the safe region for fully reverse conditions (assuming zero residual stresses on the samples); as a result the effect of residual stress is eliminated and the results represent variations due to surface defect size.

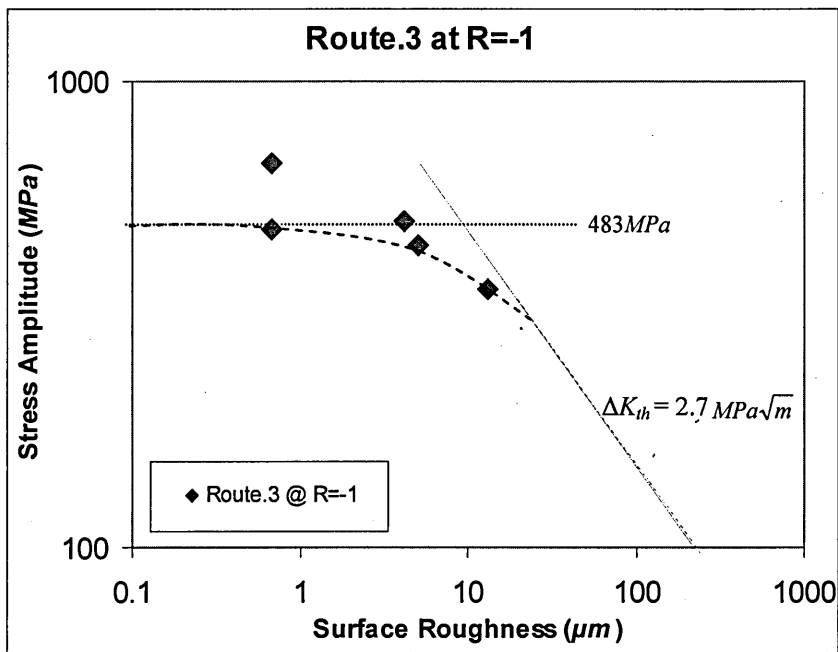


Fig.144: K-T Plot for Route.3 at $R = -1$.

These K-T plots can be used to assess the safe operating condition with respect to manufacturing process variations.

8.6. Variation of Fatigue Performance with Surface Roughness (Surface Defect Size) and Residual Stress Values for Ti-6Al-4V

The variation of fatigue limit (F_L) against residual stress (R_S) and surface roughness (S_R) in Phase.1 (data No. 13-20) and Phase.2 (data No. 1-12) are given Table.17 and illustrated in Fig.145 and Fig.146 respectively. Observing the distributions of data, it is difficult to rationalise any relationship of variation of fatigue limit with either residual stress or surface roughness, especially for the Phase.2 distribution. However an attempt has been made to formulate a relationship between these three parameters, i.e. F_L , R_S and S_R . This is discussed in this section.

No.	Surface Roughness $S_R - (\mu m)$	Residual Stress $R_S - (MPa)$	Fatigue Limit $F_L - (MPa)$
1	6.6	+136	365
2	40	-431	585
3	47	-308	523
4	46	-309	523
5	6.2	-424	682
6	51	-311	510
7	50	-315	510
8	4.2	-436	712
9	13.1	+35	345
10	5	-392	613
11	0.68	-337	643
12	0.68	+102	599
13	0.2	-313	595
14	6	-255	522
15	21	-211	444
16	52	-204	363
17	0.2	+64	455
18	6	+136	365
19	21	+164	326
20	52	+175	235

Table.17: Variation of F_L against S_R and R_S .

The range of data covering each variable is,

Surface roughness(S_R)	-	0.2 μm to 52 μm
Residual stress (R_S)	-	+175MPa to -436MPa
Fatigue Limit (F_L)	-	235MPa to 712MPa

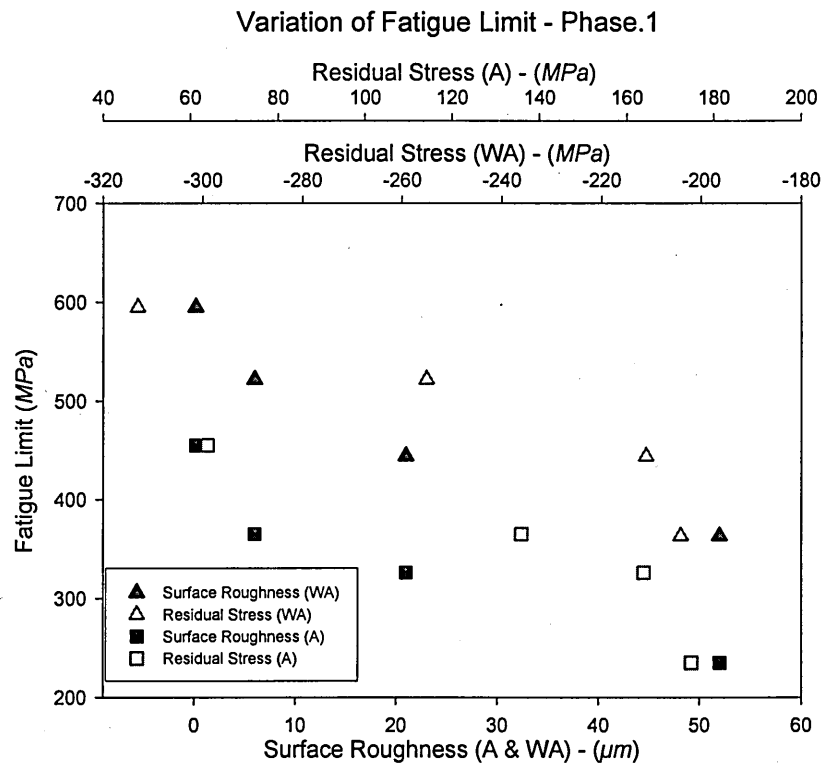


Fig.145: Variation of fatigue limit with surface roughness and residual stress levels of the sample under Phase.1.

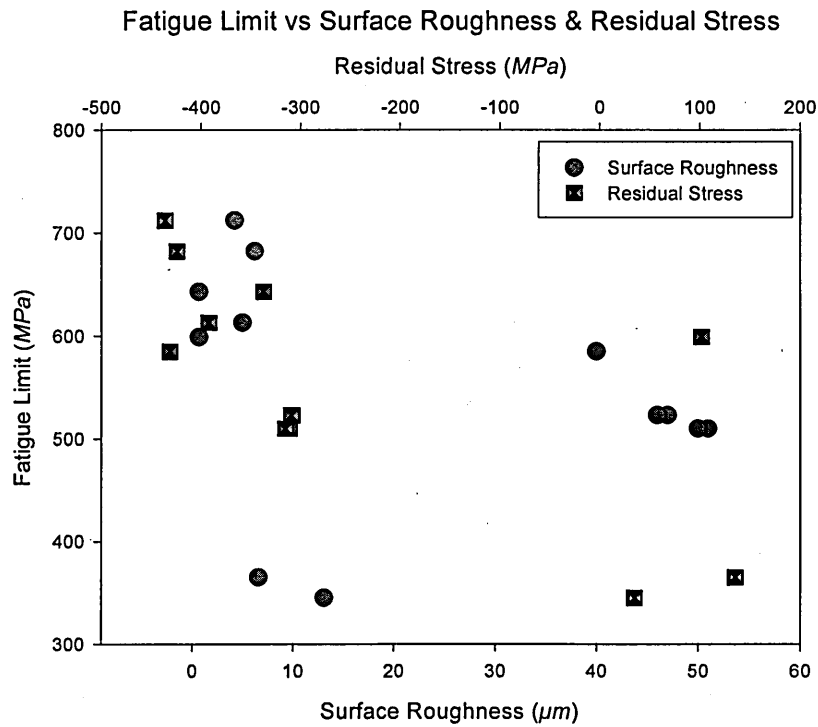


Fig.146: Variation of fatigue limit with surface roughness and residual stress levels of the sample under Phase.2.

The F_L of the samples at each stage is varies with S_R and R_S values.

i.e. $F_L = f(S_R, R_S)$

By considering R_S and S_R as independent variables and F_L as the dependent variable, it is assumed that the relationship between F_L , S_R and R_S is in the form of,

$$F_{Li} = x + y \cdot R_{Si} + z \cdot S_{Ri} \quad (i = 1, 2, \dots) \quad (34)$$

Where x , y and z are constants. Multiple regression analysis is used to derive the relationship and to test the dependency of F_L on R_S and S_R . To test the dependency, two null hypotheses (NH) and two alternative hypotheses (AH) are considered, which are,

$NH1 - y = 0$; *i.e.* F_L does not depend on S_R

$AH1 - y \neq 0$; *i.e.* F_L does depend on S_R

$NH2 - z = 0$; *i.e.* F_L does not depend on R_S

$NH2 - z \neq 0$; *i.e.* F_L does depend on R_S

The multiple regression output obtained using 'Minitab' software for the data given in Table.17, is as follows,

The regression equation is;

$$F_L = 474 - 0.485 R_S - 2.85 S_R$$

Predictor	Coef	SE Coef	T	P (Pivot)
Constant	473.67	20.77	22.80	0.000
R_S	-0.48474	0.06001	-8.08	0.000
S_R	-2.8517	0.6444	-4.43	0.000

S = 58.8232 R-Sq = 81.8% R-Sq(adj) = 79.7%

Analysis of Variance

Source	DF	SS	MS	F	P(Overall Pivot)
Regression	2	264801	132400	38.26	0.000
Residual Error	17	58823	3460		
Total	19	323624			

Unusual Observations

Obs	RS	FL	Fit	SE Fit	Residual	St Resid
12	102	599.0	422.3	23.7	176.7	3.28R

The significance of the relationship between F_L , S_R and R_S are assessed by the P (pivot) value. The smaller the pivot value (zero or close to zero), the higher the significance of the relationship (*i.e.* if the corresponding pivot value for R_S is zero, it indicates the existence of a significant relationship between R_S and F_L). The overall P value of the regression output is zero, concluding the overall model is highly significant. Also the P value of R_S is zero, therefore null hypothesis 1 can be rejected and alternative hypothesis 1 is accepted, *i.e.* the residual stress value is highly significant in determining the fatigue limit. The pivot of S_R is also zero. Again null hypothesis 2 can be rejected and alternative hypothesis 2 is accepted, *i.e.* the surface roughness is also highly significant in determining the fatigue limit.

The derived relationship between F_L , S_R and R_S is,

$$F_L = 474 - 0.485 R_S - 2.85 S_R, \quad (35)$$

The fatigue limit values determined from equation (35) are compared with experimental data shown in Fig.147. Good correlation is observed with the exception of data point No. 12.

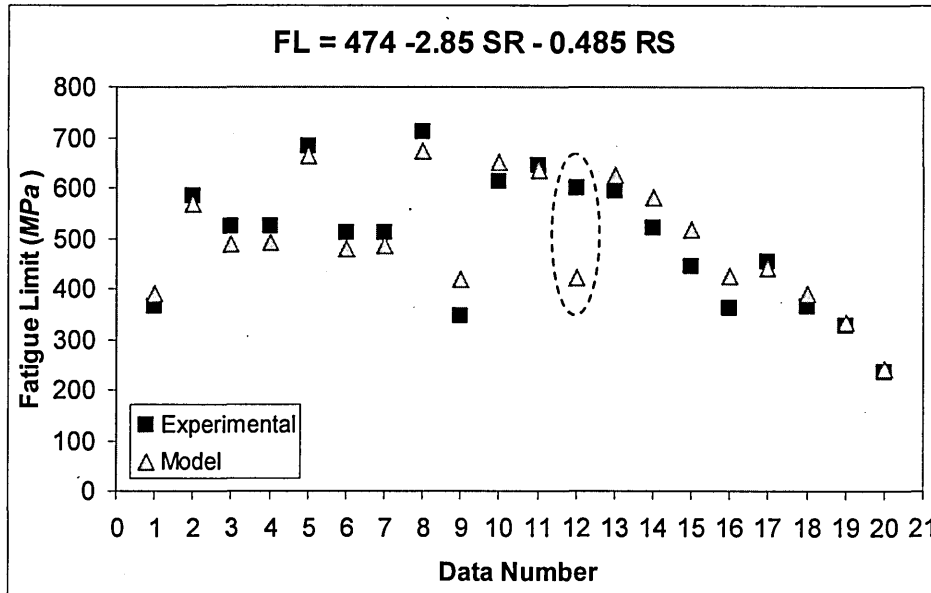


Fig.147: Comparison of the fatigue limit values calculated from derived equation (35) with the experimental results.

Data No.12 represents Stage.F in Route.3 (final annealing stage). This stage does not take place in the actual implant manufacturing process. As discussed in section 8.4.3., the fatigue limit is higher than the expected value. Hence with the exception of data point No.12 the average difference between the experimental and model values shows a variation of around 8.3%.

Further multiple regression results shows more accurate model can be obtained by eliminating the data No.12. The relationship derived without incorporating data No.12, is,

$$F_L = 445 - 2.41 S_R - 0.538 R_S \quad (36)$$

The multiple regression output for equation (36) is as,

The regression equation is

$$F_L = 445 - 2.41 S_R - 0.538 R_S$$

Predictor	Coef	SE Coef	T	P (Pivot)
Constant	444.55	14.09	31.56	0.000
RS	-0.53819	0.03878	-13.88	0.000
SR	-2.4136	0.4105	-5.88	0.000

S = 36.6903 R-Sq = 93.1% R-Sq(adj) = 92.2%

Analysis of Variance

Source	DF	SS	MS	F	P(Overall Pivot)
Regression	2	290863	145432	108.03	0.000
Residual Error	16	21539	1346		
Total	18	312402			

The regression result concludes a highly significant relationship between F_L with S_R and R_S and is more accurate than equation (35). The distribution of experimental and calculated values from equation (36) for fatigue limit is shown in Fig.148 and Fig.149.

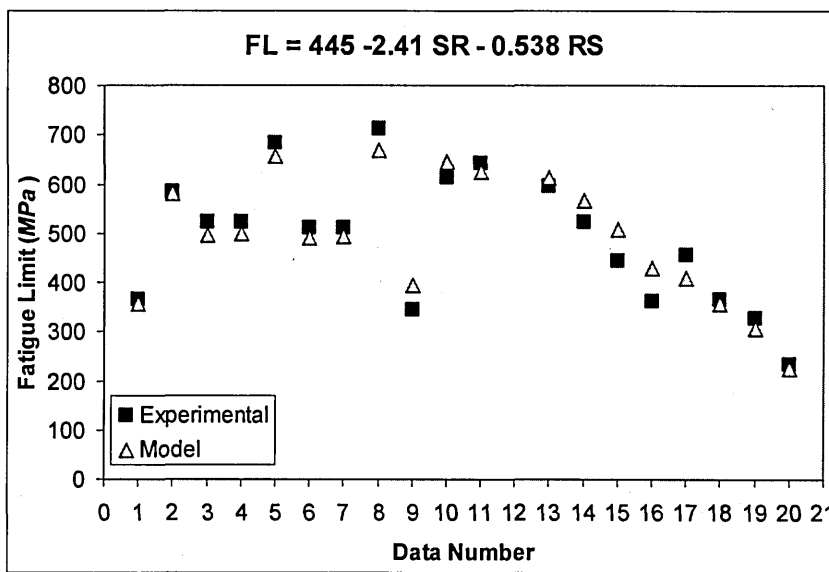


Fig.148: Comparison of the fatigue limit values calculated from equation (36) with the experimental results.

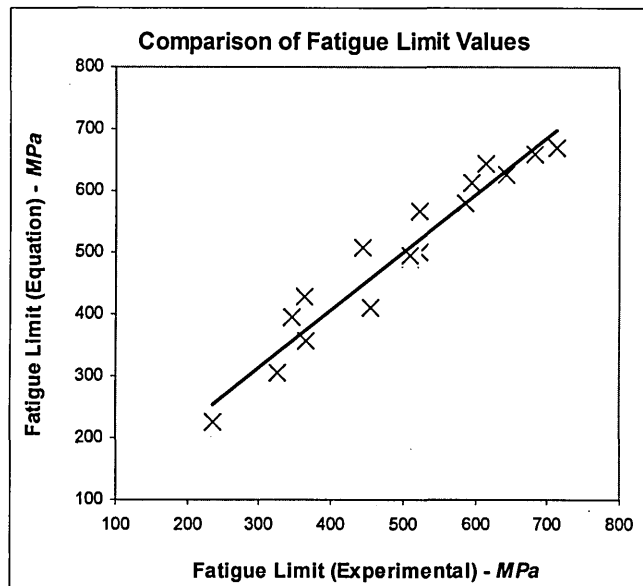


Fig.149: Comparison of the fatigue limit values calculated from equation (36) with the experimental results.

The calculated and experimental values for the fatigue limit differ in accuracy by around 5.9%. The accuracy of Phase.2 (actual implant manufacturing processes) tests results is better, being around 4.6%. Fig.148 and Fig.149 show an existence of a very good agreement between the experiments and the model predictions. Equation (36) is recommended for calculation of the fatigue limit for a known residual stress and surface roughness condition.

The Effect of Constants on Model Predictions: The sensitivity of the model has been checked by changing the constants y and z , which are associated with surface roughness and residual stress values respectively. Each constant is changed independently and checked for sensitivity. Fig.150 shows the sensitivity of y . The value of y is changed by $\pm 10\%$ and the variation of the fatigue limit is not significant. Fig.151 shows the sensitivity of z . The value of z is also changed by $\pm 10\%$; again the variation of the fatigue limit is not significant but more sensitive than y . Sensitivity check has been carried out to optimize the constants and it can be concluded that marginal changes in constants y and z do not have any significant or dramatic changes on the value of F_L .

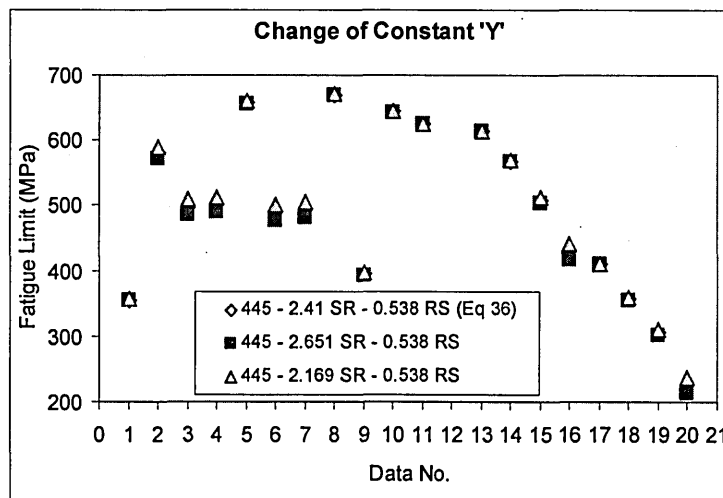


Fig.150: Effect of model fatigue limit due to the change in constant Y .

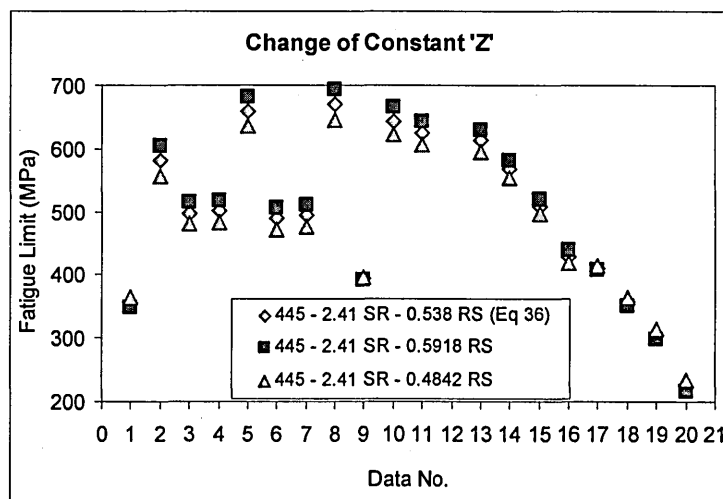


Fig.151: Effect of model fatigue limit due to the change in constant Z .

8.7. Fatigue Crack Growth Modelling and Life Time Predictions on Ti-6Al-4V

A comparison of experimental results obtained by smooth specimens fatigue tests, with the results obtained from the model (ref. Chapter.7) is tabulated in Table.18 and illustrated in Fig.152. The smooth specimens fatigue tests are conducted in Phase.1 ($0.2\mu\text{m}$ surface finished samples) and Route.3 - Stage.E, which are presented in section 6.4.2 and 6.5.3 respectively.

Specimen	Stress Amplitude (MPa)	Fatigue Life (Experimental) (No. of Cycles)	Fatigue Life (Model) (No. of Cycles)	% Variation
A1 (Phase.1)	690	54610	54992	0.7
A3 (Phase.1)	612	136981	117078	14.5
96 (Phase.2)	699	47820	51336	7.3
97 (Phase.2)	650	79975	83485	4.4

Table.18: Comparison of experimental results obtained by smooth specimens with the results obtained from the model.

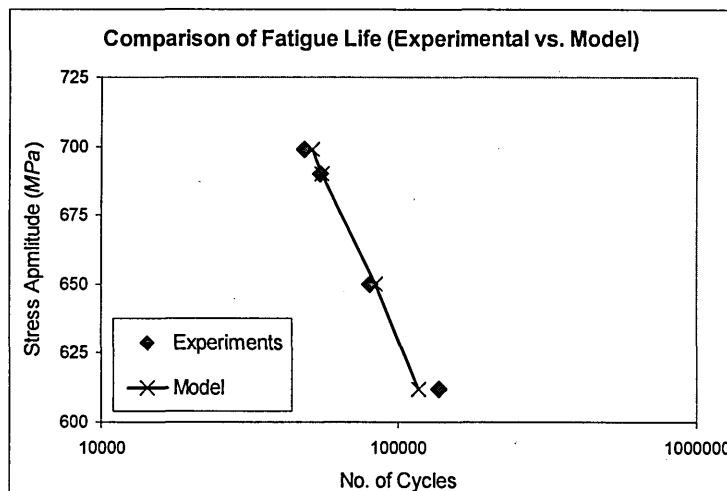


Fig.152: Life time predictions, experimental results obtained by smooth specimens vs. the model.

The comparison shown in Table.18 and Fig.152 suggests the crack propagation model successfully predicts the fatigue life of the smooth specimen for constant amplitude loading for the limited number of points available to this comparison. The accuracy (variation) of the predictions is from 0.7% to 14.5%.

The Effect of Material Constants on Model Predictions: As discussed in Chapter 7, the material constants were calculated using crack growth models to obtain an iterative best fit to the smooth specimen $S-N$ curves. To demonstrate the sensitivity and, the effect that changes of material constants have on the model, each constant is changed independently. Figures 153, 154, 155 and 156 illustrate the effect on model $S-N$ curve of changes in material constants A , B , m and n respectively.

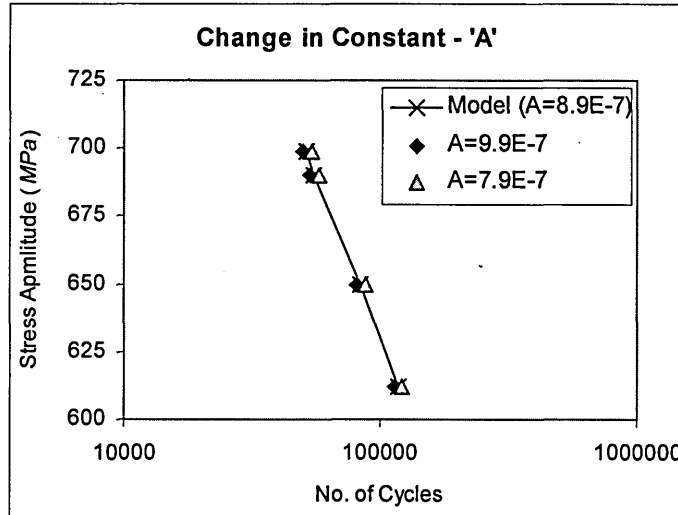


Fig.153: Effect on model $S-N$ curve of changes in material constant A .

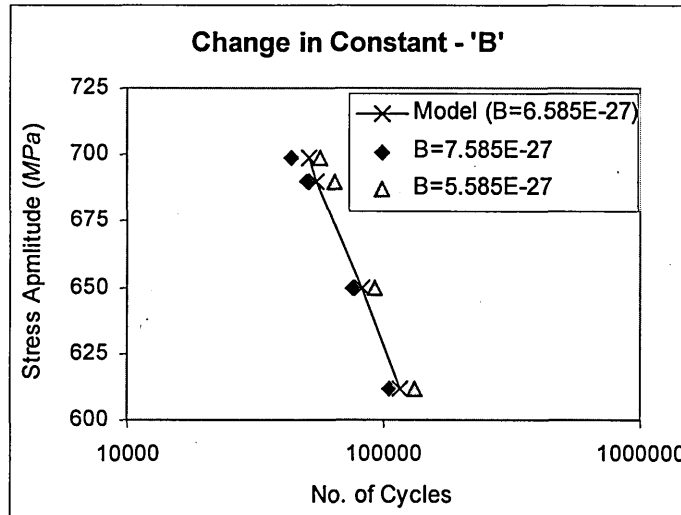


Fig.154: Effect on model $S-N$ curve of changes in material constant B .

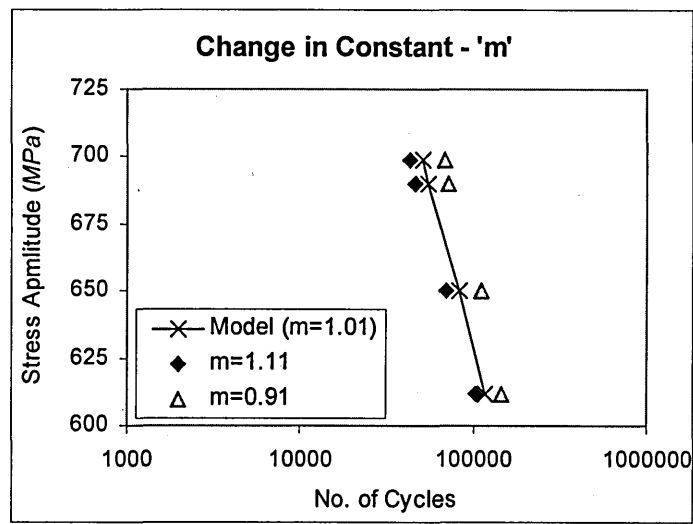


Fig.155: Effect on model S-N curve of changes in material constant m .

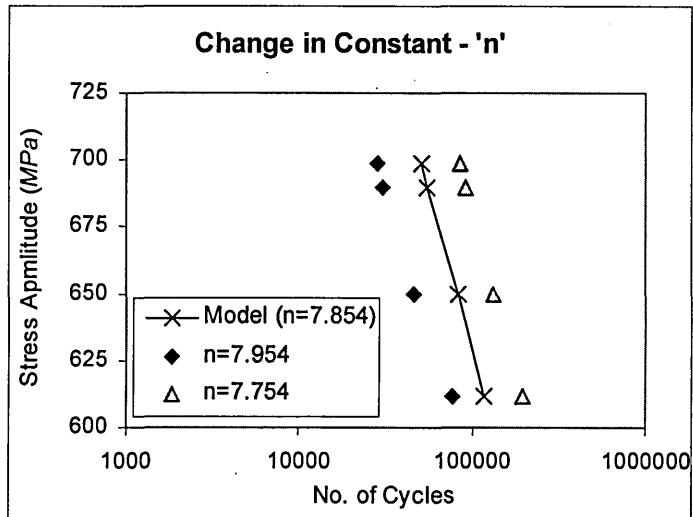


Fig.156: Effect on model S-N curve of changes in material constant n .

The changes in the material constants have been carried out to evaluate the effect on each on the final results of the model, but the collective effect of all constants is obviously more involved. It can be seen from the above figures that the most noticeable change in fatigue life occurs when constant ' n ' is changed. However the accuracy of the results is a combined effect of all material constants.

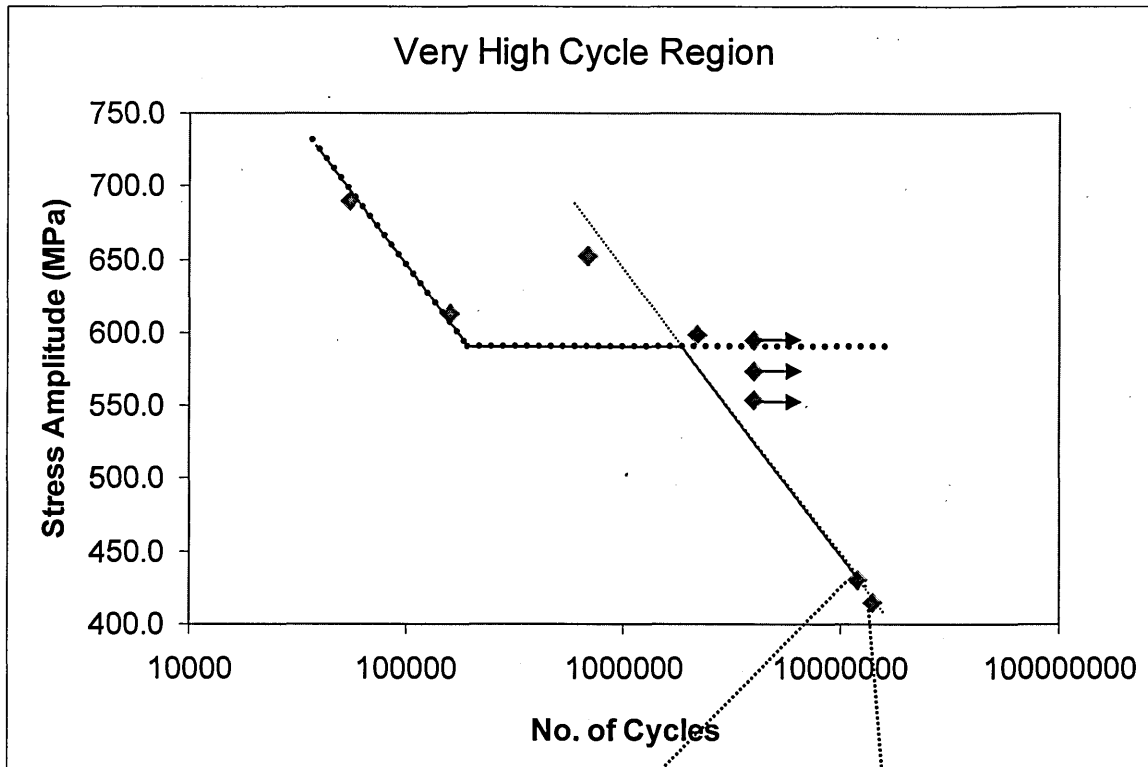
8.8. Observations in Very High Cycle Fatigue Regime

Fatigue failures in the very high cycle regime are observed during tests. These failures are observed below the general high cycle fatigue limit of Ti-6Al-4V.

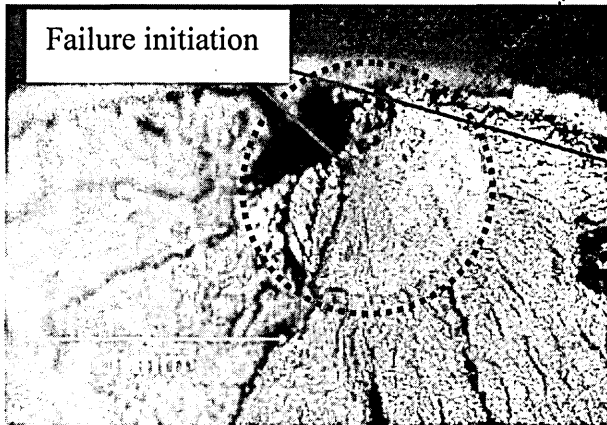
Failures were observed for two samples, notably one after 11956847 cycles and other after 13989585 cycles at stress amplitudes of 430MPa and 415MPa respectively. Both stress levels are below the fatigue limit of polished samples. In Fig.157(a) these failures are tabulated on the S-N diagram of Phase.1 (0.2 μ m surface finish). Here it can be seen that these failures fall on a line drawn from the two data points at 651MPa and 598 MPa. Similar type of behaviour has been observed by Murakami *et.al.* (73), see Fig.22. As shown in the Fig.157(b) and (c) the dominant crack initiation mechanism for these two tests is of sub-surface origin, showing the appearance of a fish-eye like pattern. Also pit-like features penetrating into the material from the surface can be identified. Some sub-surface defects which are not associated with any foreign particulate matter are also visible in sample 7, shown in Appendix.15.

As discussed in section 2.6 these high cycle failures can occur at different types of sub-surface features, such as microstructural defects [72], non-metallic inclusions [76], shrinkage pores, trapped hydrogen [71] and flaws.

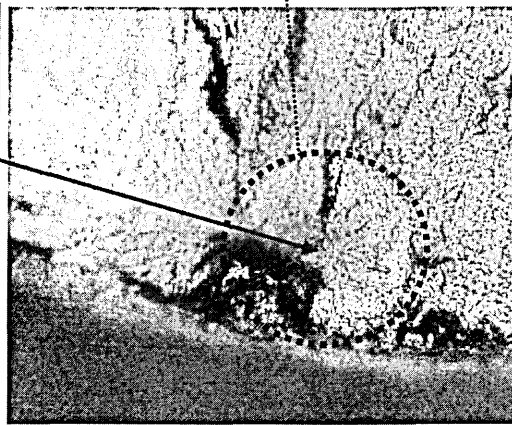
These results confirmed that Ti-6Al-4V alloys can exhibit failure within the very high cycle fatigue failure region, *i.e.* beyond 10^6 - 10^7 cycles at stress levels below an 'established' fatigue limit. More experiments and specific fractography analysis is required to understand the nature and cause of these failures. This is beyond the scope of this study.



(a)



(b)



(c)

Fig.157: (a) S-N diagram containing high cycle fatigue results, (b) (c) Fracture initiation sites of samples

Conclusions Based on the In-vivo Failure Investigation;

A. Failures at Cone Region;

1. Low life fatigue failures, less than 2yrs service life, continually occurred regardless of the design change in the cone region of the stem. Failure is a function of the degree of proximal/distal fixation as opposed to design of the cone region of stem. These low life fatigue failures occurred in 9mm, 10mm and 12mm stems which conclude that failures are not dependent on the size of the implant.
2. High life fatigue failures (>7yrs) have not been found in blended stems within the defined 10 year service lifetime.
3. Failures with medium life span (3yrs < service life < 6yrs) were found in both blended and non-blended stems.
4. Explants having failed at the cone region show little evidence of proximal fixation and a firm distal fixation (flagpole fixation). Failures in the cone region would not occur unless the condition of flagpole fixation was satisfied. In such a case the highest bending moment acts on the cone region and this can be an influential factor for cone failures.

B. Failures at Neck Region;

5. Failure occurred only in the previous design of neck. The design change definitely prolongs the fatigue life as a result of the reduction of maximum stress. It is certain that the design modification has eliminated neck failures in short and medium service lifetimes.

6. The neck is of standard design and the distribution of neck failures consists of all sizes of stems, which can conclude that the neck failures are not depending on the size of the implant. Also failure distribution extended over the 10 year timeframe, which implies no significant relation to low life, medium life or high life regions.
7. Explants having failed at the neck region show a firm proximal fixation with the femoral bone. In such a case the highest bending moment acts on the neck region is an influential factor for neck failures.

C. General Summery of In-Vivo Failures;

8. The majority of in-vivo failures at both the cone and neck area of the implants are due to a single fatigue crack initiation at the posterior side of the implant. Surface features such as, foreign particles rich in *Al* and *O*, notch like features, cavities, surface cracks and surface contaminations can be found at the initiation areas. Delamination of H-AC and Ti layers can also be observed. Thumb nail features and gouge marks, can also be seen in fracture surfaces of neck failures.

Conclusions Based on the Material Characterization (Phase.1);

1. The threshold stress amplitude ($\Delta\sigma_{th}$) for MSC region and the threshold stress intensity factors (ΔK_{th}) for different conditions are as follows;

At WA condition: $\Delta\sigma_{th} = 595MPa, \Delta K_{th} = 5.9 MPa\sqrt{m}$

At A condition: $\Delta\sigma_{th} = 455MPa, \Delta K_{th} = 3.6 MPa\sqrt{m}$

For R = -1: $\Delta\sigma_{th} = 470MPa, \Delta K_{th} = 4.8 MPa\sqrt{m}$

For R = 0.1: $\Delta\sigma_{th} = 301MPa, \Delta K_{th} = 4.0 MPa\sqrt{m}$

The value of ΔK_{th} decreases with increasing *R* ratio. For fully reversed loading (*R*=-1), *i.e.* zero mean stress, the value of a_o (El Haddad correction) is calculated as $33.5\mu m$.

Conclusions Based on characterization of Manufacturing Process (Phase.2);

1. Each manufacturing process creates its own surface roughness and residual stresses on the surface of the samples, which results a clear variation in fatigue limits/performance from one process to another. It is impossible to observe a direct individual relationship of fatigue limit with either residual stress or surface roughness figures.
2. Each manufacturing process creates specific features which influence fatigue crack initiation, such as,
 - Groove like features and turning tool marks create by machining.
 - Deep surface dents and scratch marks due to rumbling.
 - Inclusions rich with elements *Al* and *O*.
 - Notch like indentations of H-AC through Ti coat down to base metal.
 - Deep irregular groove like features created by glazing.
 - Inclusions rich with elements *Si* and *C*.
 - Minute surface features on polished samples.
 - Delamination of coatings.
3. The Ti coating process has almost no effect on fatigue performance.
4. H-AC coating process has strong negative influence on fatigue performance.
5. The machining stages in Route.2 / Stage.B ($6.2\mu\text{m}$) and Route.3 / Stage.B ($4.2\mu\text{m}$) show a difference in fatigue limit. The only difference in the processes is the depth of final cut which is 0.2mm in Route.2 and 0.1mm in Route.1.

These machined samples (Route.B, both Phase.1 and Phase.2) indicate unexpected higher fatigue limits compared to other samples. Since the surface finish is less than the average grain size ($7\mu\text{m}$) the initiation defect is within the first grain and will have to overcome the initial microstructural barrier, which

can be one reason for the higher fatigue limit. Further investigations are required to fully quantify this behaviour.

6. Inclusions rich in *Al* and *O* originated from the grit blasting are one of the major causes of fatigue crack initiation for Routes 1 and 2. Inclusions rich in *Si* and *O* found in at crack initiation sites (Route.3) originated from the glazing and polishing operations.

Conclusions based on the results obtained by analysis of surface cracks by surface replication;

1. Surface replication results shows (at $\Delta\sigma_{th} = 630MPa$) an existence of microstructural barrier $\approx 7-8\mu m$. The relative threshold stress intensity factor at this dimension is $3-5 MPa\sqrt{m}$.

Conclusions Based on the Mathematical Models Developed using Fatigue Test Results;

1. A mathematical model to quantify the fatigue limit of a component with known surface roughness/defect size (S_R) and surface residual stress (R_S) is proposed. The values of fatigue limit predicted by the model are in good agreement with experimental results. The calculated and experimental values for fatigue limit consists an overall accuracy of 5.9% (variation). The accuracy of the values in Phase.2, relating to actual implant manufacturing processes, is 4.6% (variation).
2. Based on two existing models for MSC and PSC regimes separately, a crack growth model is developed to predict fatigue life of the Ti-6Al-4V implant grade alloy for given stress amplitudes. The accuracy of the predictions varies from 0.7% to 14.5%.

Conclusions Based High Cycle Fatigue Tests;

1. Very high cycle fatigue failures ($>10^7$ cycles) have been observed for Ti-6Al-4V alloy. Further investigations are required to understand the mechanism of failure at these lifetimes.

1. Inclusions such as alumina (Al_2O_3) particles contribute strongly to the initiation of fatigue cracks in grit blasted, Ti coated and H-AC coated samples resulting in premature failure. Apart from crack initiation, these embedded particles reduce the contact area of Ti-6Al-4V and Ti coating layers, which may reduce the adhesion of Ti coat with Ti-6Al-4V base metal which in turn lead to de-bonding of the H-AC layer. This will not only alter the expected fatigue performance of the implant but also will affect fixation to the host bone. Special care must be given to remove embedded alumina particles from the surface. The ultrasonic cleaning process may be improved by prolonging cleaning time of the cycles or by adding additional cleaning cycles.
2. The rumbling process (Route.1 / Stage.B) creates deep surface dents, which initiates fatigue and may also trap blasting particles firmly into the surface. This may be eliminated by smoothing the surface before blasting through the introduction of belt or bead blasting operation. In addition the blasting parameters such as blasting angle, shape and size of blasting media and duration should be evaluated to give optimum surface finish.
3. Inclusions rich in *Si* and *C* have found at initiation sites in Route.3 / Stage D. These inclusions can be embedded in the final product. It is therefore recommended that another ultrasonic cleaning process before Route.3 / Stage.D is introduced to make sure all the inclusions are removed after polishing.
4. It is advisable to keep the final depth of cut as small as possible which increases the fatigue limit through making a smooth surface finish.
5. The H-AC coating process does not change the surface roughness at the Ti / Ti-6Al-4V interface. Although the H-AC coating process does not reach temperatures where stress relief may occur, it may have the potential of changing the residual stresses levels beneath the surface of the coating and at the interface. It is recommended to introduce shot peening process to create additional compressive

surface stress before H-AC coating. However the adhesion of the coating should be investigated before incorporating shot peening.

6. Fracture surfaces also reveal the H-AC coating has penetrated through Ti layer to the Ti-6Al-4V base metal. These may act as notch like features which cause fatigue initiation. Uniformity of coating layers are therefore important to minimise the risk of fatigue failures.
7. The polished samples (Route.3 /Stage.E and F) shows small surface features at fatigue initiation areas. The neck area of the implant possesses the same surface finish and therefore extra care should be taken while handling the implant during surgery so as not to damage the neck area.
8. Future fatigue testing of the implants (in accordance with ISO 7206) could be conducted on implant stems of known surface roughness and residual stress at the neck and cone regions.
9. Fatigue tests should be conducted below the conventional fatigue limit to understand the behaviour of the material in the very high cycle fatigue range.

REFERENCES

1. Singh S, Trikha SP, Edge AJ., Hydroxyapatite ceramic-coated femoral stems in young patients - A prospective ten-year study, *J Bone Joint Surg*, 2004; 86-B, pp. 1118-23.
2. Katti KS., Biomaterials in total joint replacement. *Colloids and Surfaces B: Biomaterials* 39, 2004; pp. 133-142.
3. Ignotov VP, Petrovskaya TS., *Proceedings KORUS 2003, 7th Korea-Russia International symposium on science and Technology (IEEE cat. No. 03EX737)*, 2003; Par 01, Vol. 01, pp. 197-201.
4. Charnley J., Factors In The Design of An Artificial Hip Joint, *Proc Instn Mech Engrs*, 1966-67, Vol. 181 Pt 37, pp. 2.
5. Brunette DM, Tengvall P, Textor M, Thomson P., *Titanium in Medicine*, Springer, Springer-Verlag Berlin Heidelberg, 2001; ISBN 3-540-66936-1.
6. Sitting C, Textor N, Spencer ND., Surface characterization of implant materials c.p. Ti, Ti-6Al-7Nb and Ti-6Al-4V with different pretreatments, *Journal of Materials in Medicine*, 1999; 10, pp. 35-46.
7. Machado AR, Wallbank J., Machining of titanium and its alloys- a review, *Proc Instn Mech Engrs*, 1989; Vol. 204, pp. 53-60.
8. Sitting C, Textor N, Spencer ND., Surface characterization of implant materials c.p. Ti, Ti-6Al-7Nb and Ti-6Al-4V with different pretreatments, *journal of materials in medicine*, 1999, 10, pp. 35-46.
9. Jha AK, Diwakar V, Pant B, Sreekumar K., Failure analysis of a Ti-6Al-4V gas bottle, *Engineering Failure Analysis*, Volume 13, Issue 5, July 2006, pp. 843-856.
10. Metallic material for surgical implants, specification for wrought titanium 6-aluminium 4- vanadium alloy, BS 7252 - Part 3, 1997.
11. Boyer R, Welsch G, Collongs EW., *Materials Properties Handbook: Titanium Alloys*, ASM International, 1994; ISBN 0-87170-481-1.
12. Implants for surgery – Hydroxyapatite, Part 4: Determination of coating adhesion strength, BS ISO 13779-4 : 2002.
13. Change CK, Wu JS, Mao DL, Ding CX., Mechanical and histological evaluations of hydroxyapatite-coated and non coated Ti-6Al-4V implants in tibia bone, *J Biomed Mat Res*, 2001, 56, pp. 17-23.
14. Geesink RGT, Groot KD, Klein CPAT., Bonding of born to apatite-coated implants, *J Bone Joint Surg*, 1988, 70-B, pp. 17-22.

15. Wang BC, Change E, Lee TM, Yang CY., Changes in phase and crystallinity of plasma-sprayed hydroxyapatite coatings under heat treatment: A quantitative study, *Journal of Biomedical Materials Research*, Vol.29. pp. 1483-1492, 1995.
16. Oonishi H, Yamamoto M, Ishimaru H, Tsuji E, Kushitani S, Aono Mm, Ukon Y., The effect of hydroxyapatite coating on bone growth into porous titanium alloy implants, *J Bone Joint Surg*, 1989, 71-B, 213-6.
17. LeGeros RZ., Review paper, Biodegradation and bioresorption of calcium phosphate ceramics, *Clinical Mater*, 1993, 14, pp. 65-88.
18. Dalton JE, Cook SD., In vivo mechanical and histological characteristics of HA-coated implants vary with coating vendors, *J Bio-med Mater Res*, 1995, 29, pp. 239-45.
19. Lynn AK, DuQuesnay DL., Hydroxyapatite coated Ti-6Al-4V, part 1: The effect of coating thickness on mechanical fatigue behaviour, *Biomaterials* 23, 2002; pp. 1937-46.
20. Klein CPAT, Patsa P, Wolke JGC, Blicke-Hogervorst JMAD, Groot KD., Long-term in vivo study of plasma-sprayed coatings on titanium alloys of tetra-calcium phosphate, hydroxyapatite and α -tricalcium phosphate. *Biomater*, 1994, 15, 146-50.
21. Sousa SR, Barbosa MA., Effect of hydroxyapatite thickness on metal ion release from Ti-6Al-4V substrates, *Biomaterials*, 1996; 17, pp. 397-404.
22. Lacefield KWR. Hydroxyapatite coating, *Ann NY Acad Sci*, 1988, 523, pp. 72-80.
23. Li TT, Lee JH, Kobayashi T, Aoki H., Hydroxyapatite coating by dipping method, and bone bending strength, *J mater Sci Mater Med*, 1996, 7, pp. 355-7.
24. Ducheyne P, Raemdonck WV, Heughebaert JC, Heughebaert MM., Structural analysis of hydroxyapatite coating on titanium, *Bio-materials*, 1986, 1986, 97-103.
25. Work Instructions on Coatings, JRI Ltd.
26. Sharma DK, Brooks S, Creasey S, Lewis B., Fracture of fully hydroxyapatite-coated titanium femoral stem of a total hip replacement-a report of 3 cases, *Acta Orthop Scand*, 2004; 75 (6), pp. 768-71.
27. Recorded data: Quality Checks, JRI Ltd.
28. Evans SL, Gregson PJ., The effect of plasma-sprayed hydroxyapatite coating on the fatigue properties of Ti-6Al-4V, *Materials Letters*, 1993; 16, pp. 270-4.
29. Suresh S., *Fatigue of materials*, Cambridge Solid State Science Series, Cambridge University Press, 1991, ISBN 0 521 36510 4.
30. Wohler A., (1860) Versuche uber die festigkeit der eisenbahnwagenachsen, *Seitschrift fur Bauwesen* 10; English Summary (1867), *Engineering*, 4, pp. 160-1.
31. *Fatigue and Fracture*, ASM handbook, Volume 19, ASM International, 1996; ISBN 0-87170-385-8.

32. Brown LM, Ogin SL., Role of internal stress in the nucleation of fatigue cracks, In: Bilby, Miller, Willis, Fundamentals of deformation and fracture, Eshelby memorial symposium, pp. 501–528, 1984.
33. Irwin GR., Analysis of stresses and strains near the end of a crack traversing a plate, Journal of Applied Mechanics, 24, pp. 361-364.
34. Zang W., 1991, Short fatigue crack behaviour under different loading conditions, Ph.D thesis, University of Sheffield.
35. Fatigue Design Handbook, Second Edition, Society of Automotive Engineers, Inc., 1988; ISBN 0-89883-011-7.
36. Brown MW., Interface between short, long, and non-propagating cracks, EGF Pub.1 (edited by Miller KJ, de los Rios ER), 1986, Mechanical Engineering Publications Ltd, London, 1986, pp. 423-39.
37. Bannantine JA, Comer JJ, Handrock JL., Fundamentals of Metal Fatigue Analysis, Prentice Hall, Englewood Cliffs, New Jersey 07632, ISBN 0-13-340191-X.
38. Suresh S., Fatigue of Materials, 2nd Edition, University of Cambridge, Cambridge, 1998; ISBN 0-521-57847-7.
39. Mughrabi H., Microscopic Mechanisms of Metal Fatigue, Strength of metals and alloys (Edited by P. Haasen, V. Gerold, and G. Kostorz), 1980; vol. III (Pergamon, Oxford) pp. 1615-38.
40. Taylor D., Modelling of Fatigue Crack Growth at the Microstructural Level, Computational Materials Science, 25 (2002). pp. 228-236.
41. Hobson PD., The growth of short fatigue cracks in a medium carbon steel, Ph.D Thesis, University of Sheffield, Sheffield.
42. Brown MW. Miller KJ, Fernando US, Yates JR, Suker DK., Aspects of multiaxial fatigue crack propagation, Fourth International Conference on Biaxial/Multiaxial Fatigue , may 31-June 03, 1994, Paris, France.
43. Paris PC, Erdogan F., (1963), A critical analysis of crack growth propagation laws, Journal of Basic Engineering, 85, pp. 528-34.
44. Miller KJ., The Propagation Behaviour of Short Fatigue Cracks, Department of Mechanical Engineering, University of Sheffield, Sheffield, 1987.
45. Fatigue Propagation Behaviour of Short Cracks in Titanium Alloys, ESDU International, ESDU data item No. 92023, Issued on November 1992 with amendment A on March 1993.
46. Basquin OH., (1910), The exponential law of endurance test, Proceedings of the American Society of Testing and Materials, 10, pp. 625-30.
47. Coffin LF., (1954), A study of the effect of cyclic thermal stresses on a ductile material, Transactions of American Society of Mechanical Engineers, 76, 931-50.

48. Manson SS., (1954). Behaviour of materials under conditions of thermal stress, National advisory commission of aeronautics, Report 1170, Cleveland Lewis Flight Propulsion Laboratory.
49. Jin O, Hamm RW, Johnson WS., Microstructural influences on the growth of small cracks in Ti-6Al-4V, 2002 Blackwell Science Ltd, Fatigue Fract Engng Mater Struct, 25, pp. 563-574.
50. Lutjering G, Gysler A., Fatigue - Critical Review, Proc 5th Int Conf on Titanium, West Germany, 1985, pp. 2065-2083.
51. Lutjering G, Gysler A, Wagner L., Proc Sixth world conference on titanium, Paris, France 1988.
52. Handbook of Residual Stress and Deformation of Steel, ASM International, ISBN 0-87170-729-2, March 2005.
53. Hines JA, Peters JO, Lutjering GL., Microcrack Propagation in Ti-6Al-4V Alloys, Fatigue behaviour of Titanium alloys, 1999.
54. Akid R, Miller KJ., Short fatigue crack behaviour of low carbon steel under corrosion fatigue condition, Fatigue Fract Engng Mater Struct, 1991; vol14, no 6, pp. 637-49.
55. Miller KJ., The behaviour of short fatigue cracks and their initiation, Part II - A General Summary. Fatigue Fract Engng Mater Struct, 1987; vol.10, no. 2, pp. 93-113.
56. Wagner L, Lutjering G., Microstructural Influence on Propagation Behaviour of Short Cracks in an ($\alpha+\beta$) Ti Alloy, Zeitschrift fur metallkunde, 1987; 78, 5, pp. 369-75.
57. Kitagawa H, Takahashi S., Applicability of fracture mechanics to very small cracks or the cracks in the early stage, In: Proceedings of the Second International Conference on Mechanical Behaviour of Materials. Metals Park, OH: ASM; 1976; pp. 627-31.
58. The behaviour of short fatigue cracks, edited by Miller KJ, de los Rios ER, Mechanical Engineering Publications Ltd, London, 1986, pp. 2.
59. Vasudevan AK, Sadananda K, Glinka G., Critical parameters for fatigue damage, International Journal of Fatigue, Volume 23, Supplement 1, 2001, pp. 39-53.
60. Pearson S., Initiation of fatigue cracks in commercial aluminium alloys and the subsequent propagation of very short cracks, Engng Fract Mech, 1975; 7, pp. 135-47.
61. Hines JA, Lutjering G., Propagation of microcracks at stress amplitudes below the conventional fatigue limit for three references, Fatigue Fract Engng Mater Struct, 1999; vol.22, iss.8, pp. 657-65.

62. El Haddad MH, Smith KN, Topper TH., Fatigue crack propagation of short cracks, The American Society of Mechanical Engineering, Revised manuscript, Feb 15, 1978; Paper No. 78-mat-7.
63. El Haddad MH, Topper TH, Topper TN., Fatigue life prediction of a smooth and notched specimens based on the fracture mechanics, Journal of Engineering Materials and Technology, 1980; pp. 91- 96.
64. Chapetti MD., Application of a threshold curve model to high cycle fatigue behaviour of small cracks induced by foreign-object damage in Ti-6Al-4V, international journal of fatigue, 2005; 27, pp. 493-501.
65. Zhou S, Turnbull A., Influence of pitting on the fatigue life of a turbine blade steel, Blackwell Science Ltd. Fatigue Fract Engng Mater Struct, 1999; 22, pp. 1083-93.
66. Eberhardt AW, Kim BS, Rigney ED, Kutner GL, Harte CR., Journal of Applied Biomaterials, Vol. 6, 171-174, (1995).
67. Guilherme AS, Henriques GEP, Zavanelli RA, Mesquita MF., The Journal of Prosthetic Dentistry, Vol 93, No.4, pp. 378-385.
68. Miller KJ., O'Donnell WJ. The fatigue limit and its elimination, Fatigue Fract Engng Mater Struct, 22, pp. 545-57, 1999.
69. Bathias C., There is no infinite fatigue life in metallic materials, Fatigue Fract Engng Mater Struct, 22, pp. 559-65, 1999.
70. Mughrabi H., Fatigue mechanisms in the ultrahigh cycle regime, Proceedings of 9th international fatigue congress, May 2006, Atlanta, USA.
71. Murakami Y, Nomoto T, Ueda T., Factors influencing the mechanism of superlong fatigue failure in steels, Fatigue Fract Engng Mater Struct, 22, pp. 581-90, 1999.
72. Bathias C., Damage mechanisms in gigacycle fatigue, Proceedings of 9th international fatigue congress, May 2006, Atlanta, USA.
73. Murakami Y, Nagata J, Matsunaga H., Factors affecting ultra long life fatigue and design method for components, Proceedings of 9th international fatigue congress, May 2006, Atlanta, USA.
74. Nishijima S. Kanazawa K., Stepwise S-N curve and fish-eye failure in gigacycle fatigue, Fatigue Fract Engng Mater Struct, 22, pp. 601-7, 1999.
75. Wang QY, Berard JY, Rathery S, Bathias C., Technical note; High cycle fatigue crack initiation and propagation behaviour of high-strength spring steel wires, Fatigue Fract Engng Mater Struct, 22, 673-77, 1999.
76. Harlow DG, Wei RP, Sakai T, Oguma N., Crack growth based probability modelling of S-N response for high strength steel, International Journal of Fatigue, Volume 28, Issue 11, November 2006, pp. 1479-1485.

77. Wagner L., Mechanical surface treatments on titanium, aluminium and magnesium alloys, *Material Science and Engineering*, A263, pp. 210-216, 1999.
78. Nakajima K, Terao K, Miyata T., The effect of microstructure on fatigue crack propagation of $\alpha+\beta$ titanium alloys- in-situ observation on short fatigue crack growth, *Material Science and Engineering*, 1998; A243, pp. 176-81.
79. Benson DK, Grosskreutz JC, Shaw GG., Mechanisms of fatigue in mill annealed Ti-6Al-4V at room temperature and 600°F, *Metal Transactions*, 1972; vol. 3, issue 5, pp. 1239-48.
80. Eylon D, Pierce CM., Effect of microstructure on notch fatigue properties of Ti-6Al-4V, *Metallurgical Transactions*, 1972; vol. 7, issue 1, pp. 111-21.
81. Hall JA., Fatigue crack initiation in alpha-beta titanium alloys, *International Journal of Fatigue*, 1997; vol. 19, supp no 1, pp. s23-s37.
82. Le Biavant K, Pommier S, Prioul C., Local texture and fatigue crack initiation in a Ti-6Al-4V titanium alloy, 2002, Blackwell Science Ltd, *Fatigue Fract Engng Struct*, 25, pp. 527-545.
83. Wagner L, Lutjering G., Microstructural Influence on Propagation Behaviour of Short Cracks in an ($\alpha+\beta$) Ti Alloy, *Zeitschrift fur metallkunde*, 1987; 78, 5, pp. 369-75.
84. Sadanandan K, Vasudevan AK., Fatigue crack growth behaviour of titanium alloys, *International Journal of Fatigue*, 2005; 27, pp. 1255-66.
85. Miller KJ., The behaviour of short fatigue cracks and their initiation Part I – A review of two recent books, *Fatigue Fract Engng Mater Struct*, 1987; vol. 10, 1, pp. 75-91.
86. Brown CW, Smith GC., The Effect of Microstructure and Texture on the fatigue Crack Growth Threshold in Ti-6Al-4V, *Intergovernmental Conference-EU*, 1982, Vol 1, pp. 329-343.
87. Irving PE, Beevers CJ., Microstructural Influences on Fatigue Crack Growth in Ti-6Al-4V, *Mat. Sci. and Eng.*, 1974, Vol.14, pp. 229-238.
88. Organ-Hough CVJ, Tavakkolizadeh A., Case Report, Fatigue Failure of the Femoral Component of a Cementless Total Hip Arthroplasty, *The Journal of Arthroplasty*, 2004; vol. 19, No. 5, pp. 658-60.
89. Fernando US., Finite element elastic stress analysis of JRI Ferlong® 9mm and 10mm femoral stems, Report Ref:ENG/F3/C8/4526-7, JULY 2000.
90. Fernando US., Finite element elastic stress analysis of JRI Ferlong® 10mm femoral stems, Report Ref:ENG/F3/C8/4526-7a, July 2002.
91. Private discussions with Fernando US, 2006.

92. BS 7251-part5 (1990), Orthopaedic joint prostheses – Method of determination of endurance properties of stemmed femoral components of hip joint prostheses with application of torsion.
93. ISO 7206-Part 4 (1989), Implant for Surgery - Partial and Total Hip Prosthesis – Determination of Endurance Properties of Stemmed Femoral Components with Application of Torsion.
94. FDA Guided Document for Femoral Stem Prostheses, JRI Ltd, Doc Ref. Stems test 12a.
95. Itoga H, Tokaji K, Nakajima M, Ko H.-N., Effects of surface roughness on step-wise S-N characteristics in high strength steel, international journal of fatigue, 2003; 25, pp. 379-85.
96. Maiya PS., Geometrical characterization of surface roughness and its application to fatigue crack initiation, Material Science and Engineering, 1975, 21, pp. 57-62.
97. Murakami Y, Endo Mm., Effects of defects, inclusions and in homogeneities on fatigue strength, Int J Fatigue, 1994; 16, pp. 163-82.
98. Murakami Y, Takahashi K, Yamashita A., Quantitative evaluation of the effect of surface roughness on fatigue strength (effect of depth and pitch of roughness), Trans Jpn Soc Mech Rng, 1997; A63 pp. 1612-9.
99. Bahbou MF, Nylen P, Wigren J., Effect of Grit Blasting and Spraying Angle on the Adhesion Strength of Plasma-Sprayed Coating, Journal of Thermal Spray Technology, Vol. 13(4), pp. 508-514, December 2004.
100. The guide to surface texture parameters, Operation manual given with Taylor Hobson stylus type surface measuring apparatus.
101. Handbook of Residual Stress and Deformation of Steel, ASM International, ISBN 0-87170-729-2.
102. Webster GA, Ezeilo AN., Residual stress distributions and their influence on fatigue lifetimes, Int J Fatigue, 2001; vol. 23, Sup. 1, pp. 375-83.
103. Yang YC, Chang E., Influence of residual stress on bonding strength and fracture of plasma-sprayed hydroxyapatite coatings on Ti-6Al-4V, Biomaterials, July 2001; vol. 22, Issue 13, pp. 1827-36.
104. Elsing R, Knotek O, Balting U., The influence of physical properties and spraying parameters on the creation of the residual thermal stresses during the spraying process, Surface and Coatings Technology, 1990; 41, pp. 147-56.
105. Yang YC, Chang E., Measurement of residual stresses in plasma-sprayed hydroxyapatite coatings on titanium alloy, Surface and Coatings Technology, 2005; 190, pp. 122-31.

106. Noyan IC, Cohen JB., Residual Stresses in Material, American Scientist, Vol 79-2, pp. 142-53, 1991.
107. Xiaoping Y, Richard LC, Grandt AF., An Experimental Study on Fatigue Life Variance, Residual Stress Variance, and Their Correlation of Face-Turned and Ground Ti 6Al-4V Samples, Journal of Manufacturing Science and Engineering, Nov.2002, Vol. 124/809.
108. Prevey PS., X-ray Diffraction Residual Stress Techniques, Metals Handbook, 10, Metals Park, OH, American Society for Metals, 1986, pp. 380-392.
109. Bolton W. Newnes Engineering Materials Pocket Book, Third Edition, Newnes, ISBN 0-7506-4974-7.
110. Withers PJ, Bhadeshia HKDH., Residual stresses, Part 1 - Measurement techniques. Material Science and Technology, April 2001; vol.17, pp. 355-65.
111. Prevey PS., Current Applications of X-ray Diffraction Residual Stress Measurement, ASM International, Materials Park, OH, 1996, pp. 103-110.
112. Middleton JC., Residual Stress and X-rays, NDT International [0308-9126], 1987; vol.20, Iss. 5, pp. 291-4.
113. Cullity BD, Stock SR., Elements of x-ray diffraction, Upper Saddle River, NJ: Prentice Hall, 2001; ISBN 0-20161-091-4.
114. Hammond C., The Basic Crystallography and Diffraction, International Union of Crystallography, Oxford Science Publications, New York, 1997, ISBN 0-19-855966-6 (Hbk).
115. A National Measurement Good Practice Guide No. 52, Determination of Residual Stresses by X-ray Diffraction – Issue 2, National Physical Laboratory, 2005; ISSN 1744-3911.
116. Lipson HS., Crystals and X-rays, Wykeham publications (London) Ltd, 1970, ISBN - 0 85109 150 4.
117. Martinez SA, Sathish S, Blodgett MP, Shepard MJ., Residual stress distribution on surface treated Ti-6Al-4V by X-ray diffraction, Society of Experimental Mechanics, pp. 141-147, 2002.
118. Noyan IC, Cohen JB., Residual Stress – Measurement by Diffraction and Interpretation, Springer-Verlag New York Inc. 1987, ISBN 3-540-96378-2 (US).
119. Hauk V., Structural and Residual Stress Analysis by Nondestructive Methods; Evaluation – Application – Assessment, Elsevier Science B.V., 1997, ISBN 0-444-82476-6.
120. Operational Manuals, Philips X-pert Stress Analysis Equipment, Sheffield Hallam University, Sheffield.
121. Manufacturing Route Cards, JRI Ltd, Sheffield, UK.

122. Manufacturing Route Cards, Doncasters Ltd, Sheffield, UK.
123. Filiaggi MJ, Coombs NA, Pilliar RM., Characterization of the interface in the plasma-sprayed HA coating/Ti-6Al-4V implant system, *Journal of Biomedical Materials Research*, Vol. 25, pp. 1211-1229 (1991).
124. Huaxia JI, Ponton CB, Marquis PM., Microstructural characterization of hydroxyapatite coating on titanium, *Journal of Material Science: Materials in Medicine* 3 (1992), pp. 283-287.
125. Tsui YC, Doyle C, Clyne TW., Plasma sprayed hydroxyapatite coatings on titanium substrates Part 1: Mechanical Properties and residual stress levels, *Biomaterials*, 19 (1998), pp. 2015-2029.
126. Berndt CC, Haddad GN, Farmer AJD, Gross KA., Thermal spraying for bioceramic applications, *Mater Forum*, 1990; 14: pp. 161-73.
127. Lin JHC, Liu ML, Ju CP., Structure and properties of hydroxyapatite-bioactive glass composites plasma sprayed on Ti-6Al-4V, *J Mater Sci Mater Med*, 1994; 5: pp. 279-83.
128. Brossa F, Cigada A, Chiesa R, Paracchini L, Consonni C., Adhesion properties of plasma sprayed hydroxyapatite coatings for orthopaedic prostheses, *Biomed Mater Eng*, 1993; 3: pp. 127-36.
129. Anselm K., The electropolishing of titanium and its alloys, *Metal Finishing*, , June 2004, pp. pp. 80-86.
130. Griffiths BJ, Gawne DT, Dong G., The erosion of steel surfaces by grit blasting as a preparation for plasma spraying, *Wear*, 194 (1996), pp. 95-102.
131. Finnie A, Grimaud P, McFadden DH., Fundamental mechanism of the erosion wear of ductile metals by solid particles, *Erosion, Prevention and useful Applications Symp*, ASTME, October 1977, pp. 36-58.
132. Hutchins IM., Mechanism of erosion of metals by solid particles, *Erosion, Prevention and useful Applications Symp.*, ASTME, October 1977, pp. 58-76.
133. Nishida S.-I, Young S, Hattori N, Tsuchiyama A., Evaluation of surface treatment of Ti-6Al-4V alloy specimens, *Computational and experimental methods*, vol 7, 2003, pp. 3-12.
134. Clyne TW, Gill SC., Residual Stresses in Thermal Spray Coatings and Their Effect on Interfacial Adhesion: A Review of Recent Work, *Journal of Thermal Spray Technology*, Vol.5(4), Dec 1996, 401.
135. Gill SC, Clyne TW., Stress Distributions and Material Response in Thermal Spraying of Metallic and Ceramic Deposits, *Mettallurgical Transactions B*, Vol. 21 B Apr 1990-377.

136. Gill SC, Clyne TW., Modelling of the Generation of Residual Stress During Thermal Spraying of Ceramic Coatings, High Performance Ceramic Films and Coatings, Vincenzini P. (Editor).
137. Gill SC, Clyne TW., Investigation of residual stress generation during thermal spraying by continuous curvature measurement, *Thin Solid Films*, 1994, 250, pp. 172-180.
138. Liu SS, Valle AGD, Besculides MC, Gaber LK, Memtsoudis SG., Trends in mortality, complications, and demographics for primary hip arthroplasty in United States, *International Orthopidics (SICOT)*, DOI 10.1007/s00264-008-0549-4, Springer-Verlag, 2008.
139. Kurtz S, Ong K, Lau E, Mowat F, Halpern M., (2007), Projections of primary and revision hip and knee arthroplasty in the United States from 2005 to 2030. *J Bone Jt Surg Am* 89: pp. 780–785.
140. Wroblewski BM., (1984), Current trends in revision of total hip arthroplasty. *Int Orthop* 8(2): pp. 89–93.
141. Berry DJ, Harmsen WS, Cabanela ME., (2002) Twenty-five-year survivorship of two thousand consecutive primary Charnley total hip replacements: factors affecting survivorship of acetabular and femoral components. *J Bone Jnt Surg Am* 84-A(2): pp. 171–177.
142. Ong A, Wong KL, Lai M., (2002) Early failure of precoated femoral components in primary total hip arthroplasty. *J Bone Jnt Surg Am* 84-A(5): pp. 786–792.
143. Maris I, Spyros I D, Victor K, Angela E, Konstantinos K., Mechanical failure of a Thompson's hemiarthroplasty stem 28 years post-implantation: an investigation with electron microscopy, *Journal of Materials Science: Materials in Medicine*, Volume 18, Number 6, June 2007 , pp. 1135-1139(5).
144. Bhatia M, Edge J., Fracture of hydroxyapatite coated prostheses: a report of two cases of stem failure in hip hemiarthroplasty, *European Journal of Orthopaedic Surgery & Traumatology*, (2004) 14: pp. 42-44.
145. Kobayashi S, Saito N, Horiuchi H., (2000), Poor bone quality or hip structure as risk factors affecting survival of total-hip arthroplasty. *Lancet* 355(9214): pp. 1499–1504.
146. Cameron HU., The two- to six-year results with a proximally modular noncemented total hip replacement used in hip revisions, *Clinical orthopaedics and related research*, nov, 1994, 298, pp. 47-53.
147. Bauer TW, Schils J., The pathology of total joint arthroplasty II. Mechanisms of implant failure, *Skeletal Radiology*, Volume 28, Number 9, Sep. 1999, pp. 483-497.

148. Meldrum RD, Wurtz LD, Feinberg JR., (2005), Does smoking affect implant survivorship in total hip arthroplasty? A preliminary retrospective case series. Iowa Orthop J 25: pp. 17–24.
149. Alberton GM, High WA, Morrey BF., (2002), Dislocation after revision total hip arthroplasty : an analysis of risk factors and treatment options. J Bone Jnt Surg Am 84-A(10): pp. 1788–1792.
150. Lavernia C, D'Apuzzo MM, Hernandez V, Lee D., Thigh pain in primary Total Hip Arthroplasty - The Effects of Elastic Moduli, The Journal of Arthroplasty, Vol. 19, No. 7 Suppl. 2, 2004.
151. Ulrich SD, Seyler TM, Bennett D, Delanois RE, Saleh KJ, Thongtrangan I, Kuskowski M, Cheng EY, Sharkey PF, Parvizi J, Stiehl JB, Mont MA., Total hip arthroplasties: What are the reasons for revision?, International Orthopaedics, DOI. 10.1007/s00264-007-0364-3, Apr. 2007.
152. Wroblewski BM., (1984), Current trends in revision of total hip arthroplasty. Int Orthop 8(2): pp. 89–93.
153. Heinz BC, von Mallek D., Survey of incidents associated with hip and knee replacements devices - Analysis of the surveillance and registration system for medical products for the year 2000 to 2002, Orthopidics, 2005, V. 34, 47-54, sep. 2007.
154. Chao J, Lopez V., Failure analysis of a Ti-6Al-4V cementless Hip Prosthesis, Engineering Failure Analysis 14, 822-830, 2007.
155. Ong A, Wong KL, Lai M, Garino JP, Steinberg ME., Early failure of a roughened surface, precoated femoral component in total hip Arthroplasty, The Journal of Bone and Joint Surgery (American) 84: pp. 786-792 (2002).
156. Rimnac CM, Wright TM, Bartel DL, Klein RB, Petko AA., Failure of Orthopedic Implants: Three case histories, Materials Characterization, 26, pp. 201-209, 1991.
157. Klein GR, Parvizi J, Vegari DN, Rothman RH, Purtill JJ., Total Hip Arthroplasty for Actual Femoral Neck Fractures Using Cementless Tapered Femoral Stem, The Journal of Arthroplasty, Vol. 21, No. 8, pp. 1134-1140, 2006.
158. Kishida Y, Sugano N, Ohzono K, Sakai T, Nishii T, Yoshikawa H., Stem Fracture of the cementless spongy metal lübeck hip prosthesis, The Journal of Arthroplasty, Volume 17 , Issue 8 , pp. 1021 - 1027.
159. Griza S, Reis Mm, Reboh Y, Reguly A, Strohaecker TR., Failure analysis of uncemented total hip stem due to microstructure and neck riser, Engineering Failure Analysis, 15 (2008), pp. 981-988.

160. Ducheyne P, de Meester P, Aernoudt E., Fatigue Fracture of the Femoral Component of Charnley and Charnley-Muller Type Total Hip Prostheses, J. Biomed. Mater. Res. Symposium, No. 6, pp. 199-219, 1975.
161. Rostoker W, Chjao EYS, Galante JO., Defects in failed stems of hip prostheses, Journal of Biomedical Materials Research, Vol. 12, pp. 635-651, 1978.
162. Harvie P, Haroon MM, Henderson N, El-Guindi MM., Fracture of the hydroxyl apatite- ceramic coated JRI-Furlong femoral component, J Bone Joint Surg [Br], 2007, 89-B, 742-5, Jan. 2007.
163. JRI Quality Complaints Records, JRI Ltd.
164. Design Drawings, JRI Ltd.
165. Blasting Specification, JRI work instruction (JRIC-22B); Section - Two, Issue - Three, 01 October 2004.
166. Process settings (ii) Cleaning Process, JRI work instruction (JRIC-22B); Section - Two, Issue - Three, 01 October 2004.
167. Parameter Listings, VPS Coating, JRI work instruction (JRIC-5.7b); Section - Five, Issue - Two, 07 January 2005.
168. Quality Checks, Coatings, JRI work instruction (JRIC-6.2); Section - Six, Issue - Thirteen, 02 December 2004.
169. Work Instructions, Polishing Shop, JRI work instruction (WI PS 01); Issue - Thirteen, 2005.
170. Work Instructions, Machine Shop, JRI work instruction (WI M/C 03); Issue - One, April 2005.
171. ASTM F 1160-91; 'Standard test method for constant stress amplitude fatigue testing of porous metal-coated metallic materials'.
172. ASTM F 1659-95; 'Standard test method for bending and shear fatigue testing of calcium phosphate coatings on solid metallic substrates'.
173. Maennig W., Statistical planning and evaluation of fatigue tests, International Journal of Fracture, 1975; vol.11, no.1, pp. 123-129.
174. NPL results report on residual stress analysis, December 2006.
175. Operating manual/instructions, Philip's XL40 analytical SEM.
176. Operating manual/instructions, alicon@ Infinitefocus IFM.
177. de los Rios ER., Experimental techniques to observe and monitor short fatigue cracks, Kluwer Academic Publishers. Advances in Fatigue Science and Technology, 1989; pp. 265-81.
178. Voort GFV., Microstructure of titanium and its alloys, Industrial Heating [0019-8374], 2006, vol:73, iss:8, pp.77 -84.
179. BS 4490:1989; 'Methods for micrographic determination of the grain size of steel'.

180. Zhang W., Short fatigue crack behaviour under different loading conditions, PhD thesis, University of Sheffield, 1991.
181. Rajasekaran B, Ganesh Sundara Raman S, Joshi SV, Sundararajan G., Performance of plasma sprayed and detonation gun sprayed Cu-Ni-In coatings on Ti-6Al-4V under plain fatigue and fretting fatigue loading, *Materials Science and Engineering, A* 479, 2008, pp. 83-92.
182. Morishita T, Kuramochi EK, Whitefield RW, Tanase S., Coatings with compressive stress, in proceedings of the International Conference on Thermal Spray, OH, 1992, pp. 1001-1004.
183. Angelova D, Akid R., A note on modelling short fatigue crack behaviour, *Fatigue and Fracture of Engineering Materials and Structures*, 1998, 21, pp. 771-779.
184. Wheelhouse K., Fatigue damage accumulation under torsion and non-proportional push-pull interruption loading, PhD thesis, Sheffield Hallam University, 2002.
185. Al-Alkawi HJM., Cumulative fatigue damage under varying stress range conditions, PhD thesis, University of Sheffield, 1986.
186. Kruzic JJ, Ritchie RO., Technical note; Kitagawa-Takahashi diagrams define the limiting conditions for cyclic fatigue in human dentin, Published online 29 September 2006 in Wiley InterScience (www.interscience.wiley.com). DOI: 10.1002/jbm.a.30939.
187. Hudak SJ Jr., Small crack behaviour and the prediction of fatigue life, *Transaction of the ASME*, 26, Vol.103, January 1981.
188. Moshier MA, Nicholas T, Hillberry BM., High cycle fatigue threshold in the presence of naturally initiated small surface cracks, *ASTM special publications*, 2002, 1417, pp. 129-146.
189. Murakami Y., editor. *Stress Intensity Factors Handbook*, 1st ed. Elmsford, NY: Pergamon; 1987. Vol. 1, pp. 640.
190. Tada H, Paris PC, Irwin GR., *The Stress Analysis of Cracks Handbook*. New York: ASME Press; 2000. pp. 677.
191. Material Test Certificate of Conformity, ATI Titanium International Ltd, 2005.
192. Fernando US., The influence of H-AC coating and shot blasting on the fatigue performance of Ti-6Al-4V titanium alloy, Report Ref: ENG/F3/C8/4790-1, School of Engineering, Sheffield Hallam University, September 2000.
193. Yates JR, Grabowski L., 1990. Fatigue lifetime assessment using a short crack growth model. *Proceedings of the Fourth International Conference on Fatigue and Fracture Thresholds, Fatigue '90*, Honolulu, Hawaii, July 1990, (Eds. H. Kitagawa and T. Tanaka), EMAS, Vol. IV, pp. 2369-2376.

APPENDIX.1: Information of failures at cone region of selected JRI stems. The information is based on the failure reports of JRI quality complaints.

CR No. & Location	Time in Situ	No. of initiations	Defects at initiation region	Possible cause (eg. manu, material, surgical, other)	Remarks
1999-047 Cone	2Y	Single	The pictures are not clear but possible surface feature which resulted transgranular fracture.	Manufacturing (a machining mark).	<ul style="list-style-type: none"> • Fan shape fracture appearance. • Evidence of rubbing and wear.
2000-025 Cone	8Y	Dominant single	Surface crack and foreign particulate matter	Manufacturing	<ul style="list-style-type: none"> • The surface crack is not clearly visible in SEM images. Post-fracture deformation damage at initiation area (rubbing two surfaces). • The particulate matter ($\approx 50\mu m$) is mainly contained <i>Si, Mg, O</i>, origin is not clear.
2000-031 Cone	2Y	Single	Notch like defects $d \approx 50\mu m$, $w \approx 60\mu m$	Manufacturing	<ul style="list-style-type: none"> • The hydrogen content is significantly above maximum level. • Notch like defect with particular contamination calcium rich. Not resulted from grit blasting.
2001-013 Cone	1Y	Single	Notch like defect $d \approx 50\mu m$, $w \approx 150\mu m$	Manufacturing	<ul style="list-style-type: none"> • Notch like defect with particulate contamination mainly <i>Al</i> and <i>O</i> rich; particle associated with grit blasting process.
2002-015 Cone	1Y 6M	Single	Inclusion particle at initiation $d \approx 25\mu m$, $w \approx 80\mu m$.	Manufacturing	<ul style="list-style-type: none"> • Particulate contamination rich with <i>Al</i> and <i>O</i> (EDX). Possibly associated with JRI grit blasting. • Chemical analysis confirms high Hydrogen content.
2002-023 Cone	4Y 9M	Single	No obvious defect at initiation according to the picture available in the report.	Not clear	Surface debris at initiation; these debris contain <i>C, Cl, O, S, K, I, Cu, Na</i> and <i>N</i> . These are not associated with manufacturing. No clear initiation feature according to the report.

APPENDIX.1; Contd.

2003-006 Cone	3Y 6M		The pictures are not clear to investigate.	Not clear	<ul style="list-style-type: none"> The report stated that occasional alumina particles appear which is resulted by JRI grit blasting.
2003-021 Cone	7Y 10M	Single	No obvious feature at initiation.	Not clear	<ul style="list-style-type: none"> The pictures are not clear enough to comment on initiation. Particulate matter with high <i>Ca</i> and <i>P</i> observed, probably loose H-AC from the coating.
2005-047 Cone	1Y 2M	Dominant single	1.No sign of stress concentration feature at the initiation. 2.Stepped like features at initiation due to initiation of number of cracks which eventually propagated to form a dominant crack.	Not clear No feature which responsible for nucleation of a crack can be identified.	<ul style="list-style-type: none"> Smooth transgranular fracture confirming HCF failure.
2006-003 Cone	1Y	Dominant single	Nucleation area does not show any specific reason or surface anomalies.	Not clear	<ul style="list-style-type: none"> Transgranular fracture confirming HCF failure. No severe plastic deformation.
2006-014 Cone	1Y 6M	Dominant single	Ratchet markings on fracture surface	Not clear	<ul style="list-style-type: none"> Orientation of surface crack path suggests that the initial crack has been nucleated approximately 45° inclined to the stem axis. Transgranular fracture confirming HCF failure.

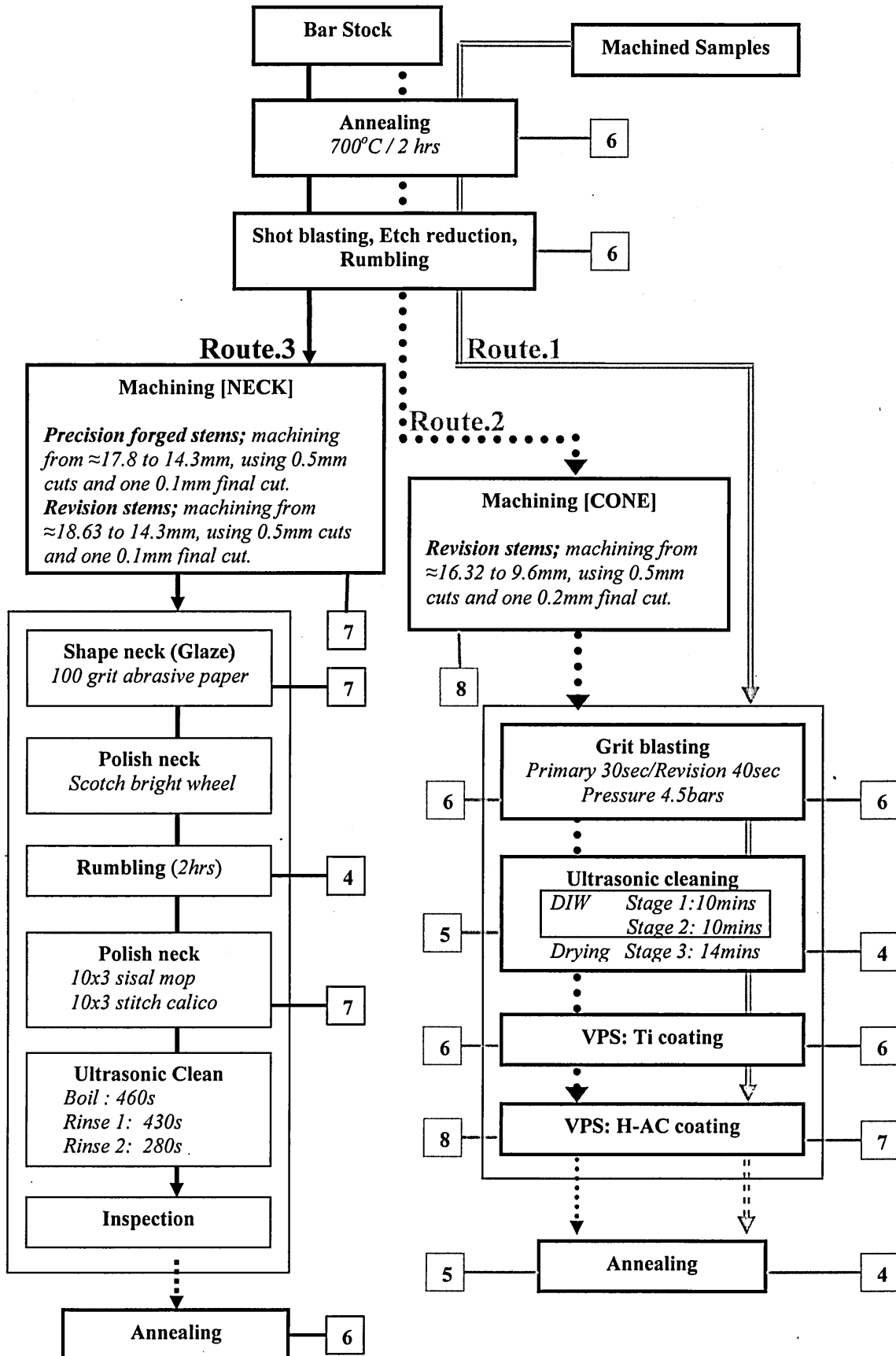
APPENDIX.2: Information of failures at neck region of selected JRI stems. The information is based on the failure reports of JRI quality complaints.

CR No. & Location	Time in Situ	No of initiations	Defects at initiation region	Possible cause (eg. manufacturing, material, surgical)	Remarks
1998-038 Neck	5Y	Single	1.Surface defects in the form of shrinkage cavities. 2.Tempered areas on stem collar face.	Manufacturing or material	<ul style="list-style-type: none"> • Deformation lip at the edge of the fracture (rubbing). • Tempered blooms on stem collar face (may be due to post sample preparation) • Shrinkage cavities can be due to solidification processes. • No foreign particles in the cavity.
2000-005 Neck	3Y 6M	Single	Surface scratches on the surface.	Manufacturing or surgical	<ul style="list-style-type: none"> • Slow fatigue propagation, implant was only just above its fatigue limit. • Evidence of scratches (due to surgery insertion or removal) or manufacturing finish. • Result of poor surface finish.
2000-021 Neck	1Y 6M	Single	Gouge marks ($>200\mu m$) at the initiation site.	Occurred during surgery or possibly post fracture or manufacturing.	<ul style="list-style-type: none"> • Folded over partial obscuring the initiation region. • Fine fatigue striations. • Gouge like defects.
2001-014 Neck	7Y	Single	1.Gouge marks($\approx 100\mu m$) (plastic deformation) 2.Surface contamination 3.Small surface anomaly (induced by ark strike)	Occurred during surgery or possibly post fracture or manufacturing.	<ul style="list-style-type: none"> • Gouge mark (mechanical deformation) mainly can be resulted during implantation or post fracture removal. It can be due to manufacturing. Also the mark can be initiated from a small surface defect due to manufacturing (e.g. machine mark). • Contamination rich in C, may due to handling and sample preparation • The arc strike can be due to coating process (but

APPENDIX.2; Contd.

					highly unlikely because the area is well masked) or at sample preparation. A surface defect at the initiation can be visible.
2001-036 Neck	3Y	Single	Notch like defect ($\approx 25\mu m$) with a particulate contamination (rich in C)	Manufacturing	<ul style="list-style-type: none">• Notch like feature and the polishing marks on the sample are remaining of manufacturing (can be polishing, rumbling).• Thumbnail region at initiation.• Microstructure not according to specifications.• Formation of lip like feature(post fracture damages) destroy the evidence and the initiation features• Faint beach marks/ rubbing of the surface. Nucleation does not show any specific reason.
2001-038 Neck	5Y	Single	1.Particulate matter($\approx 30\mu m$) not identified	Not clear	<ul style="list-style-type: none">• Thumb nail crack• Because of the lip formation no original fracture surface observable.
2003-023 Neck	NA	Single	Deformed lip at initiation.	Not clear	<ul style="list-style-type: none">• Shallow surface damage on the stem surface. Possible in surgical procedures or can be initiated from a small feature left from manufacturing (rumbling, polishing or machining), but less possibility.• Shape and locality of the damage shows Stage I fatigue crack.• Crack initiation region is damaged by severe plastic deformation/ can be post fracture rubbing.• Evidence of beach marks /high cycle fatigue
2003-045 Neck	3Y 8M	Single	1.Notch like damage at initiation. 2.Foreign particulate matter near initiation area (rich with Ca and P, H-AC particle deposited after fracture)	Surgical or Manufacturing	Significant amount of plastic deformation
2004-031 Neck	5Y 1M	Single	Not clear and no explanation regarding initiation.	Not clear	

APPENDIX.3: Description of production stages and method of sampling in three routes of implant manufacturing. Number of samples prepared at each stage is indicated in small boxes along with each process.





MANUAL ROUTE CARD

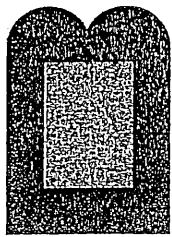
CATALOGUE No.	Qty 38 38	Job No. 13170
	Sales Order	Log No.
	Issued by PW	
	Material 12mm dia Ti-6Al-4V Barstock	
Description Rotary Bending Fatigue Specimens (For Cone)	Certificate No.	
	Drawing No. RBS 01	Drawing Issue No.
	Start Date 21/9/2006	Due Date ASAP

This is a quality record, please complete in detail at each operation, such as completion time at each operation and reason(s) for scrap. Use reverse of sheet if necessary.

ACCURATE TIMING IS ESSENTIAL FOR CORRECT COSTING OF PRODUCT

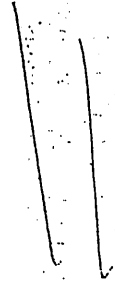
Operation No.	Operation	Qty Pass	Sign	Date	RUN Time	Remarks
1	Issue Material		<i>[Signature]</i>	11.10.06		
2	Ward Machine bar to length, chamfer and centre both ends.					
3	Act 3 produce radius, use .5mm cuts and .2mm finishing cuts as per distel end programs.	38	<i>[Signature]</i>	13.10.06		Parameters like tooling, coolant etc, should be similar to the 10mm HAC Machining practice.
4	Inspection. Check against shadowgraph. 100%	38	VKL	17/10/06		Check R=110mm & L=41.6mm 1st OK 12/10/06 VKL LAST OK 13/10/06 VKL
5	Return to PW					
6						
7						
8						
9						
10						
11						
12						
13						
14						
15						
16						
17						

Appendix 5: Annealing Specifications of the Fatigue Samples.



Bodycote Group

Member of Bodycote International Plc



FROM:

BODYCOTE HEAT TREATMENTS LIMITED
LINCOLN STREET
KOTTERHAM

VAI No: GB 593 6330 22
FAX No: 01709 928529
TEL: 01709 961047
S60 40G

INVOICE ADDRESS

JRI (MANUFACTURING) LTD
117 LEIGH STREET
ATTERCLIFFE COMMON
SHEFFIELD
SOUTH YORKSHIRE S9 2PS

DELIVERY ADDRESS

JRI (MANUFACTURING) LTD
117 LEIGH STREET
ATTERCLIFFE COMMON
SHEFFIELD
SOUTH YORKSHIRE S9 2PS

SERIAL 0783904
NUMBER
TRANSPORT DETAILS : YOURS
WORKS ORDER No. : 0685637
INCOMING ORDER No. : 26675
INCOMING CERT No.
MATERIAL SPEC/ISSUE No.: T1-6A1-4V
PAGE: 1
DATE: 270CT06
ORDER ENTRY DATE: 090CT06

LINE No.	JOB No.	DESCRIPTION	UNITS	QUANTITY
----------	---------	-------------	-------	----------

001		TEST PIECES Part No. VAC ANNEALED 2 Hrs @ 705+/-10c TEST PIECES	LOAD ITEMS	1.000 17.000
-----	--	---	------------	-----------------

Furnace Chge V1/18037

CERTIFICATE DECLARATION

Certified that the whole of the supplies/materials detailed hereon have been processed, inspected, tested and - unless otherwise stated - conform in all respects with the requirements of the contract, order or specifications.
The quality control arrangements adopted in respect of these supplies/materials have accorded with the conditions applicable to the following approvals:

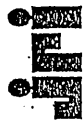
BS EN ISO 9001:2000 APPROVAL NO 05196

Certified that unless otherwise stated above, the whole of the above mentioned materials and/or parts have been processed and inspected in accordance with the terms of the contract/order applicable thereto and conform fully to the standards/specification quoted hereon and the requirements of the Civil Aviation Authority.

For and on behalf of:

BODYCOTE HEAT TREATMENTS LIMITED
Insp. Stamp

Signed:



MANUAL ROUTE CARD

CATALOGUE No.	Qty: 27 Nos. Hour Glass Samples	Job No.
	Sales Order.	Log No.
	Issued by.	
	Material: 27 nos. of Ti-6Al-4V Hour Glass Samples	
Description: Route 01: Cone Manufacturing Root for Precision Forged Stems. The samples are numbered 1 to 27.	Certificate No.: 26875	
	Drawing No.: RBS 01	Drawing Issue No.
	Start Date: 10/01/2007	Due Date: ASAP

This is a quality record, please complete in detail at each operation, such as completion time at each operation and reason(s) for scrap. Use reverse of sheet if necessary.

Operation No.	Operation	Qty Pass	Sign	Date	RUN Time	Remarks
1	Issue 27 Nos. of hour glass failgus samples.	2	MS	8/12/13	2	
2	<p>Ceramics Preparation</p> <p>Complete the following forms:</p> <p>Run number record</p> <p>Allocate sequential run number</p> <p>Run No. 07/87 + 07-88</p> <p>Drive No. 1, 3, 3, 2, 1, 3</p>	2	MS	8/12/13		
3	<p>Ceramics Grit Blast</p> <p>Follow the specs use in Furlong H-AC Titanium alloy stem grit blasting practice.</p> <p>Inspect 2 off from each run and test pieces (Roughness check - Rz=20-40, Visual check - blasted surface, blasting defects)</p> <p>Important: separate 6 Nos. samples (1-6) and remaining 21 samples proceed to the next stage.</p>	2	MS	8/12/13		All the parameters like pressure, velocity, grit type, exposure time and the distance between the nozzle to work have to be similar to the Furlong Titanium alloy H-AC stem grit blasting practice. Blasting process selling and specification: Refer JRIC-2.2B
4	<p>Ceramics cleaning (Ultrasonic)</p> <p>Stage 01 (DIW) : 10 mins</p> <p>Stage 02 (DIW) : 10 mins</p> <p>Stage 03 (Drying) : 14 mins</p> <p>Important: separate 4 Nos. samples (7-10) and remaining 17 samples proceed to the next stage.</p>	12	MS	8/12/13		Follow the same procedures and specs used to Furlong H-AC Titanium alloy stem.
5	Ceramics Inspection					Inspect all the samples.



MANUAL ROUTE CARD

6	Ceramics Masking Mask holding parts of the sample exposing middle (41.6 mm) hour glass section (pls. refer the attached drawing).	17	MA	01/02/07		
7	Ceramics VPS Coating (Step 01) Titanium bond coat only. Follow the specs used in Furlong H-AC Titanium alloy stem coating practice.	17	CB	01/02/07		Coat thickness, surface roughness, bond strength, crystallinity and all the software and hardware parameters have to be similar to which used in Furlong H-AC Titanium alloy stem. Coating parameters for titanium, Refer: JRIC-5.7b
8	Ceramics Inspection Remove masking tape. Check coating thickness. Visual inspection. Important: separate 6 Nos. samples (11-16) and remaining 11 samples proceed to the next stage.					Inspect all the samples. Quality checks and coating thicknesses, Refer: JRIC-6.2
9	Ceramics VPS Coating (Step 02) H-AC top coat. Adhere to the specs used in the Furlong H-AC Titanium alloy stem.	11	CB	01/02/07		Coat thickness, surface roughness, bond strength, crystallinity and all the software and hardware parameters should be similar to which used in Furlong H-AC Titanium alloy stem.
10	Ceramics Masking Remove the coated products.	11	MA	01/02/07		
11	Ceramics Inspection Remove masking tape. Inspection: coating thickness, uniform colour and coating defects.	11	CB	01/02/07		Inspect all samples. Quality checks and coating thicknesses, Refer: JRIC-6.2
12	Returned the samples (No. 17 to 27) to Dr. Anila Clark.					
13						
14						
Any additional remarks: Ruminda's Research Project						

Any additional remarks: Ruminda's Research Project



MANUAL ROUTE CARD

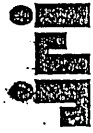
CATALOGUE No.	Qty: 38 Nos. Blanks	Job No.
	Sales Order	Log No.
	Issued by <i>Fun.../...</i>	
	Material: 38 nos. of Ti-6Al-4V Blanks	
Description: Route 02: Cone Manufacturing Root for Revision Stems. These samples are numbered from 40 to 77.	Certificate No.: 26875	
	Drawing No.: RBS 01	Drawing Issue No.
	Start Date: 10/01/2007	Due Date: ASAP

This is a quality record, please complete in detail at each operation, such as completion time at each operation and reason(s) for scrap. Use reverse of sheet if necessary.
ACCURATE TIMING IS ESSENTIAL FOR CORRECT COSTING OF PRODUCT

Operation No.	Operation	Qty Pass	Sign	Date	Run Time	Remarks
1	Issue 38 Nos. of blanks.					
2	Machining radius Act 3 procedure radius, use 0.5 mm cuts and 0.2 mm finishing cut as per distal end programs.	38	<i>[Signature]</i>	16/12/07	4 hrs	All the parameters like feed rate, tool type, coolant, cutting depth and finishing depth of cut should be similar to the 10 mm H-AC stem machining practice.
3	Inspection Check against shadowgraph (100%) Important: separate 8 Nos. samples (40-47) and remaining 30 samples proceed to the next stage. Send the remaining 30 samples to JAL (ceramics) Ltd please.					100% inspection. Check R= 110 mm and L= 41.6 mm.
4	Ceramics Preparation Complete the following forms Run number record Allocate sequential run number Split measuring ticket Run No. 07-110 / 07-111 Drive No. 1273 / 12	30				

Proquils

F403K Issue 7



MANUAL ROUTE CARD

3	Ceramics Grit Blast Follow the specs use in Furlong H-AC Titanium alloy stem grit blasting practice. Inspect 2 off from each run and test pieces (Roughness check - Row 20-40, Visual check - blasted surface, blasting defects) Important: separate 6 Nos. samples (48-53) and remaining 24 samples proceed to the next stage.	30			14/12/07 <i>[Signature]</i>	All the parameters like pressure, velocity, grit type, exposure time and the distance between the nozzle to work have to be similar to the Furlong Titanium alloy H-AC stem grit blasting practice. Blasting process setting and specification: Refer JRIC-2.2B
4	Ceramics cleaning (Ultrasonic) Stage 01 (DIW) : 10 mins Stage 02 (DIW) : 10 mins Stage 03 (Drying) : 14 mins Important: separate 5 Nos. samples (54-58) and remaining 19 samples proceed to the next stage.	30			16/12/07 <i>[Signature]</i>	Follow the same procedures and specs used to Furlong H-AC Titanium alloy stem.
5	Ceramics Inspection	19			17/12/07	Inspect all the samples.
6	Ceramics Masking Mask holding parts of the sample exposing middle (41.6 mm) hour glass section (pls. refer the attached drawing).	19			19/12/07	
7	Ceramics VPS Coating (Step 01) Titanium bond coat only. Follow the specs used in Furlong H-AC Titanium alloy stem coating practice.	6 Titanium bond coat only	19/12/07			Coat thickness, surface roughness, bond strength, crystallinity and all the parameters have to be similar to which used in Furlong H-AC Titanium alloy stem.
8	Ceramics inspection Remove masking tape. Check coating thickness. Visual inspection. Important: separate 6 Nos. samples (59-64) and remaining 13 samples proceed to the next stage.	13 Visual inspection	19/12/07			Coating Specifications for titanium, Refer: JRIC-5.7b Inspect all the samples. Quality checks and coating thicknesses. Refer: JRIC-6.2

Proquils

F403K Issue 7

Appendix.8: Manual Route Card for Manufacturing Fatigue Samples (Route.3).



MANUAL ROUTE CARD

CATALOGUE No.	Qty: 31 Nos. Blanks	Job No.
	Sales Order	Log No.
	Issued by	
	Material: 31 nos. of Ti-6AL-4V Blanks	
Description: Root 03: Neck Manufacturing Root for Neck area of the Stem. These samples are numbered from 78 to 108.	Certificate No.: 26875	
	Drawing No.: RBS 01	Drawing Issue No.
	Start Date: 10/01/2007	Due Date: ASAP.

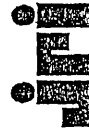
This is a quality record, please complete in detail at each operation, such as completion time at each operation and reason(s) for scrap. Use reverse of sheet if necessary.

ACCURATE TIMING IS ESSENTIAL FOR CORRECT COSTING OF PRODUCT

Operation No.	Operation	Qty Pass	Sign	Date	RUN Time	Remarks
1	Issue 31 Nos. of blanks.					
2	Machining radius Act 3 procedure radius, use 0.5 mm cuts and 0.1 mm finishing cut as per H-AC Neck machining programs.	31	<i>[Signature]</i>	9/2/7	5 hrs	All the parameters like feed rate, tool type, coolant, cutting depth and finishing depth of cut should be similar to the H-AC stem machining practice (Neck area). Last off OK. 15 OK 8-2-07
3	Inspection Check against shadowgraph (100%) Important: separate 7 Nos. samples (78-84) and remaining 24 samples proceed to the next stage.		<i>[Signature]</i>	9/2/7	6	100% inspection. Check R= 110 mm and L= 41.6 mm. Sample checks OK. Slag + Rainwater OK.
4	Glazing and Grinding 100 Grit abrasive paper Important: separate 7 Nos. samples (85-91) and remaining 17 samples proceed to the next stage.	24	<i>[Signature]</i>	9/2/7	10 min	The operations should use the same abrasive papers, grinding operations, polishing and grinding exposure time, to H-AC stem glazing and grinding practice (Neck area).
5	Polishing Scotch bright wheel.	17	<i>[Signature]</i>	9/2/7	10 min	All the parameters have to be similar to the polishing of neck and collar of Furlong H-AC Titanium alloy stem.

Proquis

F403K Issue 7



MANUAL ROUTE CARD

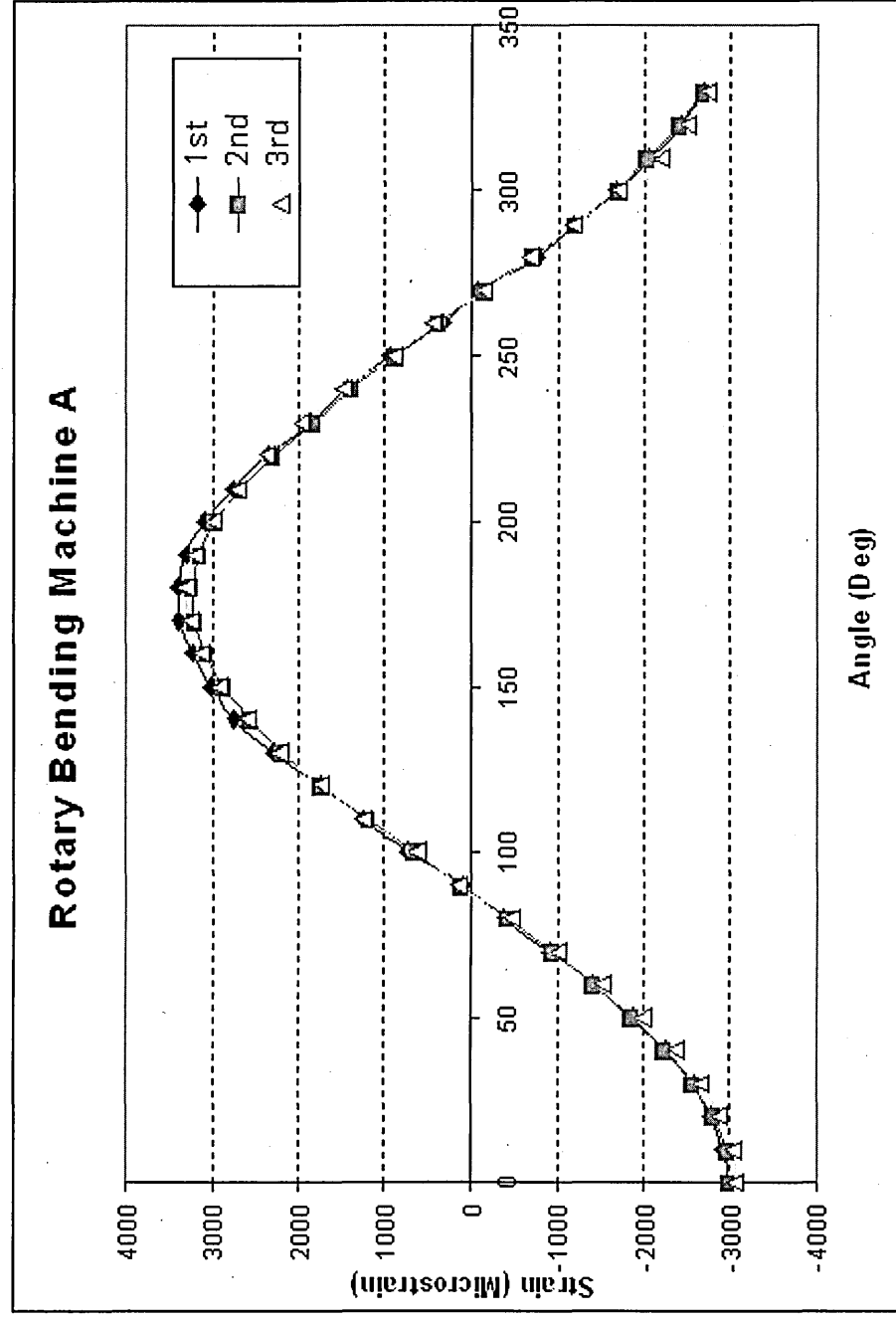
6	Rumbling 4 hrs. Important: separate 4 Nos. samples (92-95) and remaining 13 samples proceed to the next stage.	17	<i>[Signature]</i>	14/2/07	10 min	Adhere to same proc and specs which use Furlong H-AC Titanium stem.
7	Polishing 10 x 3 sisal mop 10 x 3 stitch calico Important: separate 7 Nos. samples (96-102) and remaining 6 samples proceed to the next stage.	15	<i>[Signature]</i>	14/2/07	15 min	Adhere to same proc and specs which use Furlong H-AC Titanium stem.
8	Ultrasonic cleaning Boil : 460s Rinse 1 : 430s Rinse 2 : 280s	6	<i>[Signature]</i>	14/2/07	5 min	Adhere to same proc and specs which use Furlong H-AC Titanium stem.
9	Inspection Dimensional and visual inspection. Shadowgraph inspection -					100% inspection.
10	Returned the samples (No. 103 to 108) to Dr. Anita Clark.					
11						
12						
13						
14						
15						
16						
Any additional remarks: Ruminda's Research Project						

Proquis

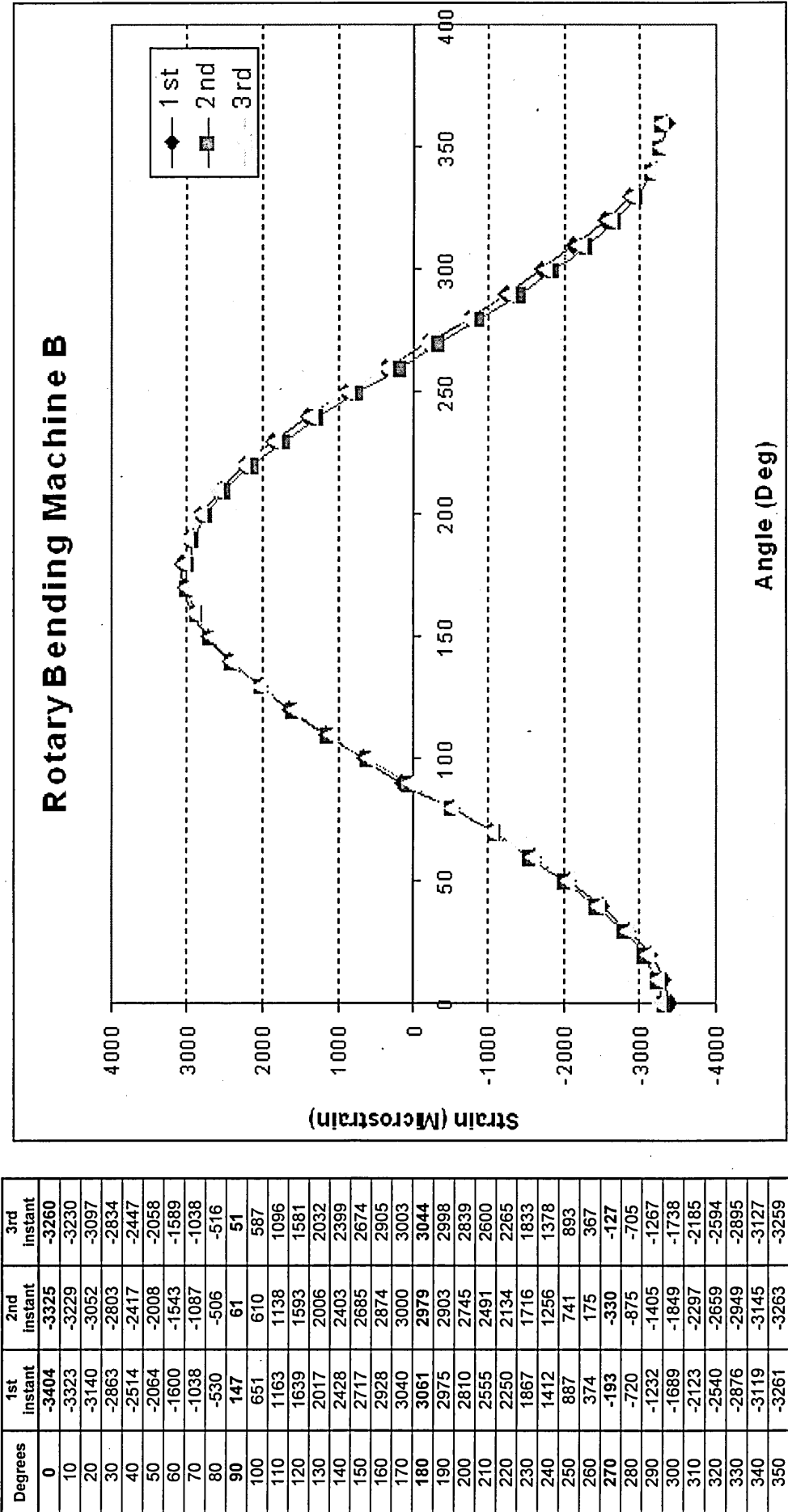
F403K

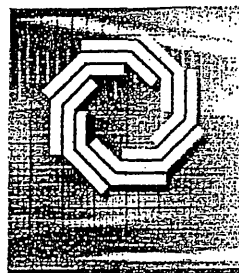
APPENDIX.9: Illustration of strain readings; calibration of Machine A.

Degrees	1st Instant	2nd Instant	3rd Instant
0	-2990	-2989	-3083
10	-2935	-2958	-3040
20	-2785	-2805	-2894
30	-2581	-2567	-2670
40	-2250	-2243	-2386
50	-1873	-1857	-2006
60	-1430	-1429	-1529
70	-910	-948	-1021
80	-393	-425	-484
90	77	118	145
100	736	667	613
110	1248	1185	1243
120	1740	1752	1741
130	2286	2194	2231
140	2745	2571	2578
150	3026	2869	2905
160	3241	3073	3124
170	3383	3210	3264
180	3398	3232	3295
190	3305	3149	3207
200	3097	2970	2987
210	2773	2681	2703
220	2372	2289	2360
230	1856	1835	1961
240	1449	1385	1486
250	927	901	906
260	309	369	441
270	-77	-143	-162
280	-769	-703	-689
290	-1197	-1206	-1197
300	-1678	-1689	-1720
310	-2057	-2019	-2199
320	-2445	-2399	-2513
330	-2695	-2679	-2750



APPENDIX.10: Illustration of strain readings; calibration of Machine B.





SHEFFIELD
TESTING LABORATORIES

50 - 56 Nursery Street, Sheffield, S3 8GP. U.K.
Telephone: 0114 272 6581 Fax: 0114 272 3248 e-mail: hq@sheffieldtesting.com

TEST CERTIFICATE



0136

Date. 25 October 20

Serial No. 51002011

Page 1 of 1 Page

ORDER NO. A3013184

OUR REF AB/AJH

CLIENT: SHEFFIELD HALLAM UNIVERSITY
SHEAF BUILDING
CITY CAMPUS
HOWARD STREET
SHEFFIELD
S1 1WB

Results of Chemical Analysis of One Sample,

<i>STL Test No.</i>	K224B
<i>Sample Description</i>	Sample (C) SHU - RM
<i>Carbon</i>	0.032%
<i>Aluminium</i>	6.40%
<i>Vanadium</i>	4.46%
<i>Iron</i>	0.27%
<i>Hydrogen</i>	38ppm
<i>Nitrogen #</i>	0.010%
<i>Oxygen #</i>	0.121%

Determined by Combustion, ICP OES & Thermal conductivity fusion Techniques.

Results marked # were subcontracted to a UKAS Accredited Laboratory.

Certified 

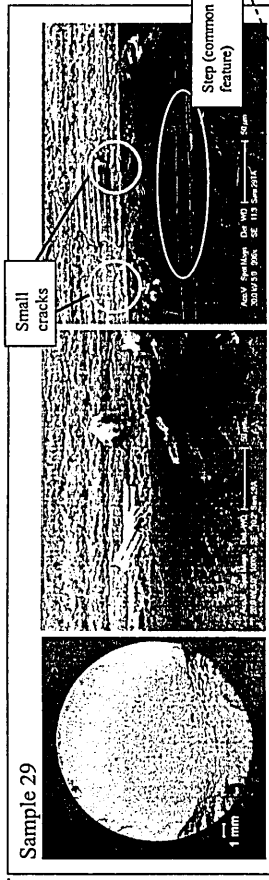
Authorised Signator
S. DEVINE

Appendix.12: Surface Roughness Measurement Results for All Stages of Phase.1 and Phase.2.

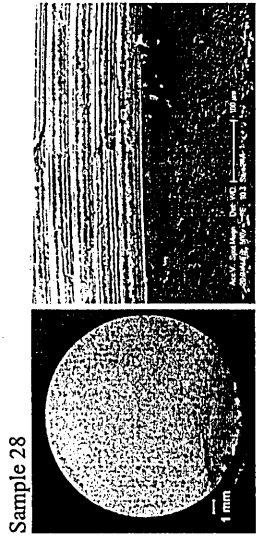
No.	Ra			Ave. Ra			Rv (max)			Ave. Rv(max)			Rp (max)			Ave. Rp(max)			Rv(max) +Rp(max)			Ave. Rv(max) +Rp(max)		
Polished samples (0.2µm finish)																								
A1	0.0176	0.0228	0.014	0.0187	0.018	0.0838	0.078	0.1271	0.0965	0.09685	0.0636	0.0901	0.0502	0.0738	0.069925	0.167								
A2	0.0473	0.0444	0.0462	0.0565	0.049	0.1467	0.462	0.1296	0.1803	0.22965	0.0938	0.0828	0.0926	0.1309	0.100025	0.330								
A3	0.0629	0.0691	0.0652	0.066	0.066	0.2444	0.2989	0.2313	0.2581	0.258175	0.0863	0.0888	0.0956	0.0957	0.0916	0.350								
A4	0.0728	0.0718	0.0743	0.0719	0.073	0.2433	0.2606	0.2905	0.2485	0.260725	0.0807	0.0861	0.0804	0.1744	0.1054	0.366								
A5	0.0094	0.0113	0.01	0.0092	0.010	0.0976	0.0888	0.1101	0.1042	0.100175	0.028	0.0351	0.0372	0.0308	0.032775	0.133								
A6	0.0169	0.0402	0.0203	0.027	0.026	0.1526	0.3229	0.2659	0.3105	0.262975	0.0731	0.1263	0.0567	0.0791	0.0838	0.347								
A1A	0.0124	0.0102	0.0101	0.0107	0.011	0.176	0.142	0.1587	0.0932	0.142475	0.104	0.0361	0.0371	0.0431	0.055075	0.198								
A2A	0.0293	0.0322	0.0295	0.0279	0.030	0.1655	0.2369	0.1329	0.0926	0.156975	0.0956	0.0899	0.0838	0.0864	0.088925	0.246								
A3A	0.0472	0.0432	0.0469	0.0465	0.046	0.1328	0.1902	0.1301	0.1739	0.15675	0.0879	0.0844	0.085	0.1114	0.092175	0.249								
A4A	0.0118	0.0111	0.0137	0.0159	0.013	0.1318	0.1866	0.1098	0.1405	0.142175	0.0352	0.0486	0.0392	0.0499	0.043225	0.185						0.2		
As machined Condition (6µm finish)																								
B1	0.4136	0.4062	0.3776	0.3797	0.394275	2.2452	3.0512	2.5833	2.8327	2.6781	1.3411	1.3753	1.4883	1.4	1.401175	4.079								
B2	0.6277	0.6093	0.6385	0.6291	0.62615	4.3357	3.5171	3.54	3.9133	3.827025	1.7653	1.896	1.9753	1.8239	1.865175	5.692								
B3	0.6944	0.6667	0.7778	0.7072	0.711525	6.7357	6.7956	6.1267	6.5979	6.563975	1.9176	2.2854	2.7102	1.8253	2.184625	8.749								
B4	0.5143	0.5272	0.498	0.5153	0.51375	6.6565	4.639	4.7287	7.3143	5.834625	1.9187	1.4453	1.5792	1.6531	1.649075	7.484								
B5	0.4232	0.4256	0.427	0.4215	0.424325	4.0872	3.4984	2.9798	3.936	3.62535	2.3261	1.7742	4.2734	2.247	2.655175	6.281								
B6	0.6658	0.7285	0.695	0.6459	0.6838	2.9562	3.3065	3.0841	2.6487	2.998875	1.9905	2.0367	2.0708	1.8002	1.97455	4.973								
B7	0.4884	0.4816	0.5492	0.5902	0.52735	3.021	2.3999	2.7631	2.8705	2.763625	1.8101	1.8458	2.8593	2.0968	2.153	4.917								
B8	0.3395	0.3174	0.3296	0.3241	0.32765	2.8101	2.5282	2.6079	2.7198	2.6665	1.0779	1.2327	1.4037	1.6733	1.3469	4.013						5.8		
21µm finish																								
C1	2.4213	2.5675	2.3583	2.326	2.418275	12.1603	10.9864	11.9917	9.8727	11.251775	13.5145	9.5154	12.9537	13.4233	12.351725	23.605								
C2	2.0216	2.0264	2.1382	2.1686	2.0887	9.5441	9.0351	14.3181	12.4701	11.34185	8.6112	7.7369	9.279	8.6383	8.57135	19.913								
C3	2.086	2.0365	2.0027	2.0749	2.050025	10.3449	8.8802	10.3642	9.7227	9.828	13.4429	7.8324	8.7444	7.8327	9.4631	19.291								
C4	2.2723	2.2435	2.0171	1.9712	2.126025	12.7258	12.1189	14.5618	13.5959	13.2506	8.4096	7.7757	10.2088	10.1277	9.13045	22.381								
C5	1.993	2.0621	2.3491	2.3884	2.19815	12.9852	13.5628	14.2845	13.9343	13.6917	8.6622	8.2316	11.1316	11.6315	9.914225	23.606								
C6	2.5572	2.521	2.2754	2.3179	2.417875	13.9638	13.8391	10.04	9.3062	11.787275	12.6855	11.8027	9.6127	9.2671	10.842	22.629								
C7	2.7053	2.8548	2.5403	2.6204	2.68025	13.1536	13.8992	14.8292	14.6116	14.1234	12.8519	12.8168	15.478	8.6378	12.446125	26.570								
C8	2.3522	2.3787	2.3544	2.4131	2.3746	10.862	11.1287	13.6882	12.3306	12.002375	10.5289	9.9684	8.3914	7.6578	9.136625	21.139								
D1A	1.7649	1.6223	1.5135	1.684	1.646175	9.1754	7.7018	7.9946	10.3734	8.8113	6.4181	9.7953	7.1966	7.9399	7.837475	16.649								
D2A	1.5173	1.4345	1.4348	1.6116	1.49955	10.0328	9.7938	9.2121	10.9102	9.984975	8.9037	6.7075	7.2321	11.2659	8.5273	18.512								
D3A	1.3113	1.3124	1.3021	1.216	1.28545	8.2061	6.4713	8.6118	8.6903	7.994875	6.1368	8.5025	8.816	11.9334	8.847175	16.842								
D4A	1.697	1.3353	1.5596	1.5338	1.531425	11.9959	10.333	9.9742	13.3141	11.4043	8.2803	7.4538	8.4962	9.8385	8.5172	19.922								
D5A	1.5204	1.673	1.5862	1.5087	1.572075	7.2422	9.4223	11.1381	10.67	9.61815	8.2207	7.8519	21.8927	8.5208	11.621525	21.240						20.9		
52µm finish																								
D1	5.0868	5.0339	4.8646	4.7564	4.935425	20.1117	25.4485	28.3764	23.5018	24.3596	28.8441	24.2132	18.8411	18.1022	22.50015	46.860								
D2	4.9783	5.0728	5.1017	4.8747	5.006875	20.3127	31.1211	29.1145	22.8179	25.84155	25.8278	19.7554	21.549	21.278	22.10255	47.944								
D3	4.6328	5.159	5.8436	4.7864	5.10545	28.739	23.4687	28.015	21.5265	25.4373	18.6988	32.994	24.0489	18.3958	23.534375	48.972								
D4	5.848	4.9362	4.8546	5.0292	5.167	30.8181	27.2064	22.7062	20.5985	25.3323	27.3382	18.1845	15.6092	16.1789	19.3277	44.660								
D5	5.8176	5.5491	6.1259	6.2562	5.9372	24.3497	29.5079	38.4459	31.4431	31.43665	29.8967	25.856	47.3055	22.6571	31.428825	62.865								
D6	7.487	6.1571	5.9716	5.619	6.308675	29.2697	24.9525	25.1656	27.6459	26.758425	44.7005	38.9958	25.7098	24.6433	33.51235	60.271								
D7	6.4275	6.0512	6.395	6.3314	6.301275	28.4824	31.6504	35.4045	25.8071	30.3361	28.0494	24.9003	31.9711	27.9806	28.32535	58.561								
C1A	4.9906	4.5874	4.759	4.0605	4.599375	24.2784	20.2006	25.79	21.7379	23.001725	35.3065	23.8542	22.0986	17.3562	24.653875	47.656								
C2A	3.2772	3.5499	4.2652	3.9433	3.7589	16.7871	26.5898	18.885	26.1474	22.102325	18.9605	41.5923	39.6336	16.7741	29.240125	51.342								
C3A	4.3662	4.0358	3.8331	4.5139	4.18725	20.4725	18.7278	20.7139	22.6243	20.634625	15.3275	18.3138	16.3513	34.1319	21.031125	41.666								
C4A	4.2323	4.6102	3.7648	4.0729	4.17005	17.866	18.8777	18.9661	17.6569	18.169175	47.8486	38.9554	21.7006	42.8161	37.830175	55.999								
C5A	3.9419	3.5304	3.7638	3.916	3.788025	29.968	31.8826	28.3829	22.2913	28.1312	41.5644	19.2733	15.0031	26.9146	25.68885	53.820						51.7		
Appendix.12 (contd)																								
Route 01: Stage A																								
28	0.644	0.6701	0.694	0.6734	0.670375	3.7584	4.1029	3.989	3.2011	3.76285	2.5115	5.4769	2.77	4.6311	3.847375	7.610								
29	0.5428	0.5694	0.5443	0.5229	0.54485	2.9307	3.0914	3.5193	2.4465	2.996975	4.2884	2.4113	3.2409	3.1724	3.06325	6.060								
30	0.8903	0.8858	0.8767	0.907	0.89	3.0024	2.8917	2.7628	2.7565	2.85335	2.9563	2.7782	3.03	3.1926	2.989275	5.843								
31	0.6372	0.6915	0.6464	0.6471	0.65555	3.2856	3.3511	2.7397	3.0605	3.109225	2.9236	3.2086	2.6661	2.7438	2.885525	5.995								
32	0.5959	0.6485	0.5993	0.5934	0.609275	3.4472	2.5588	2.1923	2.3974	2.648925	2.4686	3.2835	3.6753	3.1207	3.637025	6.286								
33	0.9015	0.8423	0.8105	0.8649	0.8548	5.0834	3.2417	3.0811	3.3565	3.690675	6.5604	3.6665	2.8595	4.1249	4.302825	7.994						6.6		
Route 01: Stage B																								
34	0.1577	0.2514	0.16	0.2079	0.19425	1.5278	7.4156	4.4726	5.8721	4.822025	0.5564	1.4672	1.0466	1.3925	1.115675	5.938								
35	0.1348	0.1571	0.1809	0.2281	0.175229	2.5134																		

Appendix.12: Contd.

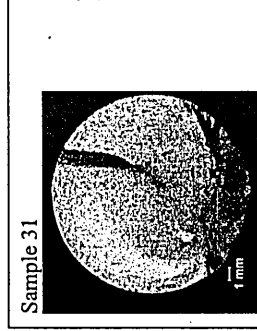
Route 02: Stage B																
40	0.9113	0.9837	0.9094	1.1035	0.9821	2.7019	4.4018	2.7888	7.2157	4.27705	2.6835	3.5145	2.8426	4.05	3.2739	7.551
42	1.092	1.0782	1.0592	1.0768	1.07655	2.6985	3.3813	3.483	3.0752	3.1595	3.5682	3.7664	3.3073	4.6423	3.8111	6.981
44	0.8029	0.8173	0.8045	0.8411	0.81645	2.384	2.5068	2.025	2.1546	2.2676	2.5999	2.8875	2.6319	3.3049	2.85605	5.124
46	0.9466	0.9059	0.9087	0.9192	0.9201	3.4155	2.8087	3.011	2.8964	3.0329	3.0844	3.0322	3.0167	3.0348	3.042025	6.075
47	0.7677	0.7379	0.7441	0.7739	0.7559	2.2677	2.1802	2.096	2.1728	2.179175	2.4383	2.6887	3.9356	2.8587	2.980315	5.160
Route 02: Stage C																
48	6.4235	5.9560	5.4966	5.5870	5.865775	26.7222	19.4474	22.7471	24.7035	23.40505	26.9978	28.4780	31.9791	20.4164	26.967825	50.373
49	6.2899	6.3218	5.5576	5.5594	5.957175	24.7670	27.2881	20.5625	22.0303	23.661975	22.4723	49.7180	28.0167	23.1645	30.842875	54.505
50	5.9126	5.5994	5.8820	6.1424	5.8841	21.1715	23.9847	24.9598	20.6588	22.6937	29.2856	28.2449	26.4888	22.7606	26.694975	49.389
53	5.1250	5.8228	5.7855	5.9547	5.672	20.2550	21.7573	27.0614	23.0802	23.038475	23.4951	35.7558	24.0613	23.5889	26.725375	49.764
Route 02: Stage D																
54	6.3300	5.3009	5.4311	5.7691	5.707775	24.1320	19.1801	23.3807	34.2855	25.344575	28.7140	23.6462	21.8800	34.9605	27.300175	52.545
56	5.0174	5.7137	5.6084	5.7890	5.531125	17.9396	27.6303	24.8402	24.8956	23.826425	19.5811	23.3846	26.6885	29.5422	24.7991	48.626
58	5.6152	5.7256	5.5098	5.5542	5.6012	22.5986	35.9238	21.0112	20.3515	24.971275	27.0980	23.2895	20.9168	25.8786	24.295225	49.267
Appendix.12 (contd)																
Route 02: Stage E																
59	10.0292	9.3396	10.5962	9.8724	9.90935	30.8839	33.1108	29.2375	28.2048	30.35925	40.5211	42.4801	57.2573	35.2640	43.880625	74.240
61	9.3777	8.7925	8.8314	8.9429	8.986125	30.1318	38.8898	27.8657	24.8926	30.394975	48.5776	42.3342	31.7529	41.5036	41.042075	71.437
62	9.4541	9.5382	9.2896	8.8676	9.287375	29.4879	29.2945	31.3659	34.2823	31.10765	41.1259	46.0172	39.0216	39.0849	41.3124	72.420
64	9.9596	10.1126	8.7464	9.4948	9.57835	34.0101	32.1053	29.4966	27.4439	30.763975	53.5482	39.9414	44.3335	46.3099	46.03325	76.797
Route 02: Stage F																
65	7.3438	5.5682	5.9990	6.1415	6.263125	26.6240	16.8032	22.4657	27.8354	23.432075	26.6596	23.4129	28.2675	30.1163	27.114075	50.546
67	6.8449	6.1351	5.8235	6.0475	6.21275	25.1226	21.5761	23.9669	20.1515	22.704275	31.1154	25.0630	35.3953	26.7711	29.5862	52.290
69	5.8135	7.2869	6.3986	5.2374	6.1841	23.1819	21.3917	26.3452	17.2480	22.0417	21.4397	34.2528	26.7498	21.7062	26.037125	48.079
71	6.2880	5.9526	5.9515	6.4384	6.157625	20.6021	20.5755	22.4023	17.9896	20.392375	26.7220	25.8903	27.0234	23.8703	25.8765	46.269
Route 02: Stage G																
73	6.4785	6.0588	5.3525	5.9018	5.9479	19.9923	21.0641	16.1196	17.3789	18.638725	27.2588	27.8795	21.1472	25.7264	25.502975	44.142
75	5.8296	6.1029	6.1620	5.9652	6.014925	20.0818	24.0919	20.0785	21.8475	21.524925	22.0075	32.3172	26.6531	29.0845	27.515575	49.041
77	6.8248	7.2963	5.6298	5.9938	6.436175	25.7306	24.1380	19.8463	19.6660	22.345225	34.9900	23.9646	21.3166	26.1488	26.605	48.950
Route 03: Stage B																
78	0.3801	0.3933	0.3871	0.4047	0.3913	1.597	1.3567	1.5332	1.4662	1.488275	1.88	1.9612	3.7113	2.6205	2.54325	4.032
79	0.3764	0.3963	0.3893	0.3661	0.382025	1.6406	2.3776	2.4532	1.5493	2.005225	2.2461	4.1491	1.817	1.6082	2.4551	4.460
83	0.3804	0.4154	0.3872	0.3546	0.3844	2.0802	2.2967	1.5308	1.4983	1.8515	1.4726	3.0359	1.4035	1.6817	1.898175	3.750
84	0.3833	0.4005	0.3772	0.3835	0.386125	1.8526	1.9141	1.5803	1.7931	1.785025	1.7948	3.1647	2.9055	2.8491	2.678525	4.464
Route 03: Stage C																
85	1.3679	1.4259	1.5012	1.702	1.49925	9.8797	11.4494	8.177	9.9463	9.8431	8.5242	6.9227	6.9556	7.9083	7.5777	17.441
86	1.115	1.0506	1.2182	0.9789	1.090675	9.2766	8.2798	6.941	6.2661	7.690875	6.0658	5.4059	5.2264	7.4117	6.02745	13.718
90	0.83959	0.9135	0.8066	0.7603	0.829975	4.4697	6.8696	5.5355	5.0721	5.486725	3.4683	7.4656	5.771	3.0089	4.92845	10.415
91	0.9571	0.7272	0.8496	0.8523	0.84655	6.2536	4.4341	6.0577	5.279	5.5061	4.937	4.5573	6.6409	4.4116	5.1367	10.643
Route 03: Stage D																
92	0.3141	0.3498	0.4412	0.3515	0.36415	2.6153	3.0136	3.1883	2.4088	2.8065	1.4281	4.9981	1.9674	2.4417	2.708825	5.515
95	0.3442	0.352	0.3385	0.3061	0.3352	2.5397	2.7025	2.1907	2.0306	2.365875	2.0036	1.7838	2.5308	2.414	2.18305	4.549
Route 03: Stage E																
96	0.0666	0.0829	0.0716	0.0638	0.071225	0.8661	0.3068	0.2311	0.5855	0.497375	0.2627	0.9757	0.2274	0.2532	0.42975	0.927
97	0.0752	0.0745	0.0675	0.0819	0.074775	0.3287	0.2835	0.8651	0.3417	0.45475	0.2922	0.2503	0.6848	0.3872	0.403625	0.858
101	0.0614	0.055	0.0684	0.0638	0.06215	0.2079	0.1985	0.2982	0.2238	0.3321	0.2464	0.3159	0.2674	0.2796	0.277325	0.509
102	0.0896	0.0969	0.0704	0.0542	0.077775	0.7681	0.4228	0.2129	0.2058	0.4024	0.3482	0.4438	0.2797	0.2514	0.330775	0.733
Route 03: Stage F																
103	0.0718	0.0717	0.0832	0.0661	0.0733	0.3031	0.2389	0.2859	0.2563	0.27105	0.2384	0.3935	0.79	0.3106	0.433125	0.704
104	0.0685	0.066	0.0665	0.0643	0.066325	0.3179	0.2525	0.216	0.2072	0.2484	0.2606	0.2108	0.2769	0.2621	0.2526	0.501
108	0.0656	0.0545	0.0837	0.0568	0.06515	0.3642	0.194	0.3346	0.1826	0.26885	0.2567	0.2083	0.3013	0.2283	0.24865	0.518



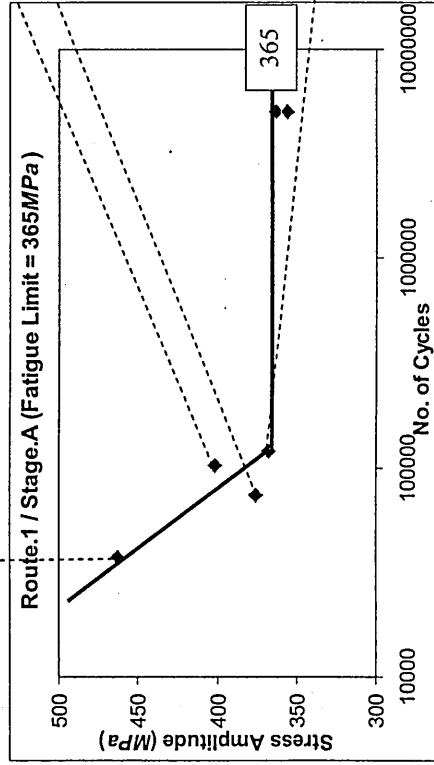
Sample 29



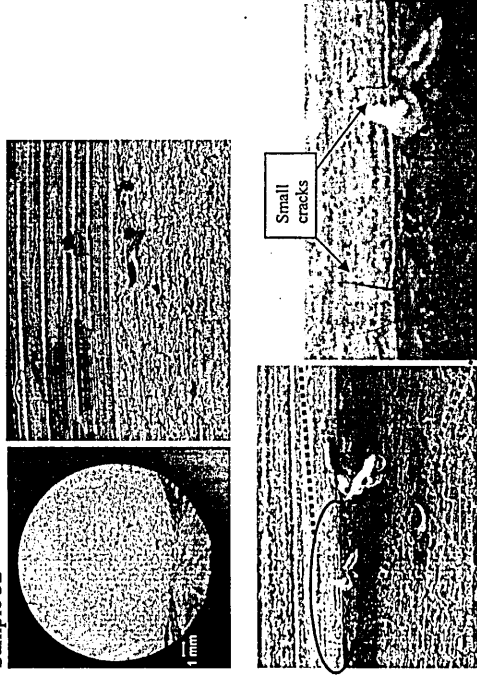
Sample 28



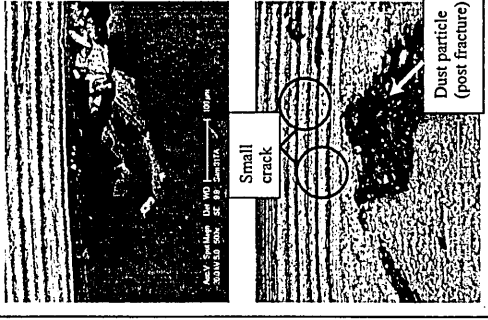
Sample 31



Sample 32



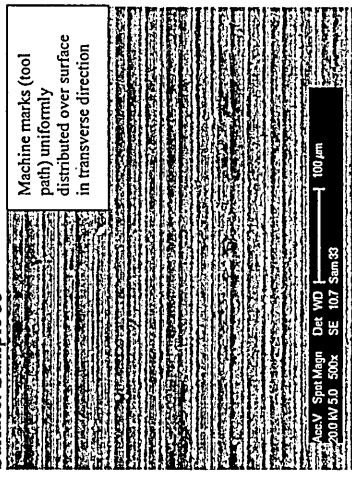
Sample 32



Sample 33

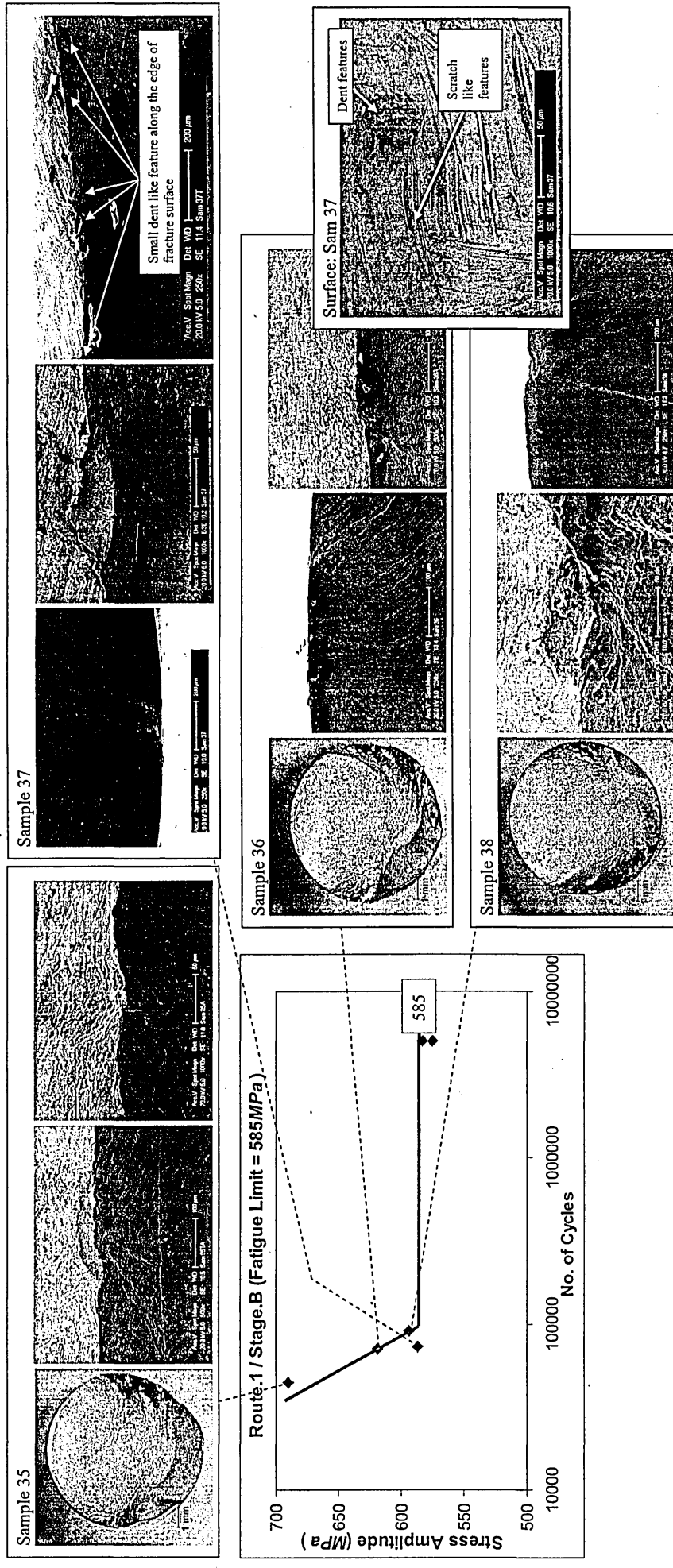
Sample No.	Stress Amp. (MPa)	No. of cycles	Surface roughness (μm), Residual stress (MPa)	No of crack initiation features: with remarks	Defects at initiation region	% fatigue vs overload	Comments related to manufacturing process
28	401	101940			Initiated and propagated along machine (tool) mark on the surface. Step like feature due to rubbing two fracture surfaces can be found just below the circumference.	85	Samples were machined in JRI Ltd, adhering to same machining procedures and parameters use to machine cone area of stem. 0.5mm cuts with a final 0.2mm cut.
29	463	37441	6.6 μm	Single dominant crack propagation.	Initiated and propagated along machine (tool) mark on the surface. Step feature below circumference. Crack like features on the surface near initiation area.	85	Surface picture shows evenly distributed machining marks, which can influence the initiation and propagation of fatigue failure.
31	376	74133	+136MPa	Initiated along the perimeter of the sample.	(tool) mark on the surface. The particulate matter found near the initiation area is post fracture contamination (EDX). Small cracks can influence the crack propagation to jump from one tool path to another to keep crack front at high stressed area.	75	
32	368	119223			Initiated and propagated along machine (tool) mark on the surface. Crack like features along surface near initiation area.	80	

Surface: Sample 33



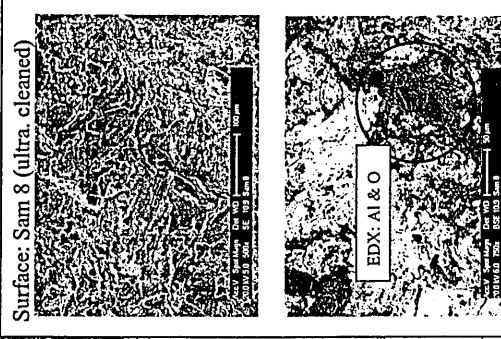
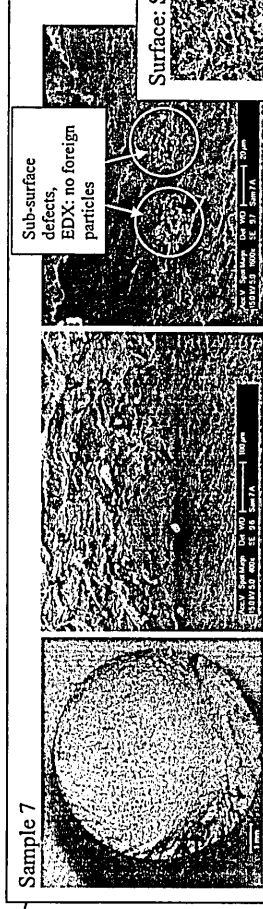
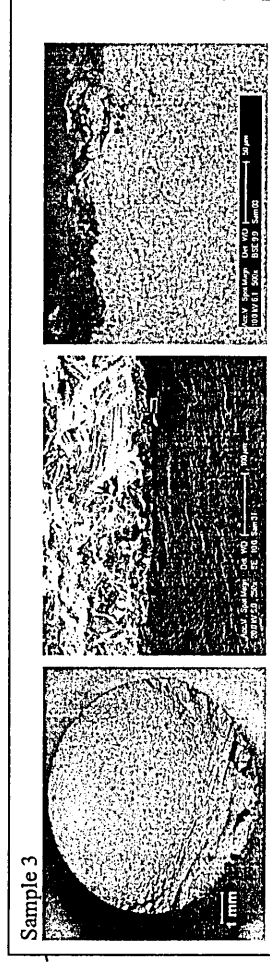
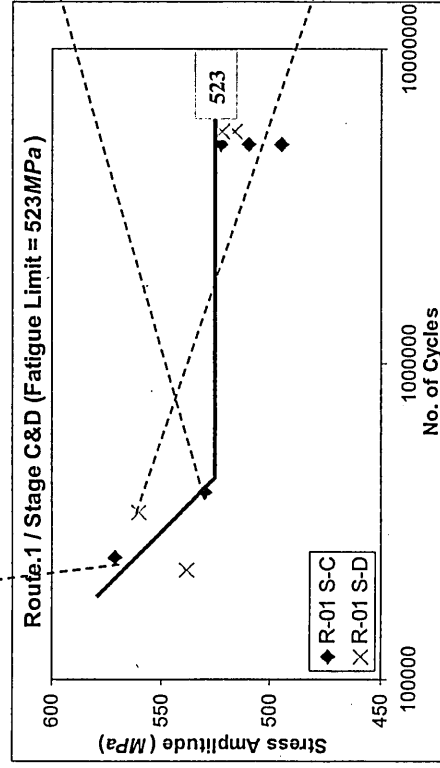
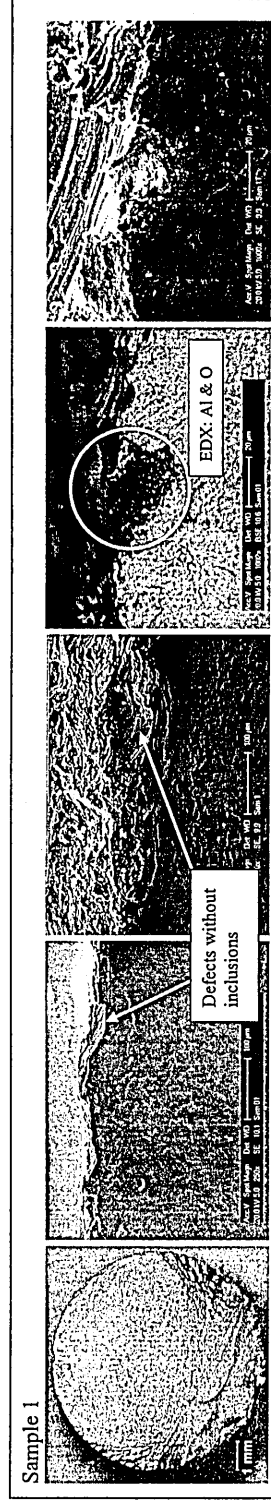
Machine marks (tool path) uniformly distributed over surface in transverse direction

APPENDIX.14; Route.1 / Stage.B (Sequence of manufacturing processes involved; machined – annealed - blasted and rumbled)



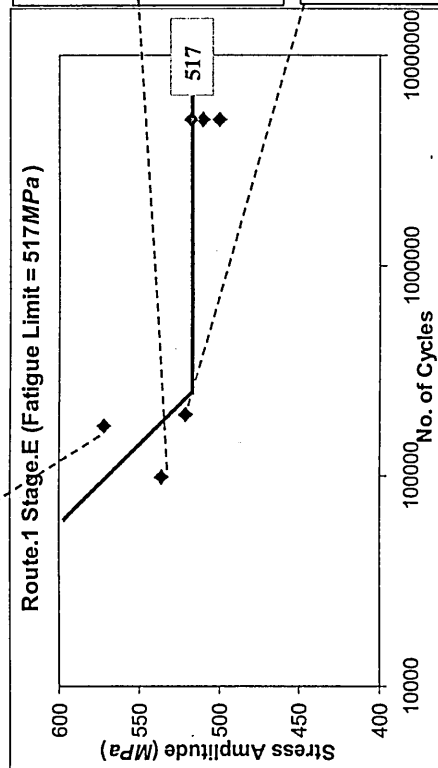
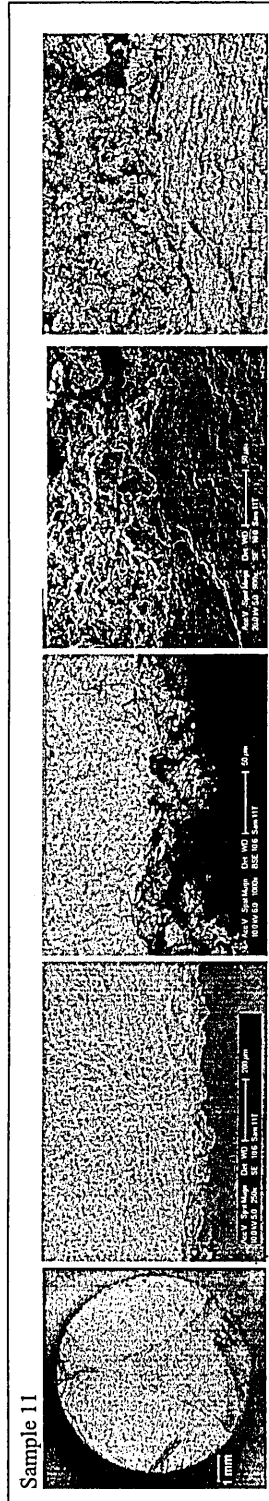
Sam No.	Stress Amp. (MPa)	No. of cycles	Surface roughness (μm), Residual stress (MPa)	No of crack initiation features: with remarks	Defects at initiation region	% fatigue vs overload	Comments related to manufacturing process	Comments related to JRI in-vivo failures (cone region)
35	690	43954		Single initiation; Initiated from a surface dent ≈420μm.	Surface feature possibly due to blasting and rumbling. Step like feature due to rubbing two fracture surfaces.	60	The indentations/dents at initiation points are possibly due to blasting/ rumbling media used. The surface of the samples clearly shows similar dent features distributed through the sample surfaces along with different other indentation features like scratches. Even Ave (Rp+Rv) is 4.1μm the depth of surface indentations/dents are about 30μm –50μm.	1. Surface defect at initiation, transgranular fracture surface.
36	619	70588	4.1μm	Single initiation; Initiated from a surface dent ≈80μm.	Surface feature possibly due to blasting and rumbling. Visible lip like feature.	55		2. Small notch like defect at initiation. More likely due to a manufacturing defect or during the surgery.
37	587	72302		Single initiation; Initiated from a surface dent ≈75μm.	Surface feature possibly due to shot blasting and rumbling. Small dent like feature distributed near edge. Feature like these can influence the propagation of failure.	60		3. Small notch like defect at initiation.
38	594	90761	-431MPa	Single initiation; Initiated from a surface dent ≈100μm.	Surface feature possibly due to shot blasting and rumbling. Step like feature. One surface shows lips like feature.	65		

APPENDIX.15; Route.1 / Stages C&D (Sequence of manufacturing processes involved; machined – annealed – grit blasted and rumbled – grit blasted and rumbled – ultra-sonic cleaned)



Sam No.	Stress Amp. (MPa)	No. of cycles	Surface roughness (μm), Residual stress (MPa)	No of crack initiation features; with remarks	Defects at initiation region	% fatigue vs overload	Comments related to JRI manufacturing process	Comments related to JRI in-vivo failures (cone region)
1	571	244727	47 μm	Single dominant initiation.	Dent like feature, possible inclusion $\approx 40\mu\text{m}$ wide and $\approx 30\mu\text{m}$ depth.	65	EDX analysis shows the initiation area is rich with Al and O. Possible inclusion due to Grit blasting.	1. Particulate matter at initiation rich with Al and O, possibly alumina from grit blasting process. 2. Surface defects in the form of cavity near initiation area
3	530	391925		Single dominant initiation.	Initiated from a dent like feature $\approx 20\mu\text{m}$ deep, resulted from unevenness of the surface due to grit blasting.	70	These dent like features may also resulted from rumbling process.	
7	560	339710	-308MPa	Single dominant initiation.	Visible sub-surface features closer to initiation. Possibly be material imperfection or may be post fracture.	70	Rough surface with irregularities due to blasting.	
8	538	222756		Single dominant initiation.	Dent like feature, possible inclusion $\approx 40\mu\text{m}$ wide and $\approx 40\mu\text{m}$ depth.	65	These dent like features may also resulted from rumbling process.	

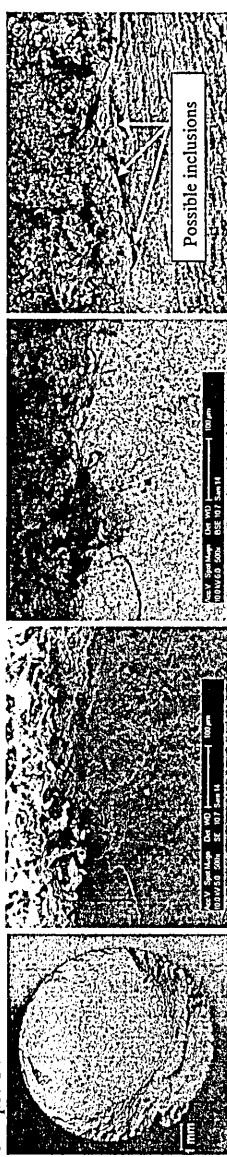
APPENDIX.16; Route.1 / Stage.E (Sequence of manufacturing processes involved; machined – annealed – grit blasted and rumbled – grit blasted and rumbled – cleaned – Ti coated)



Sample 13

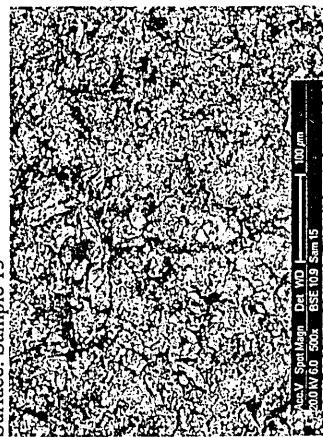


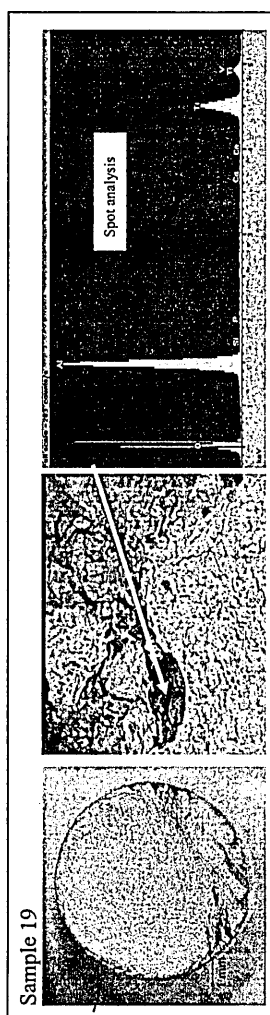
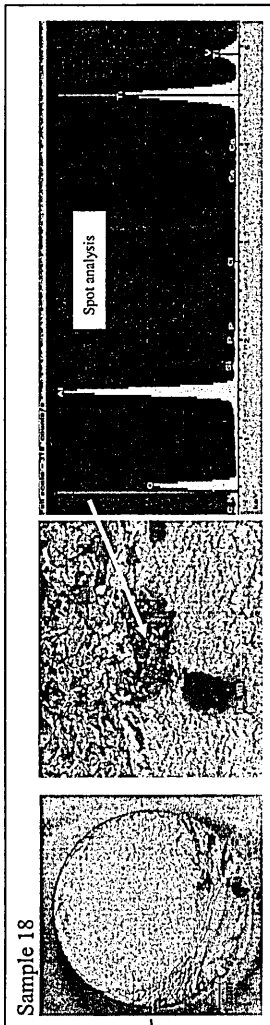
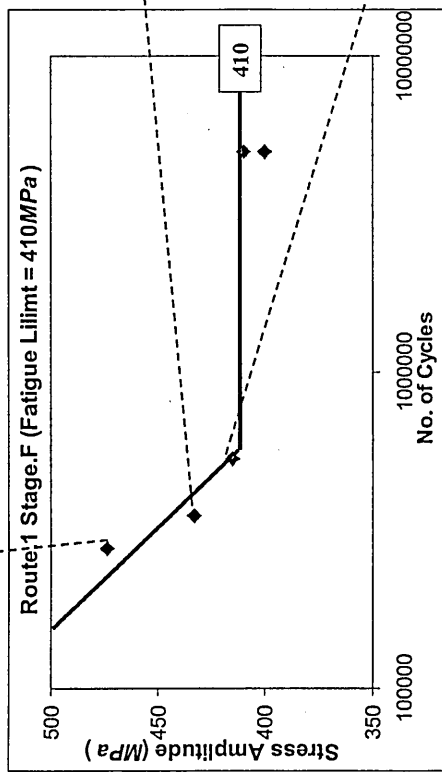
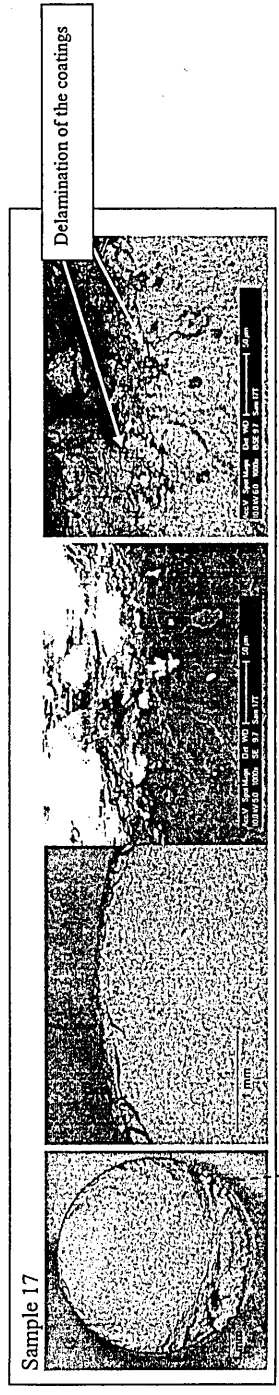
Sample 14



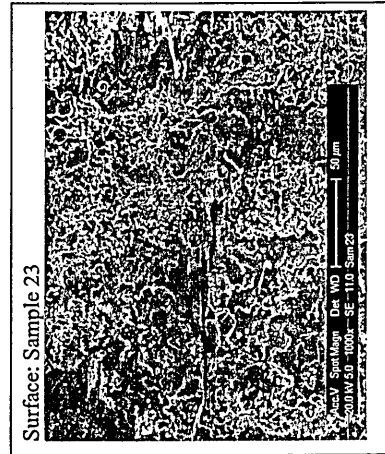
Sam No.	Stress Amp. (MPa)	No. of cycles	Surface roughness (µm), Residual stress (MPa)	No of crack initiation features with remarks	Defects at initiation region	% fatigue vs. overload	Comments related to JRI in-vivo failures (cone region)
11	572	171674	72µm +9.5MPa	Two dominant initiation points.	Initiated from the Ti/Ti-6Al-4V substrate. Step like features can be found due to HCF transgranular fracture.	50	Fatigue crack initiated and propagated from dominant fatigue crack is a typical feature of fatigue in H-AC coated titanium implant failures at cone region.
13	536	98967		Fatigue crack initiation 50µm span and finally propagated from dominant fatigue crack. This pattern of fatigue crack initiation is a typical feature of fatigue in Ti and also H-AC coated titanium samples.	Initiated from the Ti/Ti-6Al-4V substrate. The Ti coating is separated from Ti-6Al-4V near initiation.	60	
14	521	196242			EDX analysis reveals there are no foreign elements at the initiation region. The dent like feature ~80µm can be formed when grit blasting/rumbling.	70	

Surface: Sample 15

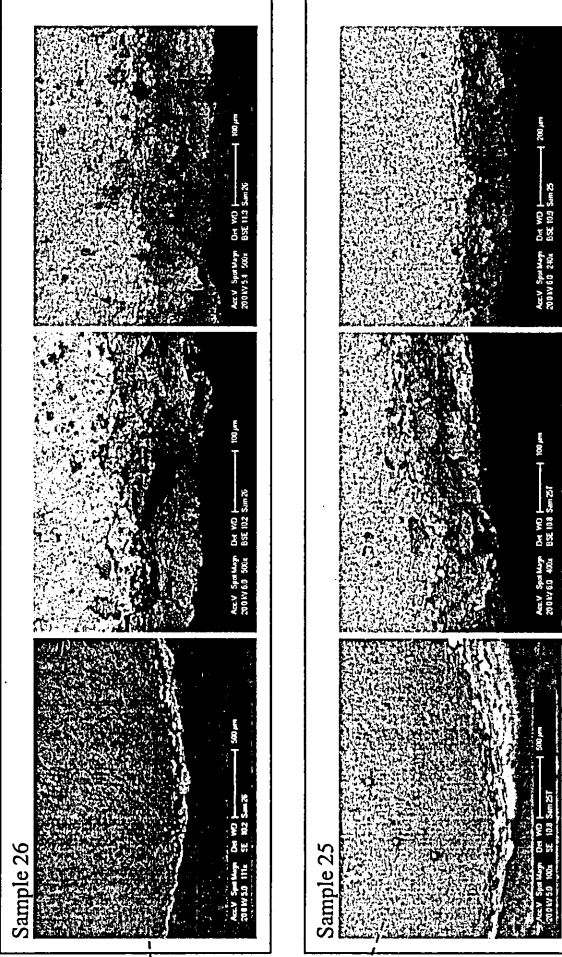
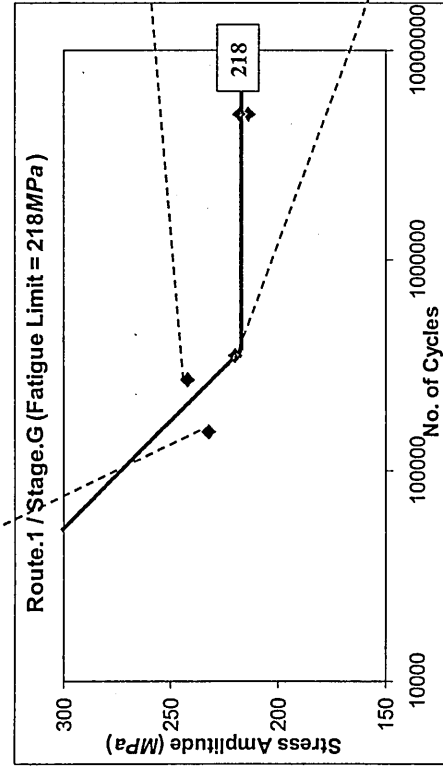
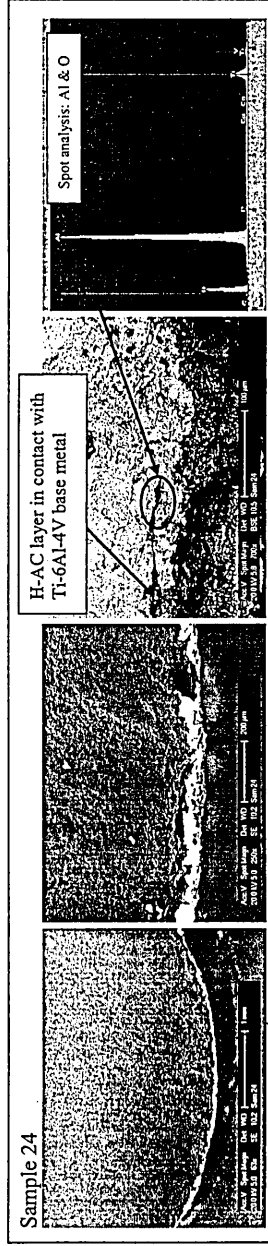




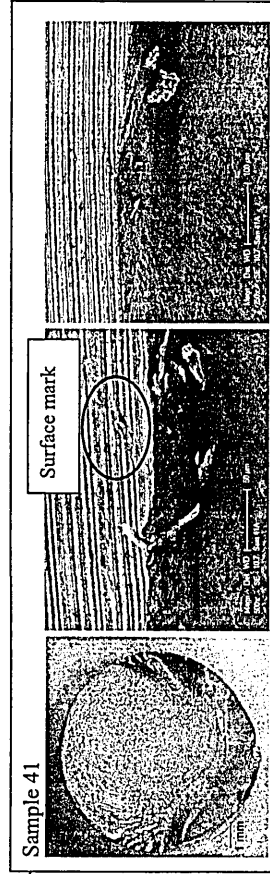
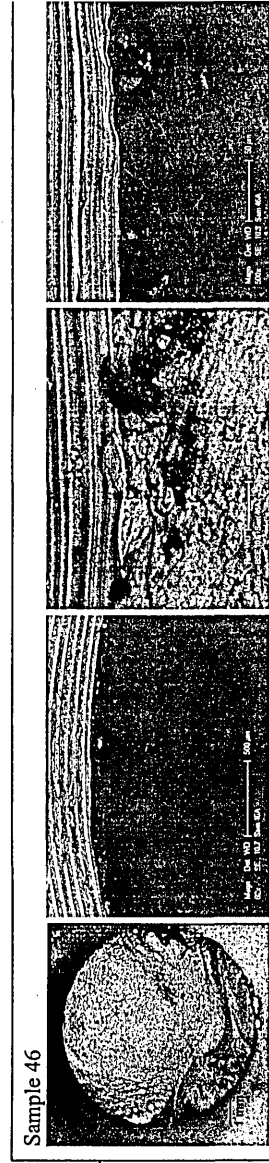
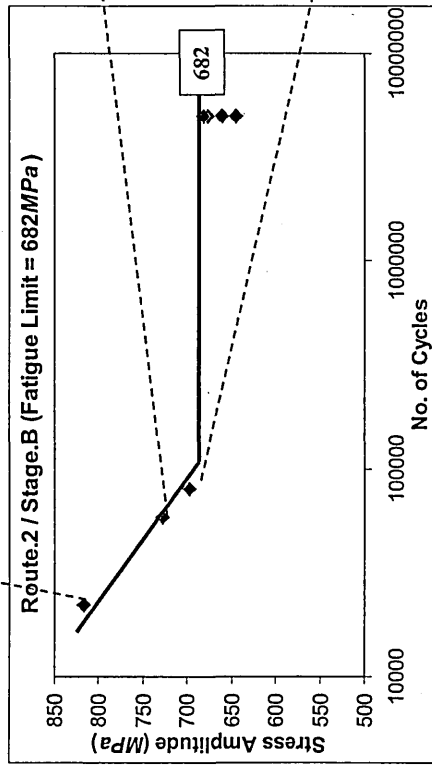
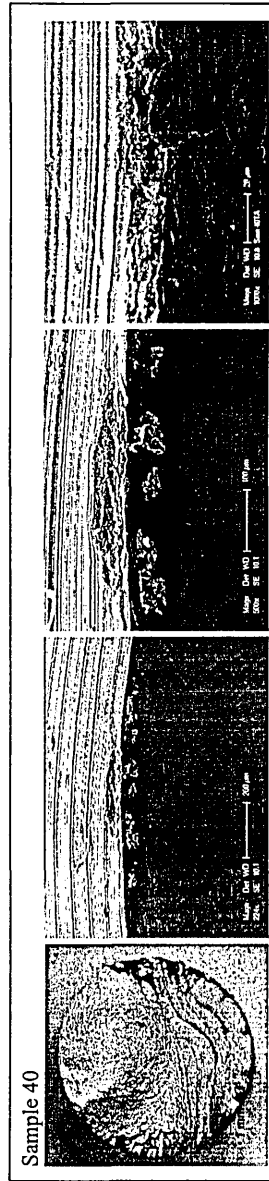
Sam No.	Stress Amp. (MPa)	No. of cycles	Surface roughness (μm), Residual stress (MPa)	No of crack initiation features with remarks	Defects at initiation region	% fatigue vs overload	Comments related to JRI manufacturing process	Comments related to JRI in-vivo failures (cone region)
17	474	277470	Surface roughness and residual stress value of the H-AC layer would not effect to fatigue performance.	Dominant single initiation. Stepped area at the initiation due multiple initiations with small area, but propagate from dominant fatigue crack.	Fatigue failure initiated at Ti/Ti-6Al-4V interface. Transgranular fracture.	70	Delamination of the coating layers at initiation.	1. Stepped area at the initiation due multiple initiations, but propagated from dominant fatigue crack.
18	433	350944	H-AC layer was removed from randomly selected sample (Sam. 72) and the residual stress status is identical to Ti coated samples in Stage.E.		Fatigue failure initiated at Ti/Ti-6Al-4V interface. Foreign particle at initiation.	70	Initiated at Ti/Ti-6Al-4V interface. Contamination rich with Al and O, found at the initiation area, which are possibly due to alumina particles embedded during grit blasting process.	2. Transgranular fracture 3. Inclusion (alumina) at initiation.
19	415	531225			Fatigue failure initiated at Ti/Ti-6Al-4V interface. Foreign particle at initiation.	70		4. Inclusion (alumina) at initiation/ transgranular striations on fracture surface.



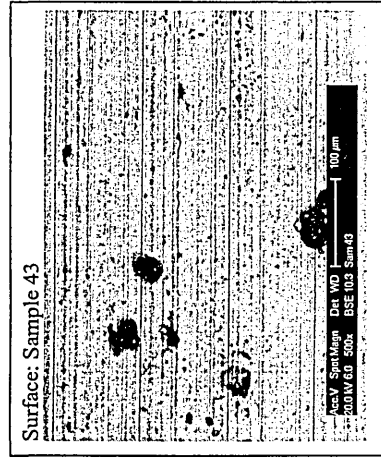
APPENDIX.18; Route.1 / Stage.G (Sequence of manufacturing processes involved; machined – annealed – grit blasted and rumbled – grit blasted and rumbled – ultrasonic cleaned – Ti coated – H-AC coated – annealed)



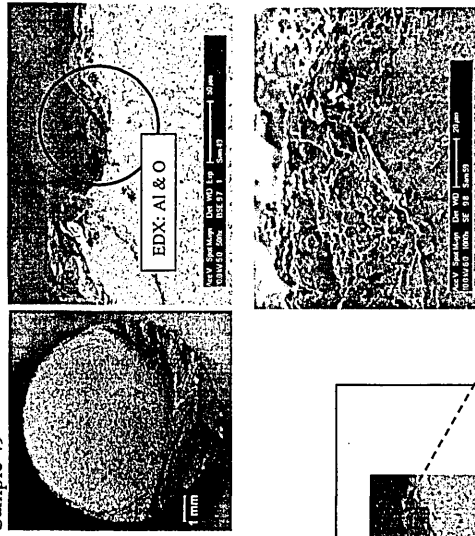
Sam No.	Stress Amp. (MPa)	No. of cycles	Surface roughness and Residual stress (μm), (MPa)	No of crack initiation features: with remarks	Defects at initiation region	% fatigue vs overload	Comments related to JRI manufacturing process
24	232	152365	Surface roughness and residual stress value of the H-AC layer would not effect to fatigue performance. H-AC layer was removed from randomly selected sample (Sample. 72) and the residual stress status is identical to Ti coated samples.	Dominant single initiation. Stepped area at the initiation due to multiple initiations with small area, but propagate from dominant fatigue crack.	Fatigue failure initiated at Ti/Ti-6Al-4V interface. Foreign particle at initiation (Al, O).	65	Contamination rich with Al and O is found at the initiation area, which are possibly due to alumina particles embedded during grit blasting process.
25	220	348068			Fatigue failure initiated at Ti/Ti-6Al-4V interface. Delamination of coatings.	70	Initiated at Ti/Ti-6Al-4V interface. No clear initiation feature at the nucleation area.
26	242	268110			Fatigue failure initiated at Ti/Ti-6Al-4V interface. Delaminating of coatings.	65	



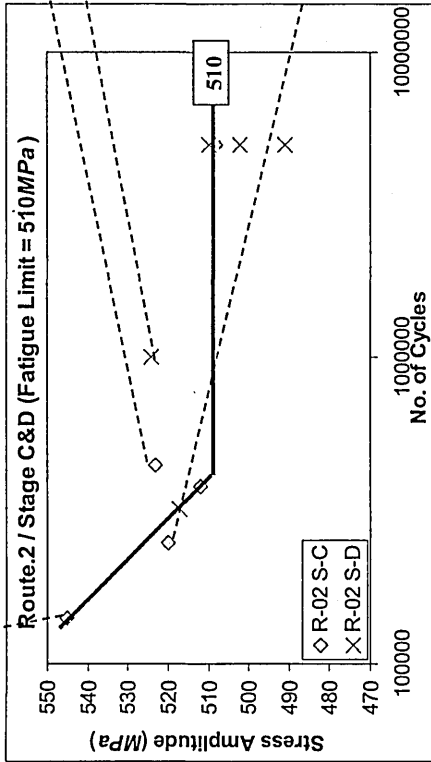
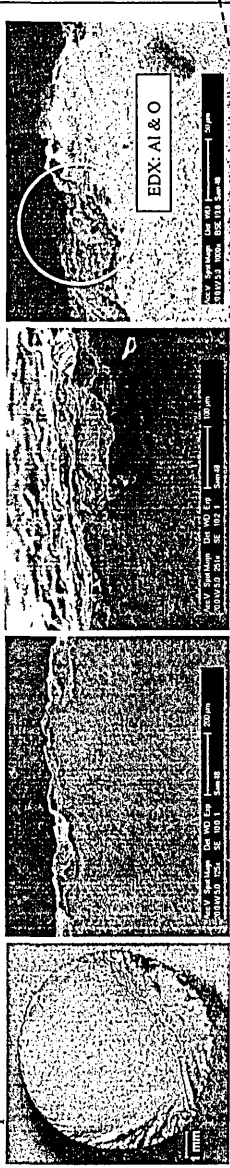
Sam No.	Stress Amp. (MPa)	No. of cycles	Surface roughness (μm), Residual stress (MPa)	No of crack initiation features; with remarks	Defects at initiation region	% fatigue vs. overload	Comments related to JRI manufacturing process	Comments related to JRI in-vivo failures (cone region)
40	816	21854		Single initiation.	Initiated and propagate along machining mark. A dent w $\approx 100\mu m$, d $\approx 20\mu m$ at initiation area.	50	Samples were machined in JRI Ltd, adhering to same machining procedures and parameters use to machine cone area of stem.	1. Fatigue originated by the influence of machined marks. Initiated from a small imperfection on the surface.
41	698	79376	6.2 μm	Single initiation.	Initiated and propagate along machining mark. Surface mark can be found on the surface and initiation coincides with this feature.	60	0.5mm cuts with a final 0.2mm cut.	
46	757	57848	-424MPa	Single initiation.	Initiated and propagate along machining mark. Surface feature $\approx 20\mu m$ at initiation. Can occurred due to rubbing of two fracture surfaces.	60		



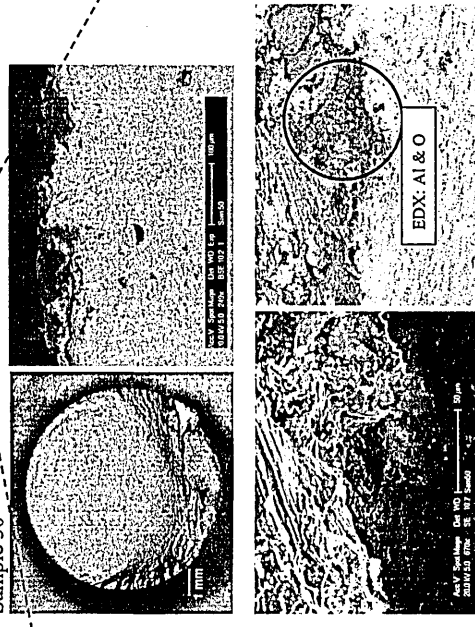
Sample 49



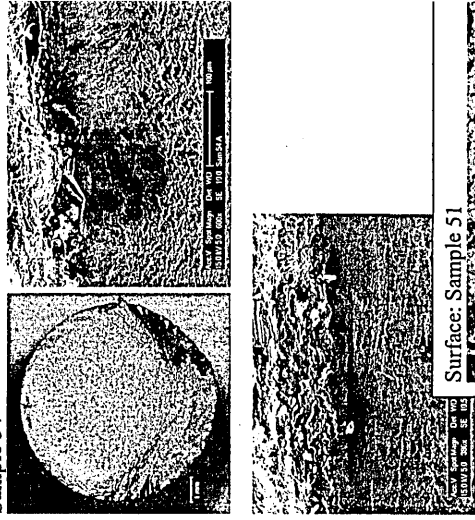
Sample 48



Sample 50



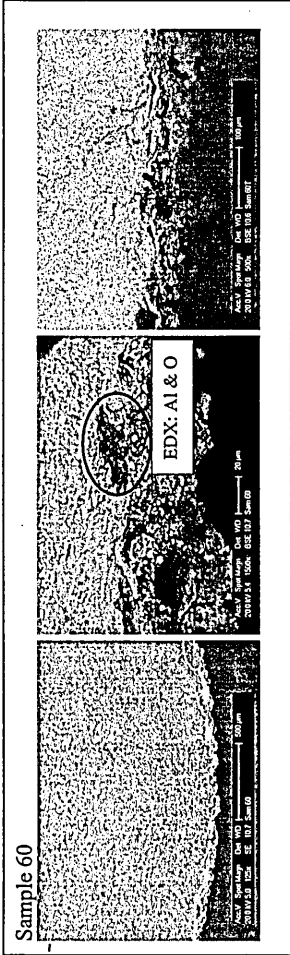
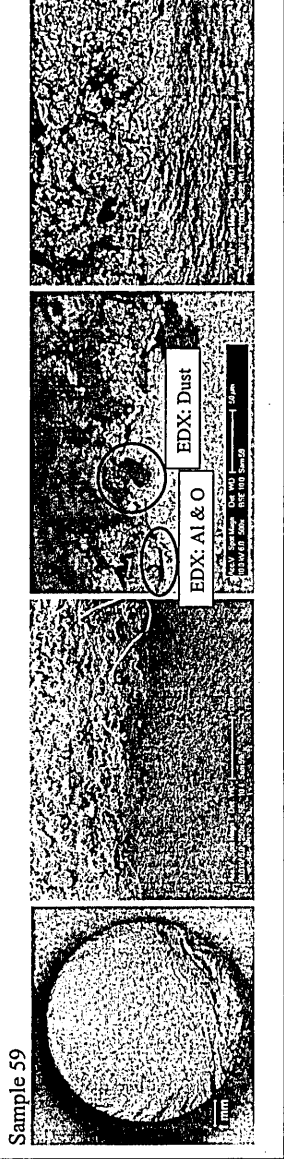
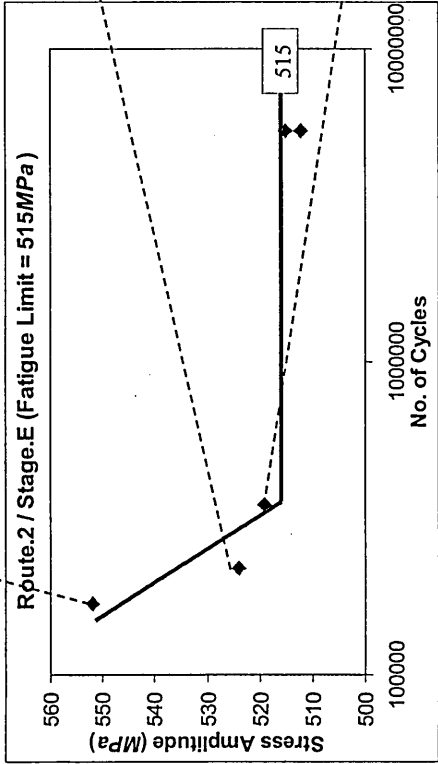
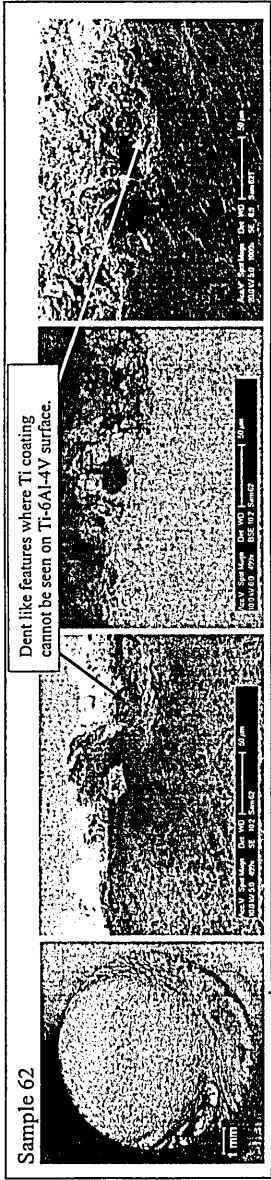
Sample 54



Surface: Sample 51

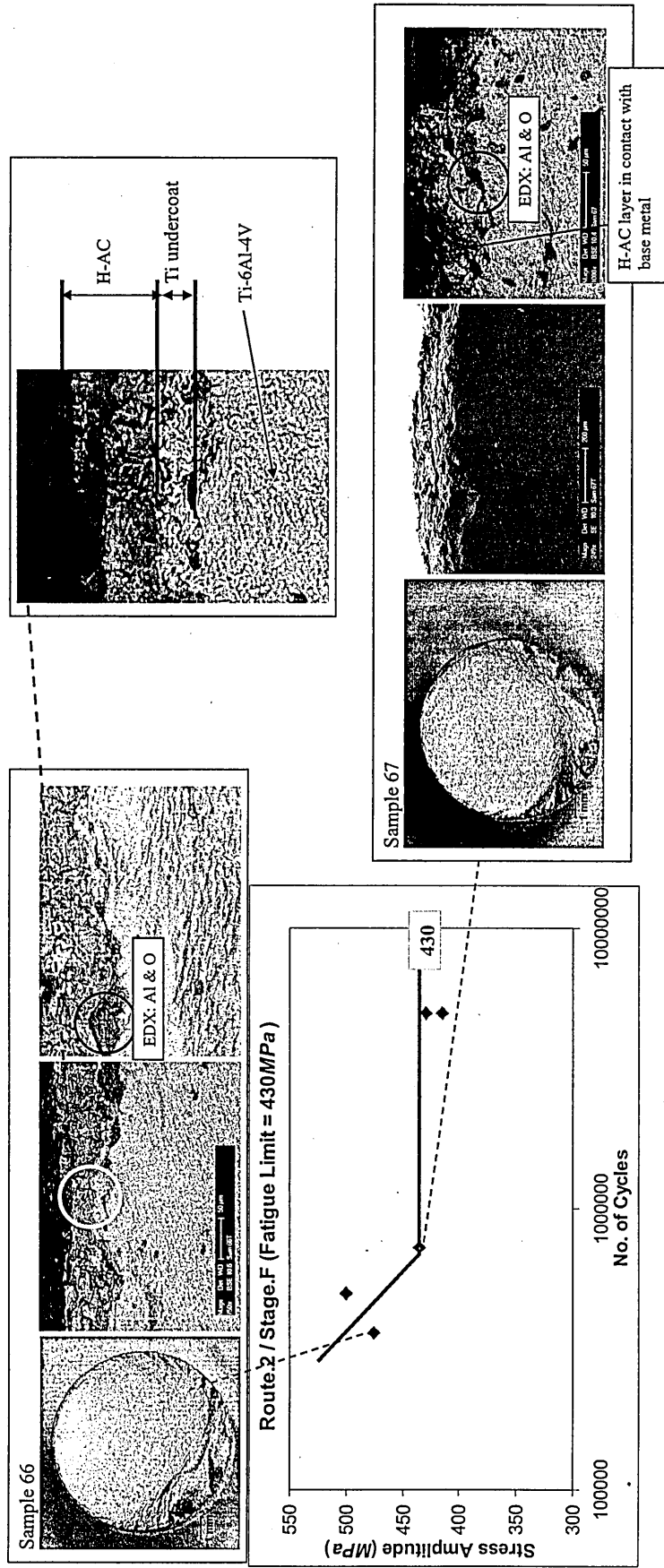


Sam No.	Stress Amp. (MPa)	No. of cycles	Surface roughness (μm), Residual stress (MPa)	No of crack initiation features: with remarks	Defects at initiation region	% fatigue vs. overload	Comments related to manufacturing process	Comments related to JRI in-vivo failures (cone region)
48	545	141289	51 μm	Dominant single initiation point.	Dent like feature $w \approx 100\mu\text{m}$, $d \approx 50\mu\text{m}$ deep with embedded particle.	75	EDX shows initiation area is rich with Al and O. Possible inclusion due to Grit blasting.	1. A notch/dent like defect at initiation.
49	523	447234		Dominant single initiation point.	Dent like feature $w \approx 80\mu\text{m}$, $d \approx 50\mu\text{m}$ deep with embedded particle.	75	EDX shows initiation area is rich with Al and O. Possible inclusion due to Grit blasting.	2. Similar to Route.1 Stages C&D
50	520	246895	-311MPa	Dominant single initiation point.	Dent like feature $w \approx 80\mu\text{m}$, $d \approx 50\mu\text{m}$ deep with embedded particle.	75	EDX shows initiation area is rich with Al and O. Possible inclusion due to Grit blasting.	
54	524	1004055		Dominant single initiation point.	Dent like feature $w \approx 80\mu\text{m}$, $d \approx 50\mu\text{m}$ deep with embedded particle.	75	Notch like feature at initiation.	



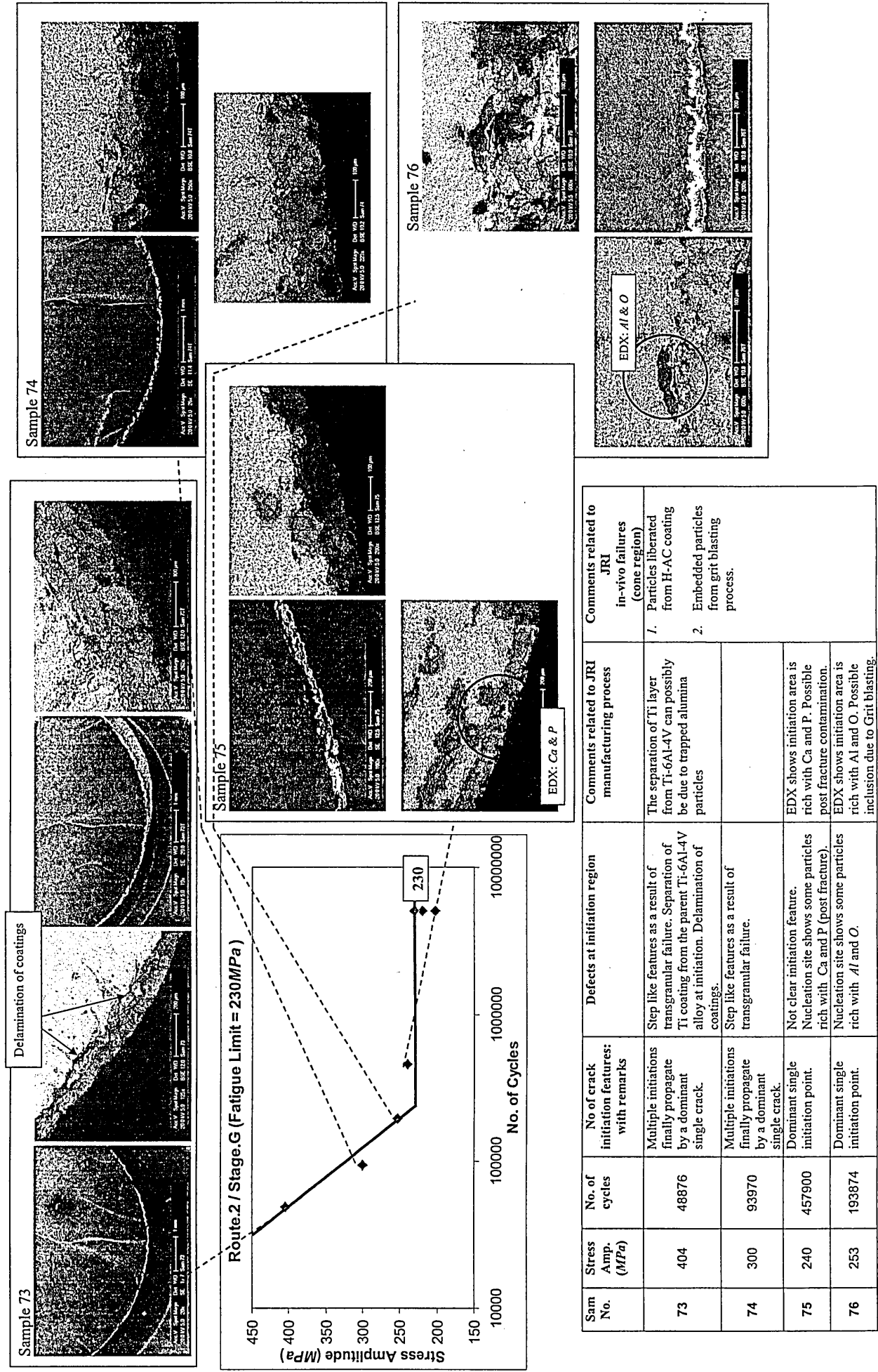
Sam No.	Stress Amp. (MPa)	No. of cycles	Surface roughness (μm), Residual stress (MPa)	No of crack initiation features: with remarks	Defects at initiation region	% fatigue vs. overload	Comments related to JRI manufacturing process
59	524	217963	73.7μm	Single dominant crack propagation.	Dent like feature ≈50μm wide, ≈5μm deep and visible inclusion near initiation.	65	Deep dent like feature can be as a result of grit blasting process.
60	519	348599	+15MPa		Embedded particle rich with Al and O	65	EDX indicates the inclusion is rich with Al and O.
62	552	168404			Embedded particle at the initiation area ≈25μm in size.	70	EDX indicates the inclusion is rich with Al and O. Possible alumina particle.

APPENDIX.22; Route.2 / Stage.F (Sequence of manufacturing processes involved; annealed – grit blasted - ultrasonic cleaned - Ti coated - H-AC coated)

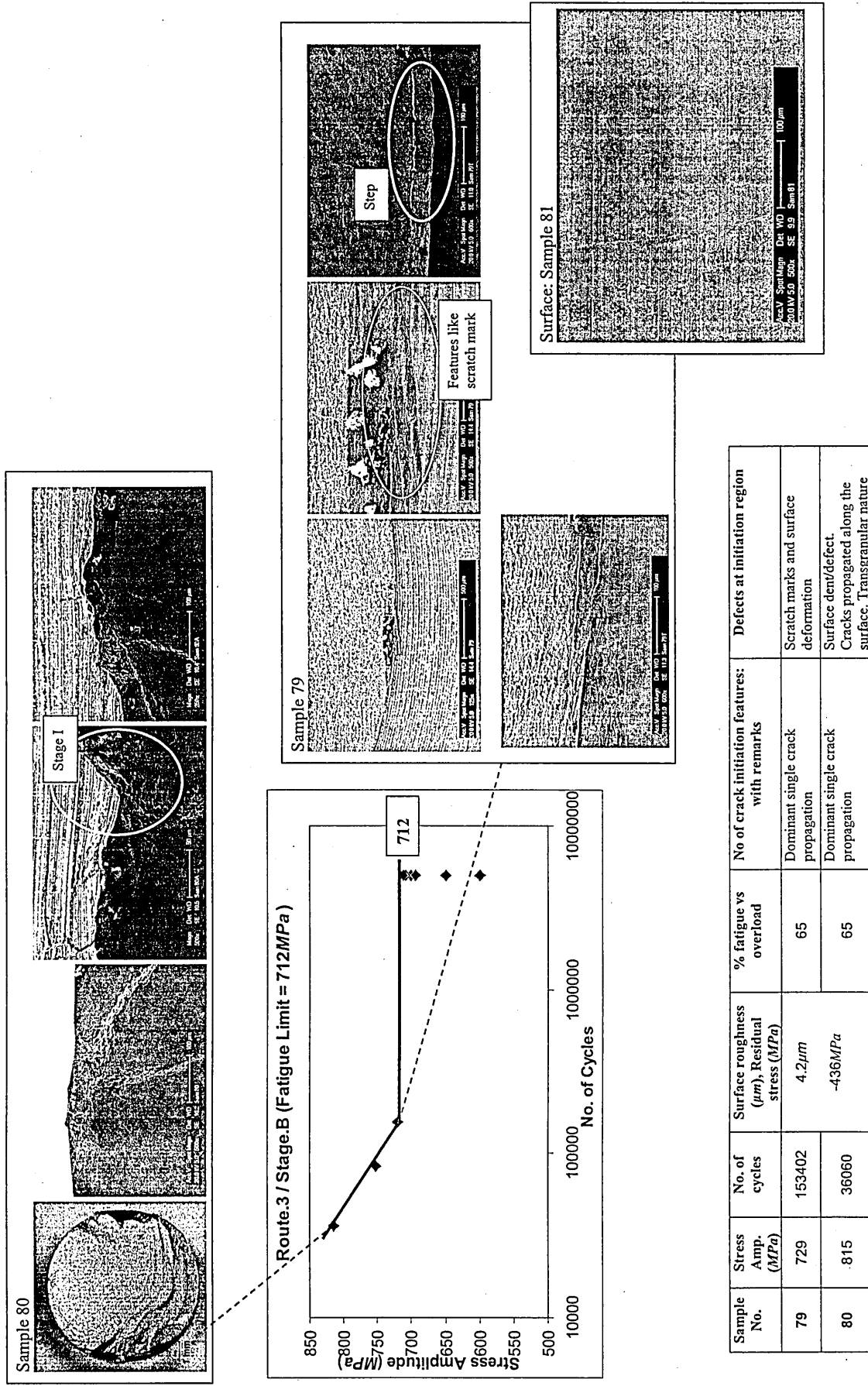


Sam No.	Stress Amp. (MPa)	No. of cycles	No of crack initiation features: with remarks	Defects at initiation region	% fatigue vs. overload	Comments related to JRI manufacturing process
66	535	725682	Single dominant propagation.	Particles embedded between Ti/Ti-6Al-4V substrate. Possible particulate matter found at the initiation point.	75	Possibly alumina particles embedded between Ti/Ti-6Al-4V interface which lead to initiate the fatigue failure.
67	475	360097	Single dominant propagation.	A separation of Ti from Ti-6Al-4V layer is visible. EDX shows these separated area are rich with foreign elements (Al and O)	75	H-AC layer in contact with Ti-6Al-4V base.

APPENDIX.23; Route.2 / Stage.G (Sequence of manufacturing processes involved; annealed – machined – grit blasted – ultrasonic cleaned – Ti coated – H-AC coated – Annealed)

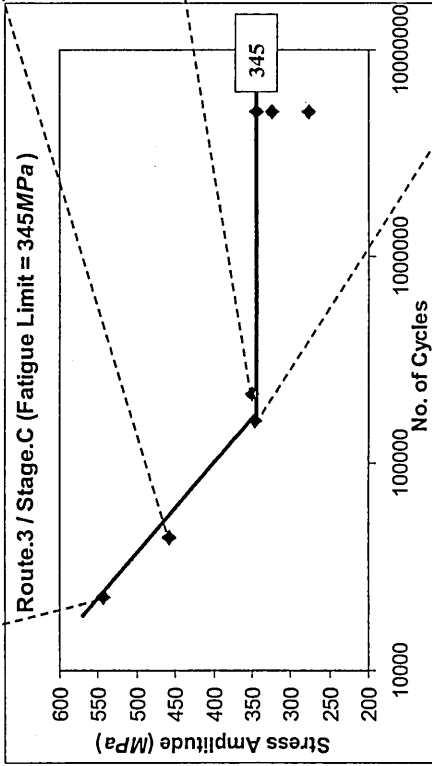
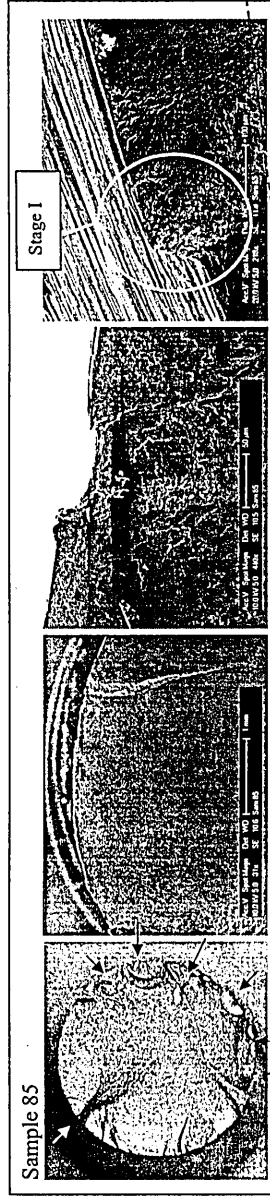


APPENDIX.24; Route.3 / Stage.B (Sequence of manufacturing processes involved; annealed – machined)



Sample No.	Stress Amp. (MPa)	No. of cycles	Surface roughness (µm), Residual stress (MPa)	% fatigue vs overload	No of crack initiation features: with remarks	Defects at initiation region
79	729	153402	4.2µm	65	Dominant single crack propagation	Scratch marks and surface deformation
80	.815	36060	-436MPa	65	Dominant single crack propagation	Surface dent/defect. Cracks propagated along the surface. Transgranular nature

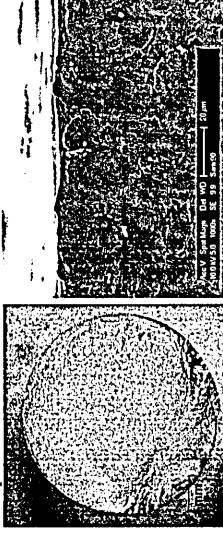
APPENDIX.25; Route.3 / Stage.C (Sequence of manufacturing processes involved; annealed – machined – shaped/glazed)



Sample 86



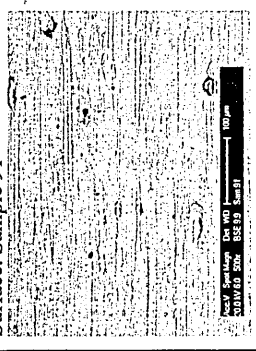
Sample 90



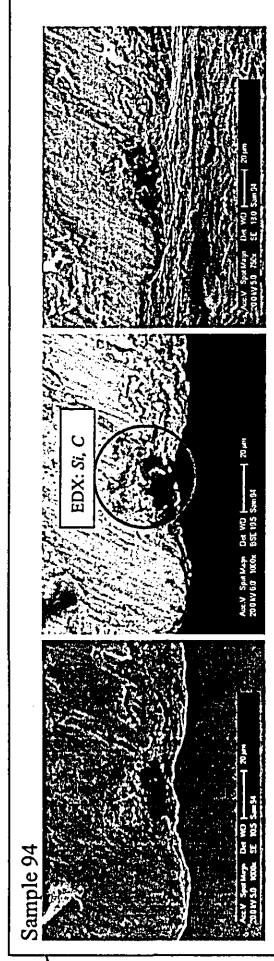
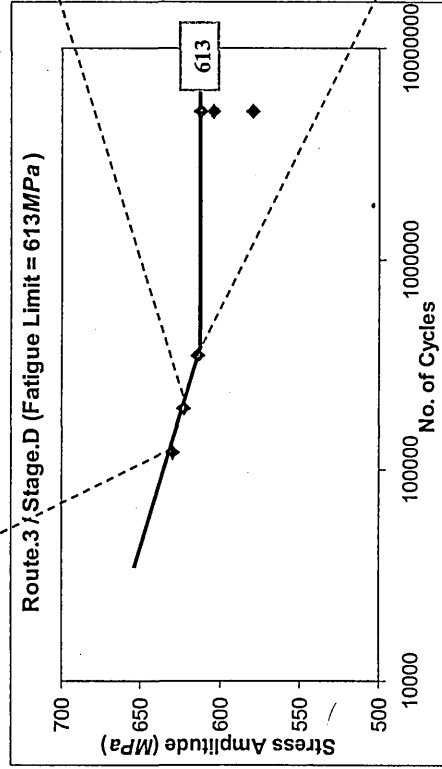
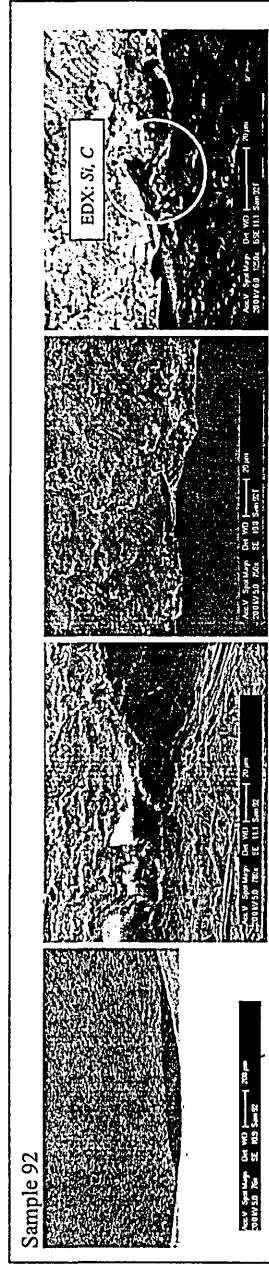
Sample 87



Surface: Sample 91

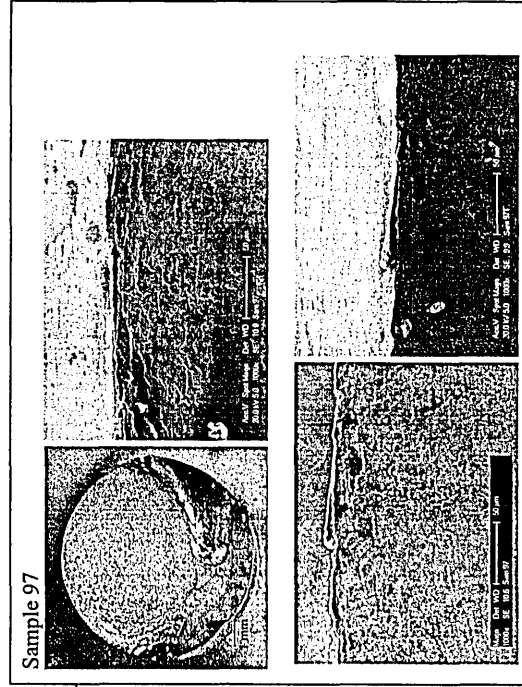
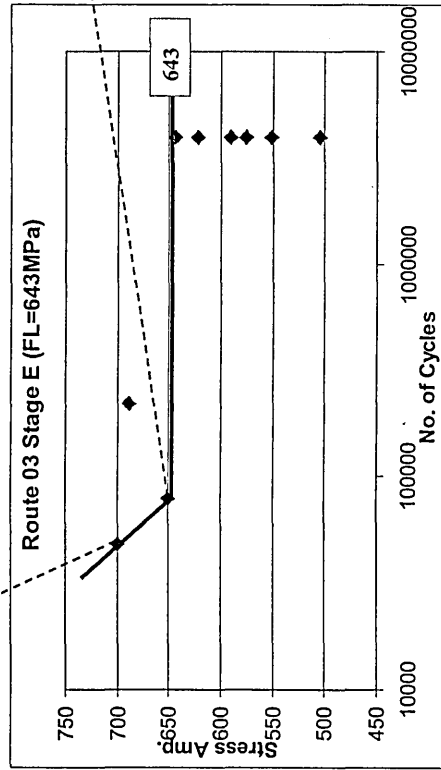
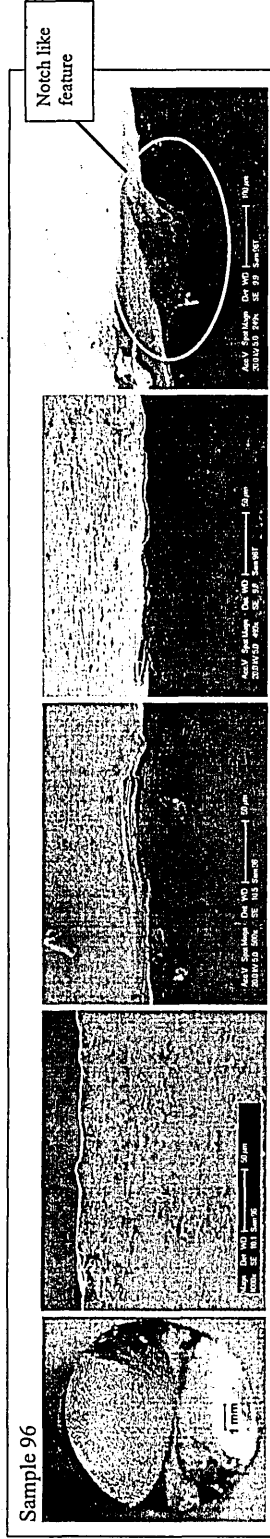


Sam No.	Stress Amp. (MPa)	No. of cycles	Surface roughness (μm), Residual stress (MPa)	No of crack initiation features: with remarks	Defects at initiation region	% fatigue vs. overload	Comments related to manufacturing process	Comments related to JRI in-vivo failures (neck region)
85	544	22782		Multiple initiation sites around the periphery.	Glazing marks can be identified on the surface and initiation always occur influencing deeper surface feature.	40	Surface is rough with uneven features. These can be formed because of machining and grinding operations. Deep machine marks remain on the surface even after glazing operation. So these can influence the initiation of failure.	Deformed lip like feature / thumb nail cracks.
86	458	44053	13.1 μm	Multiple initiation sites around the periphery.	Multi start leads transgranular fracture surface. Crack propagates along the sample surface. Lip like feature visible in one surface possibly due to rubbing of both surfaces while failure taking place.	50	Surface is rough with uneven features. These can be formed because of machining and grinding operations. Deep machine marks remain on the surface even after glazing operation. So these can influence the initiation of failure.	Deformed lip like feature / thumb nail cracks.
87	346	159984	+35MPa	Single dominant initiation.	Lip like feature along the circumference at initiation.	70	Reduction of fatigue limit can occur as a result introduction of tensile residual stress resulted by localized heating due to glazing.	Deformed lip like feature / thumb nail cracks.
90	350	218106		Single dominant initiation.	Polish or machine mark visible as a dent near initiation.	70	Reduction of fatigue limit can occur as a result introduction of tensile residual stress resulted by localized heating due to glazing.	Deformed lip like feature / thumb nail cracks.



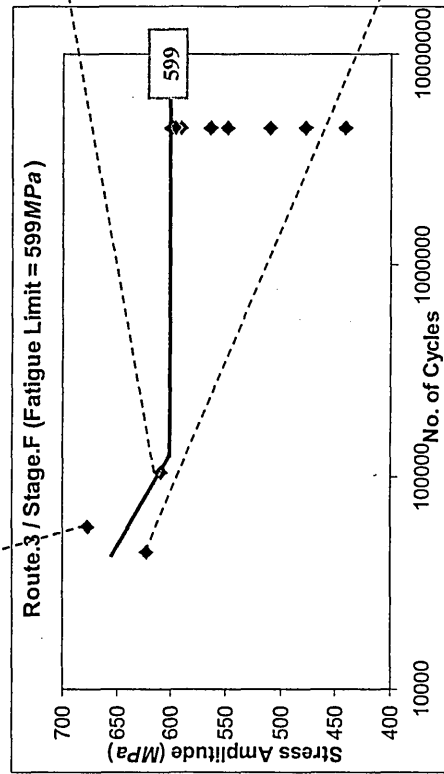
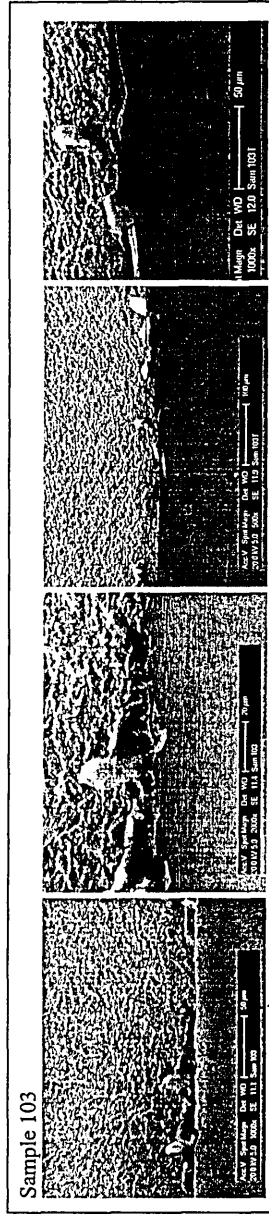
Sam No.	Stress Amp. (MPa)	No. of cycles	Surface roughness (μm), Residual stress (MPa)	No of crack initiation features with remarks	Defects at initiation region	% fatigue vs. overload	Comments related to JRI manufacturing process	Comments related to JRI in-vivo failures (neck region)
92	630	121878	5μm -392MPa	Single dominant initiation.	Lip like feature ~500μm along perimeter. Clearly visible surface feature near initiation.	65	Sample surfaces contain glazing marks, which clearly influence the crack initiation. Initiated and propagated along surface are influenced by glazing marks. The dent on the initiation on Sam 94 is rich with Si and C according to EDX due to glazing and polishing processes.	1. Shallow surface damage is visible at initiation.
94	623	196790		Single dominant initiation.	Dent like feature ~20μm deep at initiation area. Clearly visible surface feature near initiation. Inclusion rich with Si and C.	70		2. Cavities at initiation, presence of surface defects.
95	614	344663		Single dominant initiation.	Dent like feature ~20μm deep at initiation area. Deformed lip like feature along the periphery.	60		3. Formation of lip like features at initiation.

APPENDIX.27; Route.3 / Stage.E (Sequence of manufacturing processes involved; annealed – machined – glazed – polished – rumbled – polished – polished)

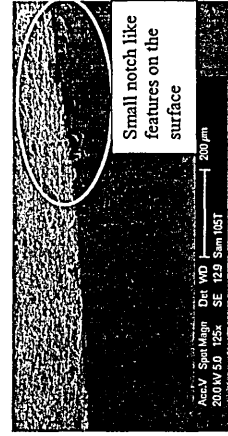
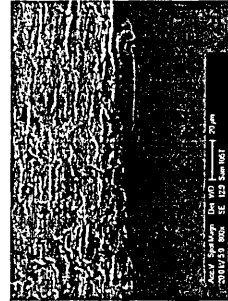
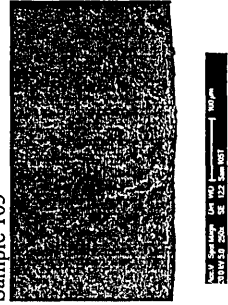


Sam No.	Stress Amp. (MPa)	No. of cycles	Surface roughness (Ave Rp+Rv, μm), Residual stress (MPa)	No of crack initiation features: with remarks	Defects at initiation region	% fatigue vs. overload	Comments related to JRI manufacturing process	Comments related to JRI in-vivo failures (neck region)
96	699	47820	0.68 μm -337MPa	Clear two initiation points. Propagates from deferent planes and resulted transgranular fracture. Single dominant initiation.	A dent $\approx 100\mu\text{m}$ width $\approx 40\mu\text{m}$ deep at initiation area. Deformed surface feature visible at the initiation.	40	Surface is very well polished. The fatigue failure initiated from a surface feature leaving some sort of plastic deformation near initiation.	I. 'Gouge' marks / surface anomaly (dent) $\approx 100\mu\text{m}$ width at the initiation.
97	650	79975				70		

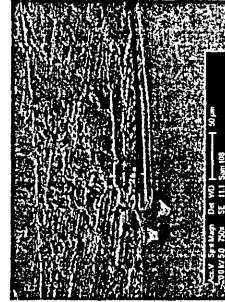
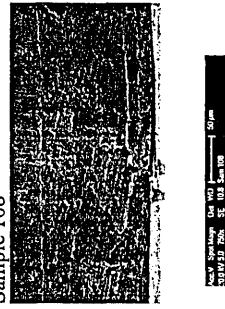
APPENDIX.28; Route.3 / Stage.F (Sequence of manufacturing processes involved; annealed – machined – shaped/glazed – polished – rumbled – polished – polished – annealed)



Sample 105



Sample 108



Sam No.	Stress Amp. (MPa)	No. of cycles	Surface roughness (Ave Rp+Rv, μm), Residual stress (MPa)	No of crack initiation features: with remarks	Defects at initiation region	% fatigue vs. overload
103	677	58259	0.68 μm +102MPa	Single dominant initiation.	Clearly visible surface defect at the initiation along transverse direction.	60
105	623	44087		Single dominant initiation.	Clearly visible surface defect at the initiation along transverse direction.	55
108	609	105554		Single dominant initiation.	Clearly visible surface defect at the initiation along transverse direction.	60